ISOLATED EARLY-TYPE GALAXIES AND THE USE OF X-RAY DIAGNOSTICS TO DETERMINE THE EVOLUTION HISTORY OF MERGING AND MERGED SYSTEMS

by

Christopher Robert Fuse

Bachelor of Science, 2000

St. Bonaventure University

St. Bonaventure, New York

Master of Science, 2002

Miami University

Oxford, Ohio

Submitted to the Graduate Faculty of the

College of Science and Engineering

Texas Christian University

In partial fulfillment

of the requirements for the degree

Doctor of Philosophy

December 2008

Acknowledgments

I would like to thank both of my advisors, Dr. Pamela Marcum and Dr. Michael Fanelli. Both have given me guidance, insight and support during my time as a member of the Astrophysics Group at TCU. I know my future as an astronomer and as an educator has been uniquely influenced by their encouragement. I would also like to thank the faculty, staff, and students in the Department of Physics and Astronomy at TCU for the past three years of stimulating conversations/lectures.

I would like to acknowledge the facilities of McDonald Observatory (operated by the University of Texas at Austin), the Chandra X-ray Observatory, and the Sloan Digital Sky Survey, which were all instrumental in the completion of this dissertation. A very special thanks goes to Dave Doss for his patience and late night assistance when problems occurred at the telescope. The project would also not have been possible without the support provided through a NASA / Texas Space Grant Consortium Fellowship, NASA grant #NNG05C53G.

Finally, I would like to thank all of my friends and family. To my parents, for giving an eight year-old that wanted to earn a Ph.D. in astrophysics the opportunity to explore to world and take apart household electronics. Most of all I need to thank my wife, Marisa, and my son, Quinn. Thank you both for putting up with me while I chased my dreams.

Table of Contents

List of Figures

List of Tables

Chapter 1

Introduction to the Manuscript

The topic of the current study is an examination of one of the rarest galaxy types, the isolated early-type galaxy. The dissertation details the identification and analysis of a sample of early-type galaxies more isolated than those found in any previous work. The work presented here will try to answer fundamental questions regarding early-type galaxies: Are these isolated galaxies pristine, having formed free of past mergers or interactions, or are they the remains of two merged disk galaxies or a merged group of galaxies? What signatures of the hot gas can be expected if an isolated elliptical is a merged group remnant or a pristine system? The frequency of pristine systems and of merger remnants can be used to quantify the importance of interactions in early-type galaxy formation. The work presented here seeks to build upon the candidate passively evolving ellipticals, KIG 557 and 824 (Marcum, Aars, & Fanelli 2004). The ultimate goal of the dissertation is to find pristine early-type galaxies that can serve as the zero-to-low interaction baseline necessary to study the properties of early-type galaxies that are the result of environment or those which are intrinsic to all E+S0 galaxies.

1.1 Aims of Current Study

The research presented herein seeks to better understand galaxy formation and evolution via an examination of early-type galaxies in extreme isolation. As previous studies have searched for evidence of mergers and interactions around isolated galaxies, results indicate that many such features are optically short-lived. Therefore, we will evaluate whether X-ray emitting hot gas in galaxies can be used as a long-lived diagnostic needed for galaxy evolution analyses. We anticipate that X-ray wavelengths will provide astronomers with a powerful tool to study galaxy evolution, because the hot X-ray emitting gas remains hot for ∼Hubble time, meaning merger signatures will be long-lived. More specifically we want to verify or refute the theory that compact groups, isolated elliptical galaxies, and fossil groups form an evolutionary sequence based on their X-ray gas properties. Prior studies have indicated that isolated ellipticals and fossil groups are the remains of a coalesced compact group. We expect those galaxies to have similar X-ray luminosities and gas temperatures, verifying the theorized evolutionary sequence.

We will also examine the X-ray emission in S0 galaxies in an attempt to gain insight into the formation and evolution of such systems. Formation mechanisms of S0 galaxies remains poorly understood and we expect that the first comprehensive examination of the S0 morphology at X-ray wavelengths will result in a better understanding of the interaction processes S0 galaxies encounter in different density environments. Both components of the X-ray investigation are significant as they rep-

resent a complete Chandra archival analysis of compact groups, isolated ellipticals, fossil groups, and S0s.

One issue arises from our X-ray investigation of isolated ellipticals. The galaxies listed as isolated ellipticals in the Chandra archive were not selected using a uniform isolation criterion. Without a consistent degree of isolation we cannot be sure that the galaxies have remained unperturbed for much of their lifetimes. In order to thoroughly evaluate formation and evolution theories, we require the creation of a sample of isolated early-type galaxies that have been selected based on a robust morphological classification and a quantifiable set of isolation criteria. The extreme isolation of the candidate galaxies would make them ideal laboratories to examine environmental effects in the evolution of early-type galaxies. Constraints could then be placed on interaction-driven evolution and the processes intrinsic to all early-type galaxies.

As the sample of isolated early-type galaxies was to be drawn from the $\sim$675,000 galaxies spectrophotometered by the Sloan Digital Sky Survey (SDSS), a method of selecting elliptical and S0 galaxies was necessary. With many parameters available to morphologically select a sample, we embarked on a test to determine which classification method would yield the most early-type galaxies while minimizing the contamination by spiral galaxies. We anticipated that the most robust classifier would use some measure of the galaxy light profile to separate spheroidal from spiral systems.

Any sample drawn from a large population will suffer from some degree of contamination as all observable galaxy properties have significant dispersion across multiple morphologies. For the proposed investigation of isolated early-type galaxies, the contamination that is most difficult to identify comes from Sa galaxies. An examination of optical and infrared parameters was performed in order to find a division between Sa and S0 galaxies. Visual inspection of galaxies images was expected to remain the easiest process to find spiral galaxies within the isolated early-type galaxy sample. However we hoped that a more quantitative and efficient method could be found.

In order to establish a sample of galaxies that have remained unperturbed for much of their lifetimes, we required definition of a strict set of isolation criteria. The advantage of selecting the isolated galaxy sample from the SDSS was the superior redshift information provided. A determination of galaxy isolation in three-dimensions is groundbreaking, as all previous authors have defined only a two-dimensional, on the sky isolation. The minimum two-dimensional distance between an isolated candidate galaxy and a companion, 2.5 Mpc, is the most extreme isolation value that has ever been employed. Three-dimensional isolation was guaranteed by requiring the recessional velocity difference between a candidate galaxy and a companion be greater than 350 km s^{-1}. The 3D isolation coupled with a robust mechanism to select early-type galaxies was predicted to yield the most highly isolated sample of elliptical and S0 galaxies ever compiled. Based on prior studies, we expected to select forty

isolated early-type galaxies, three of which would possess properties suggestive of a formation by monolithic collapse in the early universe.

One issue does arise from the use of recessional velocity to certify three-dimensional isolation. The issue has to do with peculiar velocities, those velocities of a galaxy that are not associated with the expansion of the universe. Determining a galaxy′s peculiar velocity is a difficult task. Difficulty arises when, on the flat plane of the sky, two objects appear side-by-side and they may actually be far apart and just happen to lie along the same line of sight. The major uncertainty associated with determining the three-dimensional isolation stems from the inability to account for the true peculiar velocities of a neighbor galaxy near an isolated candidate.

We have chosen to use the recessional velocity to estimate the contribution of a neighboring galaxy′s peculiar velocity towards the candidate isolated galaxy. A recessional velocity of 350 km s^{-1} was chosen as that velocity represents the average loose group velocity dispersion. The radial component of the 350 km s^{-1} velocity for any projected separation, θ, between the candidate galaxy and a neighbor is given by the following equation.

$$\cos(\theta) = \left(\frac{v_{radial}}{350\,\mathrm{km\,s^{-1}}}\right) \tag{1.1}$$

If we assume a worst-case scenario in which the neighbor galaxy had a peculiar velocity of 350 km s^{-1} directed towards the candidate we could determine the radial velocity for any angular separation between the neighbor and the candidate.

$$v_{rmax} = 350\,\mathrm{km\,s^{-1}} \times \cos(\theta) \tag{1.2}$$

Constraining the evolution of the isolated galaxies is a major aspect of the research presented here. An investigation into the optical and spectral properties were assumed to be a viable means of detecting any merger or interaction features, such as shell structures, tidal features, and enhanced star formation. Previous authors had found evidence for large-scale mergers in $\sim$50% of their samples and we expected to find a similar proportion. The excellent spectral data produced by the SDSS was hoped would provide information on the dominant stellar population, the star formation rate, and the metal enrichment of the isolated galaxies. We expected the galaxy spectra to be dominated by an older stellar population with no current star formation and near solar metallicities, all features of a typical early-type galaxy spectra.

In chapter 2 we present the results of the X-ray investigation of Chandra archival samples of compact groups, fossil groups, and isolated elliptical galaxies. The chapter will detail the examination of the theorized evolutionary path where galaxies within a compact group merge, resulting in an isolated elliptical and in time a fossil group. Chapter 2 also explores the X-ray emission in a sample of S0 galaxies across a variety of environments.

Details of the classification of galaxy morphology are highlighted in chapter 3. Also discussed in the chapter are the efforts to determine a quantitative process of removing spiral galaxy contaminants from a sample of elliptical and S0 galaxies.

Chapter 4 presents the three-dimensional isolation criteria employed in the current investigation. The sample of isolated early-type galaxies is discussed for both the

SDSS and deep McDonald Observatory imaging. Data from the integrated photometry, surface brightness profiles, and fine structure analyses are examined to achieve a better understanding of the formation and evolution mechanisms the sample galaxies have experienced.

In chapter 5 we detail the results of the analysis of the SDSS spectra of the isolated galaxies. The general trends observed for the spectra will be highlighted. Analysis of the star formation rates, as determined by the Hα emission, are presented. The metal content and nuclear activity will also be evaluated for the sample galaxies with emission-line spectra.

1.2 Classification & Morphological Characteristics

Before one can understand why isolated early-type galaxies have astrophysical significance, one first needs to become familiar with the classification of galaxies as well as an understanding of the relationship between galaxy morphology, environment and their effects on galaxy evolution. The predominant classification scheme was developed by Edwin Hubble (Hubble 1926). The Hubble classification and the majority of classification systems that have followed have been based on the appearance of a galaxy′s shape at optical wavelengths and as such do not account for a galaxy′s physical properties.

The Hubble classification scheme, seen in Figure 1.1, separates ellipticals by axial ratio and organizes spiral galaxies by disk-to-bulge ratio and the winding of arm

structure. Theories had postulated that Hubble's Tuning Fork was an evolutionary sequence, with galaxies evolving from ellipticals into spiral galaxies. Work by Eggen (1962) showed that evolution from left to right along the Hubble sequence was an unlikely scenario. Numerical simulations have shown that there is no process by which an elliptical can begin to spontaneously rotate about a preferred axis and transform into a spiral galaxy (Barnes 1989). Later simulations suggest evolution occurs from right to left along the Hubble diagram (Toomre & Toomre 1972). Spirals can interact and merge, eventually developing into elliptical galaxies (Barnes 1985). Support for such a model comes from the fact that ellipticals and other early-type galaxies are most often found in regions of increased merger activity, such as rich clusters and groups. In these clusters, mergers are thought to be common and a likely mechanism for forming ellipticals (D′Onghia et al. 2005).

Early-type galaxies are the catch-all term for elliptical and S0 galaxies. S0s, also referred to as lenticulars, are bulge-dominated systems having a disk but no arms. The absence of arms and a deficiency in interstellar gas are the principle means of distinguishing S0s from spirals (Binney & Tremaine 1987). S0s were envisioned to be an intermediate class between ellipticals and spirals, an idea supported by de Vaucouleurs (1961) and Hogg et al. (1993), which showed that S0s have colors and interstellar medium intermediate between ellipticals and spirals, respectively.

Both ellipticals and S0s lack recent star formation and appear red in color, suggesting a stellar population of old K and M stars. The important properties of elliptical

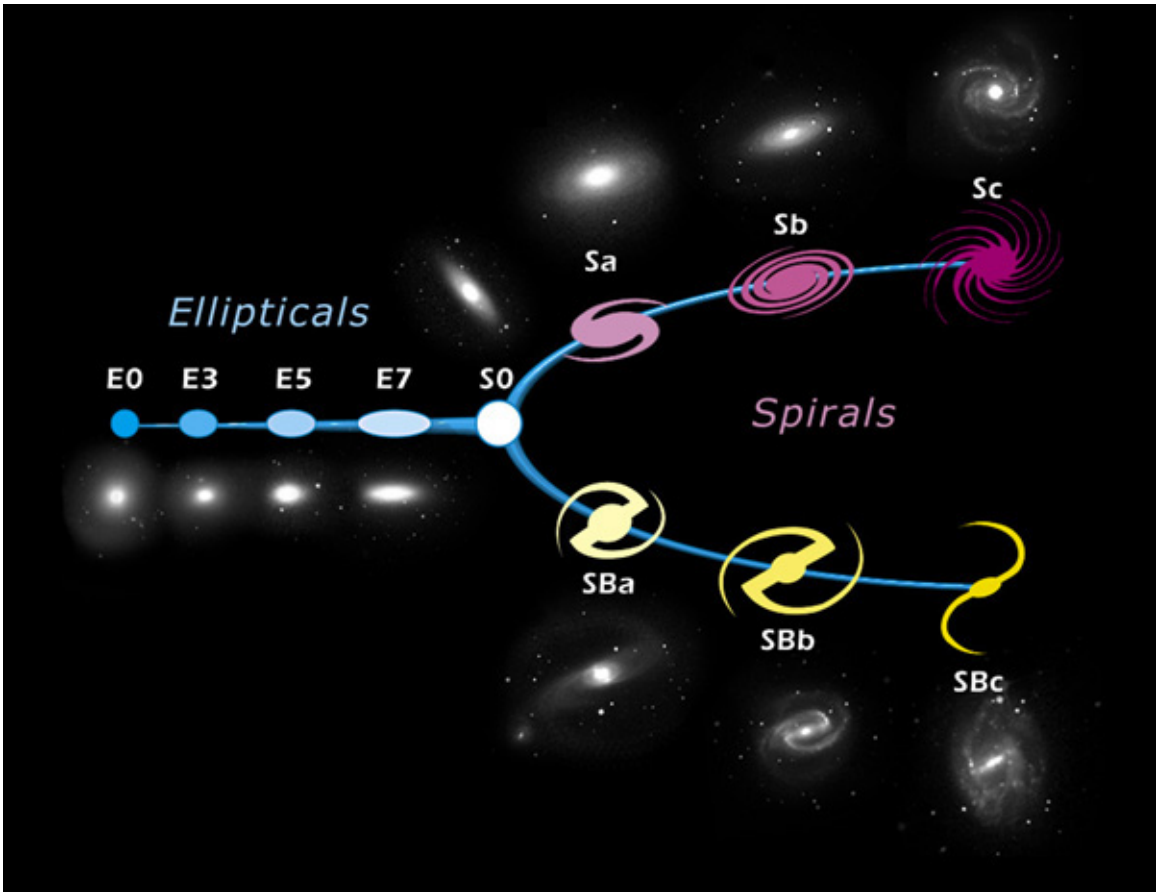

Figure 1.1: Hubble Classification (Tuning Fork Diagram)

and lenticular galaxies (Zombeck 2006) are listed in Table 1. Early-type systems can be identified by a number of properties, both physical and optical. E+S0 galaxies are predominantly found in high-galaxy density environments, such as clusters and groups. Normal elliptical galaxies exhibit red colors with $0.9 \leq \mathrm{B-V} \leq 1.0$, while typical S0 galaxies have $0.88 \leq \mathrm{B-V} \leq 0.97$ (Roberts & Haynes 1994). Most ellipticals possess low-density gas at a temperature of 1 keV, visible in X-ray emission. Lenticulars have been observed to have hot X-ray gas, but their X-ray emission is

Table 1.1. Properties of Elliptical and S0 Galaxies

Property	Elliptical Galaxies	S0 galaxies
Shape	Round or triaxial	Bulge + small disk
ISM	Low density, hot gas	Some hot gas in the bulge
Mean age	≥10 Gyrs	3-10 Gyr
Stellar Content	Old, metal-rich	Old, metal-rich
B−V color	0.9 - 1.0 mag	0.88 - 0.97 mag
Gas temperature	∼1 keV	∼0.85 keV

often dominated by luminous point sources (Fabbiano 2006). Being more rare than spirals, early-type galaxies account for ∼18% of the bright galaxies in the universe.

Early-type galaxies display robust 2D symmetry, but may have three-dimensional shapes that are oblate or triaxial. The amount of ellipticity, E_N, which is used in the Hubble classification (E0, E1, etc.) is determined by,

$$N = 10\left(1 - \frac{b}{a}\right) \tag{1.3}$$

The degree of elongation or ellipticity is not completely well defined, as many E+S0s have radially varying ellipticities. The amount of flattening may be an artificial effect of viewing angle. If the galaxy has a triaxial shape, a side-on viewing angle will cause the galaxy to appear more elongated.

The final galaxy morphology discussed here is that of dwarf galaxies. These systems had remained unstudied until the advent of sensitive CCD technology capable of detecting their low luminosities (Gallagher 1998). What separates a dwarf galaxy from a "giant" elliptical or spiral, is the galaxy′s integrated luminosity. The defining luminosity that separates a dwarf from a giant is highly debated and the value varies across different samples. Galaxies fainter than $M_B = -18.0$ were selected as dwarfs in the studies of Aaronson et al. (1985) and van Zee et al. (2000), while dwarfs were classified as galaxies with $M_B \leq -16.0$ by Tammann (1980) and Gu et al. (2006). The range in brightness for what is considered a dwarf galaxy can greatly affect the understanding of properties and evolution of these galaxies. Dwarfs are of great relevance in the current study, therefore a galaxy was considered a dwarf if its absolute B magnitude was fainter than -16.5 (Hodge 1971). These faint galaxy systems are also known to be gas-deficient and show no signs of recent star formation. Dwarf galaxies also have typical colors of $0.6 \leq B-V \leq 0.7$ (Hodge 1971).

1.3 Formation Mechanisms

Formation of early-type galaxies can be seen as a question of nature versus nurture. A number of possible scenarios can account for the properties of elliptical galaxies. Did ellipticals form by the dissipationless collapse of a cloud with no rotation (Aguilar & Merritt 1986) or did they form as a result of merging spirals in a high-density region?

The classical monolithic formation scenario for ellipticals is a single intense burst of star formation at an early epoch ($z \geq 5$), followed by passive evolution of the stellar populations to the present day (Partridge & Peebles 1967; Larson 1975; Chiosi & Carraro 2002). Simple physical arguments show that if the collapsing gas cloud has spin, the result could be an elliptical with disky structures. A monolithic collapse elliptical likely would be extremely old, having formed in the early universe.

Alternatively, ellipticals may be the end result of a merger of two spirals galaxies. Numerous simulations have shown that the remnants of colliding spirals have the appearance and properties similar to those of observed elliptical galaxies (Barnes 1985; Naab et al. 2006). Figure 1.2 gives an example of a recent simulation with two spirals interacting and merging. Ellipticals could also have formed from the continual slow build-up, by accreting small satellites and gas. Such a formation is thought to occur in clusters where mergers of spirals and dwarf companions results in an elliptical galaxy. This scenario is one of many mergers throughout the elliptical′s lifetime (Toomre & Toomre 1972; White & Frenk 1991). Such a gradual build-up of smaller galaxies would likely cause the infusion of additional gas and bursts of star formation (Kauffmann et al. 1993). The slight increase in the star formation rate would produce regions of blue colors that should easily be detectable against the old, red stellar population commonly seen in early-type galaxies (Kochefar & Burkertt 2003).

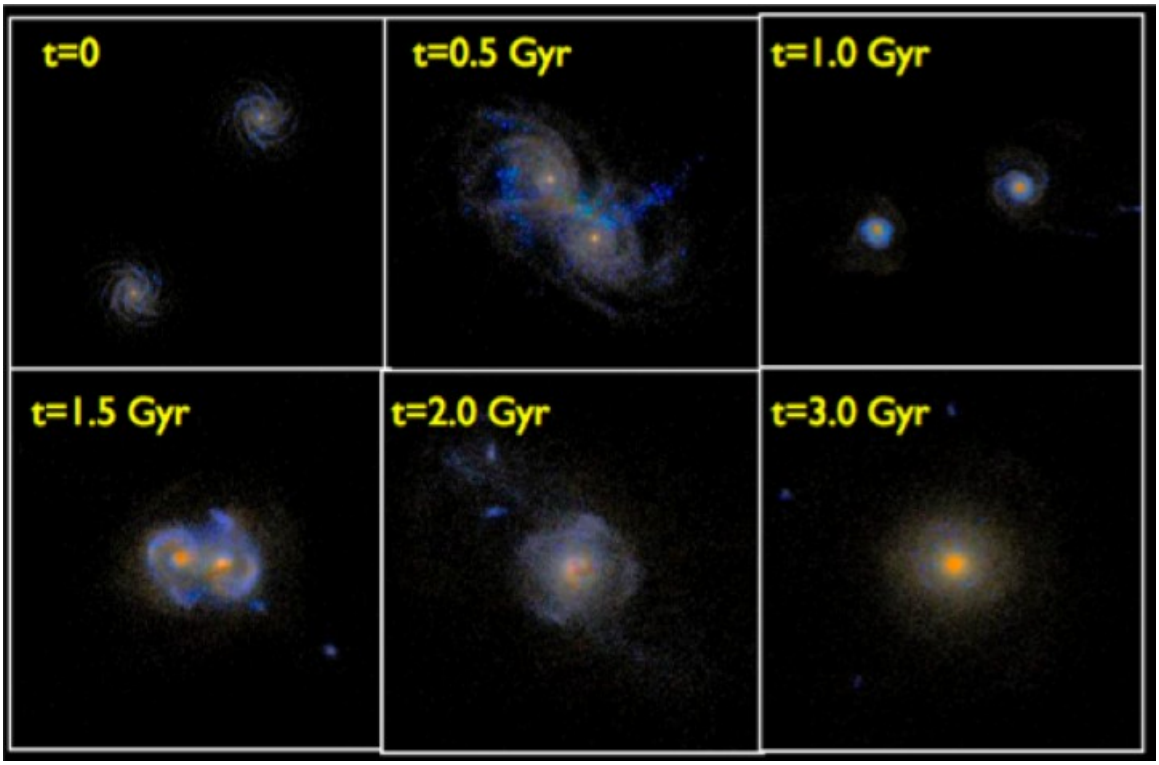

Figure 1.2: Numerical simulation of Mihos (1999): Spiral galaxies merging and forming an elliptical galaxy

The scenarios for formation of lenticular galaxies are not as well defined or understood. The current formation theories for S0s are primarily a function of environment. S0 galaxies are most often found in clusters and groups and are subject to an increased interaction and merger rate. The dominant theory for forming S0s is the stripping of gas from spirals. Spitzer & Baade (1951) proposed that galaxy-galaxy interactions could strip gas from spirals, while galaxy-cluster interactions were proposed by Goto et al. (2003). The removal of gas from spirals is still an incomplete mechanism for reproducing lenticular properties. The biggest issue arises from the theory's inability to increase the spiral bulge to match values found in S0s. While many ellipticals have

been found in the field, isolated S0s are even more rare and no sufficient formation mechanism has been postulated to explain such galaxies in low-density environments. An internal process appears necessary to form a field lenticular (Larson et al. 1980; Bekki, Shioya & Couch 2002).

1.4 Environmental Effects on Galaxies

Dressler (1980) first quantified the morphology-density relation noting that the fraction of E+S0 galaxies increases as the local galaxy density increased. Cluster and group environments increase the possibility for gravitational interactions (Thomson & Wright 1990), which can cause significant changes to a galaxy′s morphology, star formation rates and light distribution (Toomre & Toomre 1972). Tidal stripping (Aguilar & White 1990) can cause stars and gas to be redistributed. Increased star formation or the development of tidal tails can result from tidal stripping (Lee, McCall, & Richer 2003).

Ellipticals and S0s are most likely to be members of a rich cluster. A rich cluster is a gravitationally bound collection of galaxies often numbering in the thousands. Up to 60% percent of the galaxies in rich clusters are early-type systems. Since approximately one-fifth of the universe's bright galaxies are ellipticals, the majority of the brightest ellipticals are found in clusters.

Far more common than clusters are loose and poor groups. Typically, loose groups are only a few percent as massive as rich clusters. The dominant galaxy morphology

in these lower galaxy-density environments is, as expected, spirals. Of particular importance to the current work is a special class of group, known as a compact group. Compact groups generally consist of four to eight galaxies in an overall isolated environment. Compact groups share much in common with clusters. While there are only a few galaxies in a compact group, the densities have been found to reach values equal to or exceeding the galaxy density of the cores of rich clusters (Hickson 1982; Hickson et al. 1992).

A few galaxies do not belong to high-density galaxy configurations and are classified as field galaxies. Such low-density regions tend to be populated by spirals. As compared to cluster and group members, the low-density field allows galaxies to passively evolve having very low interaction and merger rates. A low interaction rate makes field galaxies excellent laboratories to study how galaxies evolve.

As multiple formation scenarios can explain early-type galaxies, there exists the possibility that field galaxies have experienced large-scale external interactions. The formation process of some field galaxies was likely due to the coalescence of a small group of galaxies. The merging of such a group would yield a galaxy in a low-density environment. Such merged systems, fossil groups, (Ponman et al. 1994; Khosroshahi et al. 2006) predict several distinct photometric and kinematic signatures, which would identify them as having had existed in a high-density environment. Features such as tidal tails, faint shells and non-uniform X-ray gas distribution would be telltale signs of an early-type galaxy being a group remnant. As indicated by Grogin & Geller

(1999) and Tovmassian et al. (2004), an E or S0 formed via mergers would be expected to be more luminous than a primordial, isolated early-type galaxy.

A primordial elliptical, the rare type of galaxy we are trying to find in the current study, could be formed by a non-rotating nebular cloud, created via proto-galactic collapse, that has undergone few interactions and hence is passively evolving (Eggen et al. 1962; Jimenez et al. 1999). An isolated elliptical can also be explained as having formed via the coalescence of a group of galaxies. Provided the group merged long ago, the properties of a primordial elliptical and a merger remnant would appear the same. One method for separating these two formation scenarios comes through the analysis of the galaxy's X-ray emitting gas. An investigation of the X-ray properties is detailed in Part II.

1.5 Environmental Studies of Isolated Early-Type Galaxies

Extensive work has been performed which studies the properties of samples of isolated galaxies. A galaxy that has not undergone perturbations and harassment over much of its lifetime stands as a powerful standard against which other similar morphology galaxies can be compared. One caveat is that isolation criteria have varied by study. Verification that a galaxy is isolated has often been done using a visual search for neighboring galaxies. The reliance of a visual search can create systematic

biases where chance alignments can cause an otherwise isolated galaxy to appear as a member of a galaxy-dense region. In order to better assure isolation, redshift information of nearby companions is needed. The accurate distance estimates provided by redshifts can be used to determine true neighbors from projected companions. Without redshifts for isolated galaxy candidates and neighbors, an isolated galaxy sample is incomplete.

Previous authors have compiled samples of isolated early-type galaxies (IEGs) using varying degrees of isolation. Many studies have found evidence of interactions, which argues that some isolated galaxies were once located in higher-density environments. Such findings illustrate the difficulty in detecting a population of galaxies that have not experienced large-scale perturbations over much of their lifetimes. The Catalog of Isolated Galaxies (Karachentseva 1973) has been used as the starting point for defining numerous samples of isolated galaxies of all morphologies. The isolation criteria employed by Karachentseva is based on a two-dimensional separation between an isolated candidate and neighboring galaxies. The KIG galaxies are considered isolated if no neighboring galaxy of diameter d (between 1/4 and 4 times the diameter D of the candidate) lies within 20d. The KIG sample did not use redshifts and as such, the possibility arises that many truly isolated galaxies were overlooked due to chance projections.

An early paper by Fasano & Bonoli (1989) was concerned with the cause of isophotal twists in a sample of isolated elliptical galaxies. The study selected from the UGC

catalog all galaxies classified as ellipticals, which were not members of an Abell cluster and had no UGC-observed companions. After a visual inspection for small companions, the final sample consisted of 110 elliptical galaxies. The authors found that the occurrence of isophotal twists or a varying position angle in their sample was comparable to estimates found for randomly selected galaxy samples. The isolation of the ellipticals was sufficient to conclude that tidal interactions with a neighbor cannot be invoked to explain the twists. The triaxial nature of some ellipticals and the growth of inner bar structure could adequately result in changes in position angle.

A sample of isolated ellipticals by Colbert, Mulchaey, & Zabludoff (2001) was drawn from the Third Reference Catalog of Bright Galaxies (RC3). The galaxies had no cataloged neighbor within a $1h_{100}^{-1}$ Mpc radius and velocity $\pm$ 1000 km s^{-1} and the study was limited to a redshift, $z \leq 0.033$. Analysis revealed that $\sim$40% of the sample had shell structure and dust lanes were found in 75% of the isolated ellipticals. The authors concluded that while tidal interactions were unlikely, the merger of a companion could easily explain the observed shells. Malin & Carter (1983) further noted that the shells in cluster environments might be quickly destroyed, yet persist in the low-galaxy density regions of isolated ellipticals.

A sample of early-type galaxies in low-density environments was compiled and analyzed by Kuntschner et al. (2002). Galaxies were selected using the FLAIR-Shapley-Hydra redshift survey. All early-type galaxies within $cz \leq 7000$ km s^{-1}, having an apparent magnitude of $m_b \leq 16.1$ and fewer than 2 neighbors within a

redshift-scaled radius of 0.8° at cz = 7000 km s^{-1}, were deemed isolated. The derived average age of the sample was 6.4 ± 1.0 Gyr, which is lower compared to 8.9 ± 0.7 Gyr for elliptical and S0 galaxies in the Fornax cluster. More than half of the sample displayed disturbed morphologies (56%), which was interpreted as evidence of late-stage mergers.

Stocke et al. (2004) created a sample of 100 isolated galaxies by selecting the brightest and most isolated early-type galaxies listed among the 1051 galaxies of the KIG catalog. The authors find that based on luminosity functions, their sample of isolated early-type galaxies is no different than comparably luminous ellipticals in clusters. Following the formation paradigm of elliptical galaxies, the luminosity functions of the ellipticals studied are consistent with formation by merger. To more precisely determine the formation history of the sample, a comparison was made to NGC 1132. Mulchaey & Zabludoff (1998) proposed that NGC 1132 was a remnant of a coalesced group of galaxies based on an extended X-ray halo and high X-ray luminosity. An X-ray observation of one sample galaxy, KIG 284, was inconclusive regarding the connection between the KIG sample and a merged group hypothesis.

The sample of Madore et al. (2004) is a reworking of the sample and selection criteria of Bothun & Sullivan (1977). The original sample yielded 34 galaxies selected from the RC3 all galaxies with recessional velocities less than 3000 km s^{-1} and no neighbors within 75 kpc radius. A reanalysis of the 34 isolated ellipticals found that on average there were 0.74 ± 0.95 catalogued companions per elliptical. A larger search

found that within 300 kpc, there were 4.5 companions per elliptical with published redshifts of $\pm$ 800 km s^{-1} of the isolated elliptical. The results indicated the selected isolated ellipticals are located in high-density regions than previously thought.

Marcum et al. (2004) analyzed 9 KIG galaxies with the goal of establishing a baseline of properties for early-type galaxies in low-density environments and comparing the nature of their sample with properties predicted for a merged group of galaxies. The candidate galaxies were separated by 2.5 Mpc from neighbors brighter than $M_V = -16.5$. A recessional velocity separation of 350 km s^{-1} ensured the candidate isolation in redshift-space. The extreme separations used were to insure the candidate had not interacted with an existing neighbor during its lifetime. Two isolated ellipticals had blue colors, disturbed morphologies and tidal features, all interpreted as signs of a merger. Additionally, two other candidate galaxies displayed blue colors but no morphological peculiarities, suggesting these systems were advanced mergers. Based on a bulge/disk decomposition, three systems were likely to be isolated S0 galaxies. Roughly half of the sample was considered probable fossil groups. Two galaxies in the sample, KIG 557 and KIG 824, displayed no unusual features and were candidates for passively evolving primordial ellipticals formed in early cosmic time.

Using the Lyon Extragalactic Database (LEDA), Reda et al. (2004) created a sample of isolated early-type systems. The criteria for isolation were no neighbors within 700 km s^{-1}, 0.67 Mpc on the plane of the sky and a B-band difference of 2 magnitudes. The magnitude difference was included to ensure that any neighboring

system would be a dwarf galaxy unlikely to exert large-scale perturbations. The sample galaxies were found to have (B−R) colors similar to early-type systems in higher-density environments. Approximately 44% of the sample has fine structure features indicative of a past merger. Four sample galaxies have published X-ray luminosities, yet only NGC 1132 has group-like X-ray properties. The X-ray data, while not for the complete sample, suggests that the Reda et al. sample was formed as a result of mergers but not the coalescence of a galaxy group.

Smith et al. (2004a, 2004b) searched the LEDA and NED databases to select all galaxies with $M_B \leq -19$ and morphological T-type $\leq$ -4 within a redshift range of 1500 km $s^{-1} \leq z \leq$ 10,000 km s^{-1}. Galaxies were considered isolated if they met the conditions of Δmag = 0.7 (2.2) for galaxies within 1 Mpc (500 kpc). The purpose of study was to characterize the environments around so-called isolated galaxies. The authors detect down to a limiting magnitude of $m_B = 14.6$, 45 $\pm$ 15 dwarfs within a 500 kpc radius of the isolated primary. The findings illustrate the difficulty in defining a truly isolated galaxy baseline. Ellipticals have dwarfs out to $\sim$500kpc, with $-16 \leq M_B \leq -15$ dwarfs within a 500 kpc radius of the isolated primary. The findings illustrate the difficulty in defining a truly isolated galaxy baseline.

An examination of the stellar populations of isolated early-type systems was performed by Denicolo et al. (2005). Galaxies were selected using LEDA where isolation was determined as no neighbors within 2 B-band magnitudes, within 700 km s^{-1} recessional velocity and within 0.67 Mpc on the sky. The final sample consisted of

40 isolated early-type systems. Most of the sample shows no signs of disturbance or tidal features, although 11 sample galaxies are included in the Arp catalog of peculiar galaxies (Arp 1966). The line-strength index - σ_0 was found to be similar to high-density ellipticals.

The Sloan Digital Sky Survey (SDSS; Stoughton et al. 2002) was used in the creation of the catalog of very isolated galaxies of Allam et al. (2005). Sample selection used a variation on the KIG isolation criteria. A projected sky separation of greater than 40 galaxy diameters in the g-band and Δm_g less than 3.0 were used to select the isolated systems. The sample had 2980 isolated galaxies from the first data of the SDSS. The authors found that on average, the selection algorithm detects 1.4 isolated galaxies deg^{-2} and the nearest neighbor to sample galaxies is 4.2 ± 0.24 h^{-1} Mpc.

Work by Galletta et al. (2006) examined a sample of isolated galaxies of all morphologies. Galaxies were extracted from the CfA2 catalog (Huchra et al. 1999) with isolation criteria of galaxies having no sizable companions within a volume large enough to ensure their evolution was not affected by other systems in the last Gyr. The Galletta et al. investigation found that the isolated systems were smaller, bluer and less massive than a comparison sample of higher-density galaxies.

Hau and Forbes (2006) used a subsample of isolated elliptical galaxies from Reda et al. (2004) to understand radial stellar kinematics. Forty percent of the sample contained galaxies with kinematically decoupled cores (KDCs) or velocity substructure,

which are interpreted as a merging event. Overall, the sample features comparable kinematic properties with higher-density ellipticals.

A reanalysis of the KIG sample of galaxies has been performed by the AMIGA project (Verdes-Montenegro et al. 2005; Sulentic et al. 2006; Lisenfeld et al. 2007; Verley et al. 2007). The work intends to obtain optical (B & Hα), infrared (FIR and NIR) and radio data for all KIG galaxies. An in-depth morphological refinement and a cataloging of neighbor galaxies are being performed. The goal of the study is to understand the interstellar medium and star forming properties of some of the most studied isolated galaxies.

Another group of studies have examined field and isolated early-type galaxies as part of larger projects. The findings of these studies all reached similar results. Work by Collobert et al. (2006) found that galaxies in low-density environments have younger stellar populations than those found in clusters. The authors speculate that low-density galaxies experienced merger-induced star formation over longer and more recent periods compared to cluster galaxies. These results are very compatible with the conclusions of Reda et al. (2004), that found field galaxies possessing bluer colors. Some field early-type galaxies had colors that are too blue to be consistent with high-redshift monolithic collapse (Menanteau et al. 1999).

Prior work into isolated early-type galaxies has proven to be an on-going effort. As can be seen from past work, the data regarding isolated systems have been inconclusive. Many authors have found isolated galaxies to have similar properties to galaxies

in higher-density environments, while other have detected distinct trends unique to a low-density environment galaxy. Previous studies have all used isolation criteria that may not have been sufficient to assure the isolated galaxies have not undergone merging or interaction.

One issue is that many previous studies have relied solely on sky separation when selecting IEGs. The absence of a redshift isolation criterion effectively overlooks isolated galaxies hidden as a result of projection effects. A complete sample of truly isolated systems therefore requires the use of redshifts.

The SDSS, in its depth and breadth, provides a unique source for finding many isolated galaxies. The large sky coverage and extensive spectroscopic survey has yielded a database of considerable size that can easily be culled for samples of isolated galaxies. The sample of IEGs described in the current study represents the largest sample compiled using the strictest set of isolation criteria.

All of these previous works confirm that searching for early-type galaxies in low-density environments is possible. Work is needed to define exactly what the full set of properties is for field early-types and how those compare to cluster galaxies of the same morphology. Most importantly, no other study has effectively utilized the redshift data provided by the SDSS. With the addition of a more precise determination of isolation by use of redshifts, the current work will create a robust sample of isolated early-type galaxies.

Chapter 2

Analysis of X-ray Emitting Gas Around Collapsing and Collapsed Galaxy Systems

2.1 Introduction

The study of galaxies was, for a long time, constrained by the fact that observations were only made at optical wavelengths. Our understanding of galaxy formation processes and evolution was severely limited to a narrow wavelength regime. As observations at IR, radio and UV wavelengths became available, astronomers began seeing a much more dynamic interplay between the gas, dust and stars within a galaxy. One important window into extragalactic astronomy was opened with the first X-ray imaging telescope, the Einstein Observatory (Giacconi et al. 1979). The Einstein Observatory performed the first systematic study of normal galaxies in the 0.3 – 4 keV range with a resolution of 5"– 45". Extended emission, highly disturbed hot gas, and individual point sources were found. Hot gas halos in and around elliptical galaxies were first observed, confirming that if stars in Es moved at $\sim$200 km s^{-1}, the

stellar ejecta would have temperatures given by,

$$\frac{1}{2}m_H\sigma^2 \sim \frac{3}{2}kT \rightarrow T \sim 10^6 K \tag{2.1}$$

The above equation represents the expected temperatures halo gas would reach if the gas were stirred by the motion of the group galaxies. The temperature indicates the halo gas would be best observed at X-ray wavelengths.

ROSAT (Truemper 1983) and ASCA (Tanaka, Inoue, & Holt 1994) X-ray observatories furthered the revolution in high energy astrophysics, extending the energy range to 0.5–10 keV. Unfortunately, the ROSAT and ASCA data lacked the needed physical and spectral resolution to answer questions raised by the Einstein data. The field of X-ray astronomy was provided a second major revolution with the high angular and precision energy resolution of the Chandra X-ray Observatory.

Early-type galaxies have been known to be luminous X-ray sources since the Einstein era (Forman et al. 1979). The X-ray emission from elliptical and S0 galaxies has been shown to arise from numerous sources. Emission from massive ellipticals is dominated by thermal diffuse gas, with the gas possibly having been enriched with metals from supernovae outflows or stellar winds. Diehl & Statler (2006), in a study of a large sample of elliptical galaxies, found that a large fraction of hot gas is expected to come from stellar mass loss. A fraction of the X-ray halo gas is expected to be acquired through mergers (Brighenti & Mathews 1998). For galaxies that have lost much of their diffuse gas through tidal or ram-pressure stripping, the contribution of emission from low-mass X-ray binaries (LMXBs) becomes increasingly important

to the total X-ray luminosity. Kim et al. (1992) and Matsumoto et al. (1997) first noted the contribution to the spectra from the point source population in Einstein and ASCA observations.

X-ray bright early-type galaxies have spectra that are best modeled using thermal bremsstrahlung and line emission codes, with temperatures of kT $\sim$ 1 keV (Forman, Jones, & Tucker 1985; Canizares, Fabbiano, & Trinichieri 1987; Jeltema et al. 2006). X-ray faint early-type galaxies exhibit a two-component emission consisting of a soft component at kT $\sim$ 0.3 (Fabbiano, Kim, & Trinichieri 1994) and a hard component best fit by a power law or thermal bremsstrahlung with kT $\geq$ 5 keV (Matsumoto et al. 1997; Allen, di Matteo, & Fabian 2000; Blanton, Sarazin, & Irwin 2001). Rich, massive galaxy clusters have bremsstrahlung emission near 10 keV, while poor clusters of galaxies produce diffuse gas emission at temperatures intermediate to ellipticals and rich clusters. Estimates of the underlying gravitational mass of X-ray emitting systems can be determined provided the X-ray surface brightness profile is well fitted by the β model, the total gravitational mass is simplified to (Jeltema et al. 2006),

$$M_{grav}(r) = \frac{3\beta T r_{core}}{G\mu m_p}\left(\frac{x^3}{1+x^2}\right) \tag{2.2}$$

where x = $\frac{r}{r_{core}}$, G is the gravitational constant and m_p is the proton mass. Derivation and explanation of thermal bremsstrahlung radiation, calculating the gravitational mass, and beta models is given in Appendix A.

The hard component of extragalactic X-ray emission is nearly proportional to the optical luminosity of the galaxy which suggests an origin associated with LMXBs.

The origin of the soft diffuse emission seen in faint galaxies has remained elusive (Fabbiano et al. 1994; Pellegrini 1994; Kim et al. 1996; Irwin & Sarazin 1998). Some possibile explanations for the low temperatures of the soft emission may be hot gas lost to galactic winds or via ram-pressure stripping due to intracluster gas. There is general agreement that the creation of X-ray binaries must be a continuous and ongoing phenomenon in the evolution of galaxies, because the binary lifetime ranges (Grimm et al. 2002) from $\sim 10^7$ yr for high-mass X-ray binaries (HMXBs) to $\sim 10^9$ yr (LMXBs). The X-ray binary population may be related to the bulk of the stars in the galaxy and that the variance in the binary population is related to the star formation history of the host galaxy (White & Ghosh 1998; Wu 2001). For a sample of early-type galaxies with typical photometric colors (Sandage 1973; Frogel et al. 1978), one would not expect the point source population to contain many HMXBs.

2.2 Previous X-ray Analyses

Nearly half of all galaxies are found in bound groups (Tully 1987). Compact galaxy groups have close configurations with the group members being separated by a few galactic nuclei. The low velocity dispersions and high galaxy densities found in compact groups, which are comparable to or exceed the cores of rich clusters, make them ideal locations to study galaxy interactions and mergers (Barnes 1989; D′Onghia et al. 2005). The Hickson compact groups (HCGs) are some of the most well studied high-galaxy density configurations (Hickson 1982), with many showing

signs of interaction, such as tidal tails (Mendes de Oliveira & Hickson 1994) and H I gas deficiencies due to stripping (Verdes-Montenegro et al. 2001).

Numerous multi-wavelength studies have observed the galaxy members of the HCGs (Hickson, Kindl & Auman 1989; Rubin, Hunter & Ford 1991; Severgnini et al. 1999; Merluzzi, Shaker & Longo 2000). X-ray observations of the HCGs have been performed since the Einstein observatory, in attempts to better understand the emission mechanisms as well as to use the hot gas emission as a means to assure galaxy member concordance. The results of ROSAT analysis found the hot gas in the HCGs can be used to estimate the evolutionary stage of the group (Ebeling et al. 1994; Pildis et al. 1995; Ponman et al. 1996).

Simulations by Barnes (1989) showed that if galaxies in a compact group (CG) were to merge, an elliptical galaxy could be formed on a timescale shorter than a Hubble time. The motivation for studying a collapsing CG was work done by Merritt (1985) and Barnes (1985). They found that the relatively low velocity dispersion of galaxies in groups make such environments ideal for mergers. Simulations predict that such merger remnants will display an $r^{1/4}$ surface brightness profile (Mihos 1999), as is seen in elliptical galaxies.

The utility of X-ray observations also extends to understanding the connection between compact groups, isolated ellipticals and fossil group galaxies. Following the current formation theories, fossil groups are the remnants of a coalesced compact group of galaxies (Ponman et al. 1994; Vikhlinin et al. 1999). Through the use

of the ROSAT all-sky survey, many fossil groups (FG) have been found, with fossil groups being defined as an elliptical galaxy having $L_X > 10^{42}$ ergs s^{-1} and with a companion at least 2 R-band magnitudes fainter than the FG primary. The short crossing times, with HCG median of $0.016{H_0}^{-1}$, argues for short lifetimes although a large population of post-group remnants has remained elusive (Zepf et al. 1991; Sulentic & Rabaca 1994). Evidence that fossil groups are the result of a merged system of compact groups has been found through the existence of large halos of hot gas with high X-ray luminosities, which are typical of a group of galaxies.

As the merger of remaining companions with the fossil group will result in an isolated elliptical galaxy, there should exist a sequence of evolution where galaxies in a compact group merge and form a fossil group and in time the remaining companions accrete leaving an isolated elliptical. Toomre (1977) first suggested that field ellipticals could be the end result of a merged compact group. We intend to study diffuse X-ray emission along the proposed sequence in order to test the likelihood of such a formation scenario. The remnants of merger and interaction in the form of signatures in the diffuse hot gas, are expected to be visible in X-ray and will remain detectable for a few billion years longer than structures at optical wavelengths (Mulchaey & Zabludoff 1999). The signature of the X-ray emitting gas will remain observable for the estimated cooling time given by,

$$t_{cool} = \left(1.602 \times 10^{-9}\right) \times \frac{3kT\rho V\mu_e}{2\mu L_X} \tag{2.3}$$

where kT is the temperature of the gas, V is the volume (in cm^{-3}), L_X is luminosity (in ergs s^{-1}), ρ is electron number density (in cm^{-3}) and μ_e and μ are the mean mass per electron and the mean particle mass of the gas, respectively. The above equation assumes that the gas has reached thermal equilibrium and has a constant density. For a low-density ($\rho \sim 10^{-3}$) 1 keV gas, $t_{cool} = 6.9$ Gyrs, the cooling time will quickly approach a Hubble time. The cooling time allows for an estimate that any features found in the hot gas can be used as a long-lived diagnostic for determining galaxy evolution. We will use X-ray luminosities, gas temperatures and abundances as diagnostics to understand how the hot gas evolves along the compact group-isolated elliptical formation sequence.

While formation and evolution theories can be used to explain the X-ray emission of hot gas in the HCG-FG-isolated elliptical evolution pathway, lenticular galaxies remain a puzzle. Understanding how S0 galaxies form is a long-standing goal in extragalactic astronomy. One proposed formation mechanism is the fading of the arms of spiral galaxies (Christlien & Zabludoff 2004). Passive spirals have been suggested as the transition between spirals and S0s. Samples of passive spirals have been observed (Couch et al. 1998; Dressler et al. 1999; Poggianti et al. 1999; Goto et al. 2003) with spectral features indicating star formation has ceased. Using theoretical models, Bekki et al. (2002) found that as spirals are "starved" due to galaxy–intracluster medium interactions and no further accretion occurs, spiral arms fade within ~ 3 Gyr. GALEX observations of passive spirals in a cluster environment (Moran et al.

2005) found that while starved spirals cannot build the entire population of local S0s, passive spirals represent an important transition population at intermediate-redshift. An investigation of the X-ray properties and populations of a sample of lenticular galaxies could be used to shed light onto the formation and evolution of S0s in a variety of environments.

The excellent spatial resolution of the Chandra X-ray observatory has allowed the diffuse emission and the LMXB population to be separated and both emission mechanisms extensively investigated. An early analysis of the X-ray populations of the S0 galaxy NGC 1553 was performed by Blanton et al. (2001). NGC 1553 was found to have 49 discrete sources which accounted for 30% of the total X-ray emission, while diffuse gas made up the remainder of the emission. Most of the resolved sources had X-ray colors similar to those of the faint elliptical galaxy, NGC 4697 (Sarazin et al. 2000). NGC 1553 lacks the supersoft point sources found in NGC 4697. The central source, CXOU J041610.5-554646, has hard X-ray colors suggesting a strongly absorbed AGN. The point source population was found to have a break luminosity, $L_b = 4.1 \times 10^{38}$ ergs s^{-1}. The soft component of the total X-ray spectrum was modeled using MEKAL (Fabbiano, Kim, & Trinichieri 1994) and the temperature was found to be ~ 0.47 keV with an abundance of ~ 0.16 solar. The temperature and abundance are consistent with the temperature – velocity dispersion correlation and the temperature – abundance relation (Davis & White 1996). The total emission

of NGC 1553 was found to be $L_X = 1.0 \times 10^{41}$ ergs s^{-1} and the sum of the point sources yielded $L_X = 4.08 \times 10^{40}$ ergs s^{-1}.

Work by Irwin et al. (2002) analyzed Chandra observations of NGC 1291. The morphology of NGC 1291 is cited as either an Sa or S0 galaxy. The diffuse emission was observed to be circularly symmetric, with some asymmetries at intermediate radii. Forty-eight point sources were detected within the bulge region. The authors find one supersoft source and a number of very soft sources. The central source displays hard colors, but there appears to be an unexpected over-abundance of soft emission. There were no LMXB sources with luminosity greater than 3×10^{38} ergs s^{-1}, while seven were expected based on scaling with the point source population of NGC 4697. The diffuse emission was fit using a MEKAL model, with a temperature of 0.32 keV and metallicity of 0.06 solar.

NGC 5102 was examined at X-ray wavelengths by Kraft et al. (2005) in an extensive examination of the properties of the X-ray source populations. Previously observed with ROSAT, NGC 5102 was theorized to have a significant population of HMXBs due to its recent star formation. The authors detected 55 sources in the X-ray image, with only 11 sources falling within the D_{25} boundary. In the 0.5 – 5.0 keV band, the 11 sources had an X-ray luminosity of 5.6×10^{37} ergs s^{-1}. NGC 5102 has significantly fewer X-ray binaries than expected from an extrapolation of more massive early-type galaxies. The best-fit temperature and X-ray luminosity of the diffuse emission were found to be 0.31 keV and 4.1×10^{37} ergs s^{-1}, respectively.

Arguments have been made suggesting that the low luminosity of the majority of point sources and the large on-going star formation is consistent with the population of HMXBs found in our Galaxy (Grimm et al. 2002).

2.3 Chandra X-ray Observatory

The third of NASA's Great Observatories, Chandra X-ray Observatory was launched on July 23, 1999. Consisting of the smoothest mirrors and the most precisely shaped and aligned telescope system ever constructed, Chandra is able to obtain images twenty-five times sharper than recorded by any prior X-ray telescope (Weisskopf et al. 2000).

The Chandra telescope system consists of four pairs of mirrors. Due to their high energies, X-ray photons will penetrate into the mirrors, necessitating the need for the mirrors to be aligned nearly parallel to the incoming X-rays. With a field of view of 1.0 degree, spatial resolution of 0.5 arcseconds, and an energy range of 0.2 – 10 keV, the Chandra X-ray Observatory stands as the most sophisticated X-ray telescope ever built (Weisskopf et al. 2000). The unique energy and spatial resolution allows for the separation of diffuse gas and point sources emission, which is needed in order to answer the major questions in high-energy astrophysics.

2.4 Selection Criteria

Samples of compact groups, isolated ellipticals and fossil groups, were created to study the relations between the X-ray properties of isolated galaxies and their likely progenitors, compact groups. All Hickson compact groups in the Chandra archive were selected. The compact group sample includes eleven Hickson compact groups, HCG 16, 30, 37, 40, 42, 51, 62, 80, 90, 92, and 97. With velocity dispersions of 100 – 400 km s^{-1}, the HCGs are expected to have gas temperatures between 0.2 – 1.2 keV, well within the Chandra energy range. Dynamical properties of the HCGs and data on each group member are listed in Tables 2.1 and 2.2, respectively.

The HCG sample is comprised of systems in many different states of dynamic evolution. Following the evolutionary sequence defined by Coziol, Brinks & Bravo-Alfaro (2004), HCGs 16, 30 and 80 are in a low stage of evolution, dominated by spiral galaxies. Evolution type B, where members galaxies are in apparent close contact and possibly in a pre-merging phase, are predicted for sample members HCG 37, 40, 51, 90 and 97. Sample compact groups, HCG 42, 62 and 92 are in the type C evolutionary stage. Type C is defined as a group dominated by elliptical galaxies and with group members lacking nuclear activity. The variety of compact groups allows for an objective comparison on the properties of the hot gas and an estimate of the state of the hot gas during multiple evolutionary stages.

The fossil group and isolated elliptical galaxy samples were also selected using the Chandra archive. All observing programs listed in the archive that described a study

of either isolated ellipticals or fossil groups were examined for candidate galaxies. Ten fossil groups and nine isolated ellipticals comprise those samples, respectively. Tables 2.3 and 2.4 list the names and positions of the fossil group and isolated elliptical samples, respectively.

All of the galaxies in the fossil group sample have previously been studied at X-ray wavelengths and had results published. A detailed study of the sample fossil groups was performed, including ESO 306G170 (Sun et al. 2004), NGC 1550 (Sun et al. 2003) and RXJ1340.6+4018 (Jones et al. 2000).

There is no intrinsic difference between a fossil group and isolated elliptical galaxy. In essence, both systems are isolated early-type galaxies. The samples presented here have not been selected based on a uniform definition of isolation. Isolated elliptical galaxies in our sample are found in numerous other isolated studies. The elliptical galaxies, NGC 766, NGC 1132, NGC 3209 and NGC 7618 are found in the sample of isolated galaxies of Colbert et al. (2001) and have no cataloged neighbors within $1h_{100}^{-1}$ Mpc and $\pm$ 1000 km s^{-1}. Other members of the isolated ellipticals sample can be found in the samples of Madore et al. (2004), Reda et al. (2004) and Smith et al. (2004). Our sample of isolated ellipticals has varying degrees of isolation, ranging anywhere between 300 kpc and 1.3 Mpc. While we are confident that these galaxies are sufficiently isolated, differences among the X-ray parameters might be due to the variation in samples isolation criteria.

The sample of lenticular galaxies was created to study the point source population, diffuse emission, and the relations between the X-ray and optical properties. All S0 galaxies in the Chandra archive were selected. The sample includes eleven S0s: NGC 1023, 1332, 1553, 2329, 3115, 4382, 4406, 5102, 5353, 5866, and 6407. The sample represents S0s in high-galaxy density environments of clusters and groups, but also contains a field S0. The galaxies are local, with redshifts less than 0.019, yet the sample contains a variety of star formation histories as evidenced by the (B − V) colors. The stellar populations display signs of recent star formation, NGC 5102 (B − V = 0.64) and old stellar systems, NGC 3115 (B − V = 0.91). Of particular interest is the field S0, NGC 3115, as isolated and low-galaxy density S0s are extremely rare. The X-ray properties of NGC 3115 could be used to inform on the emission mechanisms found in other isolated S0s, such as KIG 412 and 684 (Marcum, Aars, & Fanelli 2004). Dynamical properties of the S0 galaxy sample are found in Table 2.5.

2.5 Data Reduction

The data were reduced using CIAO 3.4 and CALDB version 3.4.0, following the standard data processing. CIAO is distributed by the Chandra X-ray Center (CXC). Beginning with the level 1 event file, the data were reprocessed to include the latest tools to redetect hot pixels, afterglow events and to apply the most recent gain file.

The level 2 event file was further filtered keeping only events with ASCA grades 0, 2, 3, 4, and 6. Good Time Intervals (GTI) were also applied. Filtering excluded

periods when the count rate, with the exception of point sources and extended emission, was not within 20% of the quiescent rate. The energy range was restricted to 0.3 – 7.0 keV band. Sources were detected using the CIAO wavelet detection tool, wavedetect. Wavelet scales of 1, 2 and 4 pixels were set to give approximately one false detection per image. Point source regions were removed and filled via a linear interpolation using the CIAO tool `dmfilth`. Source regions were filled using the counts in background regions of radii equal to twice the source region radii. The point source-removed images were smoothed to highlight the hot diffuse emission.

Using the CIAO tool, `dmextract`, radial surface brightness profiles were extracted from the 0.3 – 7.0 keV bands. Radial profiles were determined for all of the isolated galaxies studied. The surface brightness profiles were then modeled using the Sherpa analysis package. The core radii and the beta values can be used to estimate the dynamic state of a galaxy.

Spectra were extracted for the diffuse emission in circular regions that extended to where the surface brightness profile reached 1σ above the background, similar to the procedure of Saracco & Ciliegi (1995) for ROSAT observations of Hickson Compact Groups. For compact groups, where the diffuse emission does not extend beyond the individual galaxies, spectra were extracted for the individual galaxies and for the sum of the galaxies. Background spectra were extracted from annular regions surrounding the source regions. Response files, RMFs and ARFs, were determined for the location of the diffuse emission, with the individual spectra being binned to

have 15 counts per bin. While the point sources were removed, some obscured point sources may still remain. To account for obscured sources, spectra were fit with a two-component model, comprised of a power law and either a thermal Meka model (Mewe, Gronenschild & van den Oord 1985) or thermal APEC model (Smith et al. 2001). Spectra were fit in the 0.3 – 5.0 keV range. During the spectral fitting, the neutral hydrogen column density was fixed to the galactic value, while the temperature and abundance were allowed to vary. The fit temperatures, abundances and luminosities for the HCG, FG, and isolated elliptical galaxy samples are reported in Tables 2.6, 2.7 and 2.8. Additionally, we list the effective X-ray radius, which was defined as the radius where the X-ray surface brightness profile falls to 2σ above the background.

Dynamical properties of the S0 galaxy sample are presented in Table 2.9, while the X-ray characteristics can be found in Table 2.10. Data for the point source population of the S0 galaxy sample was also analyzed. Procedures similar to those used for the extraction of the diffuse gas spectra were employed to extract the spectra for point sources having greater than 20 counts. Circular regions enclosing the point source and annular regions surrounding the source were used to extract the source and background spectra, respectively. Individual spectra were binned to have 15 counts-per-bin. Spectra were fit in the 0.3 – 7.0 keV energy range.

Hardness ratios were used to study the spectral properties of the point source population, which has the advantage that these ratios can be determined for fainter sources while detailed spectra cannot. X-ray colors were used to study Milky Way

X-ray binaries (White & Marshall 1984) and the integrated X-ray emission of galaxies (Kim et al. 1992). We have used three energy bands: soft S, 0.3 – 1.5 keV; medium M, 1.5 – 2.5 keV; and hard H, 2.5 – 8.0 keV. We have defined the two hardness ratios as done by Sarazin et al. (2000), H21 = (M − S)/(M + S) and H31 = (H − S)/(H + S). Plots of luminosity functions for the point source populations were also created. Fits to the luminosity functions will be detailed in a later analysis.

2.6 Hickson Compact Groups

Eleven Hickson compact groups were studied. The point sources population was separated from diffuse emission in order to determine the hot gas properties and relate them to observed dynamical features. Information regarding the dynamical state and X-ray properties are discussed below.

2.6.1 HCG 16

The group is composed of four late-type galaxies at a redshift of 0.0132. All group members with the exception of HCG 16b are known infrared and radio sources (Menon 1992; Allam et al. 1996). The left panel of Figure 2.1 shows a Digital Sky Survey II image of the HCG 16 group and the right panel displays the same image with contours of diffuse X-ray emission overlaid. From the image, one can see that the emission comes primarily from HCG 16c and d. No emission is detected around

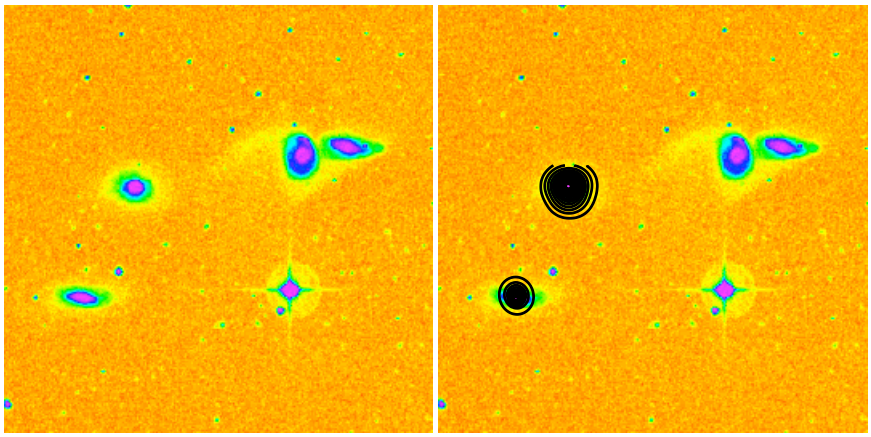

Figure 2.1: Diffuse emission contours of HCG 16 overlaid on DSS II image. The image is 140 kpc on a side.

the interacting pair HCG 16a and b or in the intragroup medium. A Meka model was used to fit the spectra of the entire HCG 16 group. The temperature of the hot gas was determined to be 0.662 keV with an abundance of 0.22 solar. The X-ray luminosity is then 7.9 $\times$ 10^{40} ergs s^{-1}, making HCG 16 one of the fainter compact groups in our sample. Our estimate of the L_X closely matches the value of log L_X = 40.74 as found by Mulchaey et al. (2003). Contrary to the results of Jeltema et al. (2008), we do not find a common X-ray halo around HCG 16c and d. We found no significant emission from HCG 16c or d, however due to the interaction of these two galaxies, stripped neutral gas will likely be heated to X-ray temperatures.

2.6.2 HCG 30

At z = 0.0154, two spirals and two early-type galaxies compose the group. Figure 2.2 displays the X-ray contours overlaid onto a DSS image of HCG 30. The emission

is not centered on any individual galaxy, as was seen in HCG 16. The HCG 30 system has gas at 0.99 keV with a solar abundance. The group has an X-ray luminosity of 2.1×10^{41} ergs s^{-1}. The group evolution appears to be at a low level with the gas yet to have been distributed into the intragroup medium. HCG 30 has been determined to be the most H I-deficient HCG in a study by Verdes-Montenegro et al. (2007). The possibility remains that as the galaxies interact, any H I in the intragroup region will be heated to X-ray temperatures.

2.6.3 HCG 37

Two ellipticals and three late-type galaxies at redshift z = 0.0223 make up the HCG 37 group. Diffuse emission contours can be found in the middle panel of Figure 2.2. Emission seen centered on 37a, is symmetric and extends only slightly into the group. The luminosity is estimated to be 1.9×10^{41} ergs s^{-1}, higher than the derived value of the spiral only system HCG 16. The hot gas has a temperature of 1.08 keV and an abundance of 0.13 solar.

2.6.4 HCG 40

The group consists of five galaxies, two early-type systems and three late-type galaxies at a redshift of 0.0223. The groups L_X is 2.9×10^{41} ergs s^{-1}. The temperature and abundance of the X-ray emitting gas is, 0.97 keV and 1.0 solar, respectively. The diffuse emission contours, shown in the lower panel of Figure 2.2, indicates that the

X-ray gas is concentrated around 40d. A single contour encompassing 40ace indicates there is some gas distributed into the intragroup region.

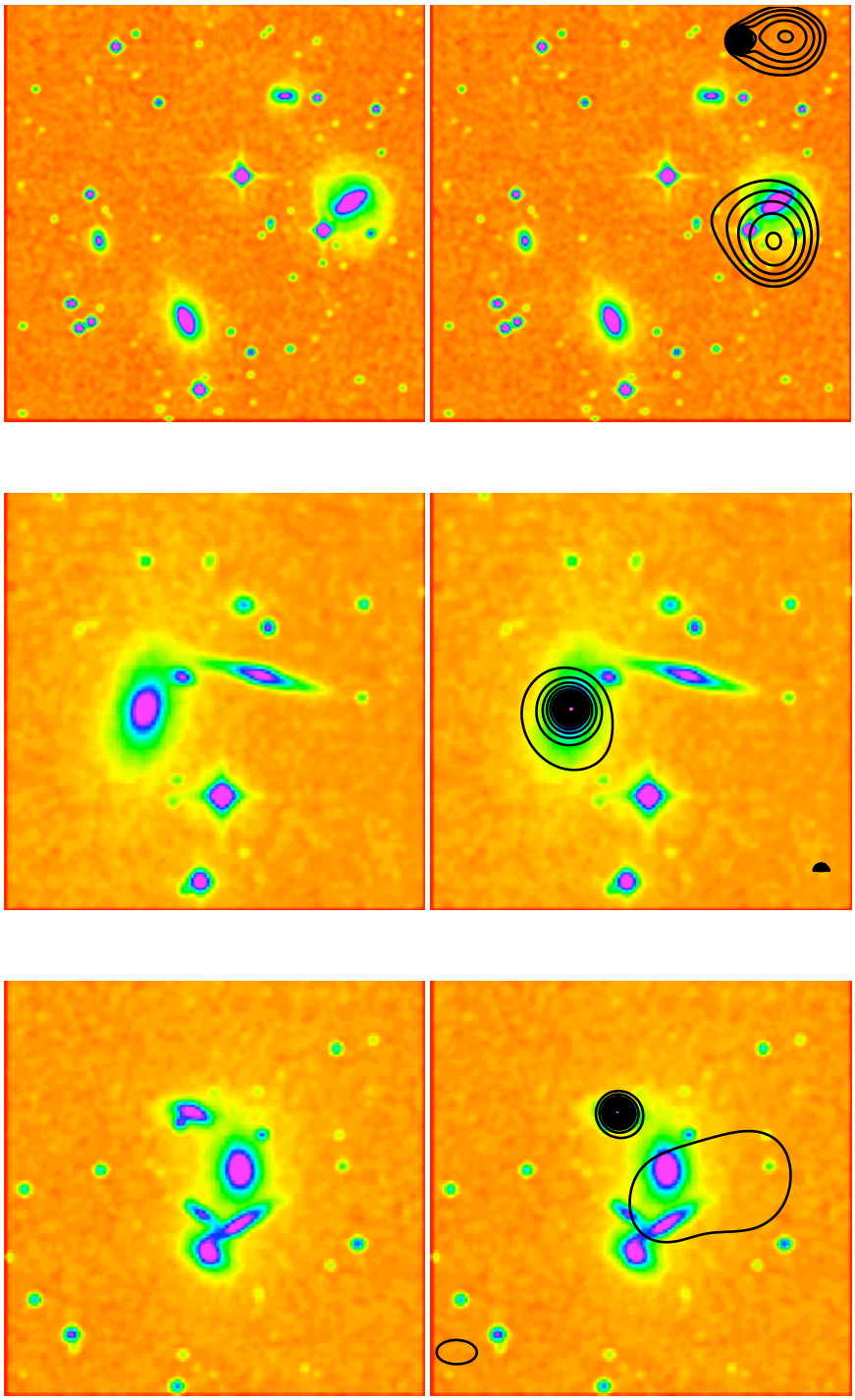

Figure 2.2: Diffuse emission contours overlaid on DSS II images. The images are 140 kpc on a side. The upper panel displays HCG 30, the middle HCG 37, and the lower HCG 40.

2.6.5 HCG 42

The four early-type galaxies in the group are centered at z = 0.0133. The diffuse emission contours in the upper panel of Figure 2.3 show emission primarily due to the brightest group member 42a. The contours are roughly symmetric in the outer regions, but have a great deal of asymmetry in the core. The hot gas extends towards 42c, indicating interaction between 42a and c. The gas has a temperature of 0.76 keV and an abundance of 0.61 solar. The group X-ray luminosity is estimated to be 3.5×10^{41} ergs s^{-1}. The gas temperature and X-ray luminosity closely match the Mulchaey et al. (2003) temperature of 0.73 keV and log $L_X = 41.59$.

2.6.6 HCG 51

At a redshift of 0.0258, HCG 51 has six members, four early-type galaxies and two late-types. The X-ray gas was determined to have a temperature of 6.0 keV with an abundance of 1.05 solar. Both values are the largest among our HCG sample. The diffuse emission contours can be seen in middle panel of Figure 2.3. The diffuse gas is seen to be concentrated on galaxy members, 51a, c, and e. A large amount of intragroup gas can also be seen. The only group member that was not detected is 51b. The X-ray luminosity of the group is 3.6×10^{42} ergs s^{-1}, the HCG sample maximum. We theorize that the high L_X value is due to high X-ray luminosities from the individual galaxies and a large amount of X-ray emitting intragroup gas. The

estimated L_X value and the gas temperature indicate HCG 51 is an ideal candidate to become a fossil group.

2.6.7 HCG 62

Four early-type galaxies at a redshift of 0.0137 make up HCG 62. An AGN has been detected in HCG 62a, while other group members are quiescent. Ponman & Bertram (1993) first studied the X-ray emission in great detail. The lower image of Figure 2.3 displays the X-ray contours. The diffuse emission extends throughout the intragroup region and encompasses HCG 62a, b, and c. X-ray cavities to the NE and S are clearly seen. These cavities likely originate from the AGN activity of HCG 62a. The spectrum, seen in Figure 2.4, was very well fitted by an APEC model. The temperature of the gas is 0.79 keV with a sub-solar abundance of 0.89. The group′s X-ray luminosity was determined to be 6.5×10^{41} ergs s^{-1}, placing it among the more X-ray luminous HCGs in our sample.

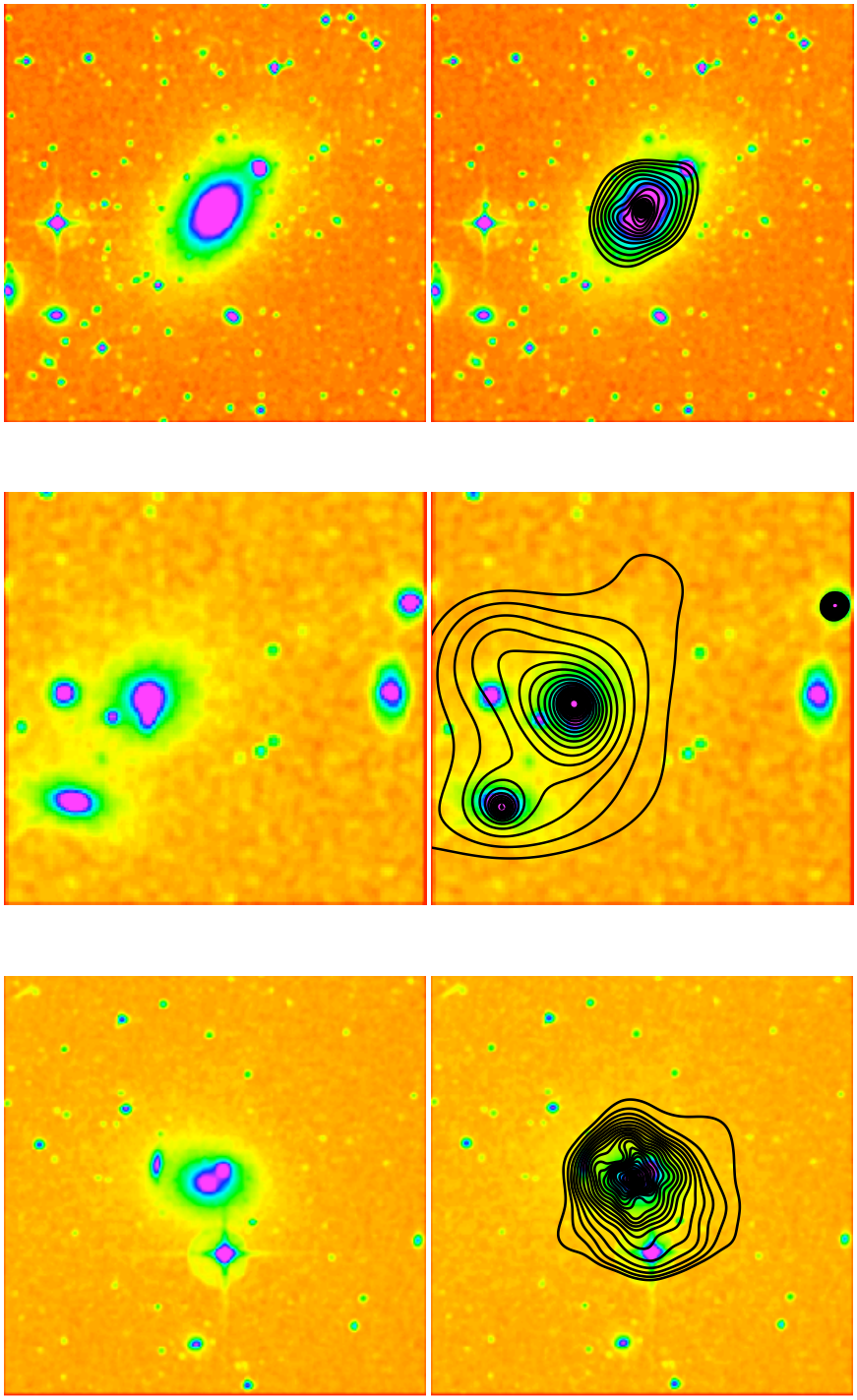

Figure 2.3: Diffuse emission contours overlaid on DSS II images. The images are 140 kpc on a side. The upper panel displays HCG 42, the middle HCG 51, and the lower HCG 62.

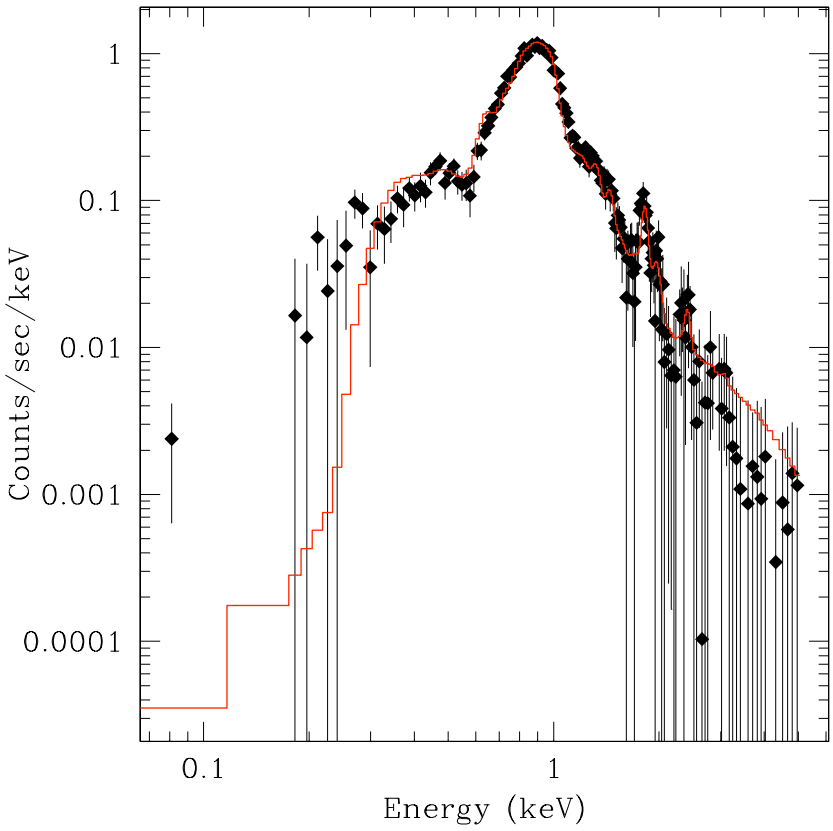

Figure 2.4: The X-ray spectrum of the diffuse hot gas in the compact group, HCG 62. The red line is an APEC thermal plasma model fit to the data.

2.6.8 HCG 80

The spiral-only group, at z = 0.0298, consists of an Sd, Sa and two Im galaxies. Figure 2.5 displays the X-ray contours in the upper image. The emission only comes from 80a and only some emission extends beyond the optical extent of 80a. The group has $L_X = 5.9 \times 10^{41}$ ergs s^{-1}, kT = 0.62 keV and 0.16 solar abundance.

2.6.9 HCG 90

The group, at z = 0.0088, is composed of three bright ellipticals and a disturbed spiral galaxy (HCG 90d) interacting with HCG 90b. In a study by Plana et al. (1998), results suggested that the group core, HCG 90bcd, is in the process of merging. The middle panel of Figure 2.5 displays the X-ray contours of the group core. The emission extends beyond the optical extent of the galaxies and is distributed into the intragroup region. The derived L_X is 3.8×10^{40} ergs s^{-1}, making HCG 90 the lowest X-ray luminosity in our sample. The hot gas is at a temperature of 0.65 keV and an abundance of 0.09 solar. Mulchaey et al. (2003) estimate the group to have log L_X = 40.60, in excellent agreement with our values.

2.6.10 HCG 92

Also known as Stephans Quintet, HCG 92 is the best studied of the Hickson compact groups. The group, at z = 0.0215, is made up of a foreground spiral (90a) and two late-type and two early-type galaxies. An AGN is found in HCG 90c, with the other members being quiescent. The estimated X-ray luminosity is found to be 5.0×10^{41} ergs s^{-1}. Using an APEC model, the derived gas temperature and abundance are 0.74 keV and 0.10 solar, respectively. The X-ray contours of the group are shown in Figure 2.5. The diffuse emission, in general, resides outside of the individual galaxies. The gas has begun to settle into the central group potential and the group members are likely near coalescence.

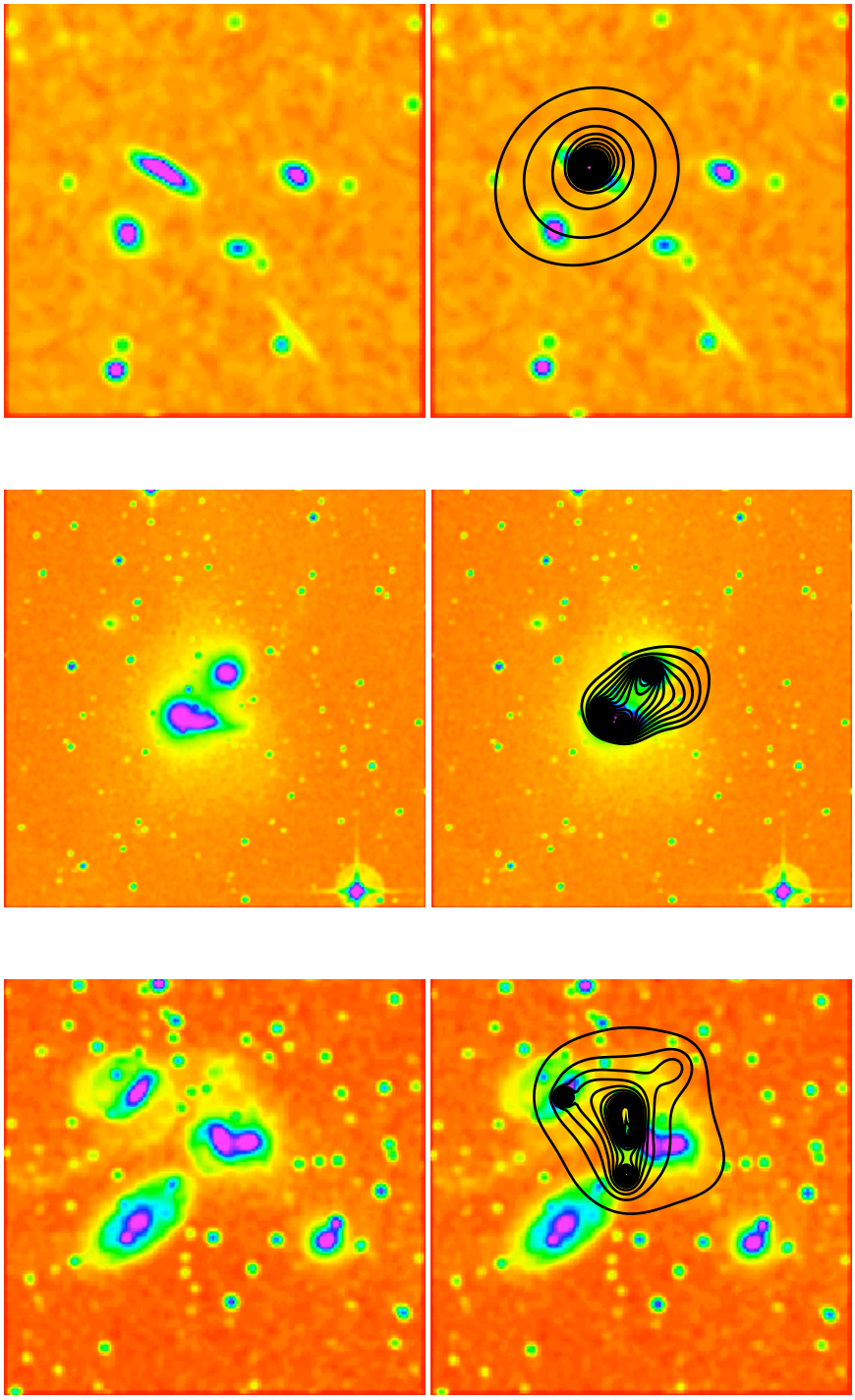

Figure 2.5: Diffuse emission contours overlaid on DSS II images. The images are 140 kpc on a side. The upper panel displays HCG 80, the middle HCG 90, and the lower HCG 92.

2.6.11 HCG 97

The group at a redshift of 0.0218 has two late-type and three early-type galaxies. The estimated gas temperature is 0.833 keV with a subsolar abundance of 0.12. The L_X is determined to be 7.8×10^{41} ergs s^{-1}. The X-ray contours are shown in Figure 2.6. The contours provide very interesting insights into the dynamics of the group. The diffuse X-ray gas is seen to extend from the group core of HCG 97a and d towards 97b and encompassing 97e. The extension towards 97b is the likely result of 97b having recently passed through the group core. The temperature and L_X values are in rough agreement with values obtained by Pildis et al. (1995) while both the derived temperature and abundance agrees with values of Saracco & Ciliegi (1995).

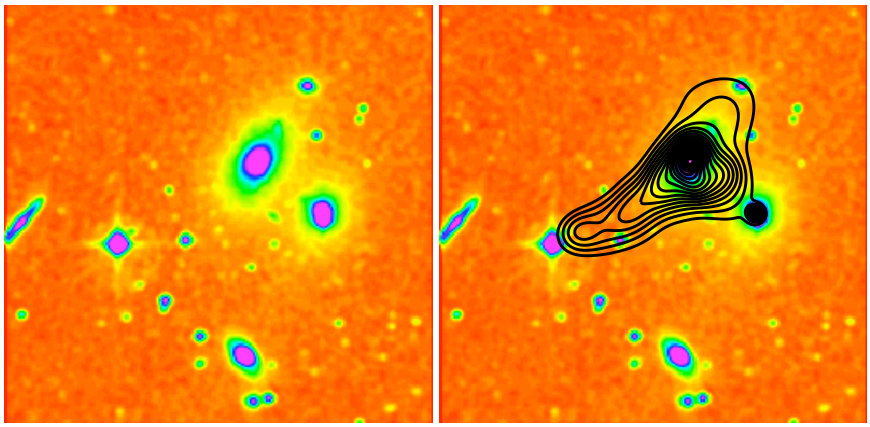

Figure 2.6: Diffuse emission contours overlaid on DSS II image of HCG 97. The image is 140 kpc on a side.

2.7 Isolated Ellipticals & Fossil Groups

Other authors have discussed the dynamical and X-ray properties of the fossil group sample and as such, we choose to list our estimated X-ray values in Table 2.7. The fossil group sample has gas temperatures in the range of 0.64 to 3.2 keV, with the average value temperature of 1.85 keV. The abundance of the X-ray emitting gas has an average value of 0.77 solar and the sample minimum of 0.13 and a maximum of 3.18 times solar. The samples L_X values vary between 1.1×10^{41} and 2.7×10^{43} ergs s^{-1}, with an average value of 9.3×10^{42} ergs s^{-1}.

The fossil group sample galaxies have X-ray contours that are symmetric, suggesting that the hot gas halos have come to thermodynamic equilibrium. The reader is referred to previously discussed studies on fossil groups for examples of X-ray contour images.

Ten fossil groups and nine isolated elliptical galaxies were studied. As was done for the HCG sample, the X-ray point source population was separated from diffuse emission in order to determine the hot gas properties and relate them to observed dynamical features. Information on the individual isolated ellipticals is presented below.

2.7.1 NGC 1132

At a redshift of 0.0231, NGC 1132 was studied at X-ray wavelengths by Mulchaey & Zabludoff (1999) and an image of the diffuse emission contours can be found therein.

The contours are only loosely symmetric, which could be a result of disturbed gas or low-resolution data. A reanalysis of the galaxy yields kT = 0.81 keV and 0.90 solar abundance for the hot halo. The halo emits an X-ray luminosity of 7.6 $\times$ 10^{41} ergs s^{-1}. All of our estimates fall below those derived by Mulchaey & Zabludoff.

2.7.2 NGC 4555

Chandra observations of this galaxy at z = 0.0223 were made by O′Sullivan & Ponman (2004). An image of the gas contours was produced by O′Sullivan & Ponman, which shows very symmetric emission indicative of gas at hydrostatic equilibrium. Our analysis determined a gas temperature of 0.77 keV with an abundance of 0.79 solar. The derived L_X value is 3.4 $\times$ 10^{41} ergs s^{-1}.

2.7.3 NGC 766

A member of the sample of Colbert, Mulchaey & Zabludoff (2001), NGC 766 is isolated by a projected radius of $1h_{100}^{-1}$ and $\pm$ 1000 km s^{-1} from any cataloged galaxies. NGC 766, at z = 0.027, has its X-ray diffuse emission contours displayed in Figure 2.7 (upper panel). Clearly, the contours are symmetric to the 1σ above background. The galaxys hot gas has an abundance of 0.1 and a temperature of 0.67 keV. The X-ray luminosity was determined to be 2.5 $\times$ 10^{41} ergs s^{-1}.

2.7.4 NGC 3065

With a redshift of 0.00667, NGC 3065 is the X-ray faintest isolated elliptical, with an X-ray luminosity of 2.1×10^{40} ergs s^{-1}. The X-ray gas has an estimated temperature of 1.0 keV and a solar abundance. The contours can be seen in the middle image of Figure 2.7. The X-ray gas is an anomaly for our sample, as the gas is entirely within the optical extent of the galaxy. The diffuse gas is not extended and shows no signs of past interactions or mergers. The X-ray faintness and modest amount of hot gas suggests that NGC 3065 was not formed as a result of coalescence of a compact group. The isolation of NGC 3065 coupled with the lack of extended emission and absence of interaction features suggest the galaxy may be a candidate primordial isolated elliptical.

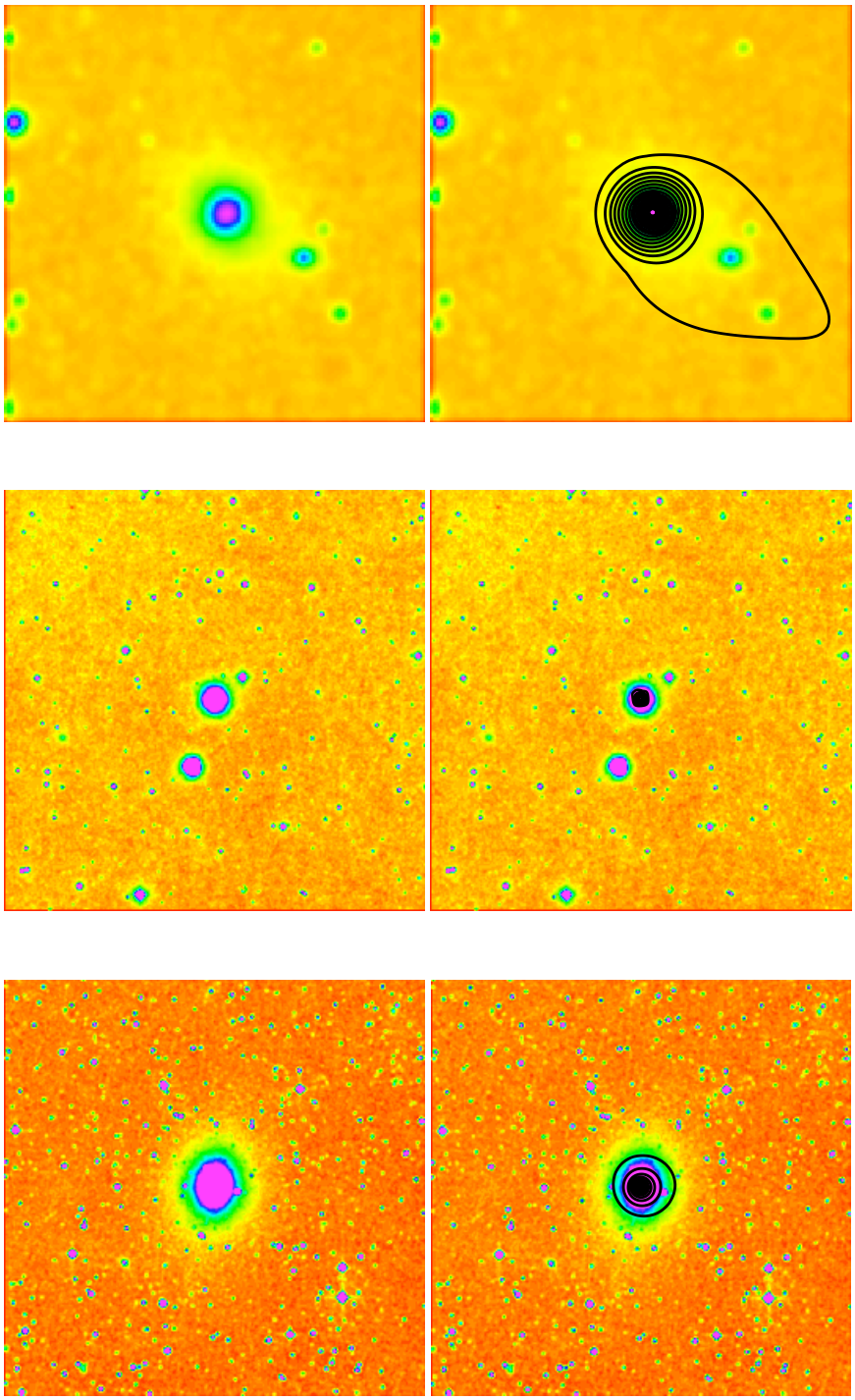

Figure 2.7: Diffuse emission contours overlaid on DSS II images. The images are 140 kpc on a side. The upper panel displays NGC 766, the middle NGC 3065, and the lower NGC 3078.

2.7.5 NGC 3078

A member of the Madore, Freedman & Bothun (2004) sample of isolated ellipticals and their companions, NGC 3078, was determined to have three comparably bright galaxies within 150 kpc. The existence of neighbors at such a close distance calls into question the validity of NGC 3078 being classified as isolated. NGC 3078 remains in the sample because it is still the brightest member of a loose group. At a redshift of 0.00832, the galaxy has the isolated elliptical galaxy samples highest gas temperature of 2.02 keV and the lowest abundance of 0.04 solar. The X-ray luminosity was estimated to be 9.3×10^{40} ergs s^{-1}. In the lower panel of Figure 2.7, the gas contours are seen to be symmetric and are tightly confined to the galaxys optical extent.

2.7.6 NGC 3209

Also part of the Colbert et al. (2001) sample, at z = 0.02075, the spectrum of NGC 3209 was fit using an APEC model. The X-ray gas has the lowest L_X value at 7.2×10^{40} ergs s^{-1} of any isolated elliptical sampled. The halo gas has kT = 0.67 keV with an abundance of 0.15 solar. The X-ray contours can be seen in the upper image of Figure 2.8. The contours are mainly symmetric, however we note that the contours extend slightly to the NE and compress to the SW. Such features have been interpreted as the galaxy moving through a larger gaseous medium, generally seen in a group or cluster.

2.7.7 NGC 5546

Figure 2.8 displays the X-ray contours of this isolated elliptical at redshift 0.0244. The diffuse gas is distributed symmetrically and primarily within the optical extent of the galaxy. The hot gas has a temperature of 0.57 keV and an abundance of 0.16 times solar. NGC 5546 has the isolated elliptical samples largest L_X value at 8.8 $\times$ 10^{41} ergs s^{-1}.

2.7.8 NGC 6487

The lower panel of Figure 2.8 displays the diffuse gas contours of the isolated elliptical at z = 0.02549. The gas shows no signs of activity or interaction and is symmetrically centered on the galaxy. The X-ray luminosity was derived to be 4.5 $\times$ 10^{41} ergs s^{-1}. The temperature was determined to be 0.76 keV with a sub-solar abundance of 0.31.

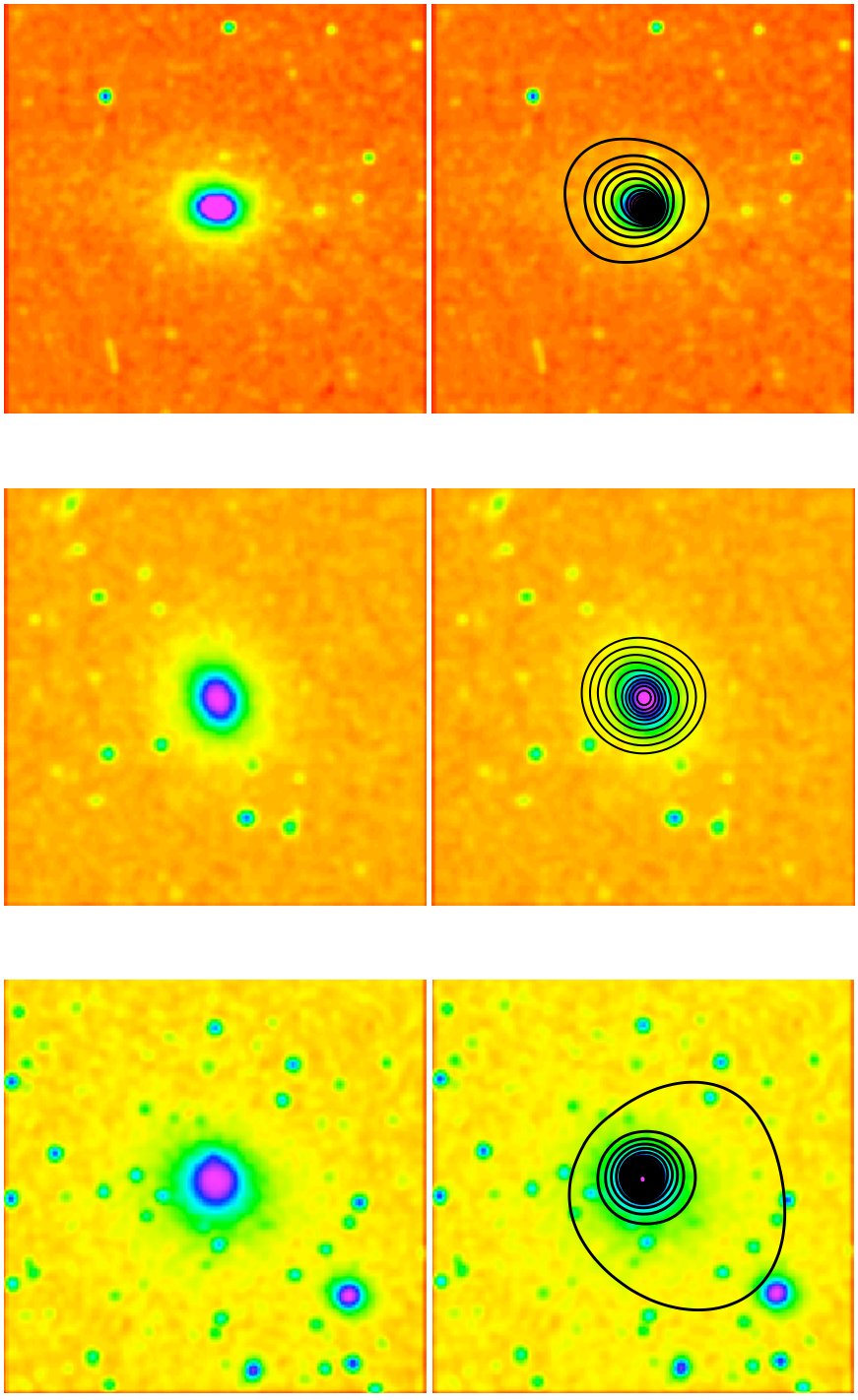

Figure 2.8: Diffuse emission contours overlaid on DSS II images. The images are 140 kpc on a side. The upper panel displays NGC 3209, the middle NGC 5546, and the lower NGC 6487.

2.7.9 NGC 7618

Studied in X-ray by Colbert et al. (2001) and Kraft et al. (2006), NGC 7618 may be the remains of a group – group merger. The galaxy′s X-ray luminosity was determined to be 7.7 $\times$ 10^{41} ergs s^{-1}. The hot gas has kT = 0.94 keV and an abundance of 0.55 solar. The contours of the diffuse X-ray emission, seen in Figure 2.9, are highly disturbed. There are numerous twists in position angle, X-ray fingers and the emission does not remain centered on the galaxy. The complex nature of the hot halo in NGC 7618 argues for relatively recent formation by multiple mergers.

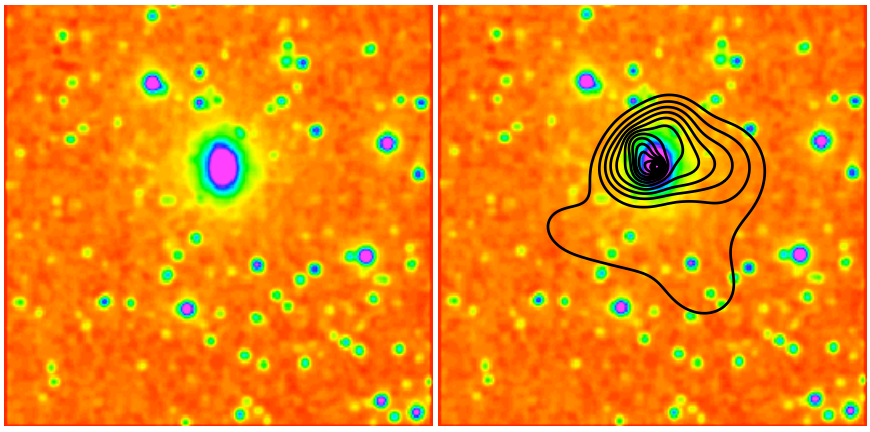

Figure 2.9: Diffuse emission contours overlaid on DSS II image of the isolated elliptical galaxy, NGC 7618. The image is 140 kpc on a side.

2.8 Lenticular Galaxies

2.8.1 NGC 1023

NGC 1023 is an SB0 galaxy at redshift, z = 0.002125. First detected as the brightest member of the NGC 1023 group by Humason, Mayall, & Sandage (1956) and subsequently listed as Lyon Group of Galaxies (LGG) 70 (Garcia 1993). The diffuse gas was fit by a Meka model and the hot gas was determined to have a temperature of 1.06 keV, an abundance of 0.14 solar. The model fit yielded an X-ray luminosity, $\log L_X = 39.2$ ergs s^{-1}. Figure 2.10 shows an image of the diffuse emission overlaid on a DSS image of the galaxy. The hot gas is symmetric and largely confined to the optical extent of the galaxy.

The galaxy has 25 resolved sources, including four supersoft sources (H31 & H21 ≤ -0.6) and two very hard sources (H31 & H21 = 1.0). Table 2.11 lists the positions, hardness ratios, fluxes, and X-ray luminosities of the point sources. Figure 2.11 displays the point sources overlaid onto a DSS image. More than half of the sources lie within or very near to the optical extent of the galaxy, which argues that these sources are truly related to NGC 1023. A plot of H31 versus H21 hardness ratios can be seen in Figure 2.12. In prior X-ray galaxy studies, point sources were found to lie along a broad diagonal strip from (H21, H31) $\sim$ (-0.3, -0.7) to (0.4, 0.5) and the sources in NGC 1023 fall well into that region. Plots such as these are meant to

highlight the overall number of sources as well as a rough estimate of the fraction of soft or hard X-ray sources. The X-ray color-color

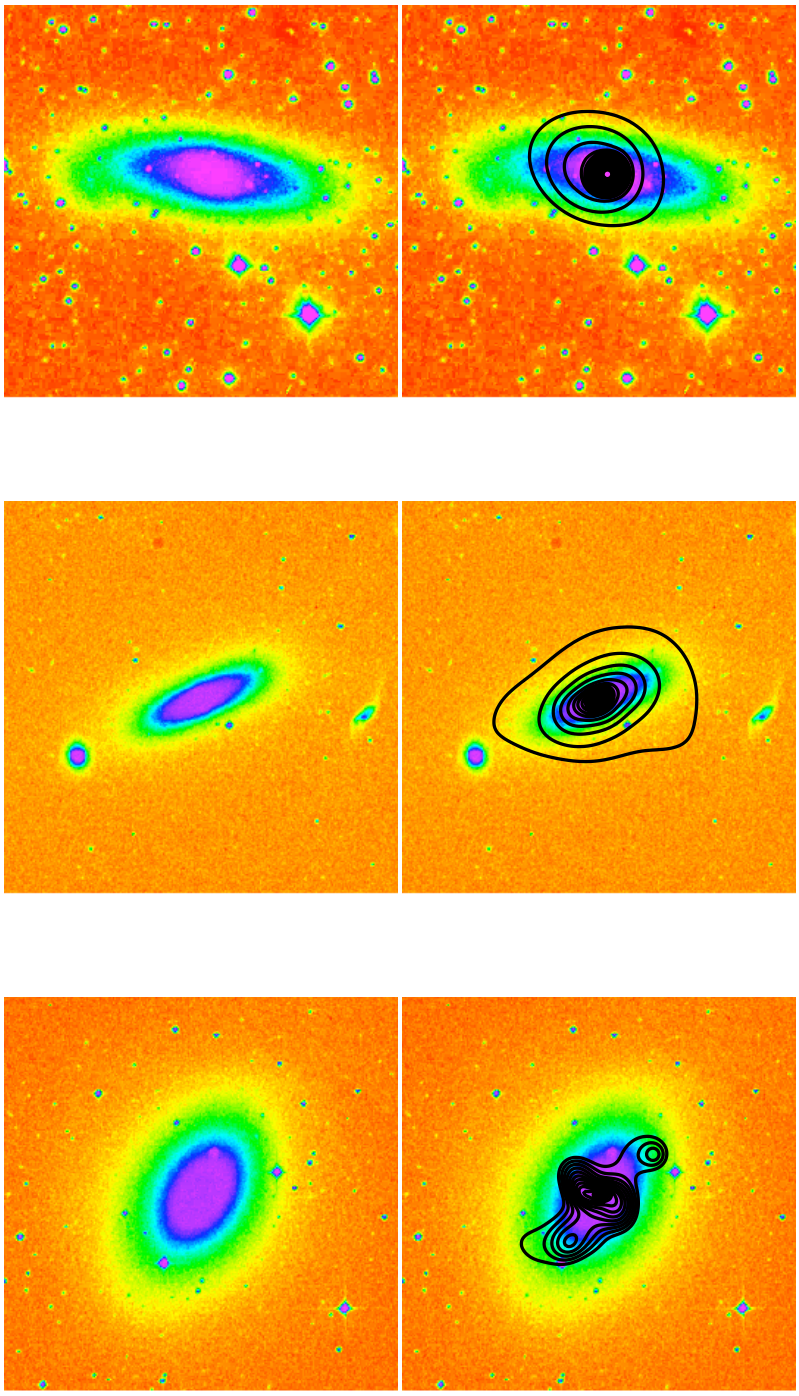

Figure 2.10: Diffuse emission contours overlaid on DSS II images. The images are 8.4 arcseconds on a side. The upper panel displays NGC 1023, the middle NGC 1332, and the lower NGC 1553.

plot shows the majority of NGC 1023 point sources are soft, with one exception. A single source can be seen to have extremely hard colors (H21, H31) = (1, 1).

The spectrum of the central source in NGC 1023 was fit using a Meka + disk blackbody model. The central source, CXOU J024023.9+390347, was found to have a temperature of 7.47 keV and log L_X = 38.9 ergs s^{-1}. The luminosity of the central source is well within the viable range of a LMXB and therefore is difficult to ascertain whether the source is an X-ray binary or an AGN.

The X-ray flux of the point sources which were unable to be fit by a model were estimated using a conversion of 1.89×10^{-5} counts s^{-1} to a flux of 8.38×10^{-14} ergs s^{-1} cm^{-2}. An additional source, CXOU J024013.0+390052, was found to have the same X-ray luminosity as the central source.

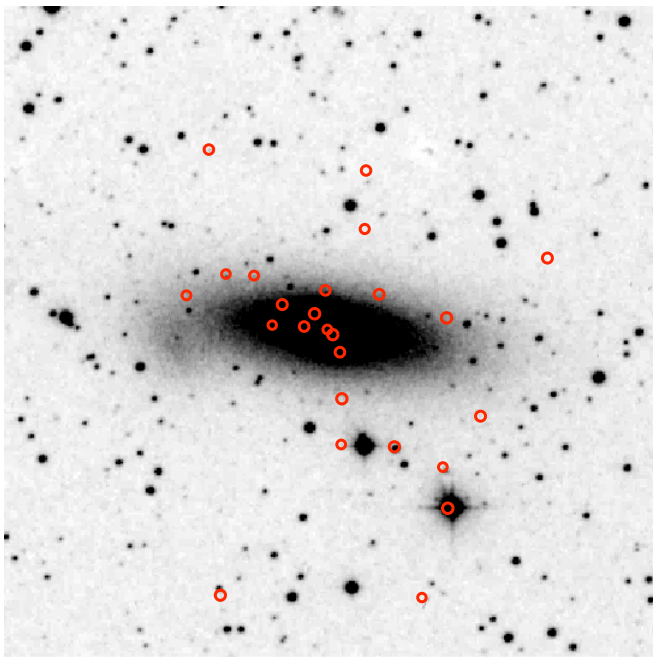

Figure 2.11: Point source population of NGC 1023 overlaid on DSS II image.

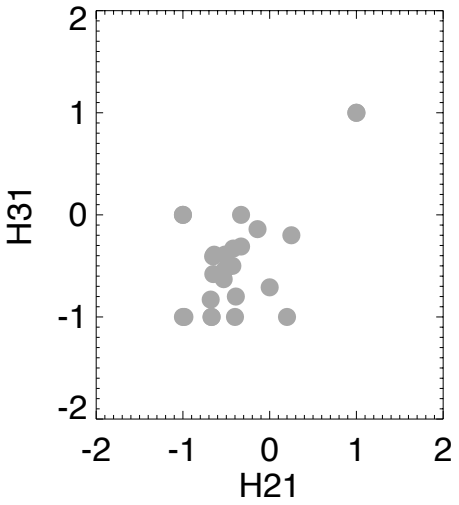

Figure 2.12: Hardness ratio plot for the point sources in NGC 1023.

2.8.2 NGC 1332

NGC 1332 is an S0 galaxy in the NGC 1315–1332 group. Located at a redshift of 0.005084, NGC 1332 is a typical lenticular, with B-V color of 0.91 mags and $M_B = -20.4$. The spectrum of the diffuse gas, fit with a Meka model, reveals a sub-solar abundance of 0.20 and a temperature of 0.58 keV. NGC 1332 was determined to have an X-ray luminosity of 2.1×10^{40} ergs s^{-1}. The contours associated with the diffuse emission, seen in Figure 2.10, are symmetric yet extend beyond the optical extent of the galaxy. No signs of ram pressure stripping or large-scale interactions with the group potential are observed.

An image of the point source population overlaid on a DSS image of NGC 1332 is displayed in Figure 2.13. Seventy-two point sources were detected. Chandra obser-

vations of the point sources in NGC 1332 were first studied by Humphrey & Buote (2004). Their Table 1 highlights the positions, count rates and luminosities of the source population. A number of sources lie far from NGC 1332 and hence may not be associated with the galaxy.

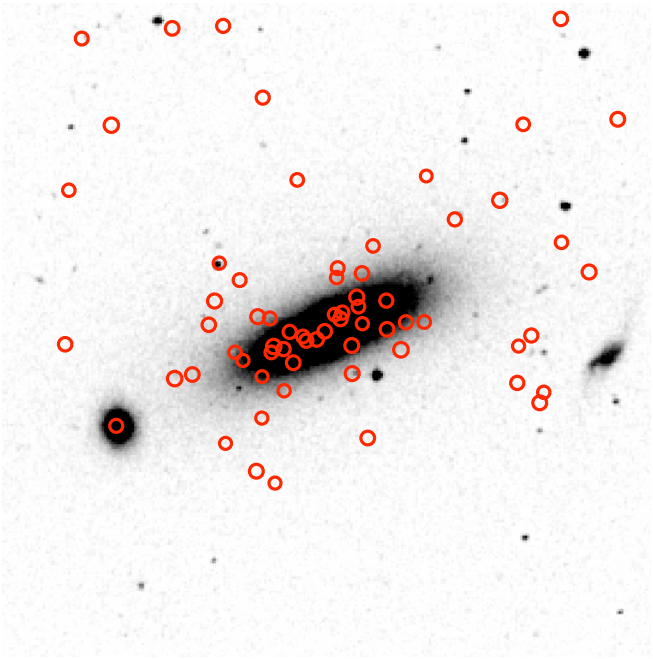

Figure 2.13: Point source population of NGC 1332 overlaid on DSS II image.

Thirteen sources are classified as super-soft. Figure 2.14 displays the X-ray color-color plot for the point sources. The central source, CXOU J032617.2-212007, is the most super-soft source with H31 = −0.93 and H21 = −0.84. Super-soft sources with hardness ratios near (−1, −1) indicate that those sources have no detectable emission above 1 keV and would be well fit by a blackbody spectrum model with Galactic absorption and a temperature of 0.1 keV (Sarazin et al. 2000).

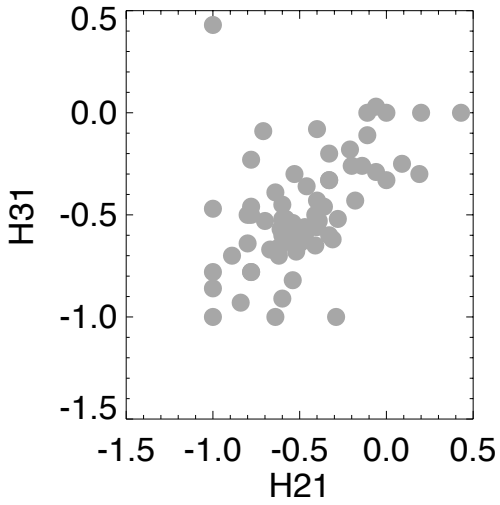

Figure 2.14: Hardness ratio plot for the point sources in NGC 1332.

Similar to NGC 1023, the spectrum of the central source of NGC 1332 was fit using a Meka + disk blackbody model. The fit resulted in a temperature of 0.56 keV, an abundance of 0.56 solar and a log $L_X = 39.99$ ergs s^{-1}. The large luminosity of CXOU J032617.2-212007 suggest an unlikely X-ray binary and an ideal AGN candidate.

The X-ray flux of the remaining sources was found using a conversion of 1.714×10^{-6} counts s^{-1} = 3.87×10^{-15} ergs s^{-1} cm^{-2}. In addition to the central source, three sources have X-ray luminosities greater than 1.0×10^{39} ergs s^{-1}, making them further examples of ultraluminous X-ray sources (ULXs). Humphrey & Buote (2004) found the X-ray luminosity function was well fit by a steep and unbroken power law. Fig. 8 of Humphrey & Buote displays their calculated luminosity function. The power-law

fit found by Humphrey & Buote is given by the following equation,

$$\frac{dN}{dL} = K \left(\frac{L_X}{L_{38}} \right)^{-\beta} \tag{2.4}$$

where $L_{38} = 10^{38}$ ergs s^{-1} . The best fit yielded $\beta = 2.3 \pm 0.4$ and an amplitude K = 60 ± 25. Unlike X-ray luminosity functions derived for the point sources populations in other early-type galaxies (Sarazin, Irwin, & Bregman 2000; Irwin, Sarazin, & Bregman 2002), a broken power law was not needed.

2.8.3 NGC 1553

NGC 1553 is a shell galaxy in the group LGG 112 (Garcia 1993) that is seen interacting with a companion, NGC 1549. Bridges & Hanes (1990) found the two galaxies separated by 11'.8. NGC 1553 is known to have cool gas and dust, being detected in all four IRAS bands (Bally & Thronson 1989). A Chandra investigation into the low-mass X-ray binaries of NGC 1553 was performed by Blanton et al. (2001).

The model-fit spectrum of the hot gas can be found in Blanton et al. (see their Fig. 8). Our analysis found the gas to have log $L_X = 40.1$ ergs s^{-1}, a sub-solar abundance of 0.11 and a temperature of 0.64 keV. Previous X-ray observations by Trinichieri, Noris, & di Serego Alighieri (1997) found evidence of X-ray substructures. Figure 2.10 displays the diffuse emission contours. The aforementioned substructures are evident. The is no symmetry observed and a strong position angle twist can clearly be seen. The hot gas has extension along the axis perpendicular to the disk.

Also roughly coincident with the disk are X-ray fingers or regions of higher X-ray emission. The cause of the X-ray fingers is uncertain.

The point source population was first listed in Table 1 and Fig. 4 of Blanton et al. (2001). We found fifty-six sources making up the point source population. The count rate-to-flux conversion for sources whose spectra couldn't be fit with a model is, 2.63 $\times 10^{-6}$ counts s^{-1} to a flux of 4.49 $\times 10^{-15}$ ergs s^{-1} cm^{-2}. Thirteen point sources had super-soft colors. A single hard source, CXOU J041606.0-554627, was found with H31 = 0.33 and H21 = 0.17. CXOU J041610.4-554648, the central source, was observed to have intermediate hardness (H31 = -0.17 & H21 = -0.19) and an X-ray luminosity fit with a broken power law yielding log L_X of 40.0 ergs s^{-1}. The central source, a ultra-luminous X-ray source, had an X-ray luminosity that would correspond to the Eddington limit for spherical accretion by a $\sim$ 120 solar mass object. Plots of the hardness ratio and the luminosity function can also be found in Blanton et al. Figs 5 & 6, respectively. The luminosity function was fit by Blanton et al. using a broken power law of the form,

$$\frac{dN}{dL_{38}} = N_0 \left(\frac{L_{38}}{L_b} \right)^{-\alpha} \tag{2.5}$$

The best fit gave $N_0 = 8.7$ and a break luminosity, $L_b = 4.1\times 10^{38}$ ergs s^{-1}. Below the break luminosity, α_l was determined to be -0.1, while above L_b, $\alpha_h = 2.7$ (Blanton et al. 2001).

2.8.4 NGC 2329

The optically dominant member of Abell cluster 569, NGC 2329 is a bright (-21.4 mag), red (B$-$V = 0.9 mag) S0 galaxy at z = 0.01933. The galaxy harbors a wide-angle tail radio source (Feretti et al. 1985) and Schombert (1986) has shown that an $r^{1/4}$ law fits the galaxy over its entire radial range. NGC 2329 is the farthest galaxy in our sample. The X-ray spectrum, was well fit using a Meka model. The galaxy displays the sample's second highest diffuse gas luminosity of log $L_X = 41.9$ ergs s^{-1}. The hot gas has solar abundance and one of the sample's largest temperatures, kT = 1.94 keV. The high temperature, approximately 1.0 keV larger than the typical early-type galaxy (Forman et al. 1985; Trinichieri et al. 1986), could be attributed to additional heating by the cluster potential and cluster members. The diffuse emission contours are seen in Figure 2.15. The emission is centered on the galaxy, yet extends well beyond the optical extent. The extension of the contours to the NE could be indicative of ram pressure stripping or the gravitational pull due to other cluster members and the cluster potential. While the gas is being pulled away from the galaxy, the gas to the SW of NGC 2329 is not compressed, ruling out ram pressure stripping. The cluster potential is likely gravitationally pulling hot gas from NGC 2329.

The point source population of NGC 2329 is extremely small, with only the central source observed. The lack of additional sources is most likely due to the short exposure time of the galaxy. The central source was found to have a soft X-ray colors, with

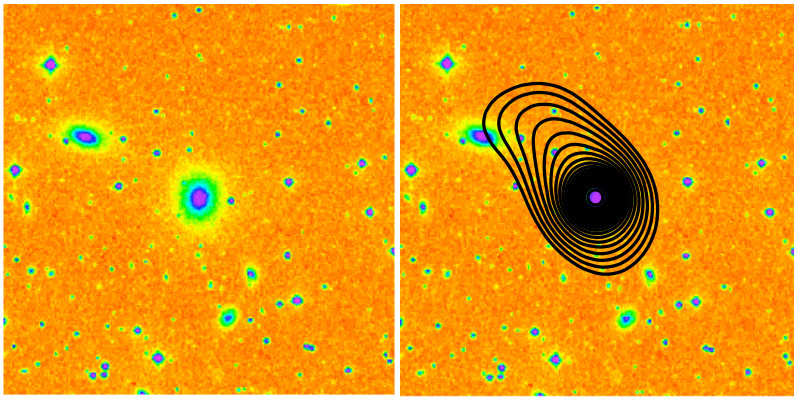

Figure 2.15: Diffuse emission contours overlaid on a DSS II image for S0 galaxy, NGC 2329. The image is 8.4 arcseconds on a side.

H31 = −0.54 and H21 = −0.46. The source spectrum was fit using a disk blackbody + thermal bremsstrahlung model. The temperature of the source was estimated to be 3.23 keV, with an X-ray luminosity of 6.3×10^{41} ergs s^{-1}. The high X-ray luminosity suggests that the central source is an AGN.

2.8.5 NGC 3115

NGC 3115, a field S0 galaxy at z = 0.002212, has colors (B−V = 0.9 mag) and brightness (M_B = −20.1 mag) typical of a lenticular galaxy. Originally classified as an E7 galaxy, Silva et al. (1989) studied the color distributions and Capaccioli et al. (1987, 1988) modeled the galaxy. The X-ray spectrum was fit with an Apec model. The diffuse X-ray gas was determined to have a temperature of 0.99 keV, an abundance of 0.38 solar, and a log luminosity of 39.9 ergs s^{-1}. The gas temperature is exactly the expected value for a typical early-type galaxy. Figure 2.16 displays the

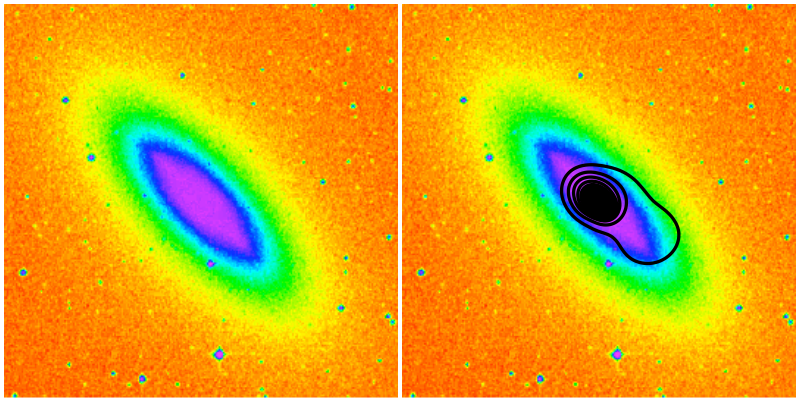

Figure 2.16: Diffuse emission contours overlaid on a DSS II image of the field S0, NGC 3115. The image is 8.4 arcseconds on a side.

diffuse contours over a DSS image. The hot gas is completely contained within the optical extent of NGC 3115. No significant structure can be seen in the diffuse gas.

The point source population of NGC 3115 is made up of 87 sources, displayed in Figure 2.17. The majority of the sources lie close to or within the optical galaxy. The central region of the galaxy has a large concentration of point sources. The positions, hardness ratios, fluxes, and X-ray luminosities of the point sources can be found in Table 2.12. The hardness ratios of sources 30, 36, 38, and 40, are hard with H31 $\geq$ 0.4 and H21 $\geq$ 0.33. The hard sources may be unrelated, strongly absorbed AGNs that produce the hard X-ray background. The X-ray color plot of the point sources can be seen in Figure 2.18. Super-soft hardness ratios are observed for fourteen sources.

The spectrum of the central source is fit with a broken power law, giving an X-ray luminosity of 5.0×10^{38} ergs s^{-1}. The central source has an L_X value consistent with either an AGN or a LMXB. The X-ray flux of the sources unable to be fit by a model,

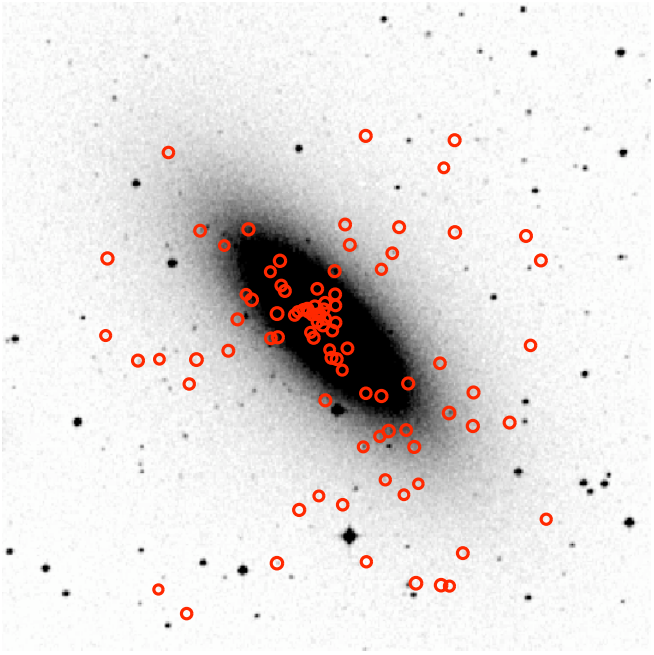

Figure 2.17: Point source population of NGC 3115 overlaid on DSS II image.

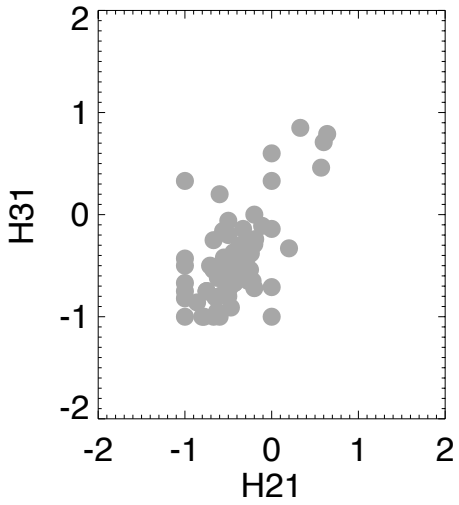

Figure 2.18: Hardness ratio plot for the point sources in NGC 3115.

were estimated using a ratio of 7.14×10^{-6} counts s^{-1} to a flux of 2.73×10^{-14} ergs s^{-1} cm^{-2}.

2.8.6 NGC 4382

A lenticular galaxy in Virgo, NGC 4382 is bright ($M_B = -20.0$ mag) with a fairly blue color (B−V = 0.83). An Apec model fit to the spectrum yielded a gas temperature of 0.42 keV and an extremely sub-solar abundance of 0.16. The galaxy's X-ray luminosity was derived as log $L_X = 39.8$ ergs s^{-1}. Both the temperature and abundance are very low, suggesting that the hot gas is nearly primordial and little heating has occurred. An image of the diffuse X-ray contours is seen in the top image of Figure 2.19. The contours are symmetric in the core, with slight distortion in the outer regions of the galaxy.

The 78 point sources found in NGC 4382 are highlighted in Figure 2.20. The sources extend nearly symmetrically around NGC 4382. The core has approximately eight sources in a tight configuration. The hardness ratios of 3 sources are classified as hard, while 14 sources meet the criteria for super-soft sources. The super-soft sources are similar to those found in the Large Magellanic Cloud and M31 (Kahabka & van den Heuvel 1997). The X-ray color-color plot is seen in Figure 2.21. The estimated count rate-to-flux conversion is 2.39×10^{-5} counts $s^{-1} = 1.92 \times 10^{-14}$ ergs s^{-1} cm^{-2}. The central source has an X-ray luminosity of 5.0×10^{38} ergs s^{-1}, as modeled

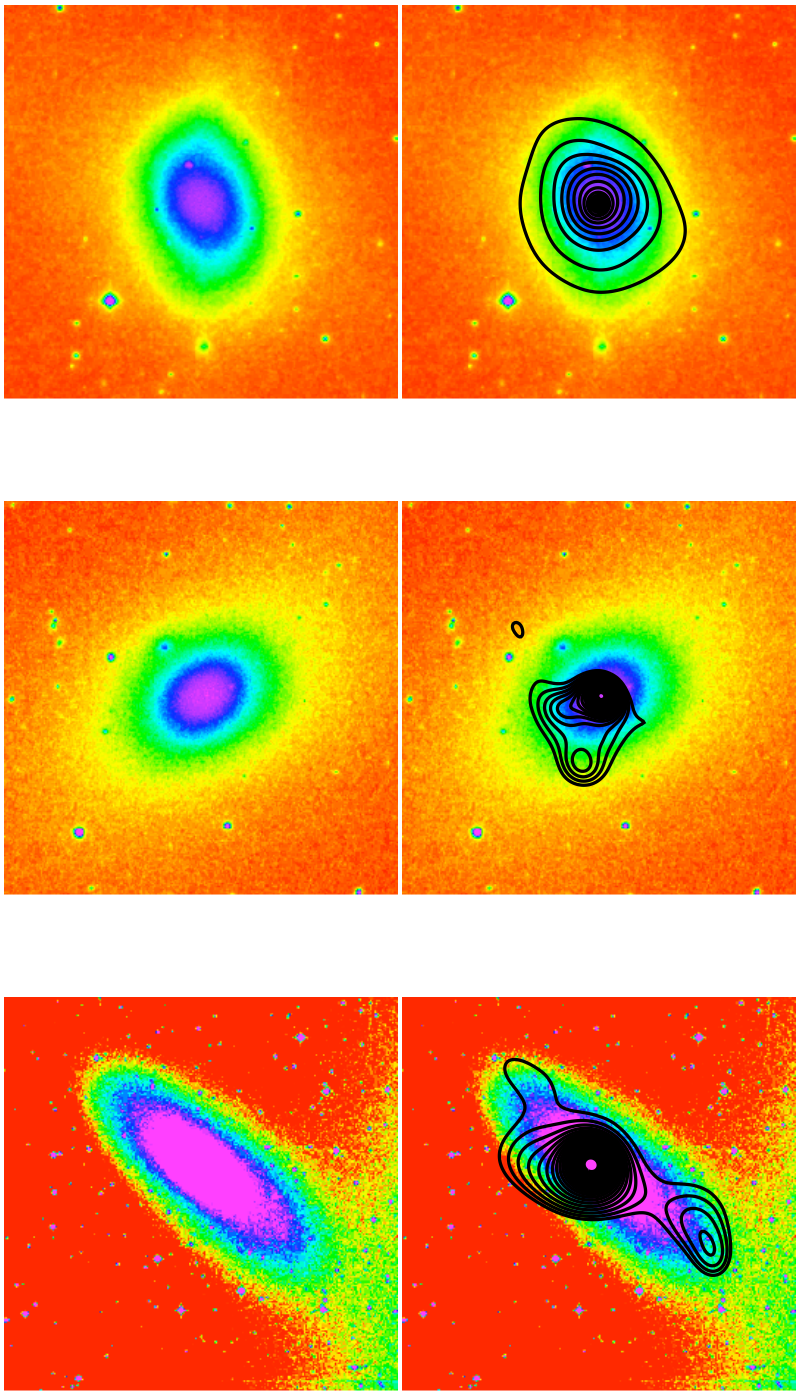

Figure 2.19: Diffuse emission contours overlaid on DSS II images. The images are 8.4 arcseconds on a side. The upper panel displays NGC 4382, the middle NGC 4406, and the lower NGC 5102.

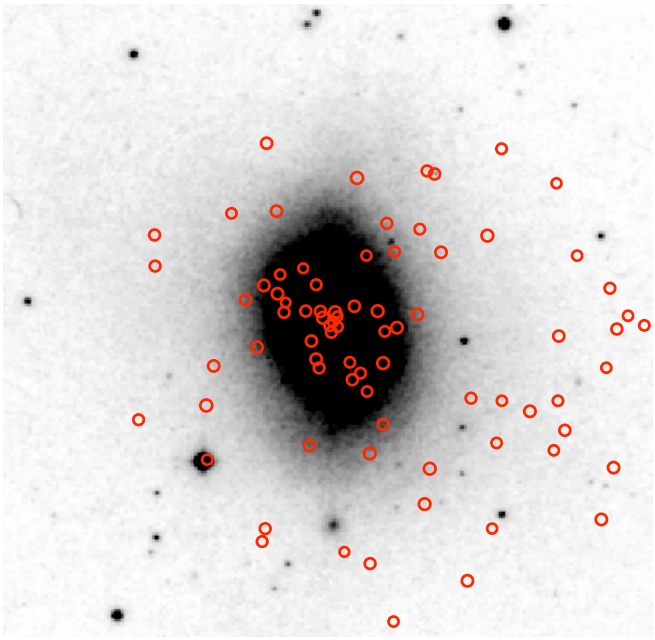

Figure 2.20: Point source population of NGC 4382 overlaid on DSS II image.

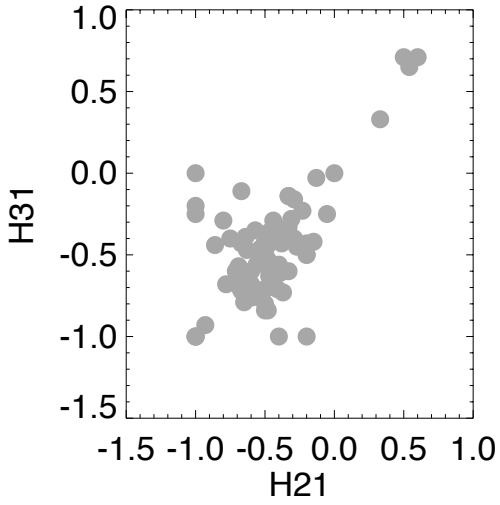

Figure 2.21: Hardness ratio plot for the point sources in NGC 4382.

by a broken power law. No sources were found with ULX luminosities. Table 2.13 summarizes the properties of the point source population.

2.8.7 NGC 4406

NGC 4406 is a very well studied S0 galaxy in the Virgo cluster. Also known as M86, NGC 4406 resides at a redshift of 0.000814 and is one of the brighter ($M_B = -20.7$ mag) galaxies investigated. The hot gas is found to have a sub-solar abundance of 0.29 and a temperature of kT = 0.75 keV. The spectrum was fit using an Apec model, giving an X-ray luminosity of 1.65×10^{39} ergs s^{-1}.

An image of the diffuse gas can be seen in the middle panel of Figure 2.19. The hot gas is the most unusual found in the sample. X-ray gas is absent from approximately 1/3 of the NW portion of NGC 4406. A ROSAT contour image of the Virgo region around NGC 4406 in a study by Kikuchi et al. (2000) shows M87 being the dominant galaxy both gravitationally and in its X-ray emission. We speculate that M87 has pulled a significant fraction of hot gas out of NGC 4406. The location of M87, toward the SE of NGC 4406, supports our claim of gravitational stripping. Most probably, NGC 4406 is also undergoing strong ram pressure stripping from the surrounding cluster gas.

NGC 4406 was observed to have 24 point sources, seen in Figure 2.22. The majority of the sources were found very close to the galaxy, which argues for their true association to NGC 4406. Table 2.14 lists the important feature of the point

sources. The central source spectrum was fit by a disk blackbody model that gave an estimated luminosity of 8.0 $\times$ 10^{37} ergs s^{-1}. The central source also has soft X-ray colors, H31 = -0.71 and H21 = -0.47. The remaining sources included nine super-soft sources and a single hard source (source 25). Three sources meet the criteria as being ULX sources. Plots of hardness ratio is displayed in Figures 2.23. For sources whose spectra could not be modeled, a conversion of 1.73 $\times$ 10^{-5} counts s^{-1} to 4.35 $\times$ 10^{-14} ergs s^{-1} cm^{-2}.

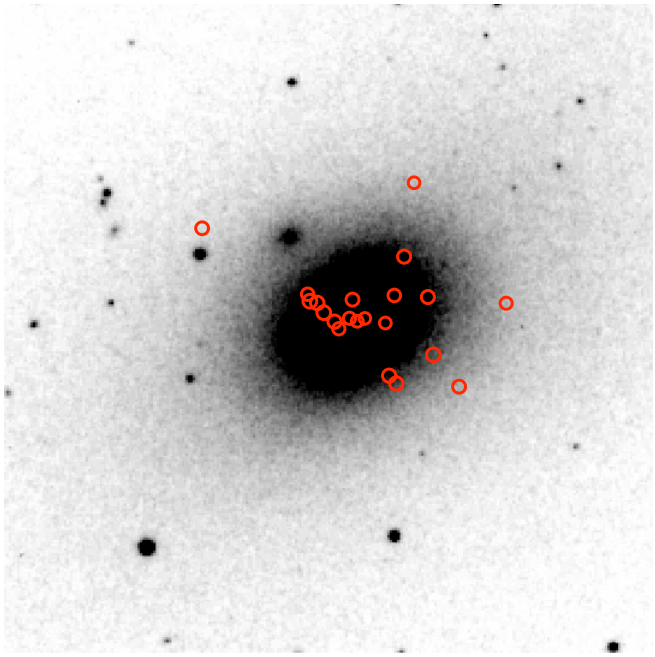

Figure 2.22: Point source population of NGC 4406 overlaid on DSS II image.

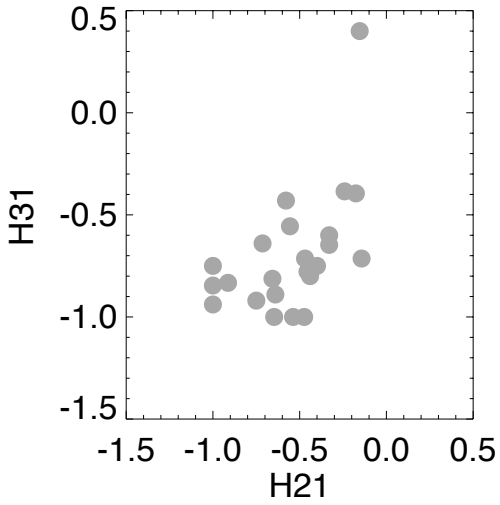

Figure 2.23: Hardness ratio plot for the point sources in NGC 4406.

2.8.8 NGC 5102

The sample's bluest (B−V = 0.64 mag) lenticular, NGC 5102 is a member of the Centarus A group. Table 1 of Kraft et al. (2005) highlights the properties of the point source population. Also found in Kraft et al. are the point sources overlaid onto a 2MASS J-band image and a plot of the luminosity function (Figs. 2 and 3, respectively). The X-ray spectrum, modeled using Apec, gives an X-ray luminosity calculated as 1.6×10^{38} ergs s^{-1}, the lowest of the sample. Additionally, NGC 5102 had the sample's lowest temperature of 0.33 keV and a solar abundance. The low temperature matches values found for X-ray faint elliptical galaxies, which are often assumed to have total luminosities dominated by point sources. An image of the diffuse emission contours is displayed in the lower panel of Figure 2.19. Features of

the contours are similar to NGC 1553, with regions of hot gas found along the edges of the galaxy's disk.

The point sources can be seen in Figure 2.24. Only two sources, the central source and an additional LMXB, fall within the optical extent of NGC 5102. Most of the remaining twenty-nine sources surround the galaxy and fall near the same radii. The spectrum of the central source was fit with a broken power law model that resulted in a luminosity of 7.9×10^{37} ergs s^{-1}. In order to estimate the X-ray luminosity of other sources, a conversion of 8.1×10^{-6} counts $s^{-1} = 1.92 \times 10^{-14}$ ergs s^{-1} cm^{-2} was used. No ULX sources were detected and the X-ray luminosities were found to be much lower than the point sources in the other S0 galaxies sampled.

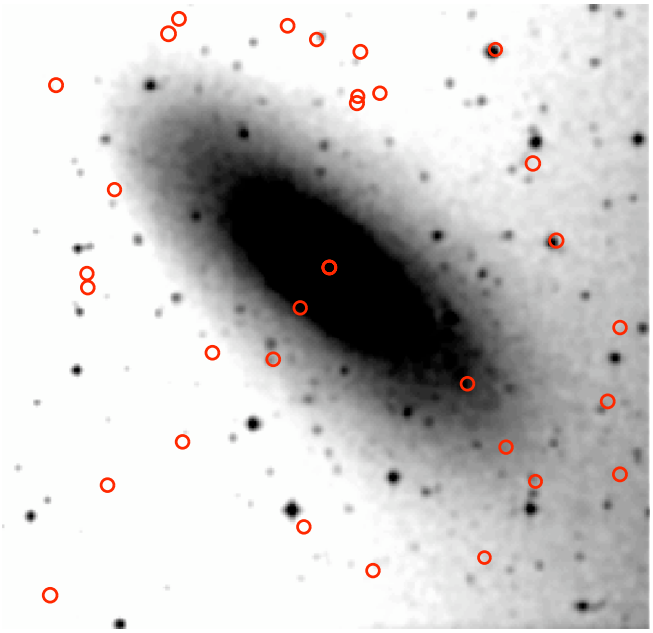

Figure 2.24: Point source population of NGC 5102 overlaid on DSS II image.

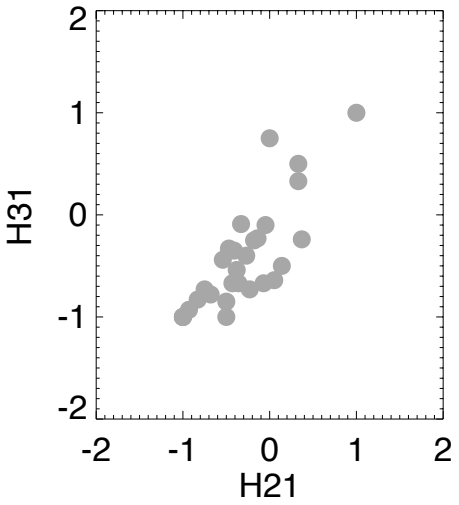

Figure 2.25: Hardness ratio plot for the point sources in NGC 5102.

The hardness ratios of the sources are seen in Figure 2.25. Eight sources had super-soft colors, including the central source, CXOU J132157.4-363751. Three sources had very hard ratios, including one source with X-ray colors of H31 =1.0 and H21 = 1.0.

2.8.9 NGC 5353

A member of the Hickson compact group 68, NGC 5353, is a bright ($M_B = -20.6$ mag) lenticular galaxy 32.3 Mpc away. Fit using an Apec model, the diffuse gas was found to have a temperature of 0.83 keV and a super-solar abundance of 1.09. NGC 5353 was the only sample galaxy to have such enriched gas. The galaxy has an estimated log X-ray luminosity of 40.6 ergs s^{-1}. The diffuse emission contours can be

seen in Figure 2.26. The possibility remains that the derived abundance and emission could

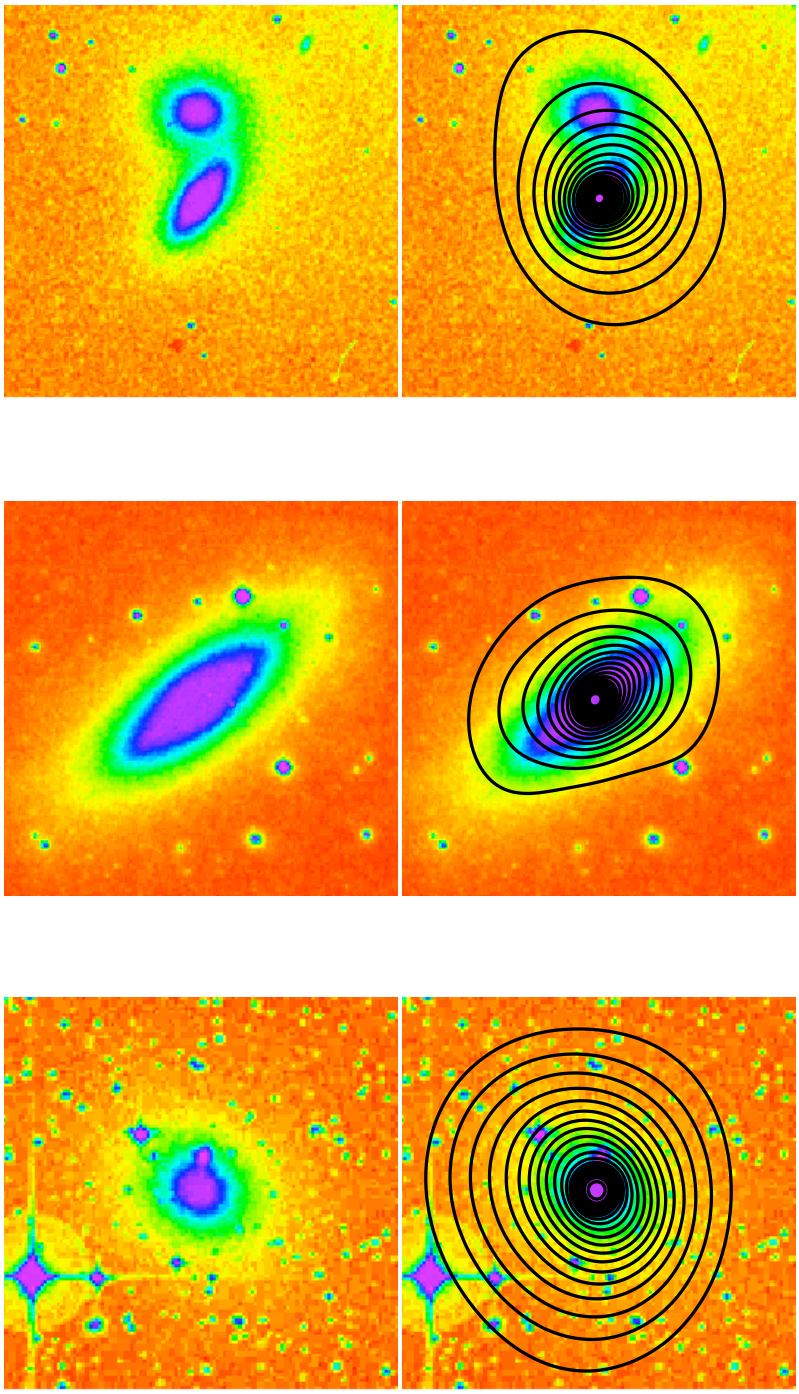

Figure 2.26: Diffuse emission contours overlaid on DSS II images. The images are 5.3, 3.5, and 8.4 arcseconds on a side top to bottom. The upper panel displays NGC 5353, the middle NGC 5866, and the lower NGC 6407.

be due to a near neighbor seen in Fig. 2.26. The hot gas extends well beyond NGC 5353 and encompasses the neighbor, NGC 5354.

The galaxy has only three detected sources, which can be seen in Figure 2.27. Table 2.15 lists the dynamical and X-ray properties of the point sources. Based on the locations of the non-central sources, there is a high possibility that only the central source is associated with NGC 5353. The central source is an extreme super-soft source with H31 = −0.91 and H21 = −1.0. Source 3, CXOU J135316.9+401356, has a hard H31 ratio of 0.56.

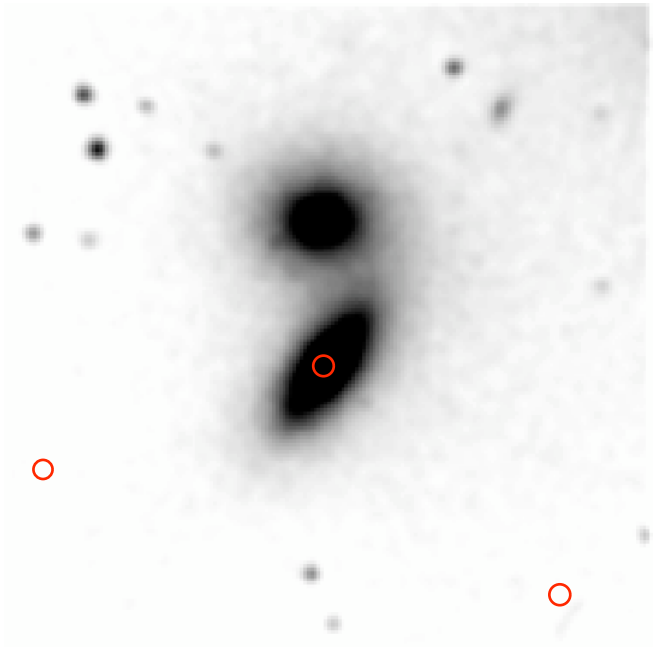

Figure 2.27: Point source population of NGC 5353 overlaid on DSS II image.

The central source, CXOU J135326.7+401659, and CXOU J135338.9+401613 are ULX sources. The third source falls just below the ULX value of 10^{39} ergs s^{-1}. Due

to the lack of sources, plots of the X-ray luminosity function and X-ray colors were not calculated.

2.8.10 NGC 5866

NGC 5866 is a member of the group LGG 396 (Garcia 1993) at redshift, z = 0.002242. The X-ray spectrum of the moderately blue (B−V = 0.78) S0 was fit using an Apec model and yielded an X-ray luminosity of 2.6×10^{39} ergs s^{-1}. The hot gas had a temperature of 0.64 keV. Similar to most of the other S0 galaxies in the sample, NGC 5866 has a sub-solar abundance, with a value of 0.24. Figure 2.26 shows the hot gas of NGC 5866. The contours are symmetric and show no signs of interaction with the surrounding group environment.

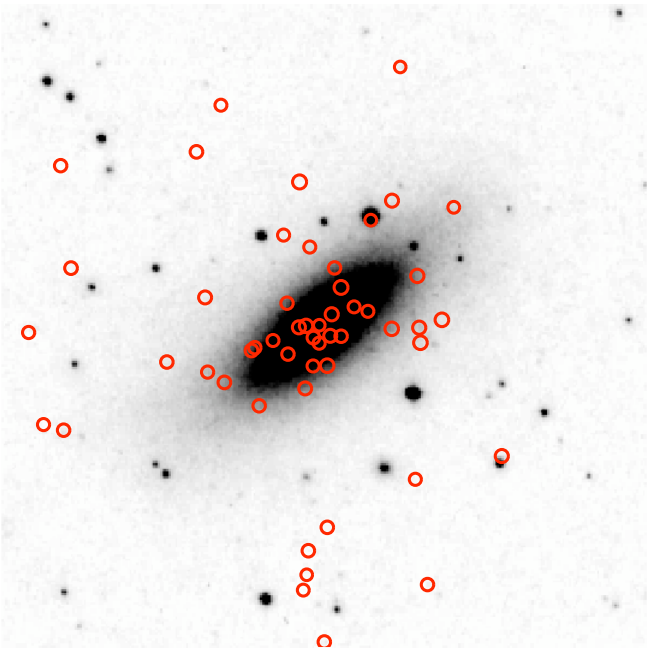

Figure 2.28: Point source population of NGC 5866 overlaid on DSS II image.

The point source population of NGC 5866 can be seen in Figure 2.28. The optical extent of the galaxy can be seen to contain many sources, with many found in the core region. The properties, both dynamical and X-ray, are listed in Table 2.16. Fourteen of the 56 sources are classified as super-soft, while five sources have very hard X-ray colors. Figure 2.29 displays a plot of the hardness ratios.

The central source was determined to have super-soft X-ray colors, H31 = -0.53 and H21 = -0.76. The spectrum of the central source, CXOU J150629.7+554547, was fit with a Meka+disk blackbody model giving an estimated log luminosity of 38.5 ergs s^{-1}. A conversion of 3.67×10^{-7} counts s^{-1} to 8.27×10^{-16} ergs s^{-1} cm^{-2} was used. No sources were determined to have greater than log $L_X = 38.5$ ergs s^{-1}.

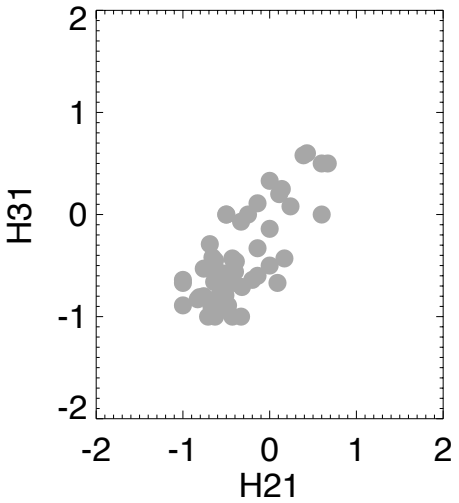

Figure 2.29: Hardness ratio plot for the point sources in NGC 5866.

2.8.11 NGC 6407

The final sample galaxy, NGC 6407 is a member of the LGG 411 group, found 64.3 Mpc away. NGC 6407 is also the sample's reddest and brightest galaxy, $M_B = -20.6$ mag. A Meka model fit to the X-ray spectrum gave a total diffuse gas X-ray luminosity of 1.3×10^{42} ergs s^{-1}, making NGC 6407 the most X-ray luminous of the sample. The gas, seen in Figure 2.26, has a temperature of 0.75 keV and an abundance of 0.26 solar. The hot gas can be seen to extend well beyond the galaxy and into the group region. Based on L_X, NGC 6407 is one of the more luminous early-type galaxies. Assuming that the group members merge into a single galaxy, a fossil group would be formed, having an extended, highly luminous X-ray halo.

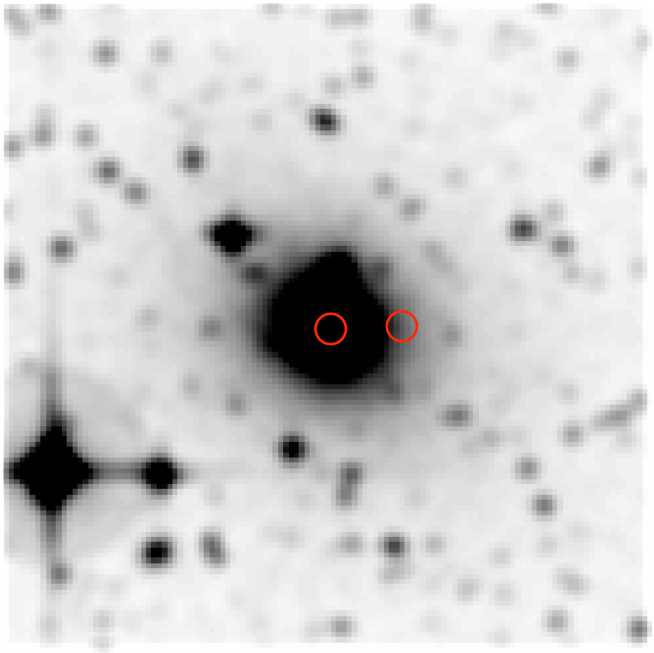

Figure 2.30: Point source population of NGC 6407 overlaid on DSS II image.

The point source population of NGC 6407 is very sparse, with only five sources detected. Table 2.17 lists the features of the point source population. Figure 2.30 shows the galaxy and two sources. The remaining two sources are much farther extended from NGC 6407 and are possibly not associated with the galaxy. Three sources are classified as having super-soft hardness ratios, including the central source, CXOU J174457.9-604424. Source 4, CXOU J174526.1-604227, is the only super-hard source, with H31 & H21 equal to 1.0. All five sources were estimated to have X-ray luminosities well in excess of the ULX minimum. Hardness ratio and luminosity plots were not created due to the scarcity of sources in NGC 6407.

2.9 Discussion

2.9.1 HCG, FG, & isolated elliptical galaxy samples

The Hickson compact group sample is seen to have narrow ranges for all of the X-ray properties studied. With the exception of HCG 51, the gas temperature has a range of 0.62 – 1.08 keV and an average value of 0.81 keV. The average gas abundance is 0.19 solar and spans the range of 0.09 – 1.0 solar. The X-ray luminosities of the HCG sample have a range of 3.8×10^{40} – 7.8×10^{41} ergs s^{-1}, with an average of 3.7×10^{41}. The fossil group and isolated elliptical galaxy samples display more symmetric and undisturbed hot gas halos when compared to the active and stirred gas seen in

the sample of HCGs. Features such as these are to be expected since the HCGs are dynamic regions, while the isolated galaxies have had few outside perturbations.

The fossil group sample has X-ray luminosities in the range of 1.1×10^{41} and 3.2×10^{43} ergs s^{-1}, with an average value of 9.3×10^{42} ergs s^{-1}. The isolated elliptical sample has an average L_X of 4.0×10^{41} ergs s^{-1} and values ranging from 2.1×10^{40} to 8.8×10^{41} ergs s^{-1}. The isolated ellipticals L_X values fall well into the range found for the HCG sample, with the fossil groups having much larger X-ray luminosities.

The hot gas temperature of the isolated ellipticals had a minimum of 0.57 keV and a maximum of 1.0 keV, with an average value of 0.91 keV. The fossil group sample had an average temperature of more than double the observed average isolated elliptical, at $kT = 1.85$ keV. The fossil groups also had a larger dispersion, with gas temperatures ranging from 0.82 keV to 3.22 keV. Again, the isolated ellipticals fall well within the range of HCG gas temperatures, while the fossil groups have much hotter halo gas.

In order to understand the emission from the HCG sample, we investigated the relation between a groups X-ray luminosity and velocity dispersion. Using the line-of-sight velocity dispersions from Hickson et al. (1992), Figure 2.31 displays log L_X against σ. Equation 2.1, which describes the expected gas temperatures due to the motion of galaxies within the gas, suggests that low velocity dispersion galaxy groups would have lower X-ray luminosities. As expected, the larger the velocity dispersion, the higher the X-ray luminosity. With the exception of HCG 51, the HCGs appear to reach a maximum log L_X value just below 42.0. HCG 51 likely has a large luminosity

due to high emission in the individual galaxies as well as an extensive amount of X-ray emitting diffuse gas distributed in the intergroup medium. The maximum luminosity is difficult to determine due to the limited sample size.

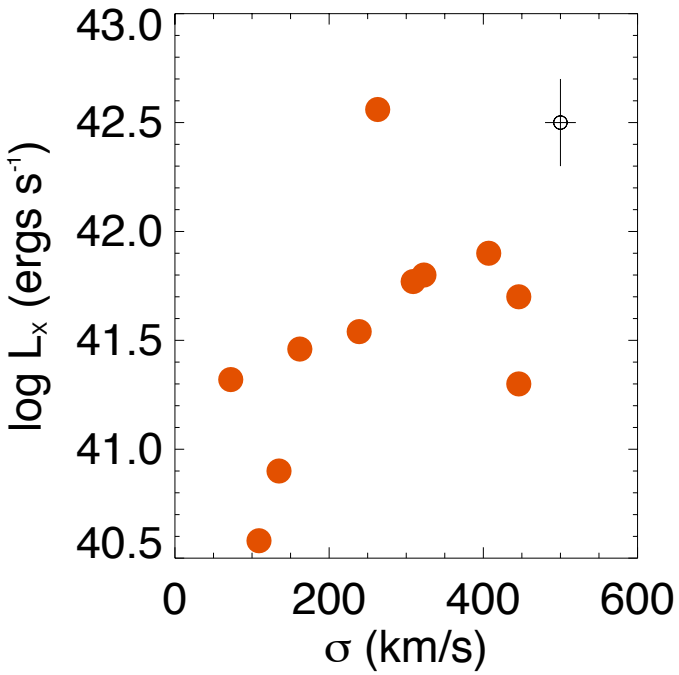

Figure 2.31: Relation between HCG σ and hot gas X-ray luminosity. Velocity dispersion values come from Hickson et al. (1992).

Previous authors have examined possible correlations between the spiral fraction and X-ray luminosity. In the study of Ponman et al. (1996), an anticorrelation was found. Contrary to the results of Ponman et al., Pildis et al. (1995) observed extended X-ray emission to be preferentially found in groups with low spiral fractions. Groups with a high spiral galaxy fraction are assumed to be young groups where galaxy

interactions have not distributed and heat gas to X-ray temperatures (Pildis et al. 1995). Based on the theory that large spiral fraction groups are young, we would not expect large L_X values for spiral-only compact groups. Plotted in Figure 2.32 is the log L_X – f_{sp}. Our results indicate no correlation between the number of spiral galaxies and the amount of emission. We recognize the possibility that because our sample was derived from archival pointed observations, the HCG sample represents the brightest known Hickson groups irrespective of galaxy member morphology.

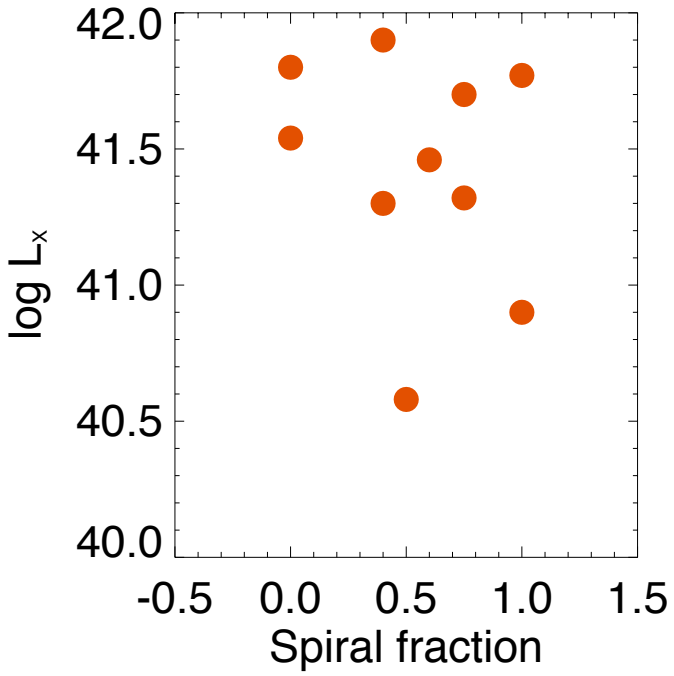

Figure 2.32: Fraction of spiral galaxies in the HCGs plotted against the L_X of the group. There appears to be no correlation between f_{sp} and X-ray luminosity. The small sample size may influence the lack of trend in the data.

The connection between fossil groups and isolated ellipticals can also be studied using the optical brightness. Evidence that FGs and isolated ellipticals formed via mergers can be determined if the galaxies have large group-like X-ray halos and large optical brightness. The merger hypothesis would suggest a trend where the optically brightest FGs and isolated ellipticals would also be the X-ray brightest galaxies. The trends followed by the FG and isolated elliptical galaxy samples are shown in Figure 2.33. The straight line is not a fit to the data, but is instead used to highlight the overall trend. As the galaxys optical brightness increases, its X-ray brightness does as well. The isolated ellipticals follow the same general trend as the fossil groups, but display lower absolute magnitudes and L_X values.

Figure 2.34 displays the logarithm of X-ray luminosity against our estimated of the effective X-ray radius. The effective radius, R_{ex}, was defined as the radius where source counts fell to 2σ above the background. The X-ray effective radius was developed as a means to quantify the size of the X-ray halo, as no satisfactory methods currently exist. The highest L_X values, namely the brightest FGs, were left off of Fig. 2.34 in order to focus on the compact groups and isolated ellipticals. Clearly seen, the effective radius increases with X-ray brightness. For the majority of the HCGs and isolated ellipticals, the R_{ex} remains below 2 Mpc. The four FGs not shown in Fig. 2.34 have effective radii as small as 6.64 Mpc and up to 12.83 Mpc. The effective X-ray radii of the samples indicate a number of intriguing features. The FGs not displayed in Fig. 2.34 have X-ray halos similar to those of clusters. The compact

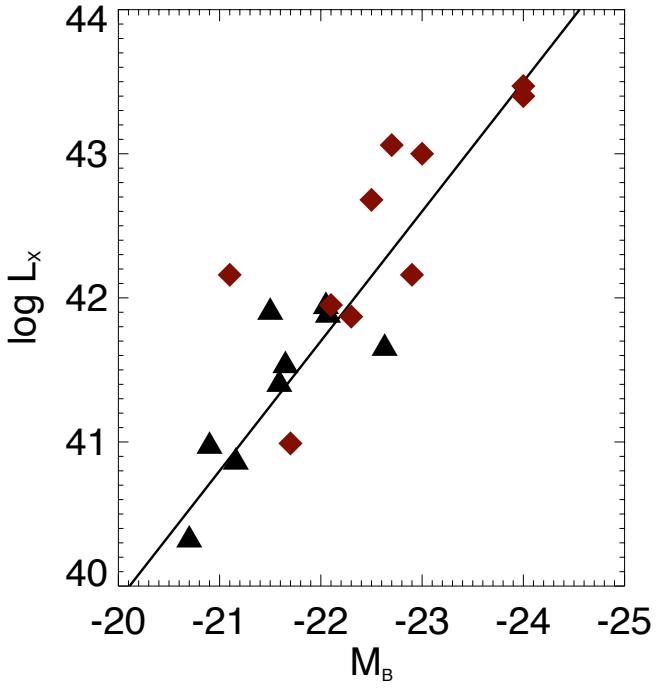

Figure 2.33: Log L_X plotted versus the galaxy absolute B magnitude. FGs are displayed as red diamonds and isolated ellipticals as black triangles.

groups, isolated ellipticals, and approximately half of the fossil groups have R_{ex} in the sub-Mpc range. Fig. 2.34 also appears to show that at log L_X greater than 42.0, the effective radii becomes significantly large.

Prior studies of groups and clusters have found correlations between X-ray brightness and gas temperature. Figure 2.35 displays the L_X-kT relation for the HCG, isolated elliptical and fossil group samples. The line drawn highlights the trend followed by all three samples. The HCG (orange circles) and isolated ellipticals (filled triangles) are observed to fall in the same locus, with temperatures near 1 keV (log kT

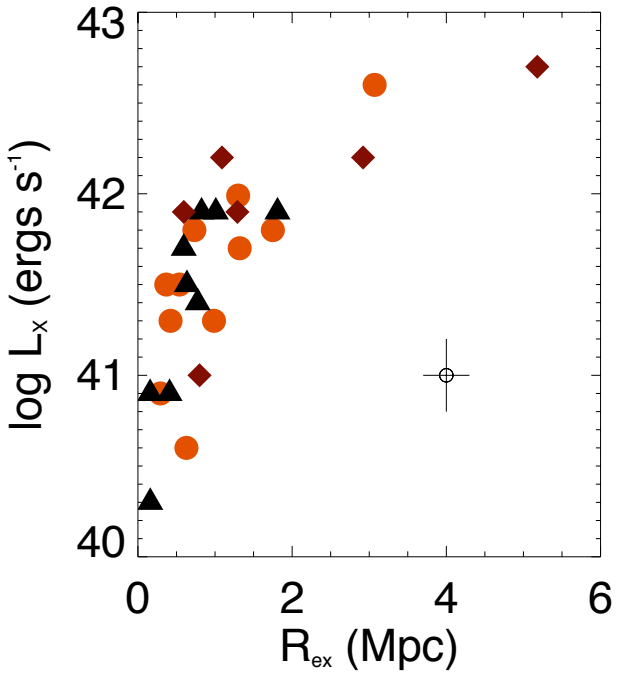

Figure 2.34: X-ray luminosity versus X-ray effective radius for the HCG, FG, and isolated elliptical galaxy samples. Red diamonds represent FGs, black triangles are isolated ellipticals, and orange circles represent HCGs. Population 1 FGs, HCGs, and isolated ellipticals have R_{ex} in the same sub-Mpc range. Population 2 FGs have considerably larger effective X-ray radii, suggesting a link between pop. 2 FGs and clusters.

$\sim$0.0) and log L_X between 40.5 and 42. The fossil group sample features a bimodal population. Population 1 fossil groups have properties similar to the HCG and isolated ellipticals. The X-ray luminosities of the population 1 FGs are fractionally larger than the HCG sample. Population 2 FGs are significantly hotter with temperatures of $\sim$3.0 keV (log kT $\sim$0.5) and more luminous, log L_X near 43.0 ergs s^{-1}. Notably, HCG 51 sits far from the common trend of the samples. As the hottest and most

X-ray luminous Hickson compact group in our sample, HCG 51 shares traits more in common with population 2 FGs. As X-ray gas temperature is a direct tracer of gravitational potential, the population 1 fossil groups exist in more massive potential wells than either the HCGs or isolated ellipticals. Larger gravitational potentials further argue that population 2 FGs are the remnants of a coalesced poor cluster. Similar conclusions were made for RXJ1416.4+2315 (Khosroshahi et al. 2006a), which was determined to be the remains of a poor cluster of galaxies.

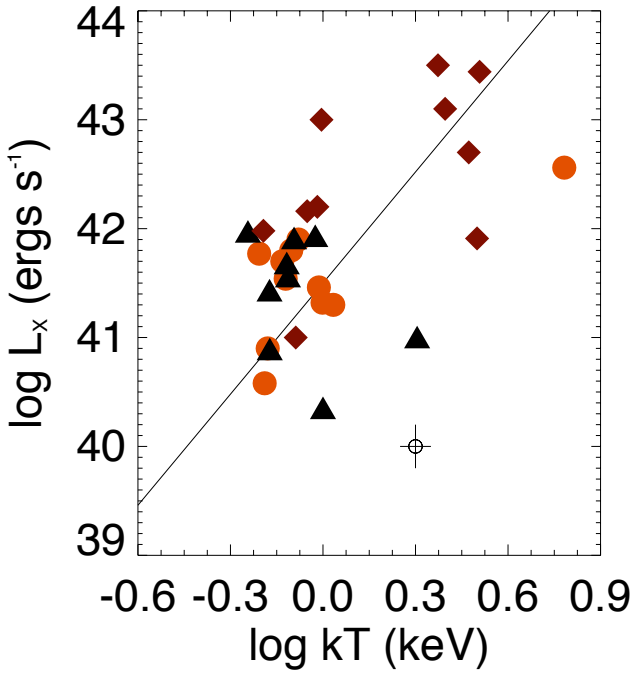

Figure 2.35: L_X:kT relation for the compact group, fossil group, and isolated elliptical samples. The symbols are the same as Fig. 2.34. An estimate of the average error of the three samples is included. The HCG, FGs, and isolated ellipticals all follow the same general trend in L_X:kT.

Figures 2.36 and 2.37 show the histograms of L_X for the HCG-isolated elliptical galaxy samples and for the HCG-fossil group samples, respectively. The HCG sample is displayed as a solid line in both figures. The L_X values of the HCGs are comparable yet slightly lower than the isolated ellipticals. Again, the fossil groups are significantly more luminous than the HCG sample. A visual inspection of the histograms would argue that, based on L_X, the HCG and fossil groups have little in common. A K-S test was performed on the L_X values of the three samples. A K-S test reveals, with 99% probability, that the L_X values of the HCGs and isolated ellipticals appear to be drawn from the same parent population. The K-S test points towards the FGs and HCGs being to distinct populations.

Based on the Figs. 2.35–2.37, less than 50% of all FGs are the results of a merged compact group of galaxies. The fact that the HCG and isolated elliptical galaxy samples reside at the same locus of Fig 2.35 argues strongly that the galaxy members of a compact group will merge and result in an isolated elliptical. The possibility remains that compact groups could evolve into a population 1 FG. The major difference between the population 1 FGs and the isolated ellipticals is simply a single companion galaxy yet to be accreted. The connection between population 1 FGs and population 2 FGs is still unclear. The two populations could simply be the opposite ends of a naturally occurring mass distribution. Larger samples of compact and fossil groups and isolated ellipticals would be needed to further determine evolutionary and mass connections.

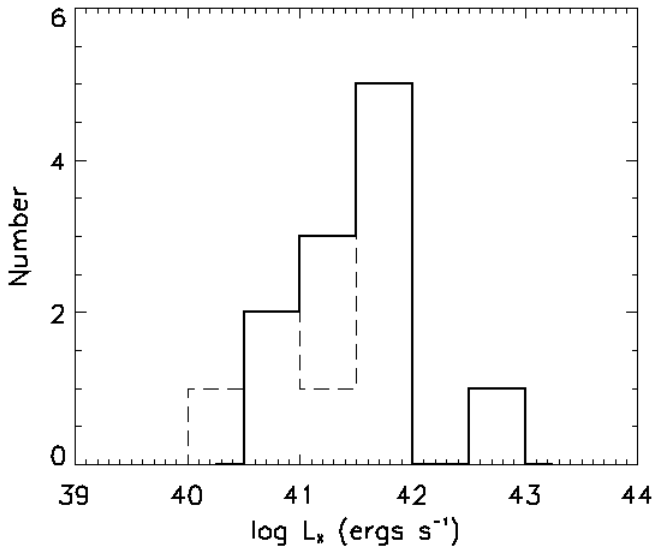

Figure 2.36: Histogram of X-ray luminosities for the compact groups and isolated ellipticals.The solid line represents the HCG L_X values, while the dashed line is the isolated elliptical galaxy values.

The data suggests that there is likely not a sequence of evolution between compact groups and fossil groups. The data suggests that at least the population 2 fossil groups are the remains of a merged poor cluster. Mendes de Oliveira (2006) found that the environment around the Hickson groups 31, 79 and 92 are too sparse to evolve into a fossil group. Their results suggest that HCG 42 or 62, both containing a wealth of dwarf galaxies, would be ideal candidates to become fossil groups. While these two HCGs may have the necessary environments, our results suggest that they are X-ray underluminous and the gas too cold to fulfill the fossil group requirements.

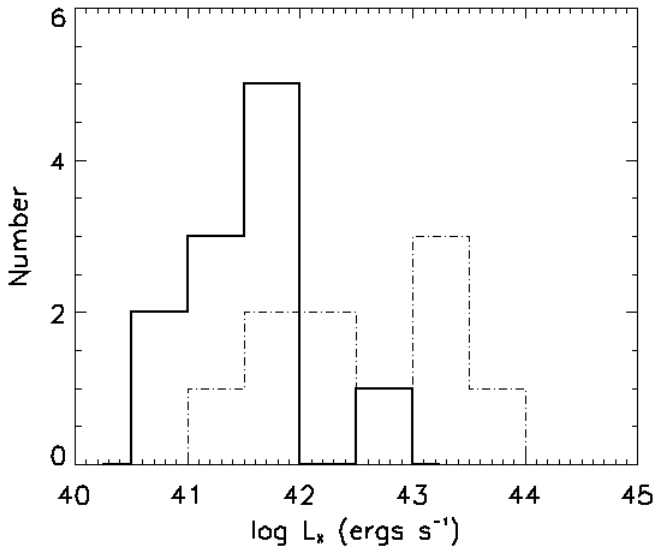

Figure 2.37: Histogram of X-ray luminosities for the compact groups and fossil group galaxies. The solid line represents the HCG L_X values, while the dashed line indicates values of the fossil group sample.

2.9.2 S0 galaxy sample

The diffuse X-ray gas in our sample of lenticulars can be used to understand both environmental influences and general trends that would be expected for future X-ray observations of S0 galaxies. The diffuse gas in NGC 1332, 5353, 5866, and 6407 all show signs of extended gas, representing four of the sample's 11 galaxies (36%). The common thread amongst these galaxies is that they are all members of groups, with NGC 5353 being a member of a Hickson compact group. Ram pressure stripping is most likely too weak to remove gas from the galaxies. The group gravitational

potential may be sufficient to pull gas away from the parent galaxy, but not to the extent that the hot gas becomes fully displaced into the intragroup region.

One sample galaxy, NGC 6407, had a very high X-ray luminosity and extended halo of hot gas, suggesting a precursor fossil group. NGC 6407 would be one of the first S0s found that matches the requirements of a future fossil group. Observations of the other group members would help determine the likelihood that the group coalesces into a single bright early-type galaxy with a large hot gas halo.

Two galaxies, NGC 2329 and NGC 4406, show signs of unusual or asymmetric diffuse emission. Both of these galaxies reside in high-density cluster environments. The presence of the strong cluster potential seems to cause major asymmetries. The strongest cause for such a scenario is NGC 4406, which is having its gas pulled by M87 and the potential of the Virgo cluster.

NGC 1553 and NGC 5102 both have diffuse emission with intensity peaks along the S0 disk. Both galaxies reside in group environments. The cause of the emission is unknown, however the emission may be evolutionary traces of past spiral arms/features. The features may arise from rotation in the disk. While the wing-like features are common to both galaxies, the core regions differ greatly. NGC 1553 has hot gas extending perpendicular to the galaxy disk, while NGC 5102 has roughly symmetric emission in the core.

The hot gas in NGC 3115 and NGC 1023 are both confined to optical extent of the galaxy and are highly concentrated in the galaxy core. The two galaxies

have very little in common, NGC 1023 is a member of a group and NGC 3115 is classified as a field S0. NGC 3115 is particularly important given that only a handful of field/isolated S0s have been observed (Marcum et al. 2004; Fuse et al. (2008) in prep.). If NGC 3115 formed via the collapse of a primordial gas cloud and has remained unperturbed, the hot gas would likely remain tightly bound to the galaxy and have little extension. Such a model would suggest a near quiescent evolution of the X-ray gas throughout the lifetime of the galaxy. The same features found in NGC 1023 are more difficult to explain. Residing in a group environment, NGC 1023 would have to lie on the outskirts of the group or be a relatively new group member. Either scenario would result in the group's potential well not having enough time to sufficiently pull gas from the galaxy.

The individual point sources were found to fall in a range of luminosities between 10^{36} – 10^{40} ergs s^{-1}. The most luminous sources were generally the central source. The total luminosity of the point sources ranged from 4.9×10^{38} to 6.5×10^{41} ergs s^{-1}. The S0 galaxies with the two most luminous total point source populations are NGC 2329 and NGC 6407, had a total of one and five detected sources, respectively. The low number of sources in these two galaxies, coupled with the very high luminosities, are yet another argument that the central sources in these lenticulars are AGN.

The formation mechanism of S0 galaxies is still poorly constrained. If mergers and interactions have dominated the evolution of S0s, then X-ray luminosity should increase as optical brightness increases. The relation between X-ray luminosity and

optical brightness is shown in Figure 2.38. A very strong trend is seen where L_X increases with increasing absolute magnitude. There is little dispersion observed, which may be due to the limited number of galaxies in the sample. The point of greatest dispersion comes from NGC 4406. We speculate that NGC 4406 is underluminous in its X-ray emission, due to gas having been removed by M87. While the X-ray brightness spans a fairly large range of 4 orders of magnitude, the range of the optical brightness only covers two orders of magnitude. A clearer understanding of the observed trend would come with a sample containing fainter lenticular galaxies.

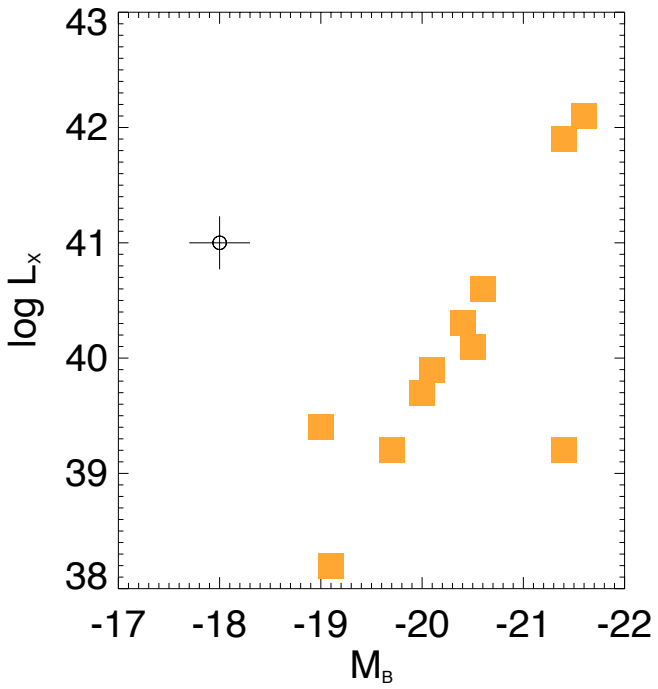

Figure 2.38: Diffuse gas L_X plotted versus absolute B magnitude for the S0 galaxies.

Figure 2.39 highlights the relation between X-ray luminosity and gas temperature. The S0 sample follows similar trends previously seen in ellipticals (Helsdon & Ponman 2000; O′Sullivan et al. 2003). Previous observations have found that the hot gas in lenticular galaxies rarely reaches "high" temperatures (kT $\geq$ 1.5 keV) and are often classified as typical or faint early-type galaxies. The absence of a significant number of faint S0s with kT $\leq$ 0.4, makes the determination of the exact relation difficult. Until a larger sample is compiled, all that can be noted is that the S0 sample follows the general trends of elliptical galaxies.

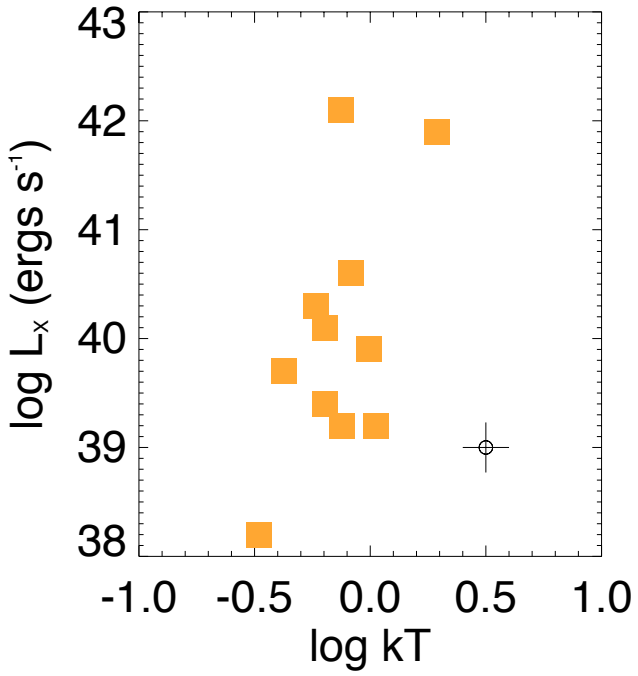

Figure 2.39: Lenticular galaxy sample correlation between X-ray brightness and diffuse gas temperature.

The correlation between exposure time and the number of detected point sources is displayed in Figure 2.40. The plot was made to determine whether the source counts were intrinsic to the galaxy or were a reflection of the exposure time. It should be obvious that as exposure time increases, more sources should be detected. That trend can be seen, as the exposure time increases, the number of sources increases. An increase in dispersion for larger exposure times is expected, as the total number of sources associated with the galaxy is a fixed value and the number of sources will reach a maximum value.

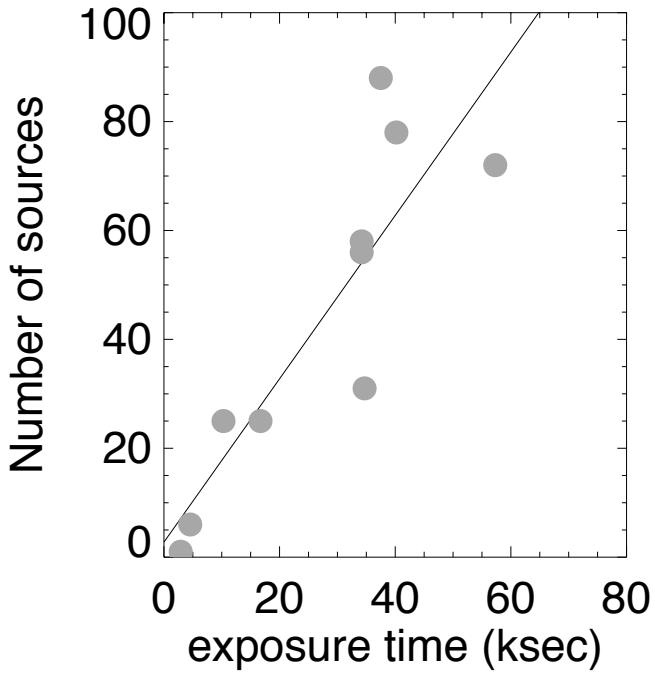

Figure 2.40: Chandra Observatory exposure time plotted against the number of detected point sources.

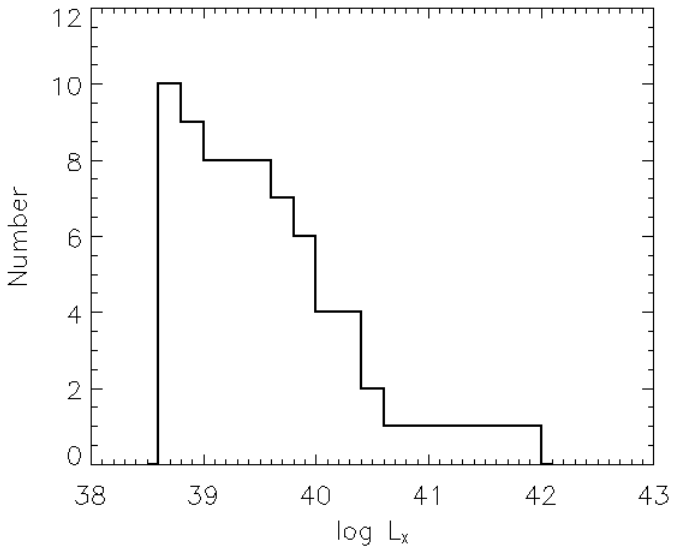

Figure 2.41: Histogram of integrated point source population L_Xs for the lenticular galaxy sample.

The total X-ray luminosity of the point sources is highlighted in a histogram of Figure 2.41. The sample shows only a moderate number of total point sources with extremely large luminosities. A larger number of high luminosity point sources would have been incontrovertible evidence that a central black hole exists in all S0 galaxies. The characteristic luminosity for the total point source population lie around 6.0 $\times$ 10^{38} ergs s^{-1}. The X-ray luminosity due to the point sources is futher investigated in Figure 2.42. For a small number of sources, the dispersion in L_X is very large. That trend is expected, as a powerful, unobscured central source could comprise a

large fraction of the point source population's brightness. Assuming the two brightest points are due to AGN, a trend can be seen in the remaining data. While the band of possible luminosities is large, as expected, the greater the number of sources results in a larger L_X for the total point source population.

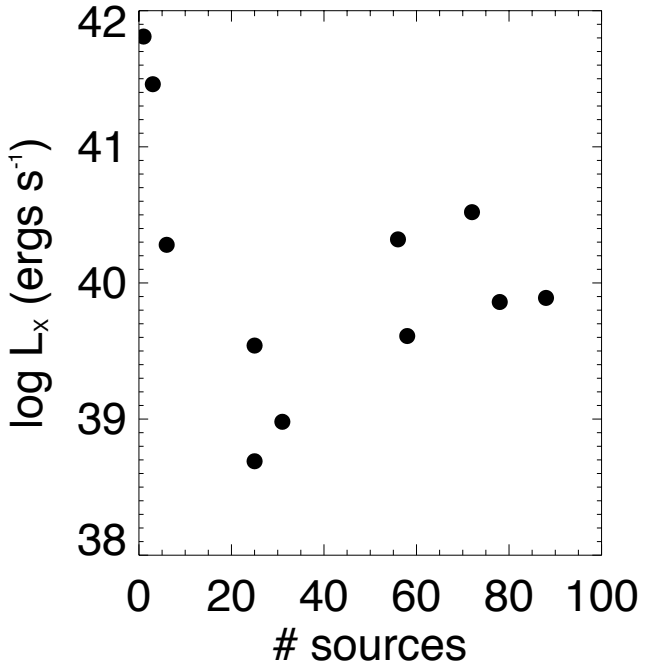

Figure 2.42: Total point source X-ray luminosity plotted against the number of detected sources.

Also of note is the lack of possible high-mass X-ray binaries (HMXBs). Although the study of NGC 5102 (Kraft et al. 2005), found a large population of HMXBs, we found that the sources in NGC 5102 were most likely LMXBs. We find approximately 15 candidate HMXBs in the entire S0 sample.

All sample galaxies had distinct sources located at the galaxy center. Based on X-ray luminosities, four of the eleven sample S0s (36%) have a strong likelihood of harboring an AGN at their core. The majority of the sample's central sources had X-ray luminosities falling in the range consistent with either an AGN or a low-mass X-ray binary. Longer exposures would help to clear any ambiguity in the nature of the central sources.

2.10 Conclusions

An investigation into the diffuse X-ray gas properties of compact groups, fossil groups, and isolated elliptical was performed on archival Chandra Observatory data. The results of the X-ray analysis have yielded the following conclusions:

- There is a correlation between optical brightness and X-ray luminosity of the fossil groups and isolated ellipticals that is interpreted as evidence the galaxies have formed as a result of major mergers.

- The X-ray properties of the isolated ellipticals most closely resemble the properties of the compact groups. The implication of the common X-ray features is that the isolated ellipticals are likely the remains of a coalesced compact group.

- There exist two populations of fossil groups. The population 1 FGs have properties similar to the compact groups and isolated ellipticals. Population 2 FGs

display X-ray luminosities an order of magnitude larger and have gas temperatures significantly hotter than the compact groups.

- The data suggests that less than 50% of the fossil groups are the remains of a merged compact group. Instead the population 2 fossil groups have X-ray properties that suggest a merged poor cluster origin.

- X-ray analysis has proven to be the long-lived diagnostic needed to evaluate the formation and evolution of galaxies.

In the first large-scale investigation into the hot gas properties of S0 galaxies, a number of general trends were discovered. Provided the current sample of S0 galaxies is a fair representation of all lenticular galaxies, the results presented here suggest:

- The halo of hot gas extends beyond the optical boundaries when the galaxy is located in a group environment, shows signs of stripping when found in a cluster, or for field/isolated S0s the hot gas would have little extension beyond the optical extent of the galaxy.

- The temperature of the X-ray emitting gas loosely follows the L_X:kT and L_X:M_B relations observed for ellipticals. Additionally, the gas has sub-solar abundances, ~ 0.25 solar.

- Twenty to seventy-five point sources would be detected in each lenticular galaxy.

- A central source with super-soft X-ray colors and an X-ray luminosity of approximately 10^{39} ergs s^{-1} would be detected. The nature of the central source is unable to be determined.

- Approximately 10% of sources will have super-soft X-ray colors and $\sim$ 1% of the sources would have very hard colors.

Table 2.1. Properties of the Hickson Compact Group Sample

Group	α	δ	Dist	number of members	θ_G
(1)	(2)	(3)	(4)	(5)	(6)
16	02:09:31.3	−10:09:31	52.8	4	6.4
30	04:36:28.6	−02:49:57	61.6	4	4.5
37	09:13:35.6	+30:00:51	89.2	5	3.2
40	09:38:54.5	−04:51:07	89.2	5	1.7
42	10:00:21.8	−19:38:57	53.2	4	6.0
51	11:22:20.9	+24:17:35	103.2	6	4.5
62	12:53:08.1	−09:13:27	54.8	4	3.7
80	15:59:12.3	+65:13:33	119.6	4	1.7
90	22:02:05.6	−31:58:00	35.2	4	7.4
92	22:35:57.5	+33:57:36	86	5	3.2
97	23:47:22.9	−02:19:34	87.2	5	5.2

Note. — Col. (1): HCG group number. Col. (2): Right ascension as listed in NED. Col. (3): Declination as listed in NED. Col. (4): Distance, in Mpc, as listed in NED. Col. (5): Number of group members as listed in Hickson et al. 1992. Col. (6): Angular size of group, in arcminutes, as listed in Hickson 1982.

Table 2.2. Properties of Galaxy Members of the Hickson Compact Groups

Galaxy	α	δ	Type	v_{rad}	Dist.
(1)	(2)	(3)	(4)	(5)	(6)
16a	02:09:24.7	−10:08:11	SBab	4073	54.3
16b	02:09:20.9	−10:08:00	Sa	3864	51.5
16c	02:09:38.6	−10:08:46	S0	3851	51.3
16d	02:09:42.9	−10:11:03	Spec	3874	51.7
30a	04:36:18.6	−02:49:53	SB0	4697	62.6
30b	04:36:30.2	−02:51:59	SAB0	4625	61.7
30c	04:36:23.4	−02:48:00	SBbc	4508	60.1
30d	04:36:36.6	−02:50:35	S0	4666	62.2
37a	09:13:39.4	+29:59:35	E	6745	89.9
37b	09:13:33.1	+30:00:01	Sbc	6758	90.1
37c	09:13:37.3	+29:59:58	S0/a	7356	98.1
37d	09:13:33.8	+30:00:57	SBdm	6131	81.7
37e	09:13:34.0	+30:02:23	E	6469	86.3
40a	09:38:53.5	−04:50:57	E	6628	88.4
40b	09:38:55.0	−04:51:57	SA0	6842	91.2
40c	09:38:53.6	−04:51:37	SBb	6406	85.4
40d	09:38:55.7	−04:50:13	SB0/a	6492	86.6
40e	09:38:55.4	−04:51:30	SABa	6633	88.4

Table 2.2 (continued)

Galaxy	α	δ	Type	v_{rad}	Dist.
(1)	(2)	(3)	(4)	(5)	(6)
42a	10:00:14.3	−19:38:13	E	3964	52.9
42b	10:00:33.1	−19:39:43	SB0	4228	56.4
42c	10:00:10.3	−19:37:19	E	4005	53.4
42d	10:00:13.0	−19:40:23	S0	4042	53.9
51a	11:22:26.3	+2417:57	E	7626	101.7
51b	11:22:14.2	+24:18:01	SBbc	8219	109.6
51c	11:22:30.0	+24:16:45	E/S0	8902	118.7
51d	11:22:30.5	+24:17:59	Sab	7529	100.4
51e	11:22:13.3	+24:19:01	E	7700	102.7
51f	11:22:26.4	+24:17:44	S0	7532	100.4
62a	12:53:05.7	−09:12:14	S0	4259	56.9
62b	12:53:04.4	−09:12:00	S0	3561	47.5
62c	12:53:09.9	−09:11:55	E	4432	59.1
62d	12:53:06.6	−09:15:28	E/S0	4174	55.7
80a	15:59:19.1	+65:13:58	Sd	8975	119.7
80b	15:59:21.6	+65:13:22	Sab	9584	127.8
80c	15:59:07.2	+65:14:02	Sd	9550	127.3
80d	15:59:12.0	+65:13:19	Im	9108	121.4

Table 2.2 (continued)

Galaxy	α	δ	Type	v_{rad}	Dist.
(1)	(2)	(3)	(4)	(5)	(6)
90a	22:02:01.9	−31:52:11	Sa	2603	34.7
90b	22:02:08.4	−31:59:23	E	2511	33.5
90c	22:02:03.2	−31:58:25	E	2497	33.3
90d	22:02:06.5	−31:59:34	Sab	2659	35.5
92a	22:36:03.4	+33:56:53	Scd	786	10.5
92b	22:35:58.4	+33:57:57	SBbc	5774	80.2
92c	22:36:03.5	+33:58:33	SBbc	6747	93.7
92d	22:35:56.7	+33:57:56	E	6630	92.1
92e	22:35:51.9	+33:56:42	E	6599	91.7
97a	23:47:23.0	−02:18:02	SB0	6932	96.3
97b	23:47:37.8	−02:19:00	Sc	6666	92.6
97c	23:47:23.8	−02:21:04	S	6003	83.4
97d	23:47:18.9	−02:18:49	E	6328	87.9
97e	23:47:19.9	−02:16:50	S0/a	6665	92.6

Note. — Col. (1): HCG group number. Col. (2): Right ascension as listed in NED. Col. (3): Declination as listed in NED. Col. (4): Morphological type listed in Hickson 1982. Col. (5): Heliocentric velocity in km s^{-1} as listed in NED. Col. (6): Distance determined using Hubble's law with the velocity in Col. (5) and a Hubble constant of 72 km s^{-1} Mpc^{-1}.

Table 2.3. Properties of the Fossil Group Sample

Group	α	δ	M_B	Dist
(1)	(2)	(3)	(4)	(5)
NGC 777	02:00:14.9	+31:25:46	−22.0	69.7
NGC 1550	04:19:37.9	+02:24:36	−21.1	51.6
NGC 4936	13:04:17.1	−30:31:35	−21.6	43.3
NGC 5419	14:03:38.8	−33:58:42	−22.3	57.4
ESO 3060170	05:40:06.7	−40:50:11	−22.7	149.2
ESO 5520200	04:54:52.3	−18:06:56	−22.5	130.9
RXJ1256.0+2556	12:56:04.9	+25:56:52	−24.0	966.7
RXJ1331.5+1108	13:31:29.6	+11:07:57	−22.9	329.2
RXJ1340.6+4018	13:40:33.4	+40:17:48	−23.0	718.3
RXJ1552.2+2013	15:52:12.3	+20:13:45	−24.0	566.7

Note. — Col. (1): Galaxy Name. Col. (2): Right ascension as listed in NED. Col. (3): Declination as listed in NED. Col. (4): Absolute B-band magnitude as listed in LEDA. Col. (5): Distance, in Mpc, as listed in NED.

Table 2.4. Properties of the Isolated Elliptical Galaxy Sample

Group	α	δ	M_B	Dist
(1)	(2)	(3)	(4)	(5)
NGC 766	01:58:42.0	+08:20:48	−21.5	112.6
NGC 1132	02:52:51.8	−01:16:29	−22.0	96.4
NGC 3065	10:01:55.3	+72:10:13	−20.7	27.8
NGC 3078	09:58:24.6	−26:55:35	−20.9	34.7
NGC 3209	10:20:38.4	+25:30:18	−21.1	86.5
NGC 4555	12:35:41.2	+26:31:23	−21.7	92.9
NGC 5546	14:18:09.2	+07:33:52	−21.9	101.8
NGC 6487	17:52:41.8	+29:50:19	−22.5	106.2
NGC 7618	23:19:47.4	+42:51:09	−21.3	72.1

Note. — Col. (1): Galaxy Name. Col. (2): Right ascension as listed in NED. Col. (3): Declination as listed in NED. Col. (4): Absolute B-band magnitude as listed in LEDA. Col. (5): Distance, in Mpc, as listed in NED.

Table 2.5. Dynamical Properties of the S0 Sample

Galaxy	Ra	Dec	radial velocity	Distance	M_V
(1)	(2)	(3)	(4)	(5)	(6)
NGC 1023	02:40:24.0	+39:03:48	637.5	8.9	−19.7
NGC 1332	03:26:17.3	−21:20:07	1525.2	21.2	−20.4
NGC 1553	04:16:10.5	−55:46:49	1080.6	15.0	−20.6
NGC 2329	07:09:08.0	+48:36:56	5799	80.5	−21.4
NGC 3115	10:05:14.0	−07:43:07	663.6	9.2	−20.1
NGC 4382	12:25:24.0	+18:11:28	729.6	10.1	−20.0
NGC 4406	12:26:11.7	+12:56:46	244.2	3.4	−21.4
NGC 5102	13:21:58.0	−36:37:49	468.3	6.5	−19.1
NGC 5353	13:53:26.7	+40:16:59	2326.5	32.3	−20.6
NGC 5866	15:06:29.5	+55:45:47	672.6	9.3	−19.0
NGC 6407	17:44:57.7	−60:44:23	4628.1	64.3	−21.6

Note. — Col. (1): Galaxy name. Col. (2): Right ascension as listed in NED. Col. (3): Declination as listed in NED. Col. (4): Radial velocity as listed in NED. Col. (5): Distance in Mpc, calculated using Col. 4 and 72 km s^{-1} Mpc^{-1} (6) Absolute B-band magnitude as listed in LEDA.

Table 2.6. X-Ray Properties of the Hickson Compact Group Sample

Group	log L_x	kT	R_{ex}	Observer	comments
(1)	(2)	(3)	(4)	(5)	(6)
16	40.9	0.66	0.29	Mamon	a
30	41.3	0.99	0.99	Ponman	a
37	41.3	1.08	0.42	Ponman	a
40	41.5	0.97	0.37	Ponman	a
42	41.5	0.76	0.54	Ponman	a
51	42.6	6.06	3.07	Vrtilek	a, b
62	41.8	0.79	0.73	Vrtilek	b, c
80	41.8	0.62	1.75	Ota	a,
90	40.6	0.65	0.63	Bothun	a, b
92	41.7	0.74	1.32	Trinchieri	b, d
97	41.9	0.83	1.30	Vrtilek	a, b

Note. — Col. (1): HCG group number. Col. (2): Model derived luminosity in the 0.3 - 2.5 energy band, in ergs s^{-1}. Col. (3): Log of model derived gas temperature in keV. Col. (4): Effective X-ray radius defined as radius where the X-ray source counts fell to 2σ above the background, in Mpc. Col. (5): PI of Chandra observation. Col (6): a – emission confined to indiv. galaxies. b – emission in intragroup region. c – depressions in diffuse emission. d – emission peak in intragroup region.

Table 2.7. X-Ray Properties of the Fossil Group Sample

Galaxy	log L_x	kT	R_{ex}	Observer	comments
(1)	(2)	(3)	(4)	(5)	(6)
NGC 777	41.98	0.64	1.29	Murray	a
NGC 1550	42.2	0.96	1.09	Murray	a
NGC 4936	41.0	0.82	0.79	Murray	a
NGC 5419	41.9	3.16	0.59	Murray	c
ESO 3060170	43.1	2.49	12.83	Murray	a
ESO 5520200	42.7	2.97	5.18	Forman	b
RXJ1256.0+2556	43.5	2.36	11.16	Jones	a
RXJ1331.5+1108	42.2	0.89	2.92	Jones	a
RXJ1340.6+4018	43.0	0.99	10.90	Jones	a
RXJ1552.2+2013	43.4	3.22	6.64	Jones	a

Note. — Col. (1): Galaxy name. Col. (2): Log of model derived luminosity in the 0.3 - 2.5 energy band, in ergs s^{-1}. Col. (3): Model derived gas temperature in keV. Col. (4): Effective X-ray radius defined as radius where the X-ray source counts fell to 2σ above the background, in Mpc. Col. (5): PI of Chandra observation. Col (6): a – symmetric, undisturbed diffuse emission. b – diffuse emission undisturbed yet lacks symmetry. c – hot gas is entirely bound within the optical extent of the galaxy.

Table 2.8. X-ray Properties of the Isolated Elliptical Galaxy Sample

Galaxy	log L_x	kT	R_{ex}	Observer	comments
(1)	(2)	(3)	(4)	(5)	(6)
NGC 766	41.4	0.67	0.78	Garmire	a
NGC 1132	41.9	0.81	1.01	Zabludoff	b
NGC 3065	40.3	1.0	0.16	Murray	c
NGC 3078	40.9	2.02	0.16	Murray	a
NGC 3209	40.9	0.67	0.41	Garmire	b
NGC 4555	41.5	0.77	0.64	Ponman	a
NGC 5546	41.9	0.57	0.83	Murray	a
NGC 6487	41.7	0.76	0.59	Murray	a
NGC 7618	41.9	0.94	1.81	Zabludoff	d

Note. — Col. (1): Galaxy name. Col. (2): Log of model derived luminosity in the 0.3 - 2.5 energy band, in ergs s^{-1}. Col. (3): Model derived gas temperature in keV. Col. (4): Effective X-ray radius defined as radius where the X-ray source counts fell to 2σ above the background, in Mpc. Col. (5): PI of Chandra observation. Col (6): a – diffuse emission is symmetric and undisturbed. b – diffuse emission appears undisturbed yet lacks symmetry. c – hot gas is entirely bound within the optical extent of the galaxy. d – diffuse emission is disturbed and lacks symmetry.

Table 2.9. X-ray Properties of the S0 Sample

Galaxy (1)	log L_X (2)	# pt. sources (3)	Model fit (4)	total pt. source log L_X (5)
NGC 1023	39.2	25	Apec	39.5
NGC 1332	40.3	72	Meka+Raymond	40.5
NGC 1553	40.1	56	Bkn pwr law	40.3
NGC 2329	41.9	1	Disk BB+Bremsstrahlung	41.8
NGC 3115	39.9	87	Bkn pwr law	39.9
NGC 4382	39.8	78	Meka	39.9
NGC 4406	39.2	24	Meka+bkn pwr law	38.7
NGC 5102	38.2	31	Meka+bkn pwr law	38.9
NGC 5353	40.6	3	Meka+bkn pwr law	40.3
NGC 5866	39.4	56	Meka+bkn pwr law	39.6
NGC 6407	42.1	5	Meka+bkn pwr law	41.5

Note. — Col. (1): Galaxy name. Col. (2): Log of model derived gas X-ray luminosity, using $H_0 = 72$ km s^{-1} Mpc^{-1}. Col. (3): Number of detected point sources. Col. (4): Model used to fit the total point source spectrum. Col. (5): Log of total point source X-ray luminosity, in ergs s^{-1}.

Table 2.10. Point Sources Population in NGC 1023

Number	Source	H21	H31	Flux	log L_X
(1)	(2)	(3)	(4)	(5)	(6)
1	CXOU J024023.9+390347	−0.51	−0.53	8.38	38.9
2	CXOU J024028.7+390350	−0.65	−0.41	2.94	38.4
3	CXOU J024027.9+390412	−0.4	−1.0	1.35	38.1
4	CXOU J024025.1+390403	0.2	−1.0	0.562	37.7
5	CXOU J024024.3+390427	−0.52	−0.39	4.94	38.7
6	CXOU J024017.8+390151	−0.68	−0.83	4.61	38.6
7	CXOU J024013.0+390052	−0.98	−1.0	7.67	38.9
8	CXOU J024036.4+390417	−0.53	−0.63	2.25	38.3
9	CXOU J024034.8+390645	−0.43	−0.5	2.92	38.4
10	CXOU J024032.9+390441	−0.33	0.0	0.562	37.7
11	CXOU J024032.4+385917	−0.42	−0.33	4.72	38.6
12	CXOU J024026.0+390350	−0.14	−0.14	1.12	38.0
13	CXOU J024023.6+390343	−0.39	−0.8	1.57	38.2
14	CXOU J024022.9+390326	0.25	−0.2	1.12	38.0
15	CXOU J024022.6+390238	−1.0	−1.0	0.674	37.8
16	CXOU J024022.5+390151	−1.0	0.0	0.449	37.6
17	CXOU J024021.1+390630	−0.33	−0.31	3.37	38.5

Table 2.10 (continued)

Number	Source	H21	H31	Flux	log L_X
(1)	(2)	(3)	(4)	(5)	(6)
18	CXOU J024021.1+390531	−0.65	−0.58	3.14	38.5
19	CXOU J024019.7+390425	0.0	−0.71	1.46	38.1
20	CXOU J024013.6+390133	−0.64	−0.39	1.68	38.2
21	CXOU J024010.5+390226	−0.67	−1.0	1.07	38.0
22	CXOU J024030.5+390440	−1.0	0.0	0.535	37.7
23	CXOU J024014.9+385920	1.0	1.0	1.16	38.0
24	CXOU J024013.7+390404	1.0	1.0	0.446	37.6
25	CXOU J024005.1+390508	−0.67	−1.0	0.535	37.7

Note. — Col. (1): Source number. Col. (2): Point source name, using Chandra naming convention. Col. (3): Derived medium-to-soft hardness ratio. Col. (4): Derived hard-to-soft hardness ratio. Col. (5): Flux determined using a model fit to the point source X-ray spectrum, in 10^{-14} ergs s^{-1} cm^{-2}. Col. (6): Log of X-ray luminosity determined using Col. (5) and a Hubble constant of 72 km s^{-1} Mpc^{-1}.

Table 2.11. Point Sources Population in NGC 1332

Number	Source	H21	H31	Flux	log L_X
(1)	(2)	(3)	(4)	(5)	(6)
1	CXOU J032617.2-212007	−0.84	−0.93	18.2	39.9
2	CXOU J032636.5-211809	−0.54	−0.64	4.13	39.3
3	CXOU J032622.9-211917	−0.21	−0.18	0.387	38.3
4	CXOU J032620.6-211713	−0.06	−0.29	0.181	37.9
5	CXOU J032620.2-211958	−0.56	−0.56	0.132	37.8
6	CXOU J032619.9-212018	−0.52	−0.68	0.206	38.0
7	CXOU J032618.9-212031	−0.62	−0.66	1.09	38.8
8	CXOU J032618.8-211814	−0.46	−0.36	0.296	38.2
9	CXOU J032618.2-212014	−0.31	−0.62	0.921	38.7
10	CXOU J032616.7-211953	−0.28	−0.52	0.929	38.7
11	CXOU J032616.4-211958	−0.49	−0.63	0.469	38.4
12	CXOU J032616.3-211953	−0.61	−0.57	0.387	38.3
13	CXOU J032615.5-211941	−0.54	−0.54	0.263	38.1
14	CXOU J032615.3-211924	−0.2	0.67	0.173	37.9
15	CXOU J032615.3-212001	−0.2	−0.26	0.509	38.4
16	CXOU J032614.9-212126	−0.40	−0.43	5.20	39.4
17	CXOU J032614.7-211903	−0.56	−0.59	0.543	38.5

Table 2.11 (continued)

Number	Source	H21	H31	Flux	log L_X
(1)	(2)	(3)	(4)	(5)	(6)
18	CXOU J032613.9-211943	−0.53	−0.3	0.206	38.0
19	CXOU J032613.2-212019	−0.14	−0.26	0.239	38.1
20	CXOU J032611.9-211811	−0.33	--0.6	0.058	37.5
21	CXOU J032631.3-211530	−0.06	0.03	0.789	38.6
22	CXOU J032630.9-211823	−0.6	−0.52	0.206	38.0
23	CXOU J032628.7-211735	0.0	0.0	0.074	37.6
24	CXOU J032628.3-212120	−0.41	--0.65	0.271	38.2
25	CXOU J032625.5-211622	0.09	−0.25	0.115	37.8
26	CXOU J032625.2-212043	−0.64	−0.39	0.123	37.8
27	CXOU J032624.2-212040	−0.78	−0.46	0.107	37.7
28	CXOU J032623.4-212002	−1.0	−0.78	0.074	37.6
29	CXOU J032623.1-211945	0.0	−0.33	0.082	37.6
30	CXOU J032622.8-211621	−0.33	−0.33	0.107	37.7
31	CXOU J032622.4-212131	−0.6	−0.91	0.222	38.1
32	CXOU J032621.9-212023	−0.47	−0.56	0.206	38.0
33	CXOU J032621.8-211929	−0.78	−0.78	0.336	38.3
34	CXOU J032621.5-212030	−0.4	−0.56	0.099	37.7

Table 2.11 (continued)

Number	Source	H21	H31	Flux	log L_X
(1)	(2)	(3)	(4)	(5)	(6)
35	CXOU J032620.8-211957	−0.33	−0.2	0.107	37.7
36	CXOU J032620.8-212151	0.24	0.75	0.708	38.6
37	CXOU J032620.6-212112	−0.29	−1.0	0.139	37.9
38	CXOU J032620.6-212041	−0.54	−0.82	0.115	37.8
39	CXOU J032620.2-211455	−0.58	−0.52	0.247	38.1
40	CXOU J032620.1-212023	−0.70	−0.53	0.279	38.2
41	CXOU J032619.4-212020	−0.5	−0.64	0.230	38.1
42	CXOU J032619.3-212051	−0.62	−0.70	0.222	38.1
43	CXOU J032619.1-212008	−0.8	−0.5	0.107	37.6
44	CXOU J032618.4-212011	−0.78	−0.5	0.289	38.2
45	CXOU J032617.6-212013	−0.78	−0.78	0.575	38.5
46	CXOU J032617.6-211507	−0.37	−0.53	0.189	38.0
47	CXOU J032616.7-211927	−0.71	−0.09	0.115	37.8
48	CXOU J032616.6-211920	−0.6	−0.45	0.107	37.8
49	CXOU J032615.8-212017	−0.8	−0.64	0.099	37.7
50	CXOU J032615.8-212039	−0.89	−0.7	0.189	38.0
51	CXOU J032615.4-211949	−0.56	−0.56	0.099	37.7

Table 2.11 (continued)

Number	Source	H21	H31	Flux	log L_X
(1)	(2)	(3)	(4)	(5)	(6)
52	CXOU J032613.9-212005	−0.11	−0.11	0.123	37.8
53	CXOU J032612.9-211959	−0.33	−0.33	0.139	37.9
54	CXOU J032611.9-211959	−1.0	−0.47	0.131	37.8
55	CXOU J032610.4-211843	−0.18	−0.43	0.197	38.0
56	CXOU J032607.9-211828	−0.64	−1.0	0.090	37.7
57	CXOU J032606.9-212043	0.43	0.0	0.082	37.6
58	CXOU J032606.9-212016	−0.36	−0.46	0.584	38.5
59	CXOU J032605.7-212058	−0.46	−0.58	0.419	38.4
60	CXOU J032605.5-212050	−1.0	0.43	0.058	37.5
61	CXOU J032604.6-211859	−0.78	−0.23	0.115	37.8
62	CXOU J032603.1-211920	0.19	−0.30	0.379	38.3
63	CXOU J032601.7-211728	−0.55	−0.55	1.25	38.8
64	CXOU J032637.1-211902	−0.41	−0.5	0.173	37.9
65	CXOU J032634.7-211755	0.2	0.0	0.058	37.5
66	CXOU J032631.1-212018	−0.67	−0.67	0.058	37.5
67	CXOU J032630.2-211631	−1.0	−-1.0	0.041	37.3
68	CXOU J032628.7-211431	−0.11	0.0	0.115	37.8

Table 2.11 (continued)

Number	Source	H21	H31	Flux	log L_X
(1)	(2)	(3)	(4)	(5)	(6)
69	CXOU J032619.8-212201	−0.4	−0.08	0.156	37.9
70	CXOU J032606.7-211731	−0.6	−0.6	0.099	37.7
71	CXOU J032606.2-212008	−1.0	−0.86	0.139	37.9
72	CXOU J032606.7-211731	−1.0	−0.2	0.082	37.6

Note. — Col. (1): Source number. Col. (2): Point source name, using Chandra naming convention. Col. (3): Derived medium-to-soft hardness ratio. Col. (4): Derived hard-to-soft hardness ratio. Col. (5): Flux determined using a model fit to the point source X-ray spectrum, in 10^{-14} ergs s^{-1} cm^{-2}. Col. (6): Log of X-ray luminosity determined using Col. (5) and a Hubble constant of 72 km s^{-1} Mpc^{-1}.

Table 2.12. Point Sources Population in NGC 3115

Number	Source	H21	H31	Flux	log L_X
(1)	(2)	(3)	(4)	(5)	(6)
1	CXOU J100513.9-074307	−0.59	−0.62	5.02	38.7
2	CXOU J100527.4-074316	−0.44	−0.39	5.53	38.7
3	CXOU J100525.4-074339	−0.5	−0.54	1.19	38.1
4	CXOU J100518.5-074138	−0.47	−0.91	1.32	38.1
5	CXOU J100517.7-074318	−0.44	−0.37	1.02	38.0
6	CXOU J100516.7-074318	−0.39	−0.55	1.68	38.2
7	CXOU J100516.5-074230	−0.44	−0.44	1.37	38.1
8	CXOU J100516.3-074235	−0.56	−0.16	0.428	37.6
9	CXOU J100515.1-074252	−0.54	−0.42	0.639	37.8
10	CXOU J100514.9-074252	−0.27	−0.36	8.29	38.9
11	CXOU J100514.7-074314	−0.28	−0.28	0.746	37.9
12	CXOU J100514.5-074318	−0.35	−0.52	0.979	38.0
13	CXOU J100514.3-074304	−0.56	−0.52	0.895	37.9
14	CXOU J100514.2-074257	−0.37	−0.49	2.73	38.4
15	CXOU J100514.3-074233	−0.86	−0.86	0.319	37.5
16	CXOU J100514.2-074544	−0.44	−0.5	1.32	38.1
17	CXOU J100513.8-074301	−-0.29	−0.32	1.62	38.2

Table 2.12 (continued)

Number	Source	H21	H31	Flux	log L_X
(1)	(2)	(3)	(4)	(5)	(6)
18	CXOU J100513.8-074416	−0.57	−0.53	0.979	38.0
19	CXOU J100513.4-074337	−0.19	−0.24	2.02	38.3
20	CXOU J100513.3-074312	−0.36	−0.51	1.53	38.2
21	CXOU J100513.2-074217	−0.22	−0.65	0.554	37.8
22	CXOU J100513.1-074239	−0.58	−0.79	4.65	38.7
23	CXOU J100513.1-074305	−0.46	−0.6	0.277	37.4
24	CXOU J100513.1-074338	−0.5	−0.71	0.192	37.3
25	CXOU J100510.4-074449	−0.5	−0.06	0.447	37.7
26	CXOU J100510.3-074413	−0.48	−0.59	0.788	37.9
27	CXOU J100510.1-074530	−0.63	−0.95	1.98	38.3
28	CXOU J100509.8-074445	−0.43	−0.48	1.49	38.2
29	CXOU J100509.6-074200	−0.49	−0.51	1.88	38.3
30	CXOU J100508.9-074543	0.57	0.46	0.470	37.7
31	CXOU J100508.2-074460	−0.62	−0.62	1.32	38.1
32	CXOU J100507.9-074534	−0.30	−0.36	0.639	37.8
33	CXOU J100506.1-074428	−0.24	−0.38	6.35	38.8
34	CXOU J100504.5-074410	−0.4	−0.47	0.554	37.8

Table 2.12 (continued)

Number	Source	H21	H31	Flux	log L_X
(1)	(2)	(3)	(4)	(5)	(6)
35	CXOU J100502.3-074437	−0.27	−0.39	1.34	38.1
36	CXOU J100501.0-074326	0.64	0.79	0.597	37.8
37	CXOU J100527.3-074204	−0.49	−0.72	3.77	38.6
38	CXOU J100524.1-074338	0.33	0.85	0.319	37.5
39	CXOU J100522.2-074402	−0.54	−0.43	0.363	37.6
40	CXOU J100521.8-074339	0.6	0.71	0.234	37.4
41	CXOU J100521.5-074139	−0.2	−0.29	0.428	37.6
42	CXOU J100519.2-074301	−0.43	−0.67	0.171	37.2
43	CXOU J100518.7-074239	−0.67	−0.54	0.341	37.5
44	CXOU J100517.2-074217	−0.8	−1.0	0.234	37.4
45	CXOU J100516.8-074646	−0.27	−0.27	0.319	37.5
46	CXOU J100516.8-074256	−1.0	−0.5	0.085	36.9
47	CXOU J100516.6-074208	−1.0	−0.67	0.256	37.4
48	CXOU J100515.7-074258	−0.11	−0.11	0.298	37.5
49	CXOU J100515.4-074558	−0.33	−0.14	0.192	37.3
50	CXOU J100514.6-074258	−0.71	−0.5	0.405	37.6
51	CXOU J100514.4-074250	−0.5	−0.8	0.298	37.5

Table 2.12 (continued)

Number	Source	H21	H31	Flux	log L_X
(1)	(2)	(3)	(4)	(5)	(6)
52	CXOU J100513.9-074252	−0.75	−0.75	0.192	37.3
53	CXOU J100513.8-074246	−0.2	0.0	0.363	37.6
54	CXOU J100513.5-074330	−0.6	0.2	0.256	37.4
55	CXOU J100513.1-074249	−0.27	−0.65	0.554	37.8
56	CXOU J100512.7-074348	−0.78	−1.0	0.192	37.3
57	CXOU J100512.5-074134	−0.25	−0.25	0.256	37.4
58	CXOU J100512.4-074329	−0.27	−0.4	0.299	37.5
59	CXOU J100512.3-074153	−0.67	−0.25	0.234	37.4
60	CXOU J100511.4-074460	−0.4	−0.56	0.256	37.4
61	CXOU J100509.1-074136	−1.0	−1.0	0.171	37.2
62	CXOU J100508.8-074444	−0.65	−0.81	0.554	37.8
63	CXOU J100508.6-074401	−1.0	−0.82	0.234	37.4
64	CXOU J100506.6-074342	−0.67	−1.0	0.128	37.1
65	CXOU J100506.6-074707	−1.0	0.33	0.128	37.1
66	CXOU J100506.1-074708	0.0	−0.14	0.234	37.4
67	CXOU J100505.7-074142	−0.25	−0.54	0.405	37.6
68	CXOU J100505.2-074637	−0.6	−0.33	0.299	37.5

Table 2.12 (continued)

Number	Source	H21	H31	Flux	log L_X
(1)	(2)	(3)	(4)	(5)	(6)
69	CXOU J100504.6-074440	−0.2	−0.72	0.234	37.4
70	CXOU J100500.0-074607	−0.37	−0.3	0.554	37.8
71	CXOU J100524.1-074710	−0.26	−0.54	1.11	38.1
72	CXOU J100523.5-074027	0.0	−1.0	0.128	37.1
73	CXOU J100522.5-074733	−0.25	−0.25	0.256	37.4
74	CXOU J100520.1-074154	−0.43	−0.67	0.171	37.2
75	CXOU J100519.8-074330	0.2	−0.33	0.128	37.1
76	CXOU J100518.4-074243	−0.4	−0.56	0.277	37.4
77	CXOU J100515.5-074254	−0.67	−0.54	0.341	37.5
78	CXOU J100512.7-074553	−0.75	−0.75	0.192	37.3
79	CXOU J100511.3-074410	−0.75	−0.75	0.192	37.3
80	CXOU J100511.2-074012	0.0	−0.71	0.277	37.4
81	CXOU J100510.3-074216	0.0	0.6	0.128	37.1
82	CXOU J100508.1-074706	−1.0	−0.43	0.149	37.2
83	CXOU J100506.4-074041	−0.6	−1.0	0.127	37.1
84	CXOU J100505.8-074016	−0.5	−0.2	0.405	37.6
85	CXOU J100501.3-074145	0.0	0.33	0.085	36.9

Table 2.12 (continued)

Number	Source	H21	H31	Flux	log L_X
(1)	(2)	(3)	(4)	(5)	(6)
86	CXOU J100500.4-074208	−1.0	−0.75	0.171	37.2
87	CXOU J100459.4-074809	−0.33	−0.06	1.75	38.3

Note. — Col. (1): Source number. Col. (2): Point source name, using Chandra naming convention. Col. (3): Derived medium-to-soft hardness ratio. Col. (4): Derived hard-to-soft hardness ratio. Col. (5): Flux determined using a model fit to the point source X-ray spectrum, in 10^{-14} ergs s^{-1} cm^{-2}. Col. (6): Log of X-ray luminosity determined using Col. (5) and a Hubble constant of 72 km s^{-1} Mpc^{-1}.

Table 2.13. Point Sources Population in NGC 4382

Number	Source	H21	H31	Flux	log L_X
(1)	(2)	(3)	(4)	(5)	(6)
1	CXOU J122524.1+181127	−0.62	−0.66	2.86	38.5
2	CXOU J122527.5+181158	−0.42	−0.38	0.578	37.9
3	CXOU J122526.9+181150	−0.54	−0.73	1.28	38.2
4	CXOU J122525.5+180937	0.33	0.33	0.206	37.4
5	CXOU J122524.9+181206	−0.48	−0.44	1.57	38.3
6	CXOU J122524.8+181049	−0.69	−0.57	0.234	37.5
7	CXOUJ 122524.7+181141	−0.53	−0.49	0.592	37.9
8	CXOUJ 122524.6+181135	−0.31	−0.29	0.661	37.9
9	CXOUJ 122524.0+181122	−0.39	−0.61	0.838	38.0
10	CXOU J122523.9+181131	−0.5	−0.71	0.496	37.8
11	CXOU J122523.6+181138	−-0.59	−0.76	1.13	38.1
12	CXOU J122523.6+181126	−0.48	−0.53	0.536	37.8
13	CXOU J122523.3+180758	−0.67	−0.72	0.467	37.8
14	CXOU J122522.8+181053	−0.93	−0.93	0.414	37.7
15	CXOU J122522.1+181043	−0.15	−0.42	0.799	38.0
16	CXOU J122521.7+181026	−0.44	−0.29	0.483	37.8
17	CXOU J122521.6+180929	−0.29	−0.4	1.14	38.1

Table 2.13 (continued)

Number	Source	H21	H31	Flux	log L_X
(1)	(2)	(3)	(4)	(5)	(6)
18	CXOU J122520.7+180955	−0.86	−0.44	0.262	37.5
19	CXOU J122520.3+181302	−0.50	−0.84	1.72	38.3
20	CXOU J122518.4+181136	0.54	0.65	0.785	37.9
21	CXOU J122518.1+180841	−0.33	−0.6	0.193	37.4
22	CXOU J122517.2+181346	−0.65	−0.79	6.34	38.9
23	CXOU J122516.8+181234	−0.48	−0.84	0.454	37.7
24	CXOU J122513.0+181016	−0.57	−0.35	0.799	38.0
25	CXOU J122509.7+180930	−0.53	−0.46	2.02	38.4
26	CXOU J122536.5+181003	−0.63	−0.63	0.262	37.5
27	CXOU J122532.2+181015	−1.0	−1.0	0.110	37.1
28	CXOU J122532.2+180926	−1.0	−1.0	0.083	37.0
29	CXOU J122531.7+181052	−0.78	−0.68	0.316	37.6
30	CXOU J122530.3+181312	−0.2	−0.43	0.427	37.7
31	CXOU J122529.5+181152	−0.56	−0.56	0.165	37.3
32	CXOU J122528.8+181108	−0.5	−0.71	0.124	37.2
33	CXOU J122528.6+180809	−0.64	−0.64	0.179	37.3
34	CXOU J122528.5+180821	−0.2	0.5	0.083	37.0

Table 2.13 (continued)

Number	Source	H21	H31	Flux	log L_X
(1)	(2)	(3)	(4)	(5)	(6)
35	CXOU J122528.3+181206	0.6	0.71	0.302	37.6
36	CXOU J122528.0+181417	−0.41	−0.71	0.276	37.5
37	CXOU J122527.5+181314	−0.69	−0.69	0.234	37.4
38	CXOU J122527.3+181215	−0.6	−0.68	0.316	37.6
39	CXOU J122525.8+181221	−0.67	−0.11	0.138	37.2
40	CXOU J122525.7+181141	−0.75	−0.4	0.342	37.6
41	CXOU J122525.3+181114	−0.39	−0.73	0.289	37.6
42	CXOU J122525.1+181057	−0.5	−0.5	0.138	37.2
43	CXOU J122522.7+181037	−0.33	−0.14	0.124	37.2
44	CXOU J122522.5+181147	−0.56	−0.75	0.138	37.2
45	CXOU J122522.2+181344	−0.05	−0.25	0.342	37.6
46	CXOU J122521.6+181232	−0.64	−0.39	0.220	37.4
47	CXOU J122520.9+181141	−1.0	−1.0	0.083	37.0
48	CXOU J122520.7+181052	−0.5	−0.5	0.138	37.2
49	CXOU J122520.3+181122	−1.0	−0.25	0.151	37.3
50	CXOU J122519.8+181236	−0.5	−0.5	0.206	37.4
51	CXOU J122519.7+181125	−0.71	−0.6	0.234	37.5

Table 2.13 (continued)

Number	Source	H21	H31	Flux	log L_X
(1)	(2)	(3)	(4)	(5)	(6)
52	CXOU J122517.6+181350	−0.5	−0.42	1.03	37.1
53	CXOU J122515.4+180730	0.5	0.71	0.526	37.8
54	CXOU J122515.0+181018	−0.23	−0.23	0.248	37.5
55	CXOU J122513.8+181249	−0.8	−0.29	0.206	37.4
56	CXOU J122513.7+180819	−0.6	−0.6	0.165	37.3
57	CXOU J122513.4+180937	−0.67	−0.43	0.110	37.1
58	CXOU J122512.8+181409	−0.52	−0.73	0.894	38.0
59	CXOU J122511.2+181007	−0.5	−0.8	0.193	37.4
60	CXOU J122509.3+181016	−0.33	−0.14	0.124	37.2
61	CXOU J122509.3+181115	−1.0	0.0	0.096	37.1
62	CXOU J122508.9+180948	0.0	0.0	0.041	36.7
63	CXOU J122506.6+180825	−0.38	−0.43	1.55	38.3
64	CXOU J122506.2+181045	−0.63	−0.47	0.483	37.8
65	CXOU J122505.8+180913	−0.47	−0.36	0.923	38.1
66	CXOU J122504.8+181133	−0.13	−0.03	0.703	37.9
67	CXOU J122503.8+181124	−0.47	−0.63	0.509	37.8
68	CXOU J122535.4+181253	−0.33	−0.33	0.248	37.5

Table 2.13 (continued)

Number	Source	H21	H31	Flux	log L_X
(1)	(2)	(3)	(4)	(5)	(6)
69	CXOU J122535.4+181224	−1.0	−0.2	0.151	37.3
70	CXOU J122527.1+181141	−0.54	--0.54	0.248	37.5
71	CXOU J122521.7+180748	−0.2	−0.5	0.165	37.3
72	CXOU J122520.3+180653	−0.2	−1.0	0.069	36.9
73	CXOU J122518.2+181255	−0.4	−0.56	0.193	37.4
74	CXOU J122517.7+180914	−0.56	−0.75	0.138	37.2
75	CXOU J122509.3+181336	−0.29	−0.16	0.358	37.6
76	CXOU J122508.1+181229	−0.4	−1.0	0.138	37.2
77	CXOU J122505.9+181159	−0.27	−0.45	0.592	37.9
78	CXOU J122505.5+181120	0.0	0.5	0.069	36.9

Note. — Col. (1): Source number. Col. (2): Point source name, using Chandra naming convention. Col. (3): Derived medium-to-soft hardness ratio. Col. (4): Derived hard-to-soft hardness ratio. Col. (5): Flux determined using a model fit to the point source X-ray spectrum, in 10^{-14} ergs s^{-1} cm^{-2}. Col. (6): Log of X-ray luminosity determined using Col. (5) and a Hubble constant of 72 km s^{-1} Mpc^{-1}.

Table 2.14. Point Sources Population in NGC 4406

Number	Source	H21	H31	Flux	log L_X
(1)	(2)	(3)	(4)	(5)	(6)
1	CXOU J122611.8+125649	−0.47	−0.71	4.35	37.8
2	CXOU J122607.8+125703	−0.4	−0.75	0.435	36.8
3	CXOU J122603.6+125658	−0.33	−0.65	0.949	37.2
4	CXOU J122619.6+125757	−0.91	−0.83	1.98	37.5
5	CXOU J122614.1+125706	−0.44	−0.8	1.07	37.2
6	CXOU J122613.9+125700	−0.33	−0.6	1.11	37.2
7	CXOU J122613.3+125652	−0.71	−0.63	0.988	39.2
8	CXOU J122612.6+125646	−0.66	−0.81	1.03	37.2
9	CXOU J122612.4+125640	−0.75	−0.92	1.16	37.2
10	CXOU J122611.7+125702	−0.58	−0.43	0.988	37.2
11	CXOU J122611.5+125646	−1.0	−0.93	1.31	37.3
12	CXOU J122611.1+125648	−0.64	−0.89	3.72	37.7
13	CXOU J122609.9+125643	−0.46	−0.79	0.949	37.2
14	CXOU J122609.5+125705	−0.24	−0.39	1.46	39.3
15	CXOU J122609.4+125558	−0.15	0.4	2.41	37.6
16	CXOU J122608.9+125735	−0.54	−1.0	0.514	36.9
17	CXOU J122608.4+125831	−1.0	−0.85	0.507	36.9

Table 2.14 (continued)

Number	Source	H21	H31	Flux	log L_X
(1)	(2)	(3)	(4)	(5)	(6)
18	CXOU J122607.5+125619	−0.47	−1.0	0.751	39.1
19	CXOU J122606.2+125554	−1.0	−0.75	0.316	36.7
20	CXOU J122554.2+130223	−0.18	−0.39	2.53	37.6
21	CXOU J122551.2+125644	−0.56	−0.56	0.435	36.8
22	CXOU J122609.8+125603	−0.65	−1.0	0.672	37.0
23	CXOU J122555.0+125409	−0.14	−0.71	0.909	37.1
24	CXOU J122552.7+125601	0.5	0.6	0.316	36.7

Note. — Col. (1): Source number. Col. (2): Point source name, using Chandra naming convention. Col. (3): Derived medium-to-soft hardness ratio. Col. (4): Derived hard-to-soft hardness ratio. Col. (5): Flux determined using a model fit to the point source X-ray spectrum, in 10^{-14} ergs s^{-1} cm^{-2}. Col. (6): Log of X-ray luminosity determined using Col. (5) and a Hubble constant of 72 km s^{-1} Mpc^{-1}.

Table 2.15. Point Sources Population in NGC 5353

Number	Source	H21	H31	Flux	log L_X
(1)	(2)	(3)	(4)	(5)	(6)
1	CXOU J135326.7+401659	−1.0	−0.91	3.29	39.6
2	CXOU J135338.9+401613	−0.33	0.0	0.784	39.0
3	CXOU J135316.9+401356	−0.33	0.56	1.57	39.3

Note. — Col. (1): Source number. Col. (2): Point source name, using Chandra naming convention. Col. (3): Derived medium-to-soft hardness ratio. Col. (4): Derived hard-to-soft hardness ratio. Col. (5): Flux determined using a model fit to the point source X-ray spectrum, in 10^{-14} ergs s^{-1} cm^{-2}. Col. (6): Log of X-ray luminosity determined using Col. (5) and a Hubble constant of 72 km s^{-1} Mpc^{-1}.

Table 2.16. Point Sources Population in NGC 5866

Number	Source	H21	H31	Flux	log L_X
(1)	(2)	(3)	(4)	(5)	(6)
1	CXOU J150629.7+554547	−0.76	−0.53	2.93	38.5
2	CXOU J150652.5+554639	0.6	0.0	0.08	36.9
3	CXOU J150644.0+554523	0.17	−0.43	0.207	37.3
4	CXOU J150640.5+554806	−0.6	−0.95	0.703	37.9
5	CXOU J150640.2+554514	−0.71	−1.0	0.09	37.0
6	CXOU J150638.8+554505	−0.62	−0.91	0.372	37.6
7	CXOU J150638.1+554842	−0.63	−0.45	0.895	37.9
8	CXOU J150635.8+554531	0.09	−0.67	0.179	37.3
9	CXOU J150632.7+554526	−0.47	−0.57	0.248	37.4
10	CXOU J150632.7+55469	−0.32	−0.71	0.674	37.8
11	CXOU J150631.2+554458	−0.76	−-0.8	0.619	37.8
12	CXOU J150630.4+554515	−0.69	−0.29	0.363	37.6
13	CXOU J150629.7+554309	−0.81	−0.81	1.49	38.2
14	CXOU J150628.8+554539	−0.5	−0.58	0.660	37.8
15	CXOU J150627.7+554538	−0.48	−0.89	0.331	37.5
16	CXOU J150625.1+554556	−0.67	−0.91	0.372	37.6
17	CXOU J150622.9+554543	−1.0	−0.89	0.275	37.5

Table 2.16 (continued)

Number	Source	H21	H31	Flux	log L_X
(1)	(2)	(3)	(4)	(5)	(6)
18	CXOU J150620.4+554543	−0.58	−0.79	2.76	38.5
19	CXOU J150620.4+554622	−0.39	−0.46	0.399	37.6
20	CXOU J150616.8+554715	−0.51	−0.79	1.19	38.1
21	CXOU J150613.3+554359	−0.63	−0.56	0.827	37.9
22	CXOU J150704+554251	−0.33	−1.0	0.08	36.9
23	CXOU J150656.7+554551	0.24	0.08	0.579	37.8
24	CXOU J150655.6+554438	0.43	0.6	0.207	37.3
25	CXOU J150653.8+554433	−0.2	−0.64	0.234	37.4
26	CXOU J150653.2+554800	0.11	0.2	0.207	37.3
27	CXOU J150640.2+554612	−0.14	−0.33	0.124	37.1
28	CXOU J150636.1+554530	−0.14	0.11	0.165	37.2
29	CXOU J150635.7+554446	−0.14	−0.6	0.110	37.1
30	CXOU J150634.0+554537	−0.56	−0.65	0.289	37.5
31	CXOU J150632.6+554605	0.0	−0.5	0.110	37.1
32	CXOU J150632.2+554220	0.39	0.58	0.385	37.6
33	CXOU J150631.8+554233	−0.56	−0.65	0.304	37.5
34	CXOU J150631.6+554251	−0.57	−0.57	0.234	37.4

Table 2.16 (continued)

Number	Source	H21	H31	Flux	log L_X
(1)	(2)	(3)	(4)	(5)	(6)
35	CXOU J150631.1+554740	0.0	0.33	0.05	36.8
36	CXOU J150630.9+554547	−0.43	−0.67	0.220	37.4
37	CXOU J150630.4+554139	−0.64	−0.66	2.46	38.4
38	CXOU J150630.3+554538	−0.25	0.0	0.193	37.3
39	CXOU J150630.3+554649	0.67	0.50	0.138	37.2
40	CXOU J150629.9+554534	−0.63	−0.86	0.234	37.4
41	CXOU J150629.2+554515	−0.83	−0.83	0.179	37.3
42	CXOU J150628.5+554555	−0.66	−0.42	1.28	38.1
43	CXOU J150628.2+554632	−0.67	−0.54	0.207	37.3
44	CXOU J150626.5+554601	−0.4	−0.56	0.165	37.2
45	CXOU J150624.6+554708	0.0	−0.14	0.151	37.2
46	CXOU J150622.6+554723	−0.63	−1.0	0.220	37.4
47	CXOU J150621.2+554908	−0.54	−0.63	1.18	38.1
48	CXOU J150620.4+554530	−0.33	−0.07	0.216	37.4
49	CXOU J150618.4+554548	−0.5	0.0	0.110	37.1
50	CXOU J150707.5+554528	−0.43	−1.0	0.09	37.0
51	CXOU J150704.6+554449	−1.0	−0.64	0.151	37.2

Table 2.16 (continued)

Number	Source	H21	H31	Flux	log L_X
(1)	(2)	(3)	(4)	(5)	(6)
52	CXOU J150703.7+554900	0.14	0.25	0.193	37.3
53	CXOU J150631.6+554546	−0.43	−0.43	0.138	37.2
54	CXOU J150627.6+554616	−1.0	−0.67	0.08	36.9
55	CXOU J150621.4+554343	−0.5	0.0	0.110	37.1
56	CXOU J150620.6+554221	0.6	0.5	0.138	37.2

Note. — Col. (1): Source number. Col. (2): Point source name, using Chandra naming convention. Col. (3): Derived medium-to-soft hardness ratio. Col. (4): Derived hard-to-soft hardness ratio. Col. (5): Flux determined using a model fit to the point source X-ray spectrum, in 10^{-14} ergs s^{-1} cm^{-2}. Col. (6): Log of X-ray luminosity determined using Col. (5) and a Hubble constant of 72 km s^{-1} Mpc^{-1}.

Table 2.17. Point Sources Population in NGC 6407

Number	Source	H21	H31	Flux	log L_X
(1)	(2)	(3)	(4)	(5)	(6)
1	CXOU J174457.9-604424	−0.79	−0.97	45.2	41.3
2	CXOU J174454.8-604423	−0.29	−1.0	2.96	39.4
3	CXOU J174532.7-604022	−1.0	−0.83	4.44	38.3
4	CXOU J174526.1-604227	1.0	1.0	1.48	38.7
5	CXOU J174517.1-604709	−1.0	−1.0	1.85	38.1

Note. — Col. (1): Source number. Col. (2): Point source name, using Chandra naming convention. Col. (3): Derived medium-to-soft hardness ratio. Col. (4): Derived hard-to-soft hardness ratio. Col. (5): Flux determined using a model fit to the point source X-ray spectrum, in 10^{-14} ergs s^{-1} cm^{-2}. Col. (6): Log of X-ray luminosity determined using Col. (5) and a Hubble constant of 72 km s^{-1} Mpc^{-1}.

Chapter 3

Morphogical Classification of Galaxies

3.1 Introduction

Morphological classification of galaxies continues to be a fundamental and developing subject in extragalactic astronomy. Classifying galaxies has remained a difficult and subjective endeavor. As more large surveys produce larger, more precise data sets, an accurate relationship between galaxy morphology and physical properties is needed (Abraham et al. 1996a; van den Bergh et al. 2001; Conselice 2003). Morphological types need to be more objectively defined in order to create homogenous subsamples of galaxies which can be studied to better understand the intrinsic properties of galaxy formation and evolution.

There are a multitude of parameters and criteria that can be used to differentiate between galaxy types. Prior studies have used colors, visually determined morphological T-type, concentration index, or spectra to select specific galaxy morphologies. One of the first attempts at classification was made by Hubble (1936). The Hubble classification system was based on visual inspection of images and involved subjective elements. The Hubble scheme has provided a basis for many extragalactic studies

(Dressler 1980; Binggeli et al. 1988) and continues today as the standard morphological classification. Since the Hubble Tuning Fork classification, other schemes have been developed in an attempt to define an objective and automated classification that can be applied to large samples without losing the accuracy of traditional visual classifications (Doi et al. 1993; Abraham et al. 1996b; Shimasaku et al. 2001; Strateva et al. 2001; Blanton et al. 2003b; Yamaguchi et al. 2005).

The desire to develop a classifier which requires minimal observations in common wavelength bands (BVR) is nothing new. Early classification attempts began in the late 1930s, when it was realized that the colors of galaxies reflect their dominant stellar populations and thus correlate with morphology (Hubble 1936). Later schemes looked to use spectral classification. Pioneered by Morgan & Mayall (1957), spectral classification provides an alternative to classification based on optical imagery. The principal advantage of the spectral approach is a direct physics-based understanding of stellar populations. Spectral classifications correlate well with prior morphological classifications and also provide information not accessible by observational images.

One of the simplest classifiers often used in literature is a parameter that characterizes the concentration of light toward the center of a galaxy (Morgan 1958). Work by Doi et al. (1993) used the concentration index to show that early- and late-type galaxies can be reasonably separated. Doi et al. found that combining concentration index and a measure of surface brightness can create a more complete sample with a lower amount of contamination. Abraham et al. (1996) furthered the use of

concentration index, C, and also introduced an asymmetry parameter. Abraham et al. found that asymmetry and concentration index can be used together to classify distant galaxies in Hubble observations (Abraham et al. 1996; Brinchmann et al. 1998).

Many works using the data from the standard reduction of SDSS (Stoughton et al. 2002) have found that the concentration index, defined as the ratio of the Petrosian radius enclosing 90% of galaxy's light to the radius enclosing 50% of the light, can be used to separate early- and late-type galaxies (Shimasaku et al. 2001; Strateva et al. 2001; Goto et al. 2003) since early-type galaxies tend to have light profiles more centrally concentrated than the profiles of late-type galaxies (Morgan 1958).

Strateva et al. (2001) found that based on a bright morphological sample, C = 2.63, separates early- and late-type galaxies with a completeness of 83%. Shimasaku et al. (2001) reccomend a different value for separating galaxies earlier than S0 and later than Sa. They suggest an inverse concentration index, 1/C, of 0.33 (C = 3.0) based on a bright sample of 456 galaxies optimized for low contamination. The success rate of the Petrosian ratio was found to approach $\sim$ 80%. Both Shimasaku et al. and Strateva et al. note that while the concentration index can be used to classify galaxies, difficultly remains in constructing a pure sample of early-type galaxies based only on the concentration index.

Later work by Yamaguchi et al. (2005) used a catalog of visual morphological classification provided by M. Fukugita, which was based on SDSS g-band images.

Yamaguchi et al. used the SDSS r-band to compute concentration indices. Early-type galaxies, those dominated by spheroidal structure, have been found to have easily quantifiable light profiles that vary as radius$^{1/4}$ (de Vaucouleurs 1948),

$$I(r) = I_e \exp\left[-7.67(r/r_e)^{1/4} - 1\right] \tag{3.1}$$

Yamaguchi et al. found that galaxies that follow a de Vaucouleurs' law had an inverse concentration index of 0.29. The light profile of a typical early-type galaxy is presented here, as it will be used as a check that the sample galaxies are spheroidal systems. The de Vaucouleurs profile will also be used when creating model galaxies to detect galaxy regions that are over- or under-luminous from the $R^{1/4}$ profile. Disk galaxies have light profiles that are best fit by an exponential,

$$I(r) = I_e \exp\left[-(r/r_e)\right] \tag{3.2}$$

The concentration indices for disk galaxies was found by Yamaguchi et al. to average 1/C = 0.44. The ∼80% completeness found by Shimasaku et al. (2001) for 1/C = 0.353 and for Strateva et al. (2001) for an inverse concentration index of 0.38 fall short of the 85% completeness reported by Yamaguchi et al. using a value of 1/C = 0.339.

Park & Choi (2005) also investigated the ability of the concentration index to quantify galaxy morphology. They found that for a classical de Vaucouleurs' light profile, the concentration index would be ∼ 5.5 (1/C = 0.18). Their work also indicated that the light profile of the exponential disks of spirals, would have C ∼ 2.3

(1/C = 0.44), in agreement with Yamaguchi et al. (2005). Park & Choi also state that the large scatter in values of concentration index for a single morphological type make C a very crude classifier, ie. (E,S0,Sa) and (Sb,Sc,Irr).

Strateva et al. (2001) also performed analysis of morphological separation using optical colors of 147,920 galaxies brighter than $g^* = 21$ observed in the SDSS bands. The authors found the sample was strongly bimodal in g−r versus u−g plane. The two peaks are found to roughly correspond to early- (E, S0, and Sa) and late-type galaxies (Sb, Sc, Irr), which suggests that colors can be used as a coarse morphological separator.

Work by Zaritsky, Zabludoff, & Willick (1995) used spectral classification methods and found that their classification scheme was able to classify to within one morphological type, determined by a visual inspection. One of the issues present in recent spectral classifications is due to the use of fixed aperture spectrograph. Kochaneck, Pahre, & Falco (2000) found that spectroscopic classification based on fixed small apertures will systematically misclassify large angular diameter, late-type galaxies as early-types since their spectra mainly sample the bulge. Such an issue is of concern, as large surveys such as the SDSS, use a fixed aperture fiber-fed spectrograph that allows for multiple spectra to be efficiently taken during one observation.

Yip et al. (2004) describe the definition of the SDSS spectral classification parameter, eClass, as using the Karhunen-Loeve principal component analysis (Karhunen 1947; Loeve 1948). Individual galaxy spectra are compared to a set of eigenspectra

in order to determine the underlying stellar population. The first application of this method to analyze galaxy spectra was due to Connolly, Szalay, Bershady, Kinney, & Calzetti (1995), which expands on a formalism developed for dealing with two-dimensional images. The eClass parameter has been shown to be an effective means of determining morphology while also providing information regarding the galaxy's stellar populations.

One issue that has remained is that the majority of classification systems use only single band measurements. Such a procedure overlooks the integrated properties of the galaxy. The morphology of a galaxy may appear vastly different at optical and infrared wavelengths. Eskridge et al. (2002) determined that on average, galaxies with B band classifications of Sa through Scd appear about one T-type (de Vaucouleurs et al. 1976) earlier in the H band, albeit with large scatter.

The chapter presents the results of an investigation of the morphological classification parameters produced in the reduction pipeline of the Sloan Digital Sky Survey. The classification parameters were studied as part of a larger project of detecting and analyzing features of a sample of extremely isolated elliptical and S0 galaxies. The chapter is organized as follows, Section 2 describes the development of training samples of E, S0 and spiral galaxies selected based on previous robust determinations of galaxy morphology. The classification parameters of the SDSS that were studied are detailed in Section 3. The procedures we employed for detecting and removing spiral

contamination in a sample of early-type galaxies is explained in Section 4. Discussion and conclusions of the current study are presented in Sections 5 and 6, respectively.

3.2 Sample Selection

Samples of galaxies that had robust morphological classifications previously performed were necessary to determine which parameters calculated by the SDSS were the most accurate. To weigh each SDSS parameter, samples of bona-fide elliptical, S0, and spiral galaxies were created using the Third Reference Catalog of Bright Galaxies (RC3) (de Vaucouleurs et al. 1992).

The SDSS has been performing a photometric and spectroscopic survey covering approximately one-quarter of the northern Galactic cap. Observing simultaneously in five filters, *ugriz*, the SDSS has as of Data Release 5 observed 215 million unique objects. The spectroscopic survey, covering a wavelength range of 3800 – 9200 Å, has recorded spectra for ∼675,000 galaxies with Petrosian r-band magnitudes less than 17.77.

All galaxies with T-type less than −4.0 listed in the RC3 were listed as ellipticals. Similarly, S0s (spirals) were designated as having $-0.5 \geq$ T-type ≤ 0.0 ($3.5 \geq$ T-type ≤ 5.0). The samples were then cross-correlated by right ascension and declination with galaxies in the SDSS spectroscopic survey Data Release 1–5 (Abazajian et al. 2003; Abazajian et al. 2004; Abazajian et al. 2005; Adelman-McCarthy et al. 2006; Adelman-McCarthy et al. 2008). All RC3 galaxies within 0.1 arcmin of an SDSS

galaxy were selected. The selection procedure yielded 41 elliptical, 32 S0, and 44 spiral galaxies. Tables 3.1, 3.2, and 3.3 list the relevant parameters investigated.

3.3 SDSS Classification Parameters

All of the parameters described below were analyzed in the SDSS r-band. One of the parameters designed for galaxy classification by the SDSS, was eClass, a spectral weighting scheme. While the eClass parameter was touted to be an excellent galaxy discriminator, few analyses have employed it. A Principal Component Analysis is used to cross-correlate the galaxy spectra with eigentemplates constructed from SDSS spectroscopic data from approximately 200,000 galaxies (Yip et al. 2004). Observed spectra are projected onto the eigenspectra to obtain the eigencoefficients. In the projections, the wavelength bins in each spectrum are weighted by the error associated with that particular wavelength bin, σ_λ, such that the weights are given by $w_\lambda = 1/\sigma_\lambda^2$. A single-parameter classifier, eClass, uses the first two expansion eigencoefficients,

$$\text{eClass} = \text{atan}\left(-eCoeff_2/eCoeff_1\right) \tag{3.3}$$

and ranges from -0.35 to 0.5, corresponding to early- to late-type galaxies. The PCA technique has often been used in classification and dimensional reduction of massive data sets.

As the work presented here is part of a larger study of early-type galaxies, our test looked at how well eClass could separate E+S0 galaxies from spirals. Multiple

values of eClass and the number of E+S0s that were lost and the amount of spiral contamination to the sample can be seen in Figure 3.1. The solid black circle display the spiral galaxies contaminating the early-type training sample. Open triangles and open circles represent elliptical galaxies and lenticular galaxies, respectively.

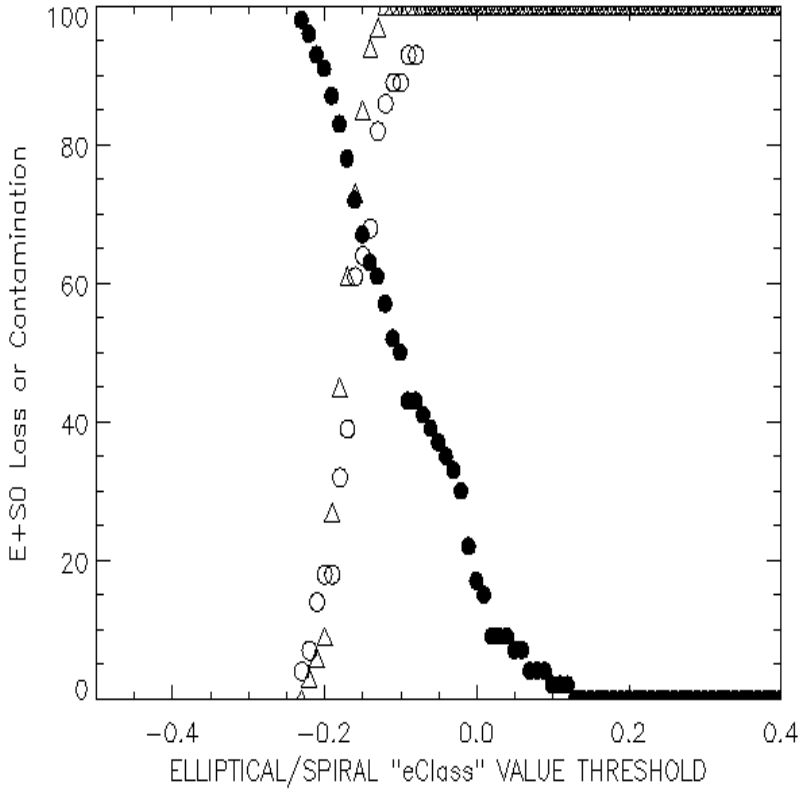

Figure 3.1: Evaluation of the SDSS eClass parameter. The plot displays the E (open circle) and S0 (open triangle) loss and spiral (solid circle) contamination.

As can be seen in Figure 3.1, no value of eClass sufficiently separates early-types from late-type galaxies. For example, when the spiral contamination is low at eClass

= 0.0, the loss of early-type galaxies approaches 100%. There is no useful value that yields even a modest sample of E+S0 galaxies with low spiral contamination.

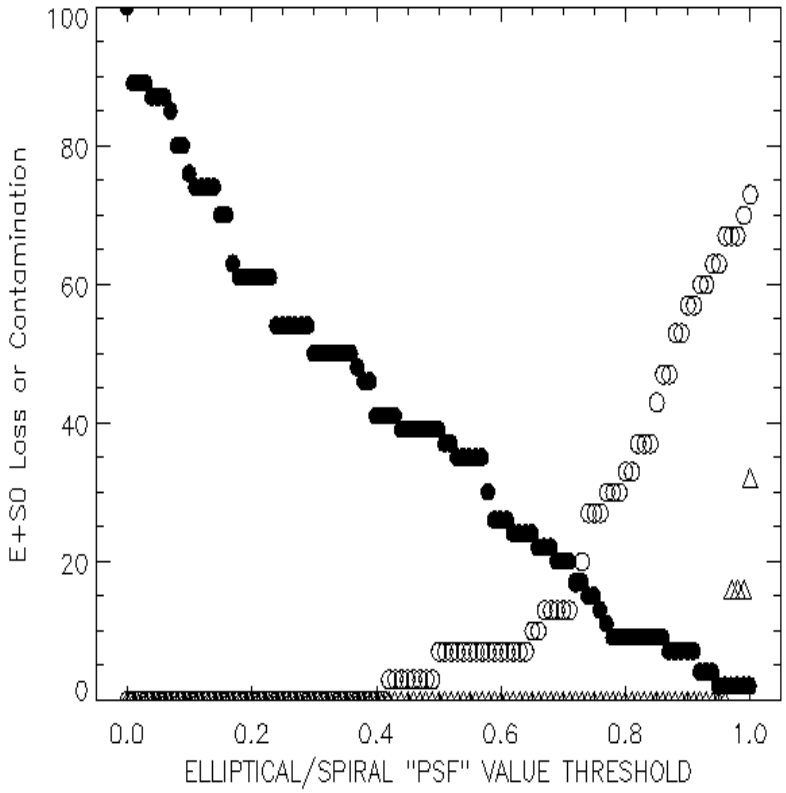

Figure 3.2: Analysis of the classification parameter quantifying the amount of galaxy light fit by an exponential profile. The symbols are the same as Fig. 3.1.

The SDSS outputs two parameters, fracpsf and fracdev, that describe how well a galaxy's light can be fit to a de Vaucouleurs or an exponential profile. A galaxy that is fit entirely by an exponential profile will have a fracpsf value of 1.0. An early-type galaxy should, in theory, display a de Vaucouleurs profile and therefore should have a low value of fracpsf. The next parameter investigated was fracpsf. Figure 3.2

displays the analysis of the fracpsf classifier. The symbols are the same as for Figure 1. The plot shows that the fracpsf and fracdev values are not absolutely correlated to morphology for the training samples studied.

The evaluation of the fracpsf values yields better results than the eClass parameter. For a fracpsf value of 0.4, there is zero percent loss in elliptical and lenticular galaxies. However, at that same value the amount of spiral contamination is very high, reaching 40%. As the research presented here is based on ealry-type morphologies, the fracpsf parameter would produce an unmanageable amount of spiral contaminants.

The ratio of the major and minor axes, b/a, was also considered as a classifier. Figure 3.3, which uses the same symbols as Fig. 3.1 highlights the axial ratio as a classifier. Ellipticals generally have axial ratios ranging between $0.4 \leq \mathrm{b/a} \leq 1.0$. An extensive study of early-type galaxies in the SDSS by Bernardi et al (2003) found the average axial ratio of ellipticals to be ≥ 0.6. One can see that for a value of $\mathrm{b/a} \geq 0.4$ could be used to separate ellipticals from S0s, however the contamination by spiral galaxies would be $\sim$40%.

A sample of E+S0s selected using a value of $\mathrm{b/a} \geq 0.3$, would result in contamination of $\sim$60%. Due to the large contamination, there is no axial ratio value that would yield a sufficiently large sample of early-type galaxies devoid of spiral interference. The use of the axial ratio was further complicated after reviewing the work by Vincent and Ryden (2005), which found that brighter ellipticals were rounder. The

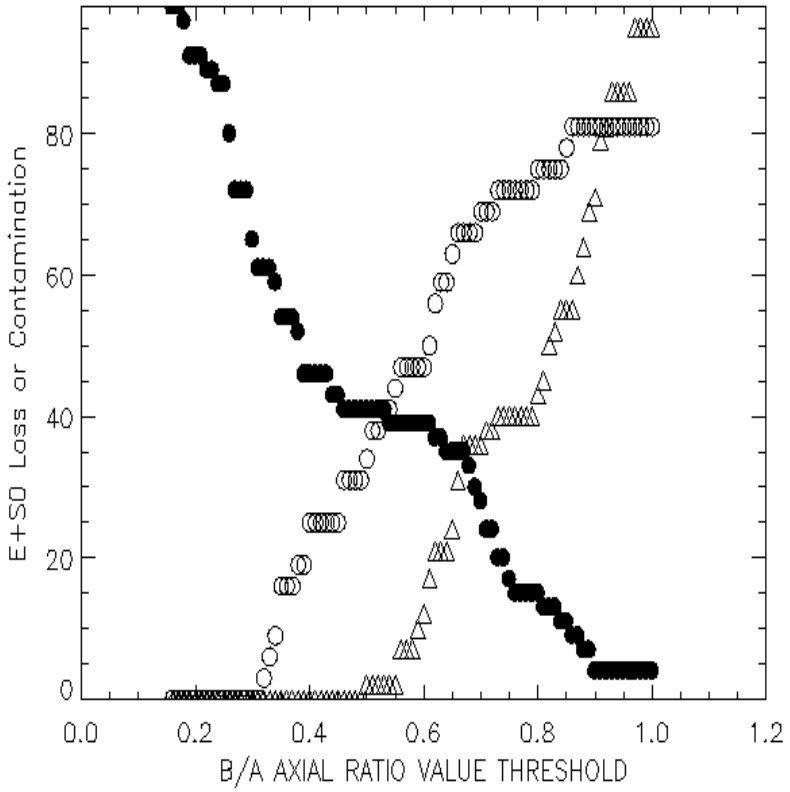

Figure 3.3: Axial b/a ratio evaluated with the training sample of E, S0, and spiral galaxies. Symbols are the same as Fig. 3.1.

use of the axial ratio would then have negated any attempts to select a sample of galaxies without constraint on the optical brightness.

The final parameter discussed is the inverse concentration index, defined via the Petrosian radius. Measuring flux for galaxies is much more difficult then for stars, as radial surface brightness profiles are not all the same and galaxies have no sharp edges. To remain consistent in measurements, the SDSS has utilized a modified version of the Petrosian system (1976) in order to avoid common biases. The Petrosian ratio,

R_P, is defined as the ratio of the local surface brightness in an annulus at r, to the mean surface brightness within an aperture of radius r (Blanton et al. 2001; Yasuda et al. 2001).

$$R_P(r) = \frac{\int_{0.8r}^{1.25r} dr' 2\pi r' I(r') / [\pi(1.25^2 - 0.8^2) r^2]}{\int_0^r dr' 2\pi r' I(r') / (\pi r^2)} \tag{3.4}$$

The size of the aperture depends on the shape of the galaxy′s radial surface brightness profile, but not the amplitude of the profile.

The radius where the Petrosian flux reaches levels of 50% and 90% of the galaxy's light are given by,

$$0.5 F_P = \int_0^{r_{50}} I(r') 2\pi r' dr' \tag{3.5}$$

$$0.9 F_P = \int_0^{r_{90}} I(r') 2\pi r' dr' \tag{3.6}$$

The inverse concentration index, P_{50}/P_{90}, is defined as the radius at which the 50% flux is reached to the radius at which the 90% flux is reached.

Figure 3.4 establishes the limits of the P_{50}/P_{90} parameter. Symbols are the same as Fig. 3.1. Contrary to the other classifiers tested, the inverse concentration index doesn't have any significant separation between elliptical and S0s. Due to the reasonably low level of E+S0 loss and the small amount of spiral contamination, the P_{50}/P_{90} parameter was chosen as the morphological classifier for our research.

As can be seen in Figure 3.4, for $P_{50}/P_{90} \leq 0.38$, there is 0% elliptical and ∼5% S0 loss with approximately 20% spiral contamination. The degree of interloping spirals closely matches values of found by Strateva et al. (2001). The value $P_{50}/P_{90} \leq 0.38$

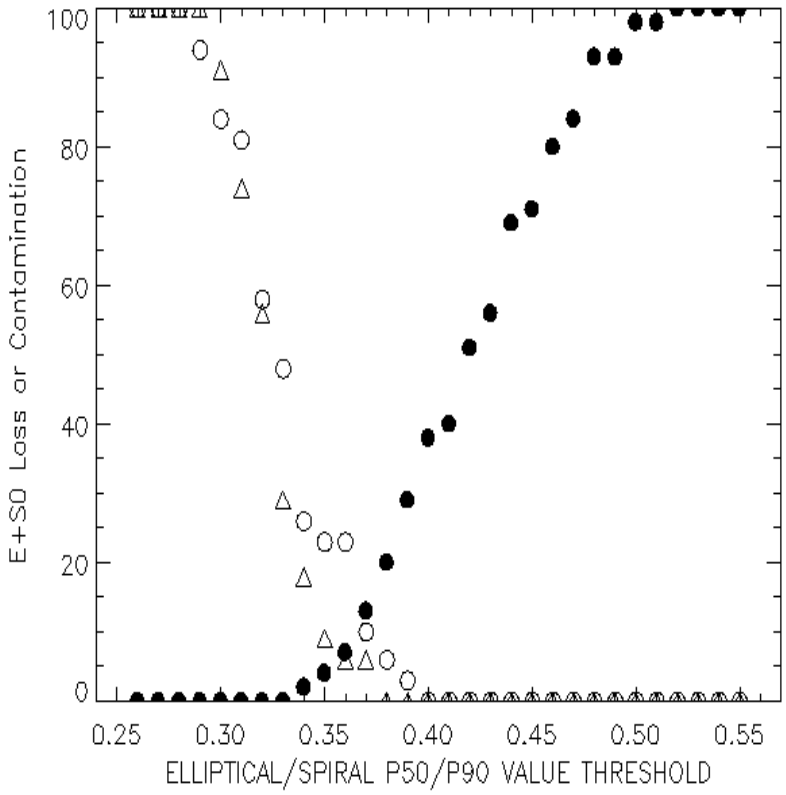

Figure 3.4: Evaluation of the inverse concentration index classification parameter, P_{50}/P_{90}. The symbols are the same as Fig. 3.1.

derived here is within the de Vaucouleurs and exponential extremes determined by Yamaguchi et al. (2005) and Park & Choi (2005). The inverse concentration index was also used by Bernardi et al. (2003) to select a sample of early-type galaxies from the SDSS. They selected E+S0s using a value of inverse concentration index less than 0.40, which is in accordance with the value chosen for the current study.

3.4 Detecting Contamination in an Early-Type Galaxy Sample

Inherent in any morphological classification which separates early- and late-type galaxies is contamination. For the purposes of the current study the primary contamination is due to Sa galaxies. S0 galaxies are often difficult to distinguish from Sa galaxies, which have tight spiral arms and can appear as featureless S0 disks. Inclination effects can also cause an Sa to look like an early-type galaxy. In order to understand the features and parameters that could be used to quickly and successfully detect Sa galaxy contamination in a sample of E+S0s, we have compiled additional training samples of S0, Sa, and S0/a galaxies chosen from NASA/IPAC Extragalactic Database (NED). Forty-four galaxies make up the S0 sample, while thirty-one Sa and eighteen S0/a galaxies are also studied. Careful analysis of these galaxies may result in a set of properties that can be used to remove any Sa galaxies from the candidate isolated early-type galaxies from our larger project.

We have chosen to study the colors and magnitudes of the SDSS and 2MASS (Cutri et al. 2003) as they can be easily found in NED. We wanted to investigate whether the combination of optical and infrared colors could yield a robust method for extracting Sa galaxies from a sample of early-type galaxies. A plot of J−H color versus SDSS g−r can be seen in Figure 3.5. The S0s, Sa, and S0/a galaxies are represented by green circles, red triangles, and blue squares, respectively. The plot

illustrates the difficulties in separating these galaxy morphologies. All galaxy types appear centered at g−r = 0.8 and J−H = 0.7. Clearly, differentiating S0s from Sa galaxies through the use of the plot is impossible.

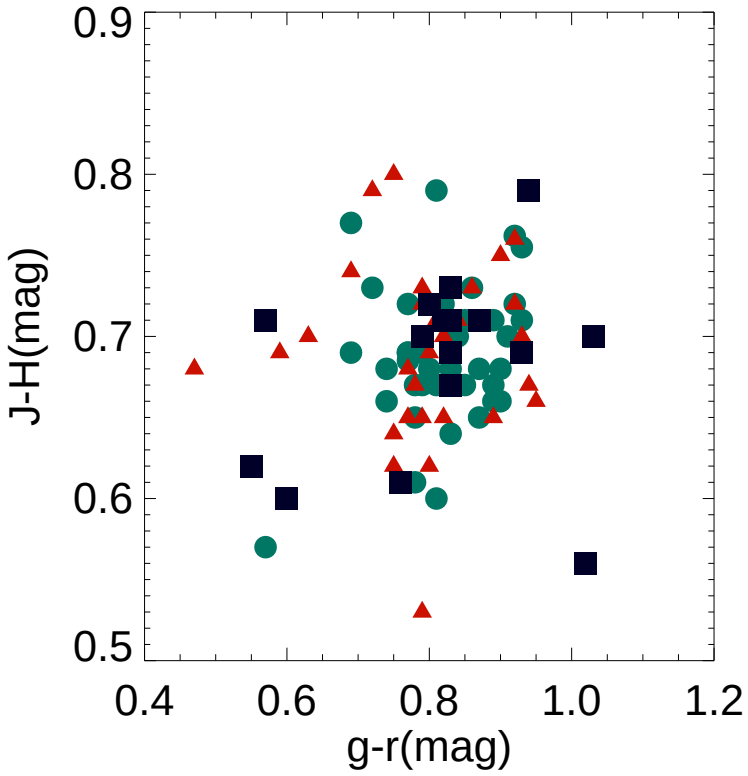

Figure 3.5: SDSS g−r color versus NIR J−H color plot. S0s are displayed as green circles, Sa galaxies as red triangles, and S0/a galaxies as blue squares. The plot has a great deal of scatter and distinguishing the morphologies is largely impossible.

Figure 3.6 displays H−K color plotted against J−H color. The symbols are the same as Figure 3.5. The amount of morphological separation in J−H is minimal, however, the H−K color clearly shows a trend. A line has been plotted at the H−K value of 0.26. An overwhelming majority of Sa galaxies, 77% also lie above the H−K

line, while more than 50% of S0 galaxies lie below. The S0/a sample is also roughly separated with half above the H−K = 0.26 line. A K-S test was performed on the S0 and Sa H−K values. The statistic value of 0.0685% was found indicating that the S0 and Sa H−K colors are not derived from the same parent population. The NIR color coupled with a quick visual inspection, provide a very powerful tool for removing spiral contamination from samples of early-type galaxies.

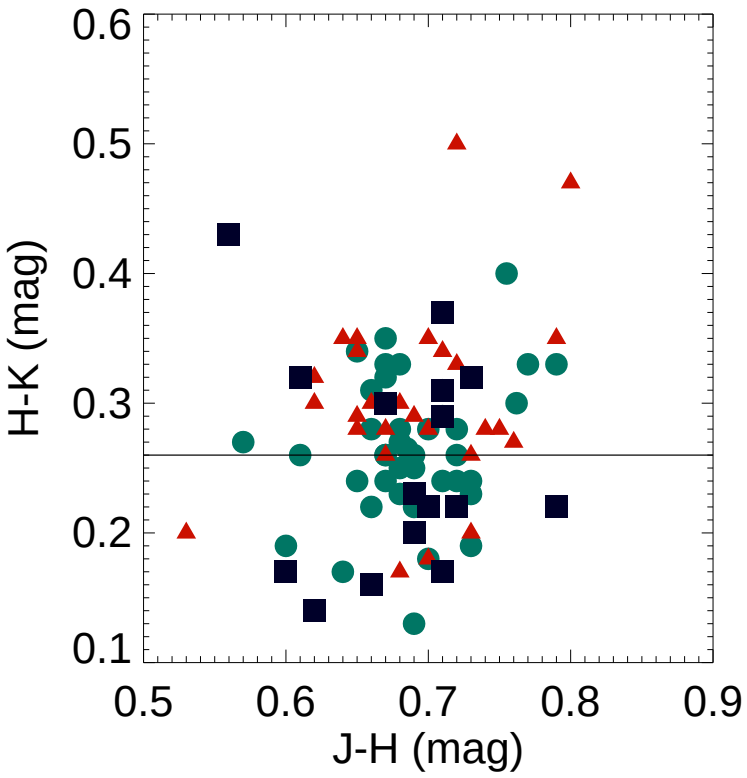

Figure 3.6: Plot of H−K vs. J−H colors. The symbols are the same as Fig. 1. A line is plotted at H−K = 0.26 to highlight the apparent separation of Sa galaxies from the majority of S0s.

3.5 Discussion

The investigation of the classification parameters available for galaxies observed with the Sloan Digital Sky Survey yields a number of interesting facts. Many of the morphological classifiers were inadequate and would be at best a very coarse means of separating galaxies. The eClass parameter was unable to create an early-type galaxy sample with a low level of contamination.

One interesting note in Figure 3.2 is that a point of E and S0s separation can be seen for the fracpsf parameter. Therefore, the possibility exists that a nearly pure sample of ellipticals could be created. Such a sample would have approximately 5% spiral contamination. As we are searching for a parameter to select early-type galaxies, a pure sample of ellipticals would not suit our needs.

With regards to the axial ratio, one issue of concern pertained to the type of objects that would be selected. It was determined that the axial ratio would primarily select objects with having a preferred orientation. The b/a parameter has no actual physical correlation to galaxy type. Many edge-on spirals with a low luminosity disks would likely be included in our sample. We did assume that some spiral contamination would be unavoidable, but feared that the axial ratio would result in an over abundance of spirals. Not wanting to unduly constrain our larger sample of isolated early-type galaxies, the axial ratio was removed from consideration as a morphology classifier.

The morphological classifier was selected as $P_{50}/P_{90} \leq 0.38$. Using that value of inverse concentration index resulted in 0% elliptical and ∼5% S0 loss and approximately 20% spiral contamination from the training samples. While the inverse concentration index appears to be a more than sufficient morphological separator for our purposes, is not in the strictest sense a robust morphological classifier. P_{50}/P_{90} can separate early- from late-type spirals, but not ellipticals from S0s. Morphological classification remains an active field in astronomy and its ultimate goal is a classification method that can separate galaxies over a less coarse morphology bin.

The ability to distinguish any spiral galaxy contamination in a sample of statistically selected early-type galaxies is paramount to developing consistent theories of galaxy formation and evolution. The plot of H−K color versus J−H color, seen in Figure 3.6, yields a trend of Sa and S0 galaxy separation at H−K = 0.26. Jarrett et al. (2003) note in their description of the 2MASS Large Galaxy Atlas, that spirals (S0, Sa, Sb) have a mean value of H−K ∼ 0.27, very close to the value found here. A K-S test was performed on the S0 and Sa H−K values. The statistic value of 0.0685% was found indicating that the S0 and Sa H−K colors are not derived from the same parent population. The NIR color coupled with a quick visual inspection, provide a very powerful tool for removing spiral contamination from samples of early-type galaxies.

3.6 Conclusions

As part of a larger study of isolated early-type galaxies selected from the Sloan Digital Sky Survey, we have presented a study of the morphological classification parameters output by the SDSS photometric pipeline. In addition to an analysis of morphological separators, we have studied possible means for quickly detecting spiral contamination in samples of early-type galaxies. The morphological investigation revealed:

- The eClass parameter is insufficient for classifying galaxies. The samples selected using eClass would likely contain spiral contamination at greater than 90%.

- The fracpsf classifier was able to select early-type samples, however the contamination was still larger than 40%. The fracpsf parameter does appear as a possibility for separating ellipticals from lenticular galaxies.

- The classification using the axial ratio yielded similar results as those found for the fracpsf parameter.

- The inverse concentration index was chosen as the morphological classifier for the larger isolated galaxy project. P_{50}/P_{90} less than 0.38 would select 100% of elliptical galaxies, $\sim$ 95% of S0s and have 20% contaminating spirals.

- A separation between Sa and S0 galaxies is observed for H−K = 0.26. The H−K color does not remove 100% of Sa galaxies, use of H−K does represent one of the first parameters that is capable of separating between two distinct morphological types.

Table 3.1. Training Sample: Elliptical Galaxies

Name	α	δ	Dist	M_B	eClass	P_{50}/P_{90}	FracPSF	B/A
(1)	(2)	(3)	(4)	(5)	(6)	(7)	(8)	(9)
NGC 163	00:35:59.8	−10:07:18	79.3	−21.2	−0.197	0.315	0.999	0.918
IC 225	02:26:28.3	+01:09:38	20.5	−16.9	0.483	0.379	0.577	0.894
IC 232	02:31:11.6	+01:15:56	84.9	−20.4	−0.178	0.321	0.00	1.00
IC 471	07:43:06.4	+49:40:03	75.9	−20.7	−0.191	0.310	0.961	0.864
UGC 4018	07:47:02.0	+41:32:10	115.3	—	−0.185	0.336	0.991	0.593
NGC 2675	08:52:04.9	+53:37:02	125.2	−21.6	−0.183	0.320	0.916	0.608
IC 2435	09:06:49.8	+26:16:31	85.1	−19.9	−0.182	0.320	0.869	0.496
UGC 4956	09:20:02.2	+01:02:18	68.3	−20.9	−0.195	0.349	0.927	0.655
NGC 2872	09:25:42.5	+11:25:56	43.2	−20.7	−0.162	0.371	1.00	1.00
NGC 2937	09:37:45.0	+02:44:50	91.1	−20.6	−0.179	0.296	1.00	0.967
NGC 3012	09:49:52.1	+34:42:51	159.1	−21.7	−0.159	0.296	1.00	0.906
PGC 28305	09:50:11.0	+28:00:47	21.9	−16.1	0.500	0.423	0.048	0.884
NGC 3158	10:13:50.5	+38:45:54	92.9	−22.3	−0.180	0.321	0.744	0.585
UGC 6071	10:59:59.5	+50:03:24	94.9	−20.9	−0.165	0.303	1.00	0.703
PGC 33572	11:06:04.8	+03:19:10	126.1	−20.5	−0.141	0.322	0.969	0.929
PGC 35400	11:29:27.3	−01:44:49	173.9	−21.3	−0.148	0.309	1.00	0.811
NGC 3731	11:34:11.7	+12:30:44	43.0	−19.2	−0.175	0.313	1.00	0.651

Table 3.1 (continued)

Name	α	δ	Dist	M_B	eClass	P_{50}/P_{90}	FracPSF	B/A
(1)	(2)	(3)	(4)	(5)	(6)	(7)	(8)	(9)
PGC 36190	11:40:06.4	−00:50:16	78.7	−19.5	−0.157	0.374	0.752	0.869
IC 725	11:43:29.3	−01:40:05	178.7	−21.8	−0.184	0.495	0.00	0.929
NGC 3847	11:44:14.0	+33:30:52	130.4	−21.5	−0.161	0.302	1.00	0.815
PGC 36944	11:49:35.4	−03:29:17	110.3	−20.4	−0.206	0.339	0.807	0.720
PGC 38052	12:02:55.6	+04:14:03	83.2	−20.1	−0.156	0.309	0.956	0.889
UGC7132	12:09:09.8	+31:34:10	93.3	−20.8	−0.163	0.306	1.00	0.964
IC 3019	12:09:22.2	+13:59:33	25.2	−18.1	0.027	0.514	0.00	0.831
NGC 4187	12:13:29.3	+50:44:29	123.1	−21.7	−0.198	0.328	0.924	0.646
PGC 39897	12:21:08.2	−03:02:41	153.3	−20.9	−0.132	0.325	1.00	0.612
NGC 4387	12:25:41.7	+12:48:38	7.34	−17.1	−0.179	0.354	0.556	0.610
NGC 4467	12:29:30.2	+07:59:34	21.6	−16.9	−0.123	0.349	0.759	0.877
NGC 4482	12:30:10.3	+10:46:46	24.6	−18.7	0.011	0.448	0.315	0.668
IC 3457	12:31:51.3	+12:39:25	17.0	−16.9	0.009	0.474	0.024	0.603
Mrk 772	12:32:33.5	+09:10:25	15.4	−15.7	0.337	0.344	0.886	0.656
Mrk 778	12:39:01.1	+00:21:56	92.6	−20.7	−0.156	0.294	1.00	0.967
IC 3652	12:40:58.5	+11:11:04	8.39	−15.8	−0.067	0.423	0.153	0.902
NGC 5173	13:28:25.3	+46:35:30	32.8	−19.7	−0.050	0.326	0.830	0.968

Table 3.1 (continued)

Name	α	δ	Dist	M_B	eClass	P_{50}/P_{90}	FracPSF	B/A
(1)	(2)	(3)	(4)	(5)	(6)	(7)	(8)	(9)
IC 989	14:14:51.3	+03:07:51	101.9	−21.5	−0.196	0.319	1.00	0.901
NGC 5546	14:18:09.2	+07:33:52	101.4	−22.1	−0.220	0.319	0.969	0.802
NGC 5831	15:04:07.0	+01:13:12	22.4	−19.8	−0.212	0.326	0.894	0.791
IC 1152	15:56:43.3	+48:05:42	78.9	−20.7	−0.178	0.304	1.00	0.872
I Zw 148	16:24:39.5	+41:01:15	109.5	−18.9	0.573	0.443	0.00	0.556
NGC 6160	16:27:41.1	+40:55:37	127.9	−21.8	−0.186	0.332	0.823	0.559
IC 1479	23:18:46.4	−10:23:57	127.7	−21.3	−0.199	0.319	1.00	0.829

Note. — Col. (1): Galaxy Name. Col. (2) & (3): Right ascension and declination as listed in NED. Col. (4): Distance, in Mpc, using Hubble's law, $H_0 = 72$ km s^{-1} Mpc^{-1} and recessional velocity in NED. Col. (5): Absolute B band magnitude as listed in LEDA. Col. (6): eClass parameter calculated by SDSS. Col. (7): Inverse Petrosian ratio calculated by SDSS using r-band radii. Col. (8): Fractional value corresponding to galaxy light profile's goodness of fit to an exponential profile. Col. (9): Axial b/a ratio calculated from SDSS r-band data.

Table 3.2. Training Sample: Lenticular Galaxies

Name	α	δ	Dist	M_B	eClass	P_{50}/P_{90}	FracPSF	B/A
(1)	(2)	(3)	(4)	(5)	(6)	(7)	(8)	(9)
NGC 217	00:41:33.9	−10:01:17	52.8	−20.9	−0.204	0.336	0.412	0.322
UGC 4008	07:46:37.7	+44:47:26	124.4	−21.8	−0.166	0.383	0.879	0.655
NGC 2522	08:06:13.4	+17:42:42	65.5	−20.4	−0.235	0.311	0.841	0.494
NGC 2524	08:08:09.6	+39:09:27	52.6	−20.5	−0.165	0.318	0.897	1.00
NGC 2562	08:20:23.6	+21:07:53	70.3	−20.7	−0.178	0.338	0.739	0.799
NGC 2638	08:42:25.8	+37:13:16	51.8	−20.5	−0.159	0.321	0.738	0.310
UGC 4731	09:01:00.1	+10:37:02	118.8	−21.4	−0.185	0.289	1.00	0.852
IC 2430	09:04:22.8	+27:57:11	42.4	−19.2	−0.0150	0.392	0.245	0.544
NGC 2789	09:14:59.6	+29:43:49	87.5	−21.1	−0.007	0.296	1.00	0.842
NGC 2858	09:22:55.0	+03:09:25	48.9	−20.1	−0.211	0.330	1.00	0.619
IC 598	10:12:48.6	+43:08:44	30.2	−19.1	−0.078	0.334	0.876	0.349
UGC 57341	10:34:15.1	+52:52:15	94.9	−21.7	−0.143	0.335	0.645	0.396
UGC 5771	10:37:19.3	+43:35:15	99.7	−20.8	−0.181	0.298	1.00	0.613
UGC 5839	10:43:29.5	+39:41:15	94.5	−20.8	−0.178	0.365	0.841	1.00
IC 653	10:52:06.8	−00:33:39	74.3	−21.0	−0.216	0.363	0.766	0.331
NGC 3524	11:06:32.1	+11:23:08	18.2	−18.6	−0.122	0.322	0.719	0.379
UGC 6570	11:35:50.0	+35:20:07	23.7	−17.8	0.244	0.333	0.812	0.453

Table 3.2 (continued)

Name	α	δ	Dist	M_B	eClass	P_{50}/P_{90}	FracPSF	B/A
(1)	(2)	(3)	(4)	(5)	(6)	(7)	(8)	(9)
UGC 6827	11:51:28.0	+35:26:04	43.9	−19.5	−0.133	0.312	0.939	0.520
UGC 7367	12:19:32.1	+49:48:57	55.0	−20.7	−0.136	0.319	0.856	0.509
NGC 4512	12:32:47.6	+63:56:21	33.8	−20.5	−0.189	0.329	0.499	1.00
NGC 4659	12:44:29.4	+13:29:55	8.75	—	−0.079	0.361	0.914	0.607
UGC 8431	13:24:20.2	+32:50:53	159.4	−21.0	−0.169	0.295	1.00	0.725
NGC 5311	13:48:56.1	+39:59:06	35.8	−19.8	−0.183	0.314140	0.984	1.00
NGC 5358	13:54:00.4	+40:16:38	32.5	−18.5	−0.139	0.315	0.728	0.395
UGC 8876	13:56:58.0	+45:58:24	27.7	−18.9	−0.163	0.285	0.955	0.454
UGC 8923	14:00:15.7	+38:30:11	75.4	−20.1	−0.168	0.367	0.669	0.349
PGC 50014	14:02:35.4	+14:32:06	56.4	−18.8	0.017	0.472	0.030	0.553
KIG 616	14:11:53.4	+38:11:39	82.2	−20.6	−0.168	0.335	1.00	1.00
NGC 5517	14:12:51.2	+35:42:39	112.1	−21.0	−0.112	0.319	1.00	1.00
UGC 9367	14:33:18.5	+34:44:04	138.4	−21.0	−0.098	0.344	0.996	0.646
UGC 10381	16:25:26.1	+39:52:14	117.1	−21.4	−0.136	0.304	1.00	0.622
NGC 7722	23:38:41.2	+15:57:17	53.7	−20.8	−0.223	0.379	0.796	0.699

Note. — Col. (1): Galaxy Name. Col. (2) & (3): Right ascension and declination as listed in NED. Col. (4): Distance, in Mpc, using Hubble's law, $H_0 = 72$ km s^{-1} Mpc^{-1} and recessional velocity in NED. Col. (5): Absolute B band magnitude as listed in LEDA. Col. (6): eClass parameter calculated by SDSS. Col. (7): Inverse Petrosian ratio calculated by SDSS using r-band radii. Col. (8): Fractional value corresponding to galaxy light profile's goodness of fit to an exponential profile. Col. (9): Axial b/a ratio calculated from SDSS r-band data.

Table 3.3. Training Sample: Spiral Galaxies

Name	α	δ	Dist	M_B	eClass	P_{50}/P_{90}	FracPSF	B/A
(1)	(2)	(3)	(4)	(5)	(6)	(7)	(8)	(9)
UGC 1934	02:27:51.4	+00:30:06	165.2	−22.0	−0.223	0.356	0.717	0.211
UGC 4132	07:59:13.0	+32:54:53	69.8	−22.1	−0.193	0.432	0.364	0.264
UGC 4301	08:16:02.2	+28:37:29	80.3	−20.9	−0.0196	0.474	0.076	0.389
UGC 4436	08:29:50.3	+48:46:52	96.5	−20.8	0.041	0.415	0.00	0.269
NGC 2619	08:37:32.7	+28:42:19	46.5	−20.8	−0.092	0.434	0.653	0.837
UGC 4521	08:40:52.6	+42:50:14	162.0	−22.0	−0.144	0.438	0.239	0.309
UGC 4529	08:41:37.8	+46:47:37	149.2	−20.5	−0.1839	0.343	0.735	0.296
UGC 4558	08:44:08.9	+33:30:57	103.1	−21.6	−0.155	0.363	0.171	0.175
UGC 4580	08:46:33.3	+48:25:48	95.9	−21.3	−0.0422	0.458	0.578	0.534
IC 2490	09:33:03.6	+29:55:42	100.9	−20.7	−0.181	0.337	0.766	0.693
NGC 2939	09:38:07.9	+09:31:26	44.8	−20.8	−0.120	0.362	0.434	0.386
UGC 5195	09:43:12.0	+00:24:51	101.4	−21.3	−0.161	0.396	0.140	0.261
UGC 595	10:21:38.2	+12:34:34	39.2	−18.1	0.016	0.454	0.141	0.754
UGC 5736	10:33:51.3	−00:33:41	126.5	−20.9	−0.179	0.478	0.770	0.678
UGC 5819	10:41:50.7	+38:43:00	145.2	—	−0.215	0.378	0.689	0.290
UGC 5872	10:46:09.5	+49:32:37	128.8	−21.5	−0.146	0.391	0.529	0.386
UGC 6129	11:04:18.0	+50:02:03	96.1	−20.1	0.127	0.457	0.234	0.857

Table 3.3 (continued)

Name	α	δ	Dist	M_B	eClass	P_{50}/P_{90}	FracPSF	B/A
(1)	(2)	(3)	(4)	(5)	(6)	(7)	(8)	(9)
IC 0677	11:13:56.7	+12:18:09	43.6	−20.4	−0.006	0.428	0.098	0.432
UGC 6411	11:24:06.5	+48:41:47	233.6	−22.8	−0.209	0.394	0.576	0.339
UGC 6529	11:32:45.4	+40:50:33	126.9	−20.7	0.012	0.445	0.399	0.708
IC 2928	11:33:29.9	+34:18:58	111.0	−20.9	−0.058	0.467	0.168	1.00
NGC 3846	11:44:29.1	+55:39:08	130.4	−22.6	−0.029	0.491	0.378	0.616
UGC 7046	12:04:00.1	+49:06:46	73.9	−19.9	0.064	0.386	0.00	0.233
IC 3229	12:22:52.8	+06:40:47	20.4	−17.5	0.096	0.413	0.00	0.309
KIG 528	12:23:58.8	+48:46:46	55.3	−21.5	−0.179	0.418	0.583	0.267
UGC 8189	13:05:46.6	+46:27:42	99.8	−21.0	−0.233	0.387	0.007	0.159
UGC 8510	13:31:17.4	+29:22:05	196.4	−21.3	−0.105	0.371	0.916	0.871
UGC 8627	13:38:13.0	+32:49:22	101.2	−20.6	−0.125	0.469	0.617	0.700
UGC 8636	13:39:10.8	+28:57:33	133.8	−20.6	−0.015	0.491	0.294	0.801
UGC 8787	13:52:50.1	+02:15:49	58.5	−20.3	−0.036	0.432	0.066	0.258
UGC 9048	14:08:52.8	+33:31:56	144.9	−21.9	−0.163	0.370	0.500	0.180
IC 996	14:17:22.1	+57:37:47	41.3	−20.0	−0.017	0.411	0.075	0.298
UGC 9313	14:29:32.5	+38:40:12	89.1	−20.2	−0.008	0.432	0.163	0.345
UGC 3909	14:29:38.5	+10:35:03	62.0	−21.4	0.007	0.389	0.586	0.372

Table 3.3 (continued)

Name	α	δ	Dist	M_B	eClass	P_{50}/P_{90}	FracPSF	B/A
(1)	(2)	(3)	(4)	(5)	(6)	(7)	(8)	(9)
NGC 5696	14:36:57.1	+41:49:41	73.3	−21.0	−0.113	0.414	0.941	1.00
UGC 9665	15:01:32.4	+48:19:11	34.2	−19.5	−0.099	0.422	0.105	0.252
UGC 9746	15:10:16.5	+01:56:03	24.4	−18.3	−0.016	0.409	0.00	0.254
UGC 10241	16:09:48.3	+42:20:02	156.2	−21.2	−0.139	0.512	0.397	0.746
UGC 10276	16:12:49.1	+31:59:35	124.7	−21.4	−0.195	0.388	0.033	0.189
UGC 10526	16:44:24.3	+25:07:30	139.0	−20.8	0.019	0.471	0.236	0.685
UGC 10545	16:46:53.0	+34:24:36	125.1	−21.5	−0.079	0.432	0.166	0.344
UGC 10706	17:06:28.5	+38:21:49	110.7	−21.3	−0.095	0.459	0.291	0.451
NGC 6390	17:28:28.1	+60:05:39	42.8	−18.9	−0.061	0.390	0.091	0.895
UGC 11859	21:58:07.4	+01:00:32	40.3	−18.9	−0.169	0.621	1.00	0.729

Note. — Col. (1): Galaxy Name. Col. (2) & (3): Right ascension and declination as listed in NED. Col. (4): Distance, in Mpc, using Hubble's law, $H_0 = 72$ km s^{-1} Mpc^{-1} and recessional velocity in NED. Col. (5): Absolute B band magnitude as listed in LEDA. Col. (6): eClass parameter calculated by SDSS. Col. (7): Inverse Petrosian ratio calculated by SDSS using r-band radii. Col. (8): Fractional value corresponding to galaxy light profile's goodness of fit to an exponential profile. Col. (9): Axial b/a ratio calculated from SDSS r-band data.

Chapter 4

Primary Sample

4.1 Introduction

The development of a comprehensive theory of galaxy formation and evolution relies on the ability to separate internal processes from interaction-induced evolution. Our objective is to construct a sample of isolated galaxies, using the Sloan Digital Sky Survey, that are sufficiently distant from neighboring galaxies and also display features of elliptical or S0 galaxies. These sets of candidate isolated galaxies will permit the investigation of galactic properties which have not been influenced by continual external interactions from neighboring galaxies.

Morphologically, early-type galaxies follow strong relations among their colors, luminosities, and other dynamical parameters (Faber & Jackson 1976; Kormendy 1977; Djorgovski & Davis 1987). The low scatter of ellipticals on the Fundamental Plane (Dressler et al. 1987; Faber et al. 1987) illustrates why studying isolated early-type galaxies (IEGs) is beneficial. Any variations in parameters that a sample of IEGs may show will be easily recognizable against normal E+S0s. As such, a sample of strictly defined isolated galaxies can serve as the zero-interaction baseline needed to develop reliable galaxy formation and evolution scenarios. Renewed interest in IEGs

has also been spurred by the discovery of fossil groups, the remnants of a collapsed compact group which are ellipticals in near isolation.

The investigation into the nature of isolated early-type galaxies is not a recent endeavor. The first reference to "isolated elliptical galaxies" came in a study by Nulsen, Stewart & Fabian (1984), who examined the X-ray emission of three galaxies in an attempt to observe predicted cooling flows. Isolated galaxies have the potential to clarify the roles of internal and environmental processes in galaxy evolution. Internal mechanisms, which are expected to be independent of environmental galaxy density, can range from supernova-driven galactic winds to the evolution of X-ray gas caused by stellar mass loss (Faber & Gallagher 1976; Gunn, Stryker & Tinsley 1981; Sanders 1981). Galaxy morphology, star formation rates and light distributions can be altered and influenced by environmental factors such as, tidal or ram-pressure stripping (Gisler 1976; Lea & De Young 1976; Takeda, Nulsen & Fabian 1984; Aguilar & White 1986; Strom & Strom 1978), galaxy interactions (Thomson & Wright 1990), and mergers with gas-rich companions (Oosterloo et al. 2002; Balcells et al 2001; Horellou et al. 2001).

The conflicting results of past analyses of isolated early-type galaxies stem from a number of probable sources. Many prior studies have not made a distinction between field and isolated galaxies. The difference in galaxy density between a field and isolated environment could easily be the root cause of conflicting data. Another possible source of large dispersion amongst previous sample properties may arise

from grouping elliptical and lenticular galaxies into a coarse morphology bin. As was stated in Chapter 1, the formation mechanisms for S0 and ellipticals may be vastly different and studying the two galaxy types as one may yield unclear results. The issue constraining the current work to grouping E+S0s was discussed in Chapter 3. There is no satisfactory morphological classifier that can separate ellipticals from S0s, which therefore necessitates the use of a broad definition of early-type galaxies.

A sample of objectively selected isolated early-type galaxies that lie in extreme isolation from large, bright companions can be used to settle a number of persisting questions. The interpretation of elliptical galaxies with isophotal twists is one such issue. Theoretical calculations by Benacchio & Galletta (1980) and Madejsky & Möllenhoff (1990) have shown that an intrinsic triaxial shape, such as an E3–7, could naturally produce isophotal twisting. Position angle twists can also occur as a result of merger with a low-luminosity companion (Balcells & Quinn 1990). R-band imaging by Fasano & Bonoli (1989) conclude that isolated ellipticals have position angle twists as frequently as galaxies with large companions.

The contradictory results of prior analyses has necessitated the creation of a set of IEGs with a strict set of isolation and morphological selection criteria. Many previous studies have relied solely on sky separation when selecting IEGs. The absence of a redshift isolation criterion effectively overlooks isolated galaxies hidden as a result of projection effects. A complete sample of truly isolated systems therefore requires the use of redshifts. Such an IEG sample could then be used to untangle the issue of which

properties are intrinsic to all early-type galaxies and those that are a function of local environment. The IEG sample presented here potentially represents a population of galaxies that have remained free of external perturbations for much of their lifetimes and represent a zero-interaction baseline needed to fully understand galaxy formation and evolution. The purpose of the current paper is to analyse SDSS *gri* coadded and BVR imaging of the sample of isolated early-type galaxy candidates.

4.2 Isolation & Selection Criteria

The SDSS, in its depth and breadth, provides a unique source for finding many isolated galaxies. The large sky coverage and extensive spectroscopic survey has yielded a massive number of objects that can be searched in redshift-space for any type of galaxy sample that is desired. In order to quickly and easily comb through the large spectroscopic sample of the SDSS, a searchable, digital database was constructed. All objects in the spectroscopic survey were input into the database. The footprint of the SDSS data on the sky can be seen in Figure 4.1. The spectroscopic data output by the SDSS is substantial and great care was taken to select the data of most importance and use to the current study. The SDSS database is a powerful tool to sample large amounts of survey data and access via IDL makes for easily designed database searches, whose parameters can be adjusted and refined. [1]

[1]The Interactive Data Language (IDL) is licensed by ittvis.com

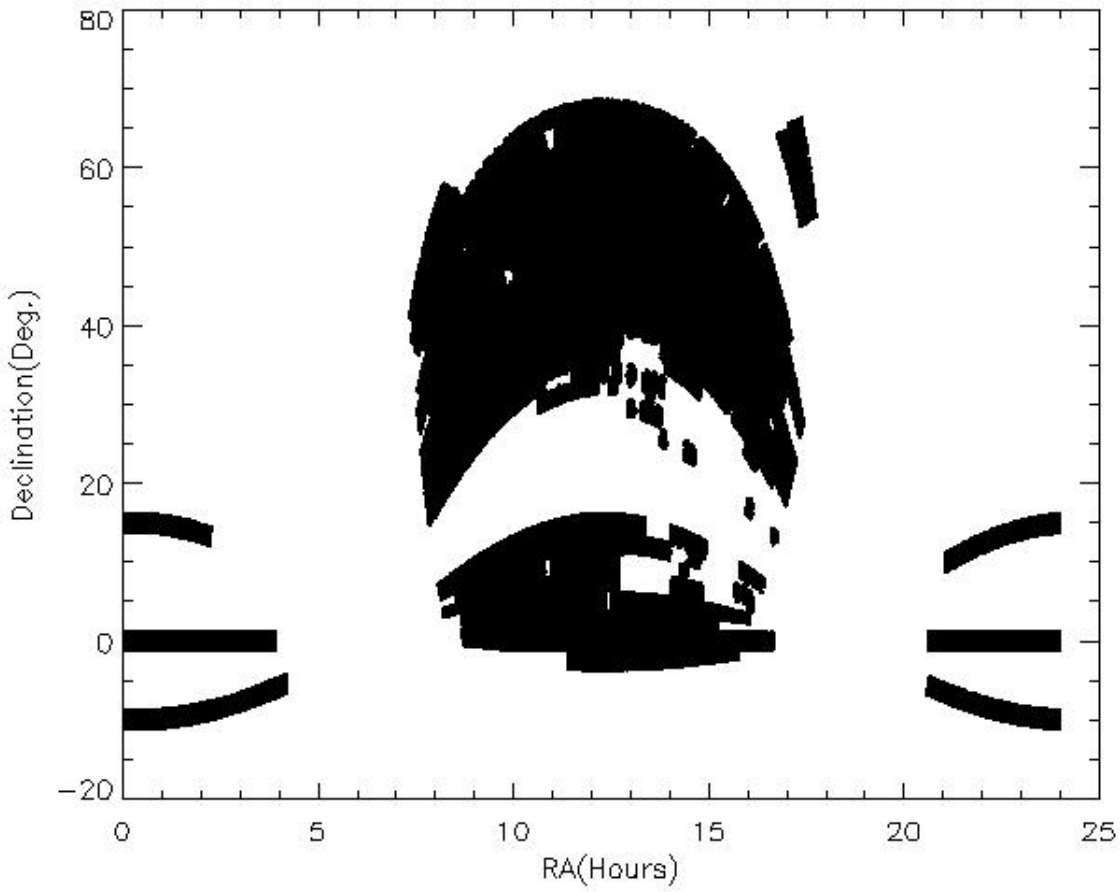

Figure 4.1: Footprint of the SDSS spectroscopic survey Data Release 5. All regions colored black represent roughly 675,000 galaxies observed by SDSS.

The main goal of the study was to define a sample of early-type galaxies in extreme low-density environments that can be used to compare the properties of near zero-interactions galaxies to properties of normal ellipticals and S0s. The use of galaxy colors, physical size and absolute magnitudes, were not considered as means to morphologically separate galaxies, because we did not want to bias the sample towards "typical" large, bright elliptical galaxies. In selecting our sample we have followed the

isolation criteria described by Marcum et al. (2004). A minimum physical separation of 2.5 Mpc to any neighbor brighter than $M_V = -16.5$ was employed. The neighbor brightness criterion does not prevent the possibility that the candidate galaxy has an associated system of dwarf galaxies. The dwarf galaxy limit is slightly fainter than the Small Magellanic Cloud. The IEGs may have satellite galaxies of the approximate luminosity of the SMC, and still meet our isolation criteria. A plot of the isolation criteria employed in the current study compared to previous isolation criteria is displayed in Figure 4.2. The y-axis spans the magnitude difference employed by many other studies. The work of Madore et al. (2004), Colbert et al. (2001), and Marcum et al. (2004) did not use as a criterion a magnitude difference between an isolated galaxy candidate and a neighbor galaxy. The minimum separation between a candidate isolated galaxy and a bright neighbor used by Marcum et al. and the work presented here are the most extreme ever employed.

The 2.5 Mpc isolation criterion is intended to limit the possibility of interactions the IEG may have had with a comparable mass galaxy over a Hubble time. Imposing a minimum recessional velocity difference of 350 km s^{-1} made a redshift-space separation, which is greater than twice the line-of-sight velocity dispersion of a typical loose group (Huchra & Geller 1982; Tucker et al. 2000). The redshift separation requires the difference in recessional velocity between a candidate galaxy and a bright neighbor must be greater than 350 km s^{-1}.

$$v_{rmax} = 350\,\mathrm{km\,s^{-1}} \times \cos(\theta) \tag{4.1}$$

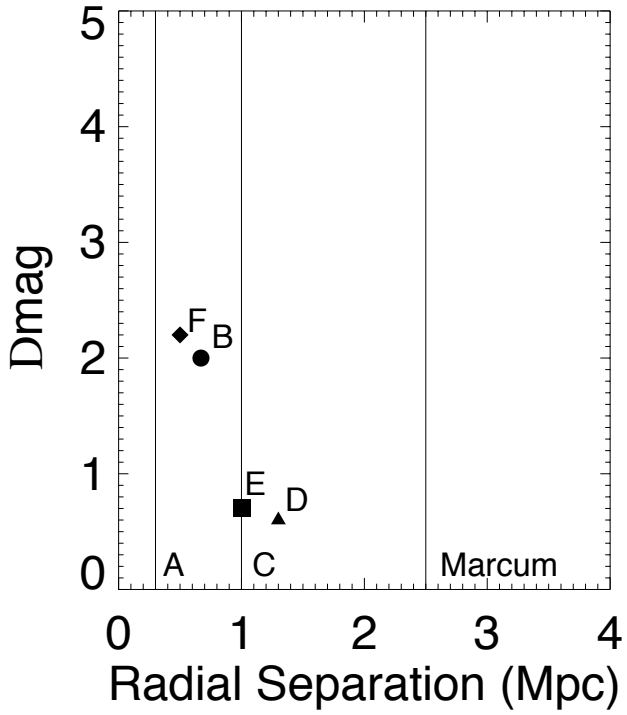

Figure 4.2: Isolation criteria of the current and previous samples. A: Madore et al. (2004); B: Reda et al. (2004) & Denicolo et al. (2005); C: Colbert et al. (2001); D: Kuntschner et al. (2002); E & F: Smith et al. (2004a,b). The criterion used here is labeled as Marcum.

Figures 4.3 and 3.4 display a visual representation of the two- and three-dimensional isolation criteria. Few, if any, loose groups have galaxies that are separated by 2.5 Mpc. The average loose group velocity dispersion was chosen as a worst-case scenario. If a neighbor were 2.5 Mpc away from a candidate and the difference in recessional velocity were 350 km s^{-1}, it is unlikely that these galaxies have interacted within a Hubble time.While the 2.5 Mpc search is a 2-dimensional check, this redshift search gives an approximate 3-dimensional detection for neighbors. In the case

of small redshift differences between the IEG candidate and possible neighbors, true 3-dimensional separation distances cannot be determined because peculiar motions, which are uncorrelated with the Hubble flow, could account for the small redshift differences. The below describes a conservative scheme, which could disqualify genuinely isolated galaxies, that deals with this uncertainty. The use of redshift to create a more complete isolation sample is a detail many previous studies have not used and makes the current study a hallmark for future works.

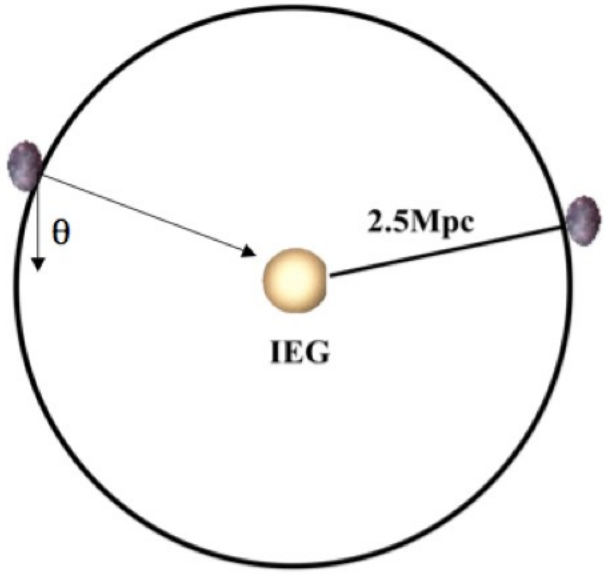

Figure 4.3: Graphical representation of the 2D isolation criteria.

One of the most important procedures performed was the separation of early-type galaxies from spiral systems. A discussion of parameters output by the SDSS pipeline that were tested to morphologically separate galaxies can be found in Chapter 3.3.

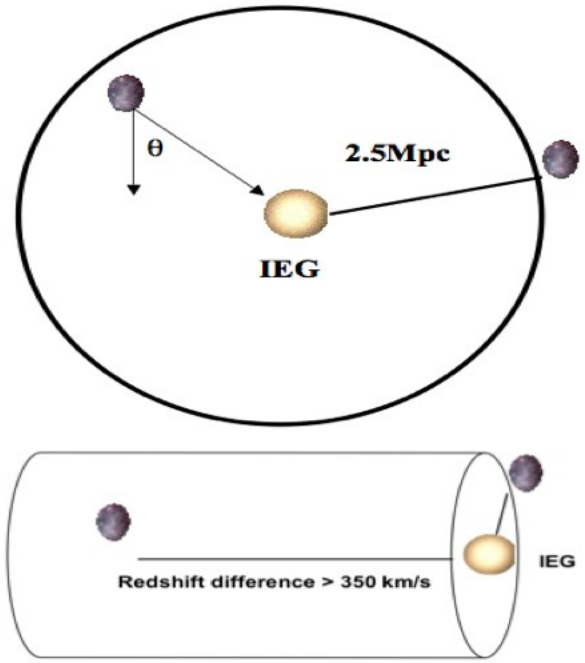

Figure 4.4: Graphical representation of the redshift-space isolation criteria.

We have chosen to use the inverse concentration index, $\frac{R_{50}}{R_{90}}$, where galaxies are deemed early-type systems if $\frac{R_{50}}{R_{90}} \leq 0.38$.

We have used all objects classified as a galaxy by the SDSS spectroscopic survey as the starting point for selecting our sample of isolated galaxies. The distance limit of 72 Mpc was chosen, as this is the distance at which low-luminosity neighbors, $M_V \leq -16.5$, would still be bright enough to be included in the SDSS spectroscopic database. Using the inverse concentration index, 304,552 galaxies in the SDSS spectroscopic database (45%) met the early-type classification. Applying the isolation criteria resulted in 66 candidate galaxies.

To ensure that the sample was comprised of early-type systems, the SDSS images were examined to remove any spiral galaxy contamination. Twenty objects were removed, as they were not early-type morphologies. One issue for which we had to correct was the dimming of neighbor galaxies due to foreground Galactic extinction. In the case where a neighbor galaxy was artificially fainter due to extinction, the candidate IEG would appear to meet all isolation criteria. After dereddening, 13 candidates were removed due to their neighbors being brighter than $M_V = -16.5$ causing the isolation criteria to be violated.

Another issue that was not expected was incomplete radial searches of SDSS data for companion galaxies. As can be seen in Figure 4.1, the SDSS survey has well defined edges. A galaxy sitting very close to the edge could erroneously be listed as a candidate IEG, even though the galaxy may be in a loose group, where the additional group members fall just off the survey edge. An example of a candidate IEG with an incomplete radial search can be seen in Figure 4.5.

In order to make a more complete radial search, NED was searched to identify any companions galaxies missed by the SDSS. A number of galaxies were removed due to poor radial searches. Of the 17 IEG candidates with poor radial searches, 3 (IEGs 71125, 261992, and 557849) were found to have neighbors brighter than the dwarf limit within 2.5 Mpc. The SDSS and supplemental NED radial search for one of the galaxies, IEG 71125, can be seen in Figure 4.6. The companions to these three IEGs are all at least 1.75 Mpc away for the candidate galaxy. While those companions

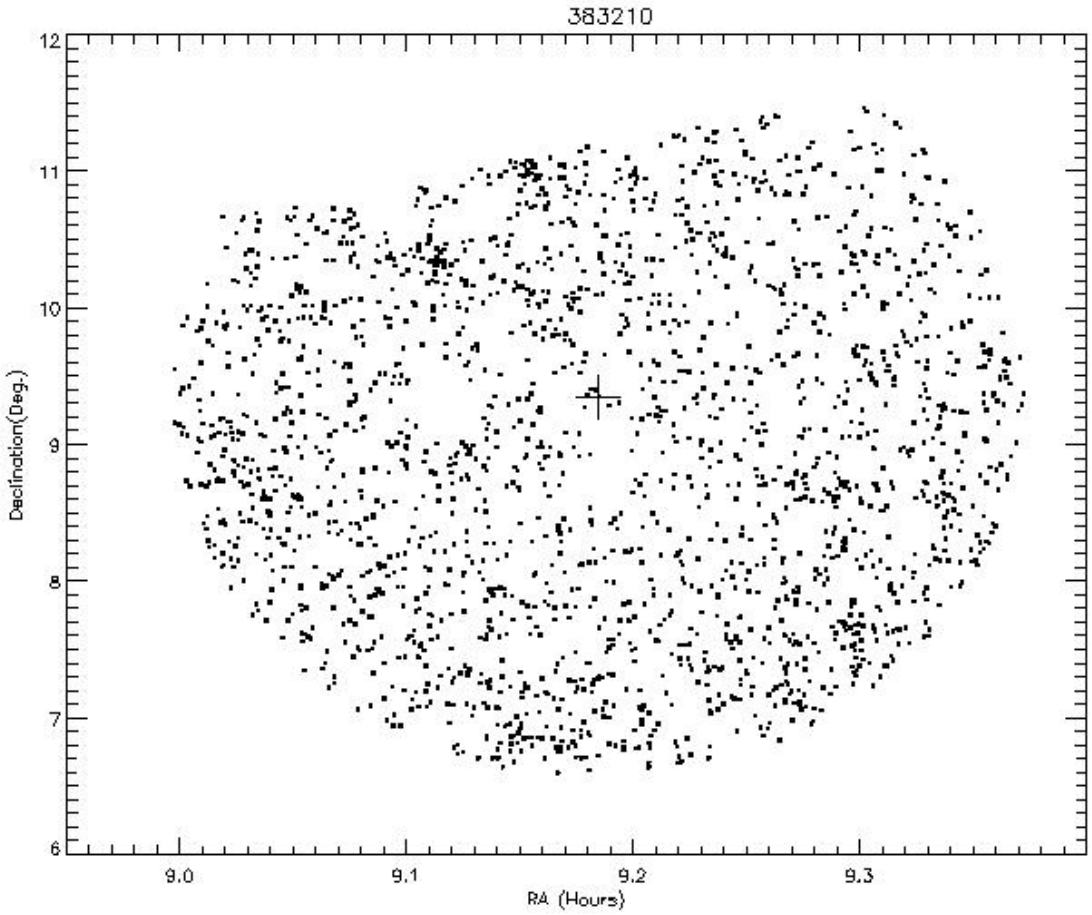

Figure 4.5: SDSS radial redshift search of IEG 383210. The candidate IEG is labeled with a cross and all surveyed galaxies are displayed as a small black square.

would violate the isolation criteria, the candidate IEGs are still in extreme low-density regions and exceed the typical separation for loose group galaxies is 0.64 h^{-1} Mpc (Tucker et al. 2000). The three candidate IEGs likely have not interacted with another bright galaxy in almost a Hubble time, and therefore they were not removed as candidates in the sample. The final sample consists of 33 isolated early-type systems. A summary of the SDSS global properties of the sample is given in Table

4.1. The SDSS footprint with the IEG sample galaxies highlighted can be found in Figure 4.7.

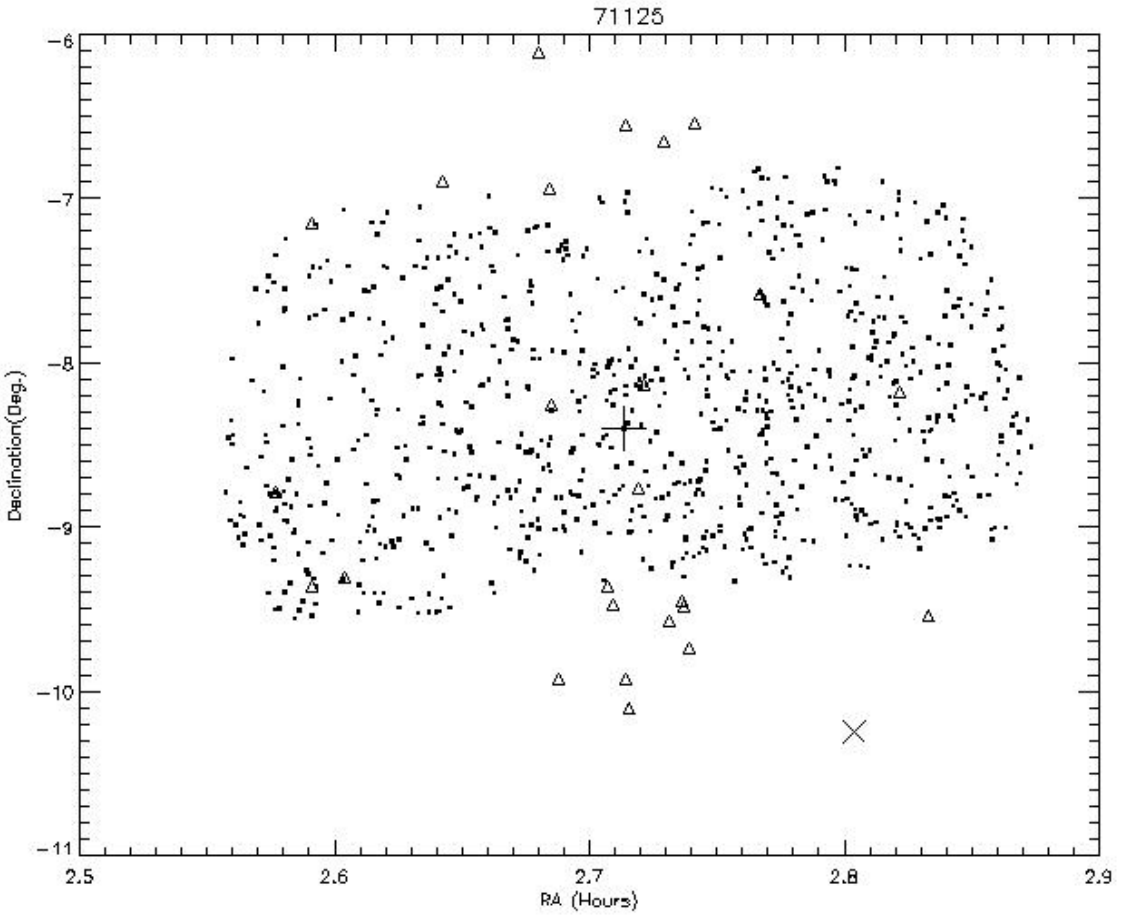

Figure 4.6: SDSS & supplemental NED radial redshift searches of IEG 71125. The candidate IEG is labeled with a cross, SDSS surveyed galaxies are displayed as a small black squares, and NED detected galaxies are labeled with open triangles. The "companion" galaxy is labeled with an X. At 2.4 Mpc, the neighbor galaxy is distant enough that IEG 71125 is truly isolated.

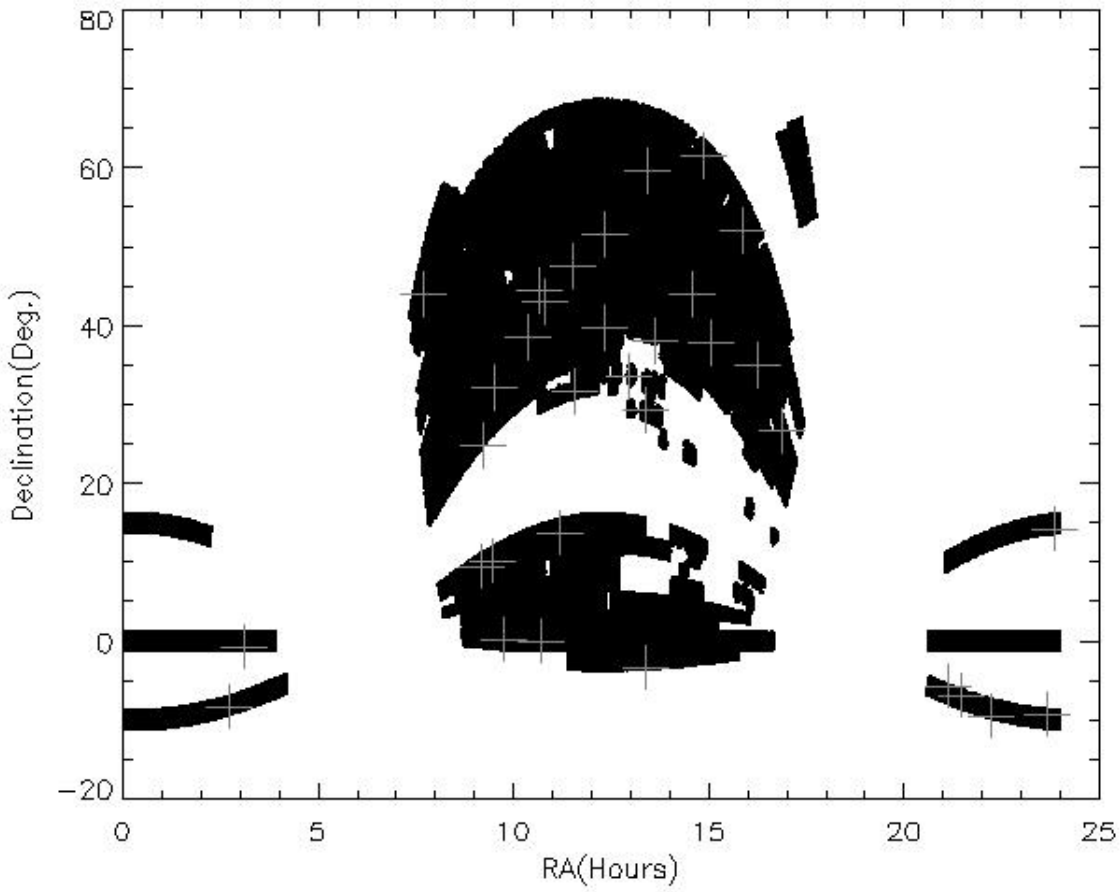

Figure 4.7: SDSS spectroscopic survey footprint with the positions of the IEG galaxies displayed as grey crosses.

4.3 SDSS Data & Data Reduction

The isolated early-type galaxies were selected from the SDSS spectroscopic survey Data Releases 1–5 (DR 1–5). As of DR5 the survey had imaged 8000 square degrees, yielding imaging and spectroscopic data for more than 674,000 galaxies. Images were obtained using the photometric mosaic camera (Gunn et al. 1998) which gives a field of view of 3 $\times$ 3 deg^2 and a spatial scale of 0.396" per pixel. Imaging data

are produced in five photometric bands (ugriz) and Table 4.2 displays the average wavelengths and magnitude limits (Fukugita et al. 1996) respectively. The SDSS reduces data using automated photometric and spectroscopic pipelines (Stoughton et al. 2002).

Galaxies targeted for spectroscopy have r-band magnitudes $\leq$ 17.77 (Strauss et al. 2002). The spectra are obtained using a multi-fiber spectrograph that can observe 640 objects simultaneously. Individual fibers are 3" in diameter and two fibers cannot be closer than 55". A minimum of three 15 minute exposures are taken to ensure adequate S/N per pixel is achieved (typically, S/N $>$ 4 per pixel for g = 20.2). Each spectrum has a wavelength range of 3800 – 9000 Å.

A modified version of the Petrosian (1976) system has been implemented by the SDSS for galaxy photometry. The Petrosian system is designed to measure a constant fraction of the total light independent of the surface brightness limit. The photometric pipeline calculates the Petrosian 50% and 90% radii, which will be used in the selection of the early-type galaxies and were discussed in section 3.3.

Images of each candidate galaxy in the g, r, and i bands were coadded to create a pseudo-open filter. The coadding procedure was performed to help aid in the identification of faint outer structure and any features indicative of interaction or merger. The exposure time for each SDSS filter is approximately 54 seconds. Therefore the coadded gri images have an effective exposure time of 162 seconds. In order to compare the photometry with previous isolated galaxy samples, the SDSS ugriz

magnitudes were converted to the Johnson system using the corrections supplied by Smith et al. (2002),

$$B = g + 0.47(g - r) + 0.17 \tag{4.2}$$

$$V = g - 0.55(g - r) - 0.03 \tag{4.3}$$

$$R = g - 1.14(g - r) - 0.14 \tag{4.4}$$

Smith et al. derived the SDSS to Johnson transformations using 158 standard stars. Magnitudes were corrected for reddening and radial velocities corrected for the infall of the Milky Way into the Virgo cluster (Karachentsev & Makarova 1996).

4.4 SDSS Properties of the IEG sample

Images of the IEG candidates are shown in Figure 4.8. Scale bars representing 10 kpc and 10" are displayed. A visual inspection of the sample reveals that many of the IEGs have disky features loosely resembling S0s. A boxy appearance can be seen for 5 of the 33 galaxies (15%). One galaxy, IEG 469932, shows weak arm features that we have interpreted not as spiral structure, but as possible tidal remains of an accreted dwarf companion. Missing in the sample are large round ellipticals. IEG 71125, 369001, and 383210 most closely resemble normal ellipticals. The largest galaxy in the sample, IEG 51108, has the appearance of a lenticular galaxy.

Figure 4.8: SDSS gri coadded images of the IEG sample. The upper bar represents an angular size of 10" and the lower bar is a scale of 10 kpc. Images are have been smoothed using a Gaussian function and are displayed on a log scale.

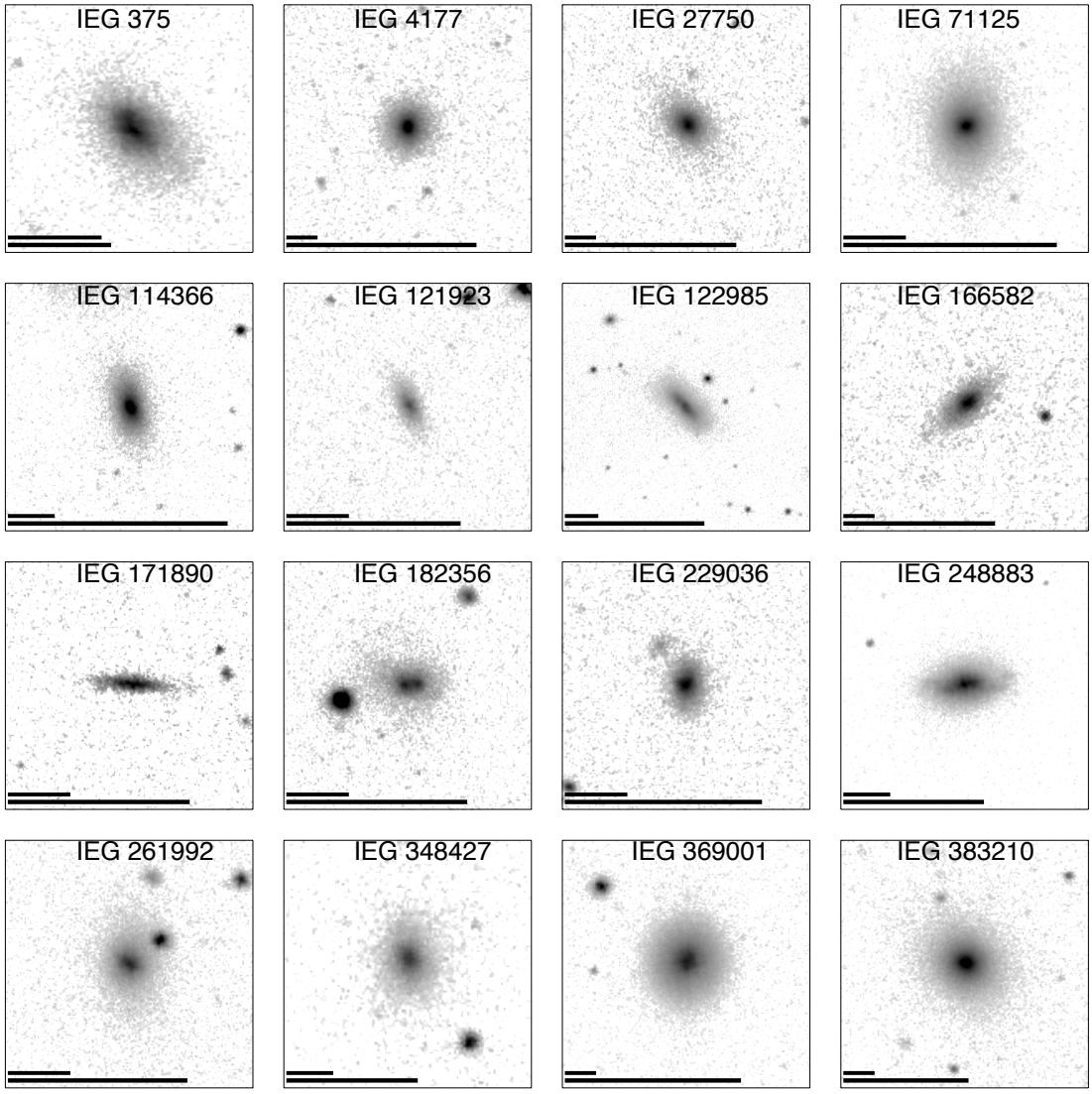

Figure 4.8 continued IEGs 375, 4177, 27750, 166582, 348427, 369001, 383210 have scale bars of 5" and 5 kpc. All other displayed galaxies have 10" and 10 kpc scale bars.

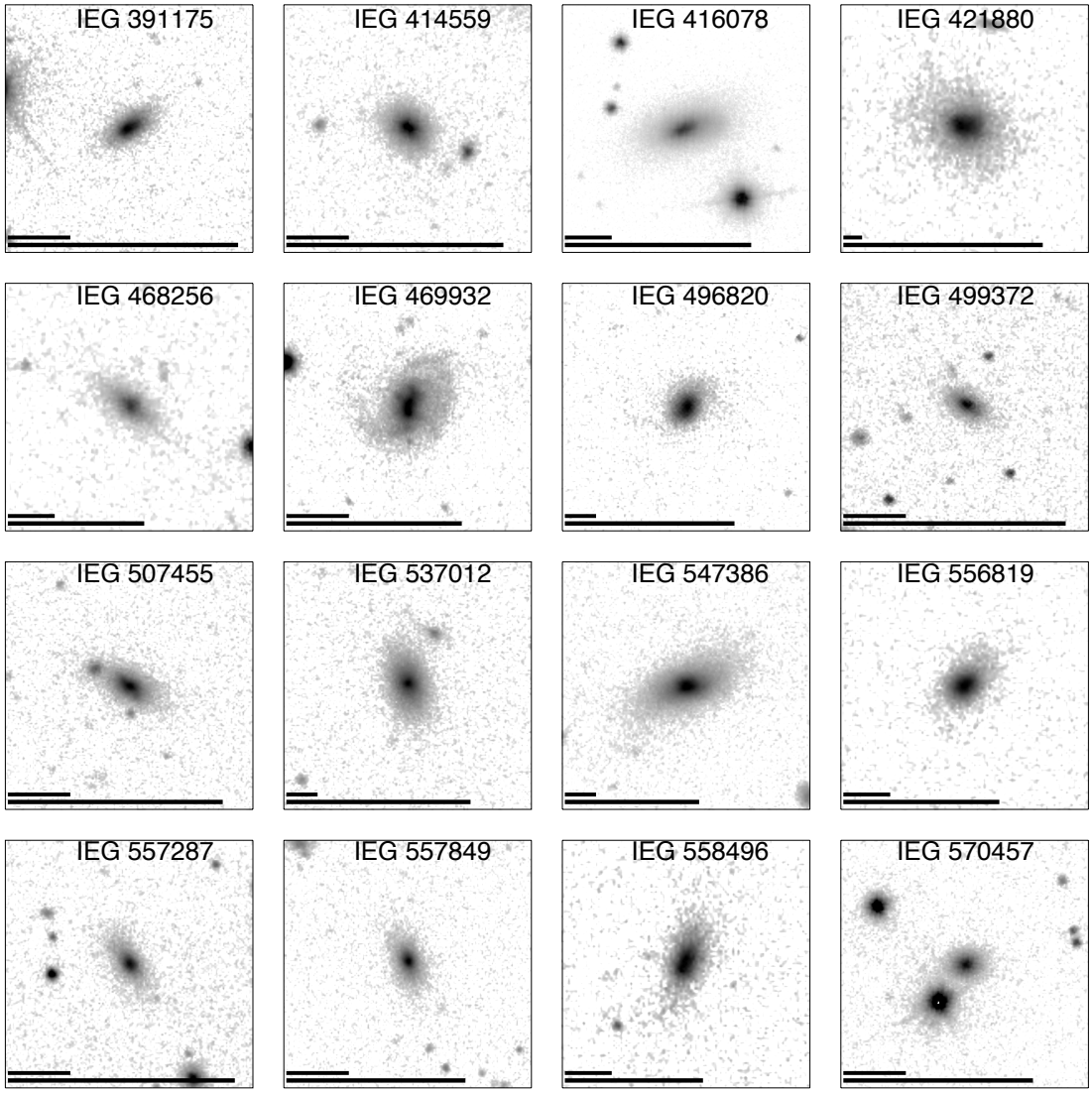

Figure 4.8 continued IEGs 468256, 496820, 537012, 547386, 556819 and 558496 have scale bars of 5" and 5 kpc. IEG 421880 has 2" and 2 kpc scale bars. All other displayed galaxies have 10" and 10 kpc scale bars.

The sample shows a number of unexpected features and trends. We predicted the sample would contain large, red ellipticals with absolute V magnitudes brighter than -19. The distribution of redshift z for the IEGs is illustrated in Figure 4.9. For even the most distant IEG, the sample describes isolated early-type galaxies in the local universe. There is a peak at the 72 Mpc, the self imposed distance limit which corresponds to $z \sim 0.0188$. It is odd that eight candidates (8/33, 24%) fall so close to the distance limit. The results suggest that there may be an under-density of isolated

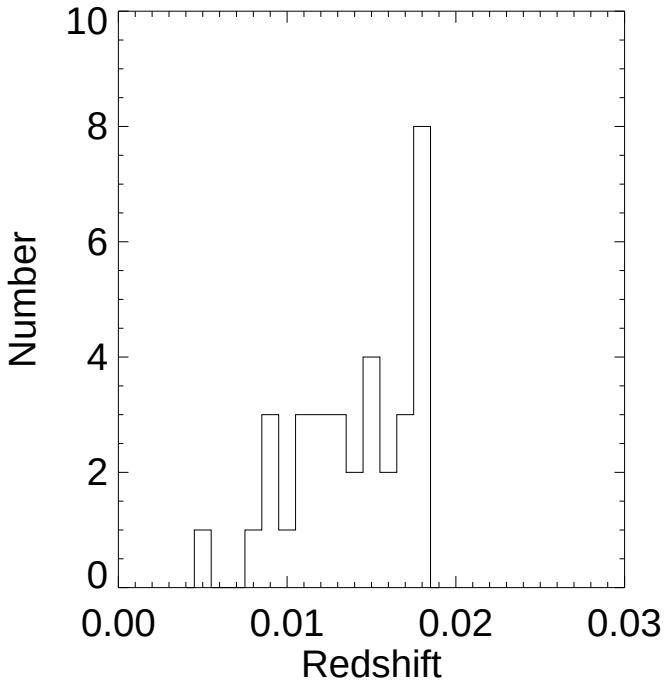

Figure 4.9: Redshift histogram of the IEG sample.

early-type galaxies in the local universe. The possibility remains that at or near 72 Mpc, the SDSS may not be able to detect companion galaxies to the brightness level

of −16.5 magnitudes as described in the search criterion. As the number density of IEGs begins increasing beyond 72 Mpc, we may want to devise a method for extending the distance limit or removing it all together. The IEGs are otherwise nearly evenly distributed in redshift-space.

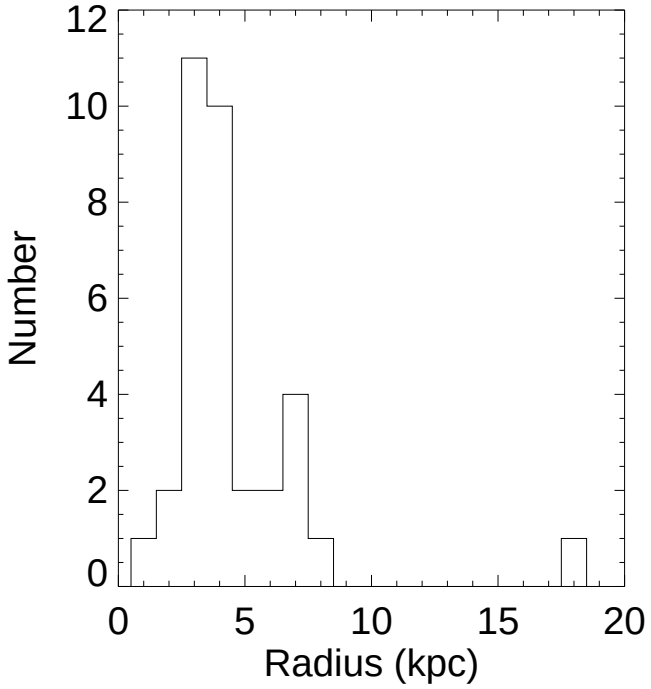

Figure 4.10: Distribution of IEG radii.

Figure 4.10 shows the distribution of the IEG radii. The radii listed are the r-band semi-major axes as calculated by the SDSS. The sample values peak at a radius of 3 kpc. Two secondary peaks are also seen at 7 and 18 kpc respectively. The peak at 18 kpc corresponds to IEG 51108. Absent from the sample are systems of intermediate

and large radius. The radii could be underestimated due to the short exposure times of the SDSS.

A histogram of the absolute V band magnitudes is displayed in Figure 4.11. The IEG sample has a peak M_V of approximately -17.0. Again a secondary peak due to IEG 51108 can be seen at $M_V = -21$. The absolute magnitudes of many of the IEGs (14/33, 42%) can best be characterized as being dwarf-like with $M_V \geq -17$. The IEGs brighter than -17 mag are still 1 – 2 magnitudes fainter than normal early-type galaxies.

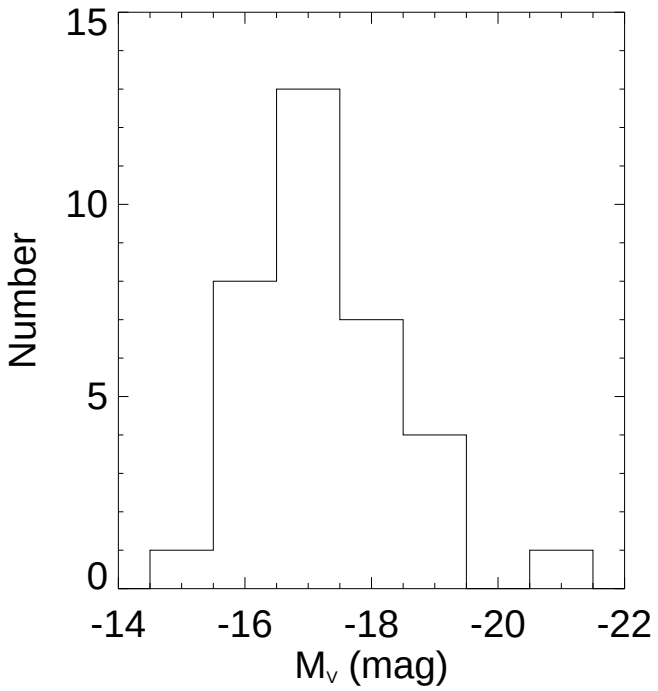

Figure 4.11: Histogram of the absolute V band magnitudes.

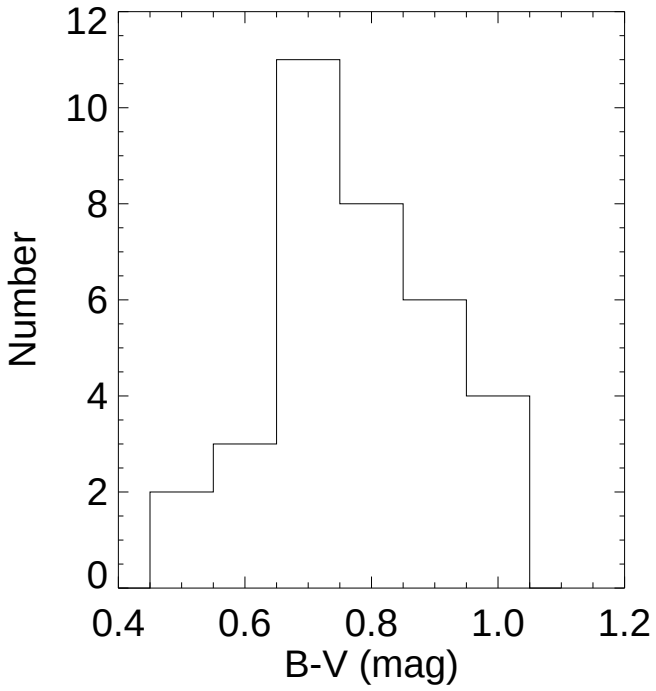

Figure 4.12: Distribution of (B − V) color for the sample.

The colors of early-type galaxies are well known with a range of $0.8 \leq B - V \leq 1.1$. The red colors found for ellipticals and S0s are indicative of an old stellar population dominated by K and M stars. The B − V colors of the IEG sample are shown in Figure 4.12. The distribution peaks at $B - V = 0.7$. This is significantly bluer than what is expected for early-type galaxies. The extreme blue colors reveal that the IEG sample has experienced recent or ongoing star formation episodes. Analysis of the spectral properties will be described in Chapter 5.

Figure 4.13 displays the B − V versus M_B relation for the IEGs. Early-type galaxies follow several well-established trends in optical color and brightness. Figure

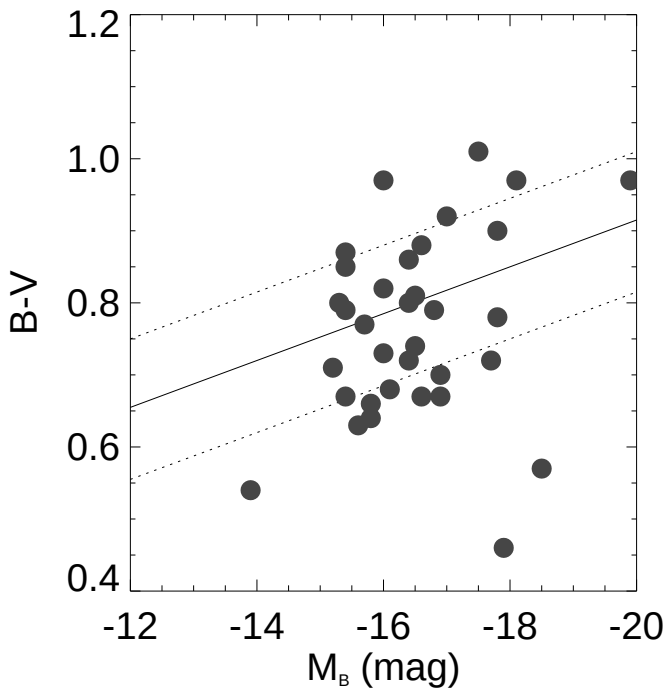

Figure 4.13: IEG sample (B − V):M_B relation. The solid line is the best-fit to the sample of Burstein et al. (1987). Dotted lines represent 3σ deviations from the Burstein best-fit.

4.13 is included to compare the IEGs with such trends. The solid line represents the relationship for typical galaxies and is a best-fit line to the Burstein et al. (1987) sample of general ellipticals. The dashed lines indicate the 3σ deviations from the Burstein best-fit linear relation. Eleven IEGs (33% of the sample) are seen to have extreme blue colors and faint magnitudes causing them to fall below the lower 3σ line. Approximately half of the IEGs (17/33, 52%) fall within the 3σ lines. However, there is not a tight correlation as was found for the Burstein et al. sample.

4.5 McDonald Observatory Data, Reduction, & Calibration

While the Sloan Digital Sky Survey provided the extensive sky coverage and redshift measurements necessary to defining the IEG candidate list, deeper imaging was required to detect the faint signs of mergers and interactions. The exposure times in each of the five SDSS bands was only 54 seconds. The first attempt to create deeper images of the IEGs was done by coadding the SDSS gri bands. These coadds constitute a pseudo-open filter with a still relatively short exposure time of 162 seconds. Not wanting to miss any low surface brightness peculiarities, the SDSS gri coadds were deemed inadequate to detect faint merger signatures.

Therefore, we carried out optical imaging of the IEG candidates, providing exposure times upwards of 600 seconds. The imagery would then enhance any faint features and details that might inform on the history of the IEG. The deeper images would then be used to perform analyses of surface brightness profiles, asymmetric structure uncovered with residual imaging, and variations of radial parameters.

Imaging of 22 of the 33 IEG candidates was performed in BVR bands in October and December 2006, February and March 2007, and March 2008 using the 2.1−meter Otto Struve telescope at McDonald Observatory, which is operated by the University of Texas at Austin. Details of those observations, the seeing conditions during observing and the number of coadds that went into making the finalized IEG images can

be found in Table 4.3. All observations were made using the "WHT guider" and the 1026 × 1024 TK4 CCD chip. After 2×2 on-chip binning, the TK4 has a pixel scale of 0.348 arcsec pix^{-1} and an angular field-of-view of 2.97 arcmin × 2.97 arcmin. The TK4 images suffer from severe vignetting on the image edges that limits the usable area of ∼60% of the quoted size.

Standard reduction procedures were used to flat field and bias-subtract individual frames after applying a mask to vignetted regions. Coadding of multiple images in a single filter was performed after flux-scaling the images and aligning them to within a fraction of a pixel. A cosmic-ray rejection algorithm was applied during coadding. The final coadded image typically represents 3 × 600-second exposures, but can be up to as many as 6 separate exposures.

As the SDSS has previously observed all of the IEGs, we undertook an uncommon method of photometrically calibrating our imagery. Between three and five stars in the fields of the IEGs were photometered in the SDSS g- & r-filter images using software developed by us in IDL. The calculated g and r band magnitudes were then converted to the Johnson system BVR magnitudes (Smith et al. 2002). Magnitudes of the same stars in the McDonald BVR bands were also calculated. The difference between the McDonald Observatory BVR values and the SDSS BVR magnitudes constituted a bootstrap calibration. The photometry of the McDonald Observatory BVR images for the IEGs were then adjusted using the bootstrap calibration values for that particular galaxy field. One note regarding the calibration procedure is that

the Smith et al. (2002) conversions from the SDSS filter system to BVR magnitudes was created for stars. As we are the first to apply the conversions to galaxies, there is some amount of uncertainty associated with our data. A check of how well the conversions work for galaxies can be seen in Figure 4.14. The plot of the McDonald calculated B−V values versus the SDSS derived B−V data reveals that the IEG colors are very nearly the same. Based on Figure 4.14, our use of the Smith et al. conversions was justified and the colors expected from SDSS data matches colors from the McDonald observations to within ±0.1 mag.

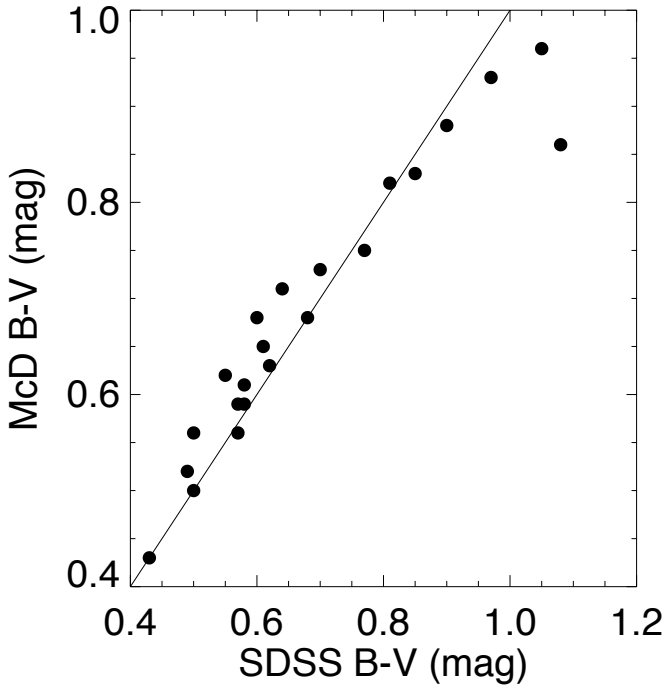

Figure 4.14: IEG sample (B − V) for both SDSs and McDonald observatory data. The solid line indicates a perfect SDSS-to-McDonald color relation. The two sets of data are well within a tenth of a magnitude, falling close to the line with a small scatter.

4.6 Properties of the Sample Compared to Higher Density Environments

The IEG sample presented here exhibits a number of properties infrequently found in past samples of isolated early-type galaxies. Based on the preliminary SDSS data discussed in section 4.4, the most notable differences are the IEGs are much bluer and fainter than all prior isolated ellipticals. The absence of "typical" properties makes comparing the IEGs to other samples difficult. The isolated early-type galaxies candidates fall somewhere between KIG galaxies and samples of dwarf elliptical and spheroidal systems. In an effort to better understand the IEG features and histories, a study of the integrated photometry of the IEGs from McDonald Observatory data was performed and is presented in what follows.

4.6.1 Integrated Magnitudes & Colors

The limiting magnitudes and surface brightnesses in the BVR images are summarized in Table 4.4, while the integrated absolute magnitudes and colors with Galactic extinctions values applied can be found in Table 4.5. Of the 22 IEGs with broadband imaging in the BVR filters, 17 (77%) have bluer B−V colors than typical early-type galaxies. A well known correlation has shown that more luminous ellipticals have redder colors then less luminous Es (Sandage & Visvanthan 1978; Bower et al. 1992).

Atypical blue colors may indicate the accretion of a gas-rich companion within the last few Gyr (Zepf, Whitmore, & Levison 1991).

Figure 4.15 displays an absolute magnitude versus color plot with data from Burstein et al. (1987) defining the regions of "typical" early-type systems. A similar plot can be seen in Figure 4.13 with the SDSS photometry. The exceptionally blue nature of the IEGs is evident in Figure 4.15. Of note in the Figure are the 15 IEGs (15/22, 68%) that fall well outside of the 3σ bounds. The bluest galaxy, IEG 469932, is unique due the clear outer structure that may be spiral arms or tidal tails. A more complete discussion of the nature IEG 469932 can be found in the following sections.

The redder IEGs (71125, 121923, 248883, 369001, 383210, and 537012) follow the trend highlighted by the Burstein relation. At a first pass, these red IEGs are the most likely galaxies to have been formed by a monolithic collapse, the so-called primordial early-type galaxies.

Given the photometry, the IEGs studied here are considered to be fainter than typical ellipticals and would likely be classified as dwarfs or intermediate-luminosity galaxies ($-16 \leq M_V \leq -18.5$). The IEGs fall about 6 magnitudes fainter than the largest ellipticals and display magnitudes fainter than those found in Marcum et al. (2004), who noted their sample was underluminous compared to cD and fossil group galaxies. The fossil groups studied in Chapter 2 (Vikhlinin et al. 1999; Jones et al. 2000; Khosroshahi et al. 2006) are red, bright systems at M_B = -23. Similar to the IEGs, the fossil groups are the dominant mass in their local environment. A

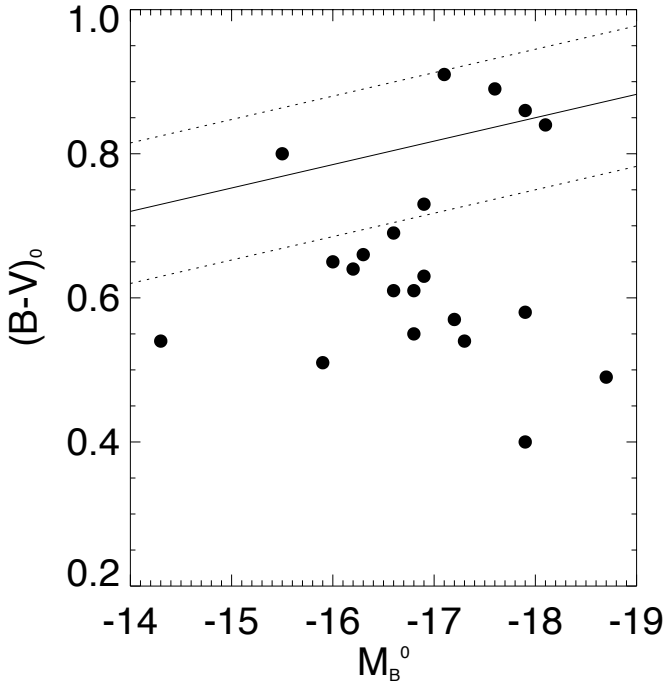

Figure 4.15: IEG $(B-V)_0$ color plotted against integrated absolute B band magnitude. Both color and brightness were corrected for extinction, with the correction values listed in Table 4.4. Overplotted is the relation from Zepf et al. (1991) and Burstein et al. (1987) showing the average values $\pm$ 3σ for "normal" ellipticals.

series of analyses of the environments of fossil groups and X-ray observed isolated ellipticals found that many of these galaxies have an extended network of faint dwarf companion galaxies (Mulchaey & Zabludoff 1999; Sun et al. 2003, 2004; Smith et al. 2004a, 2004b). The sparse neighborhoods of the IEGs is in stark contrast to the fossil groups and suggest that the IEGs are intrinsically different systems with a different formation mechanism.

The IEGs may not be the remnants of a merged bright group, however the galaxies may be the remains of a group of dwarf galaxies. Mergers between the dwarfs in such a group would result in very short-lived shell structures and tidal tails. Evidence for a merging group of dwarfs galaxies (MDG1) was found by Fanelli et al. (2007) in the SDSS, where three blue dwarf galaxies are in the process of merging and are encompassed by a common halo. An inspection of the IEG sample reveals a galaxy that may be at the next stage of dwarf galaxy group evolution. IEG 182356 can be seen to have two distinct cores and an extended blue halo. The possible formation mechanisms for the remaining IEGs will be discussed later in Chapter 4.5.

4.6.2 Fine Structure Analysis

In general, elliptical galaxies and to some extent S0s have complete two-dimensional symmetry as projected onto the sky. The surface brightness of early-type galaxies do not always smoothly decline with radius. The hidden structures within galaxies can be detected by subtracting a smooth luminosity profile from the galaxy's observed light profile (Malin & Carter 1980; Prieur 1990). Profile subtraction sometimes reveals other kinds of structures in E galaxies, including plumes, linear features or 'X-structures' often associated with boxy isophotes (Schweizer 1992). Prior works have found that at least 17% of ellipticals in the field have shell structure, but the actual percentage may be much higher, near 40% (Kormendy & Djorgovski 1989; Forbes & Thomson 1992). Shells have spectral energy distributions characteristic of

starlight (Kormendy & Djorgovski 1989). Ellipticals with fine structure are slightly bluer than "normal" early-type galaxies and based on B−V color alone, one would assume a large fraction of the IEGs would shows signs of mergers and interactions.

With more than two decades of research, the lifetime of observable shell structure has yet to be well constrained (Malin & Carter 1983). The lack of a standard timescale for shells results in a tenuous estimate of the merger date. Simulations have readily shown that shells and fan-shaped structures are the products of the accretion of a companion spiral or elliptical galaxy, respectively (Quinn 1984). The companion galaxy would supply the gas, dust, and stars that form the shells. Other simulations have found that merging is not requisite for shell formation, as strong tidal forces could dynamically pull cold stars from the host galaxy (Thomson & Wright 1990). The lifetime of shells has been estimated to range between $\sim$ 1 Gyr (Hernquist & Quinn 1989) and $\sim$ 5 Gyr (Reduzzi, Longhetti & Rampazzo 1996).

Often neglected in analyses is the formation of fan structure. Work by Van Dokkum (2005) found that broad fans of stars and possibly asymmetric deformation of inner isophotes would result from the merger of two bulge dominated systems. Assuming an intermediate-luminosity isolated elliptical could be formed via the collapse of a group of dwarf galaxies, one would expect fan structures more often than shells. Shells are not as likely because dwarfs are spheroidal shaped galaxies and the merger between two spheroidal galaxies could result in fan formation.

The detection of shell features is strongly dependent on environment (Malin & Carter 1983). Shells are believed to persist around isolated galaxies longer due to the lack of perturbations from neighboring galaxies. In early studies (Schweizer & Ford 1985; Colbert, Mulchaey & Zabludoff 2001, CMZ) $\sim 40\%$ of field ellipticals were found to possess shells. The occurrence of shells in early-type galaxies in group and cluster environments is greatly decreased to $\sim 8\%$ (CMZ). The perturbations of the surrounding galaxies, the intracluster medium and the cluster gravitational potential are assumed to disrupt and destroy shells.

While past investigations into the nature of shell and fan structures has focused on the brightest ellipticals (Schweizer 1992; Nigoche-Netro et al. 2007), almost nothing is known regarding shells in intermediate- and low-luminosity early-type galaxies. Clearly shells and tidal tails can form around faint E+S0 galaxies. The lifetime of shells surrounding faint galaxies should be considerably less than the same features around brighter, more massive ellipticals. The simple argument that any accreted companion galaxy will be of comparable-to-lower mass than the host galaxy reveals that the material in the shells will be less massive than the same structures found around larger ellipticals. Therefore, the lower mass shells will likely be extremely faint and may escape detection. The scenario for intermediate-luminosity galaxies is shell structure may be completely absent owing to faint luminosities.

The IEGs then represent a unique situation, existing in the low-galaxy density environment known to harbor long lived shells and at the same time they are a

sample of intermediate to faint galaxies where shells may be too low mass and short lived to detect. We predict that the majority of IEGs will not show signs of shells and in the unlikely scenario that one of the IEGs has shell structure, the shell-causing merger can be estimated to have occurred in the very recent past.

Figure 4.16 shows V-band images of the IEGs and model-subtraction maps. A smoothed model of each galaxy was created by employing an ellipse-fit to the isophotes using an IDL program which follows the procedures of Jedrzejewski (1987). The central coordinates were fixed while the position angle and ellipticity were allowed to vary with radius. Prior to beginning the model making program, bright stars which may have contaminated a smooth light profile were masked out. A two-dimensional model of the galaxy was constructed by applying a linear interpolation to the isophotal fits (Milvang-Jensen & Jorgensen 1999). Finally, residual images were created by subtracting the smooth models from the original galaxy images. Residual images are a powerful tool used to search for structures and regions that are over- or under-luminous from a standard de Vaucouleurs profile.

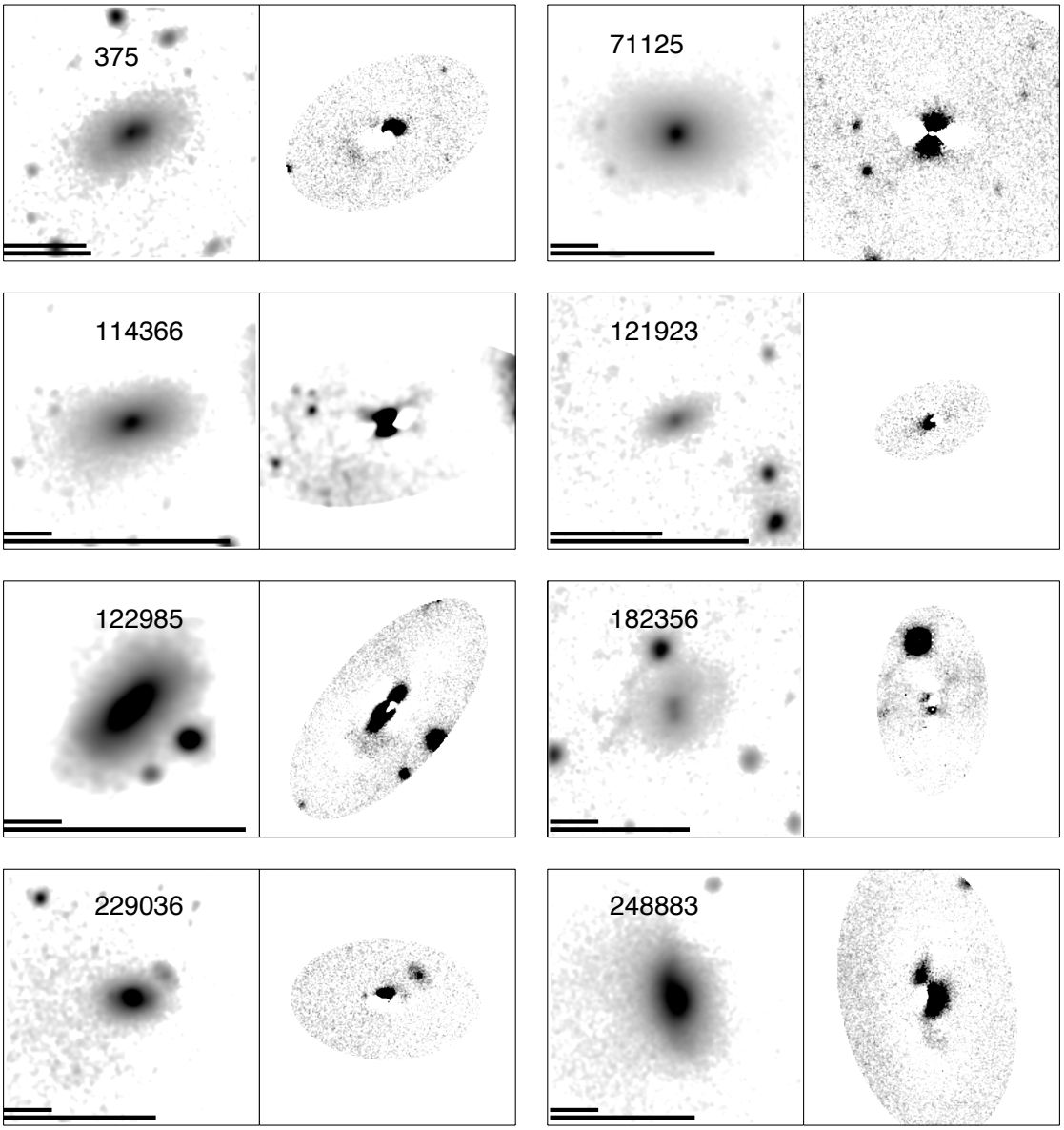

Figure 4.16: V band images and model-subtraction map for the IEGs. The scale bars are the same as those in Figure 4.8. Darker and lighter regions in the model-subtraction map represent regions which have a surface brightness which is above and below the modelled light distribution of the smooth underlying galaxy, respectively. North is up, east is to the left.

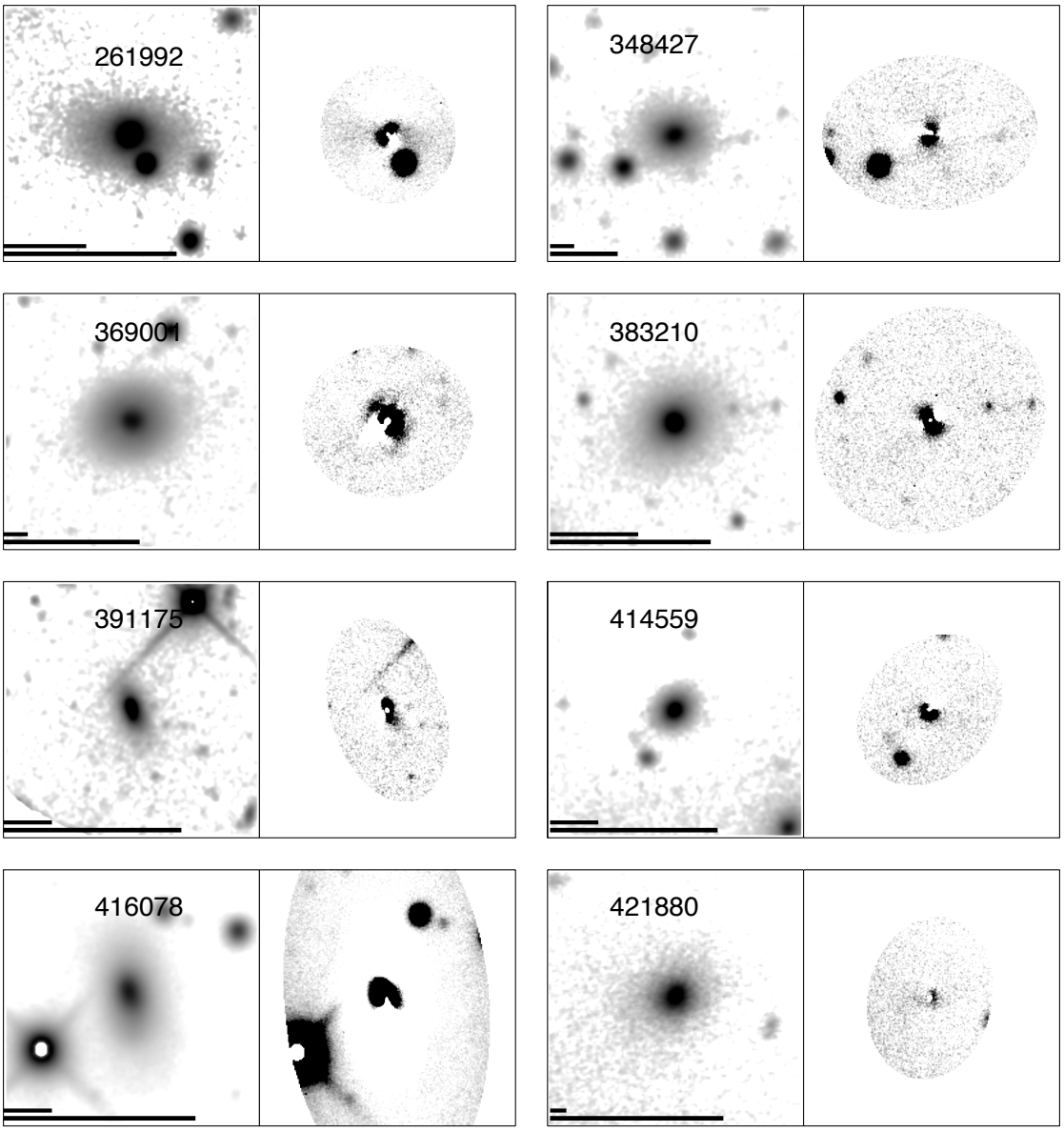

Figure 4.16 continued

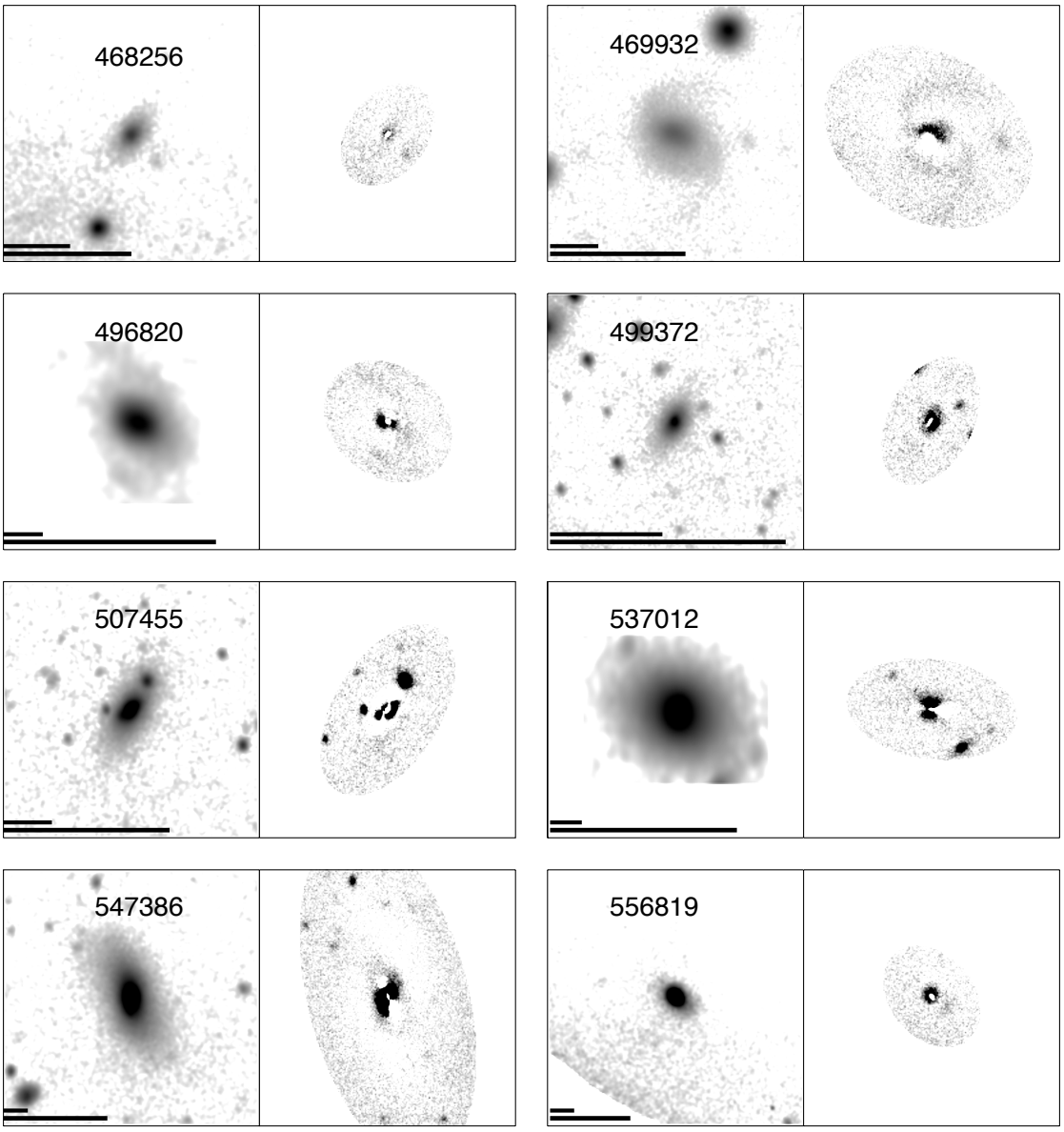

Figure 4.16 continued

The IEGs display a number of features in the residuals. Many of the IEGs have bar-like structures that may simply be the result of position angle twists, a topic to be highlighted in later sections. Evidence of only a smooth light profile can be seen in IEGs 421880 and 468256. Inner disk features are observed in the residual of IEG 507455. One IEG, 469932, has signatures that appear to have a spiral arm nature. We interpret these features not as arms but as tidal remains of an accreted companion galaxy. The extreme blue colors, $(B-V)_0 = 0.4$, support the notion of a relatively recent, $\sim$ Gyr, merger event. The surface brightness profile of IEG 469932, which is discussed in the next section, isn't fit well by an $R^{1/4}$ law, but if a merger has occurred, the galaxy may still be in a dynamically active state and may relax into the standard de Vaucouleurs profile.

Of the 33 IEG galaxies in the sample, none show shell features. Three (3/33, 9%) galaxies in the sample, IEGs 375, 229036, and 248883 have features that could be interpreted as fan structures. Most notably is the interesting system, IEG 248883. The galaxy doesn't have two-dimensional symmetry, having an asymmetric bulge to the SW. The bulge corresponds to the fan seen in the residual. Another piece of evidence for IEG 248883 having merged with a dwarf elliptical galaxy comes from a false color image created by the SDSS (not shown). The image reveals that the core of the galaxy is red, typical of an early-type galaxy, however the outer regions, particularly the area corresponding to the fan are blue. The residual evidence of a fan, the asymmetric shape and the peculiar color structure of IEG 248883 all point

to an accretion of a dwarf neighbor galaxy and subsequent intense star formation at the location of fan.

4.6.3 Surface Brightness Profiles

The variation of optical light with radius is quantified using surface brightness profiles. The surface brightness profiles of lenticular galaxies are able to be fit by a de Vaucouleurs law as frequently as ellipticals (van den Bergh 1989). Equation 3.1 defines the mathematical formula for an $R^{1/4}$ profile. The effective radius, r_e, is the radius enclosing 50% of the galaxy light and I_e is defined as the surface brightness at r_e. The upper panel of Figure 4.17 displays the light profile of the "normal" elliptical galaxy, NGC 3806. When plotted against $R^{1/4}$ the typical elliptical has a linear slope.

The surface brightness profile of spiral galaxies is best modeled using an exponential (de Vaucouleurs 1959), whose form is seen in equation 3.2. The disk scale length, r_d and the central surface brightness, I_0, define the properties of the disk. The lower panel in Figure 4.17 presents the surface brightness profile of UGC 386, a well studied lenticular galaxy. Spirals and S0s have both a bulge and a disk and the inner portion of their light profiles appear linear (bulge) and the outer region will display an exponential profile (disk).

Figure 4.18 shows the B, V, and R surface brightness profiles for the 24 IEGs observed at McDonald Observatory. The photometry was corrected for Galactic extinction. Fits to $R^{1/4}$ + exponential disk parameters were performed in each filter.

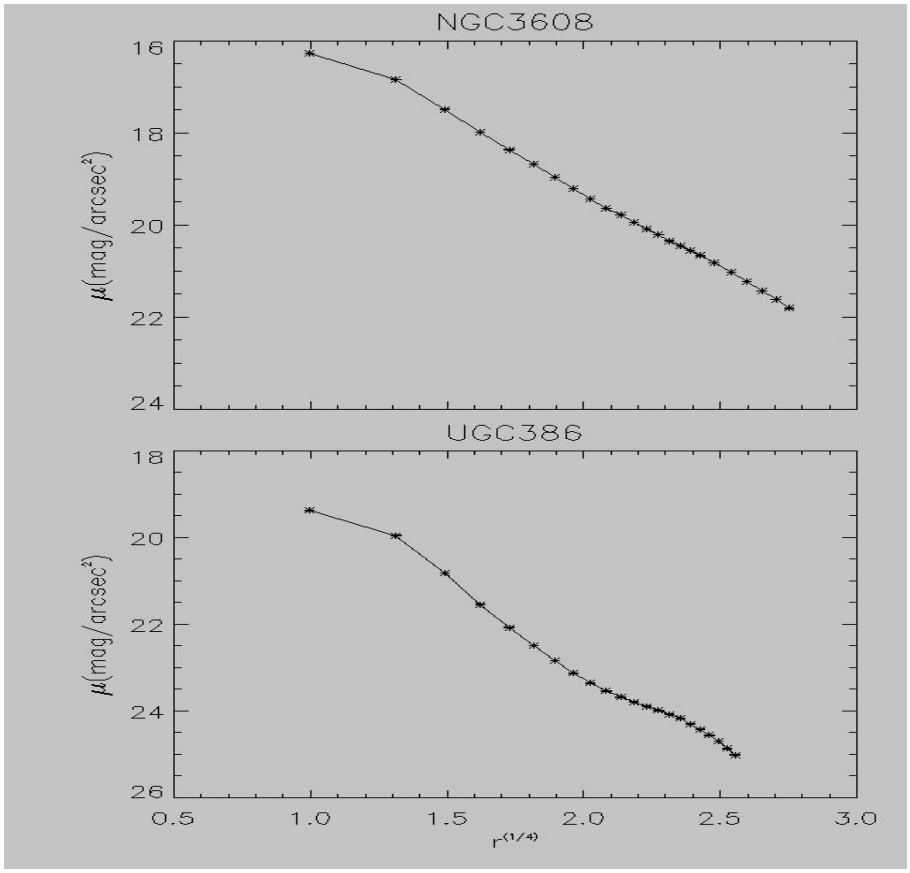

Figure 4.17: Surface brightness profiles for a bonafide elliptical, NGC 3806, and an S0, UGC 386. Both are plotted against $r^{1/4}$.

The results of the fitting routine are tabulated in Table 4.6. Overplotted on the surface brightness profiles in Figure 4.18 are the best fit de Vaucouleurs law in each bandpass. The radial extent to which the fits were performed was determined by selecting all surface brightness data having errors less than 0.15 mag.

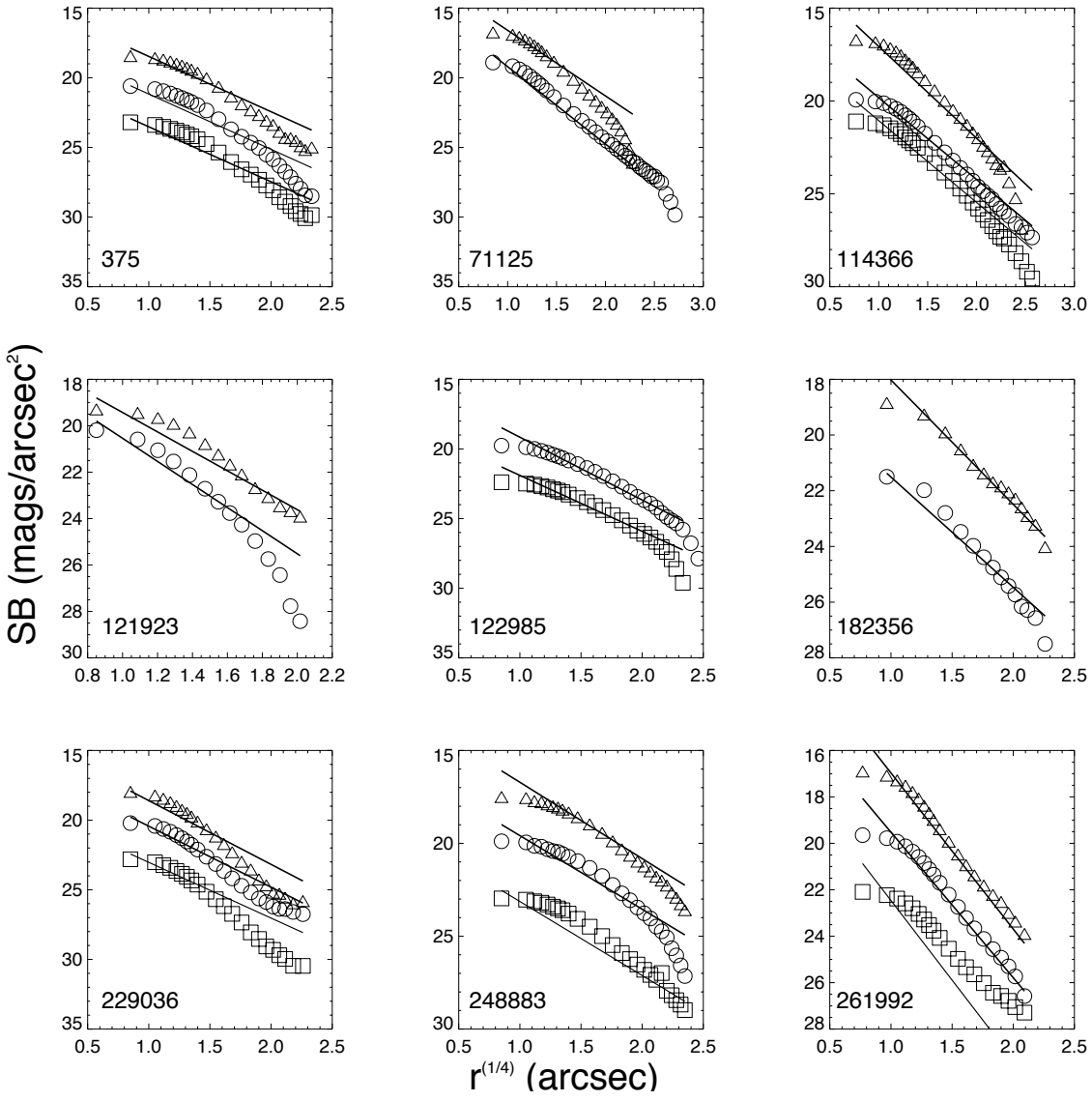

Figure 4.18: Surface brightness profiles of the IEGs in the B, V, and R bandpasses. A best fit $R^{1/4}$ profile is overplotted for each filter. The symbol for B, V, and R band data are triangles, circles, and squares, respectively.

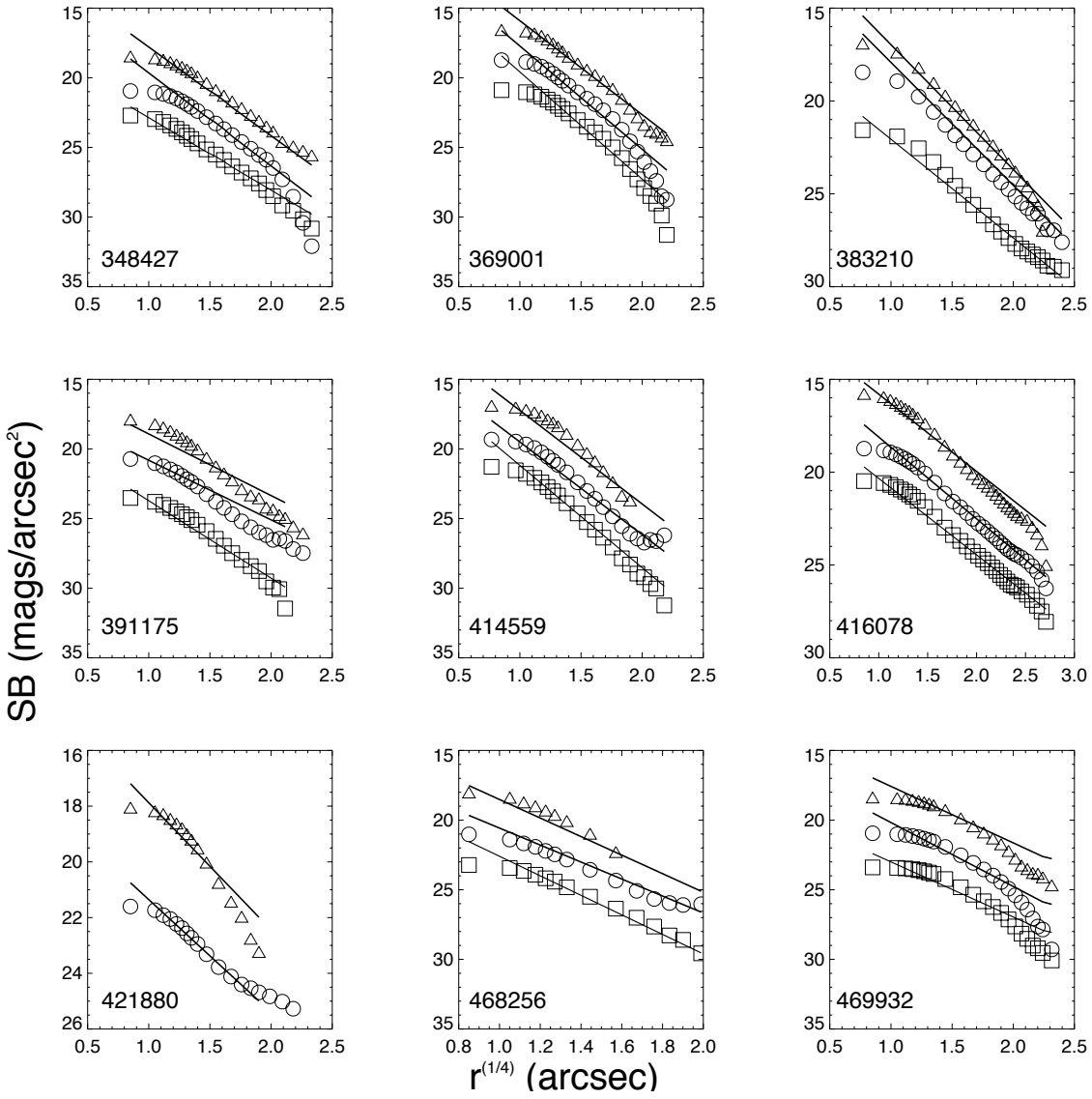

Figure 4.18 continued

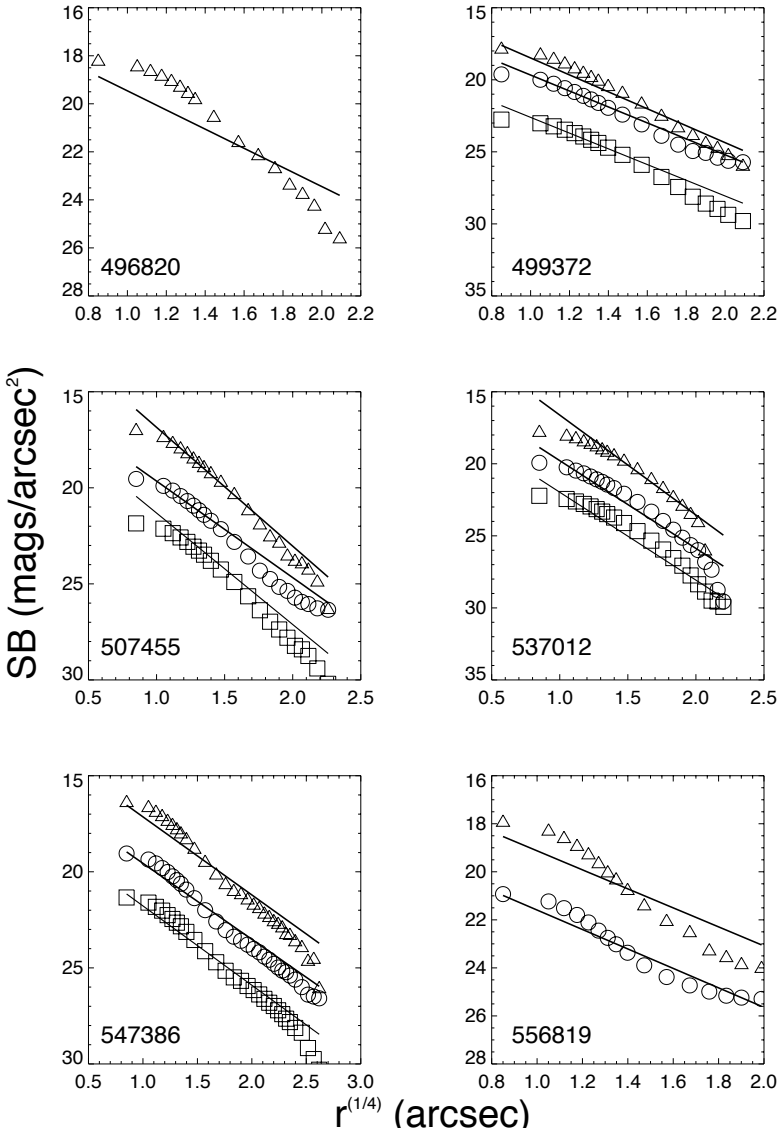

Figure 4.18 continued

Profiles of isolated ellipticals often vary with optical luminosity (Kormendy 1980; Michard 1985; Schombert 1986) and are best fit by an $R^{1/4}$ law near $M_B = -21$. .Many of the IEGs are well fit by the $R^{1/4}$ law, with a few notable exceptions. IEG 229036 has profiles in all three filters more reminiscent of an S0. Similar disk-like features are seen in the light profiles of IEGs 469932 and 556819. Disk features were expected in IEG 469932 due to the tidal tail/spiral arm structures. The V band profile of IEG 421880 has excess light in the outer regions, while the B band data is deficient in light. The surface brightness of IEG 496820 is unusual as the $R^{1/4}$ fit is very poor. The profile appears to have a bulge and weak disk components, suggesting an S0 morphology.

The average effective radius in the V band was calculated to be 2.74 $\pm$ 0.84 kpc. The IEGs have r_e values smaller than the value of 7.1 $\pm$ 3 kpc determined by Kormendy (1977) and of the sample of isolated ellipticals of Marcum et al. (2004), whose effective radii averaged 4.2 $\pm$ 1.0 kpc. The small size of the IEGs was expected as these galaxies are far less luminous than either the Kormendy or Marcum sample galaxies. The galaxies studied here more closely resemble dwarf early-type galaxies than large, bright ellipticals.

A plot of IEG effective radius and surface brightness at r_e for V band data is found in Figure 4.19. Overplotted is a line describing the Kormendy relation (1977, 1980), $\mu_e(V) = 18.79 + 3.28 \log R_e$. The Kormendy relation allows another comparison between the IEGs and the properties of typical ealry-type galaxies.The relation

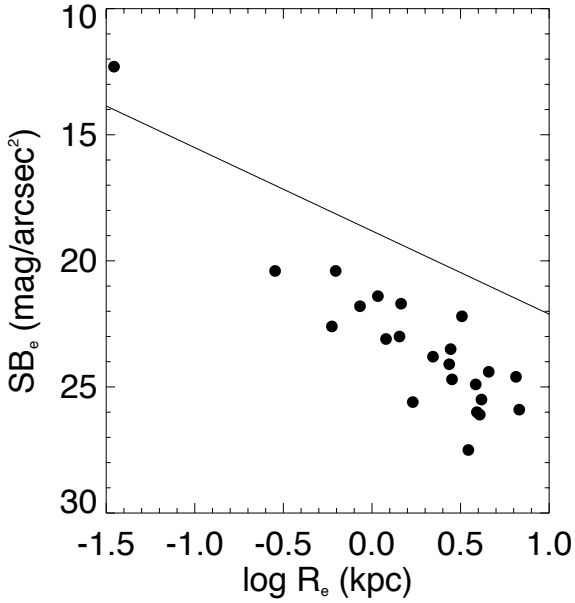

Figure 4.19: Plot of effective radius, r_e, versus effective $V-$band surface brightness, derived from $R^{1/4}$ fit to surface brightness profiles. Overplotted is the Kormendy relation (Kormendy 1980). All of the IEGs fall below the relation with the exception of IEG 414559.

between effective radius and surface brightness allows for an estimate of where the IEGs fall on the Fundamental Plane (Djorgovski & Davis 1987). The scatter determined by Kormendy (1977) was 0.3 magnitudes, while the IEGs obviously have greater dispersion. All of the IEGs are shifted below the Kormendy relation, with the exception of IEG 414559 which has an extremely small $r_e = 0.04$ kpc and a faint effective surface brightness, $\mu = 12.3$. Falling below the Kormendy relation could be expected as the IEGs have small physical sizes and have dwarf-like luminosities. The opposite trend was found by Schombert (1986), where the brightest cluster members (BCM) systematically fell above the Kormendy relation. Schombert

reasoned that the BCM galaxies were more diffuse and extended than the typical ellipticals studied by Kormendy. The fact that the IEGs still follow the general trend of the Kormendy relation indicates that a similar relation must exist for dwarf and intermediate-luminosity galaxies, implying that the Fundamental Plane extends down to faint luminosity levels. In a study of dwarf elliptical galaxies, Evstigneeva et al. (2004) found that dwarf galaxies fall below the Kormendy relation into the region inhabited by the IEGs. The Evstigneeva dwarfs do not follow the Kormendy relation slope, while a Kormendy-like slope is found for the intermediate-luminosity IEGs.

4.6.4 Analysis of Radial Parameters

The search for non-axisymmetric structure in elliptical galaxies can be used as yet another means of estimating the interaction history of the galaxy. Several authors have studied the isophotal shapes of ellipticals (Lauer 1985; Bender & Mollenhoff 1987; Jedrzejewski 1987). The isophotes of early-type galaxies can be matched by ellipses and any isophotal deviation from a perfect ellipse would point to the galaxy having disky or boxy features or atypical structures (Bender et al. 1989). Ellipticity is defined as,

$$E = \frac{a - b}{a}, \tag{4.5}$$

where a and b are the semi-major and semi-minor axis, respectively.

The most commonly used quantization of the degree of deviation uses a Fourier expansion about the polar angle. The amount of deviation from a pure ellipse is

calculated by (Carter 1978),

$$\delta R(\theta) = R(\theta) - R_{el}(\theta) = a_0 + \sum (a_n \cos n\theta + b_n \sin n\theta) \tag{4.6}$$

where, R_{el} describes the best-fit ellipse. The most significant deviation comes from the b_4 parameter (corresponding to the 4th cosine term). Perfectly elliptical galaxies would have higher order n-coefficients equal to zero at all radii. Negative b_4 values indicate boxy isophotes, while positive b_4 values correspond to disky structures. Boxy isophotes are often regarded as the products of interaction phenomena (Kormendy & Djorgovski 1989). Values as small as $\sim 10^{-3}$ are considered slightly boxy/disky, while values larger than 0.01 represent strong features (Governato, Reduzzi & Rampazzo 1993; Hao et al. 2006). The above equation will be used to calculate the b_4 boxiness parameter for the sample galaxies in order to quantify elliptical deviations. Figure 4.20 gives examples of disky and boxy isophotes.

Whether boxiness is a signature of a past merger or is a property intrinsic to a galaxy is a major concern if elliptical deviations are to be considered a reliable diagnostic. Simulations have found that boxy isophotes can indicate a past merger event (Binney & Petrou 1985), although the degree of boxiness may be the result of viewing angle (Lima-Neto & Combes 1995). Boxiness can come about dynamically, or be manifest through the presence of large amounts of dust (Lauer 1985, Mahabal et al 1996). Many of the most luminous ellipticals tend to harbor boxy isphotes as well as merger features (Bender & Surma 1992), which suggest that boxiness is a result of mergers. Alternatively, strong disky isophotes are believed to be a sign of

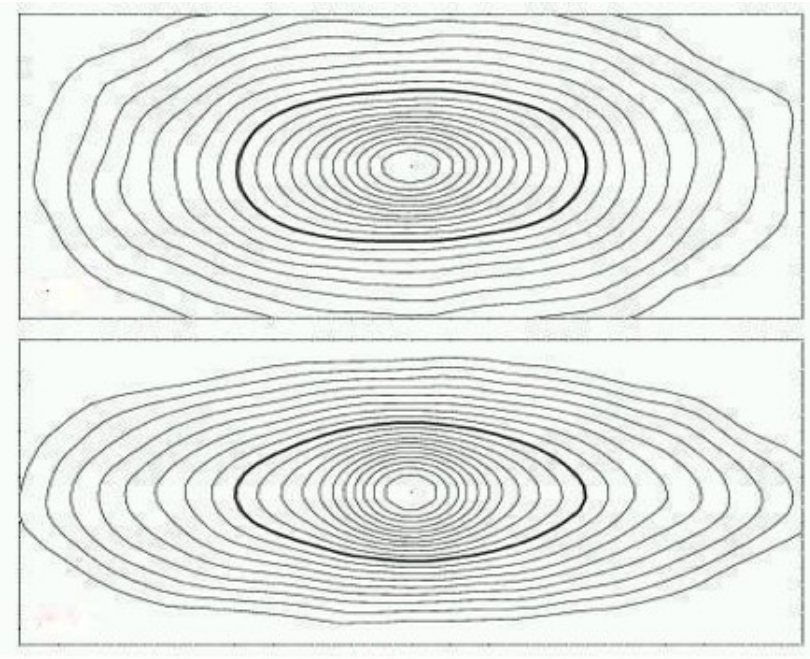

Figure 4.20: The upper panel shows a boxy elliptical and the lower panel the isophotes of a disky elliptical. The image comes from Naab et al. (2006).

recent star formation in a small central gaseous disk, which may have been accreted (deJong & Davies 1996).

Caution is needed in the interpretation of isophotal analysis, as the origin of isophote deviations and position angle twists remain unknown. The body of work has thus far been inconclusive.

The effect of environment on isophotal shapes is very important to the current study. DiTullio (1978, 1979) found that isolated elliptical galaxies on average have ellipticities that decrease with radius, while more recent investigations (Reda et al. 2004; Hao et al. 2006) did not reach the same conclusion. Shioya & Taniguchi (1993) examined isophotal shapes for a large sample of elliptical galaxies. They found that

disky ellipticals are preferentially found in the field and boxy Es exist in high-galaxy density environments. The disky ellipticals tended to be fainter systems that lacked strong radio and X-ray emission, while boxy ellipticals were optically bright with significant amounts of X-ray gas (Ferrarese et al. 1994; Faber et al. 1997; Lauer et al. 2005).

Figure 4.21 shows the position angle (PA), ellipticity, b_4, and B−V color profiles for the sample of McDonald observed IEGs. A blank plot indicates no data for that IEG. Of special interest are the color profiles. Typical B−V colors should become bluer with increasing radius. Authors have suggested that reversed color gradients are a sign of interactions (Gu et al. 2006).

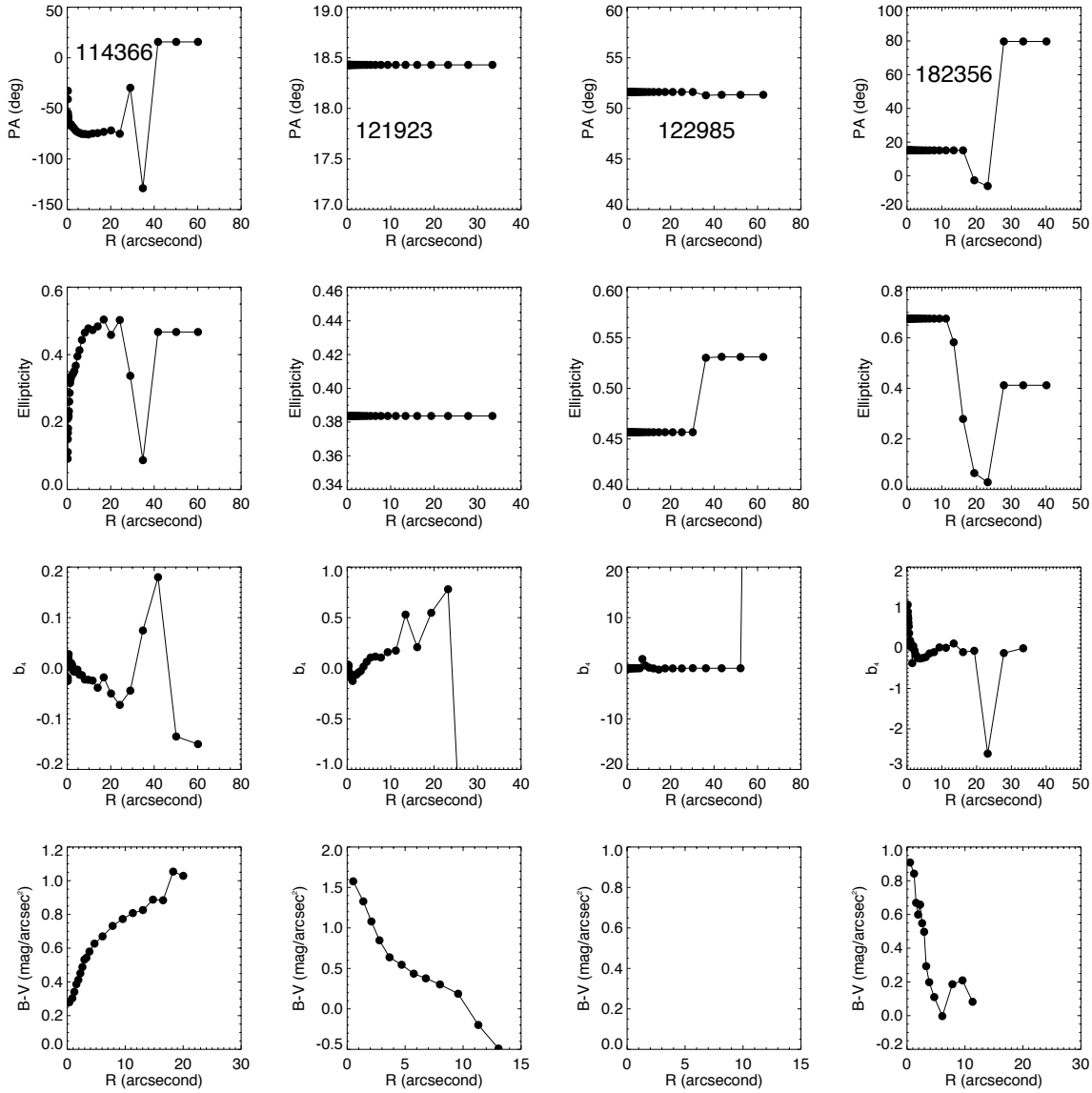

Figure 4.21: Plots of radial variation of position angle, ellipticity, b_4, and B−V color for the IEGs.

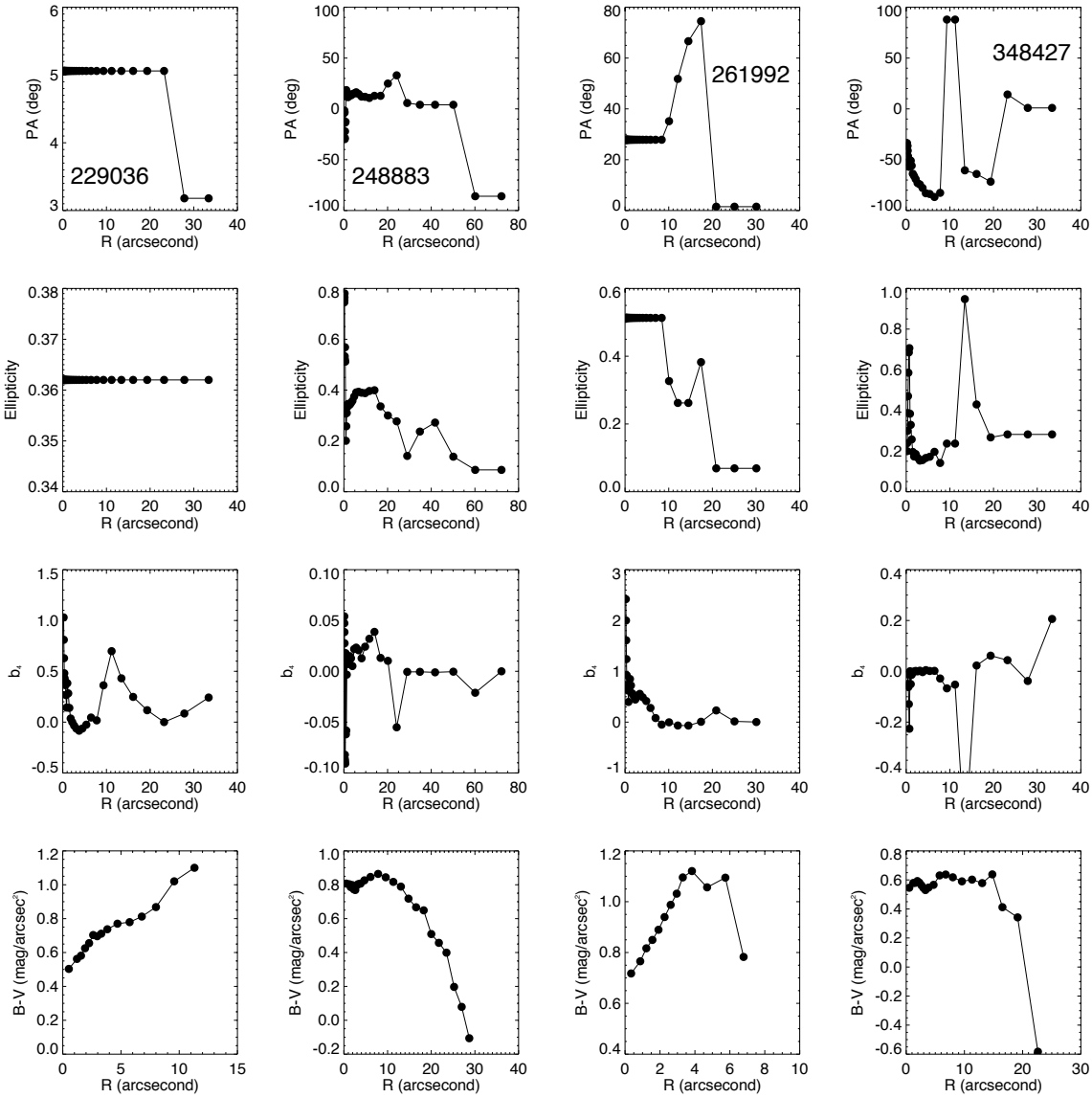

Figure 4.21 continued

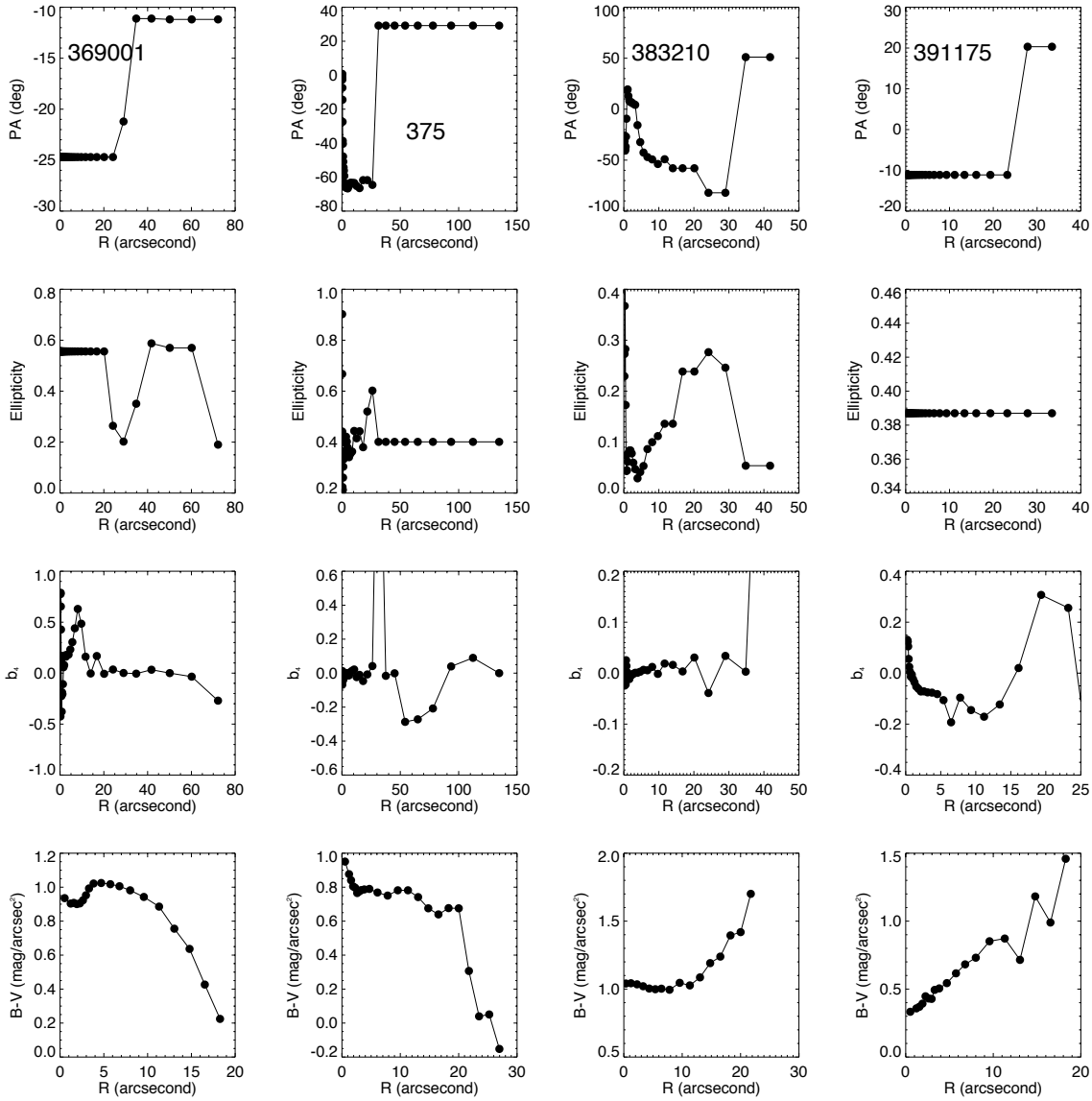

Figure 4.21 continued

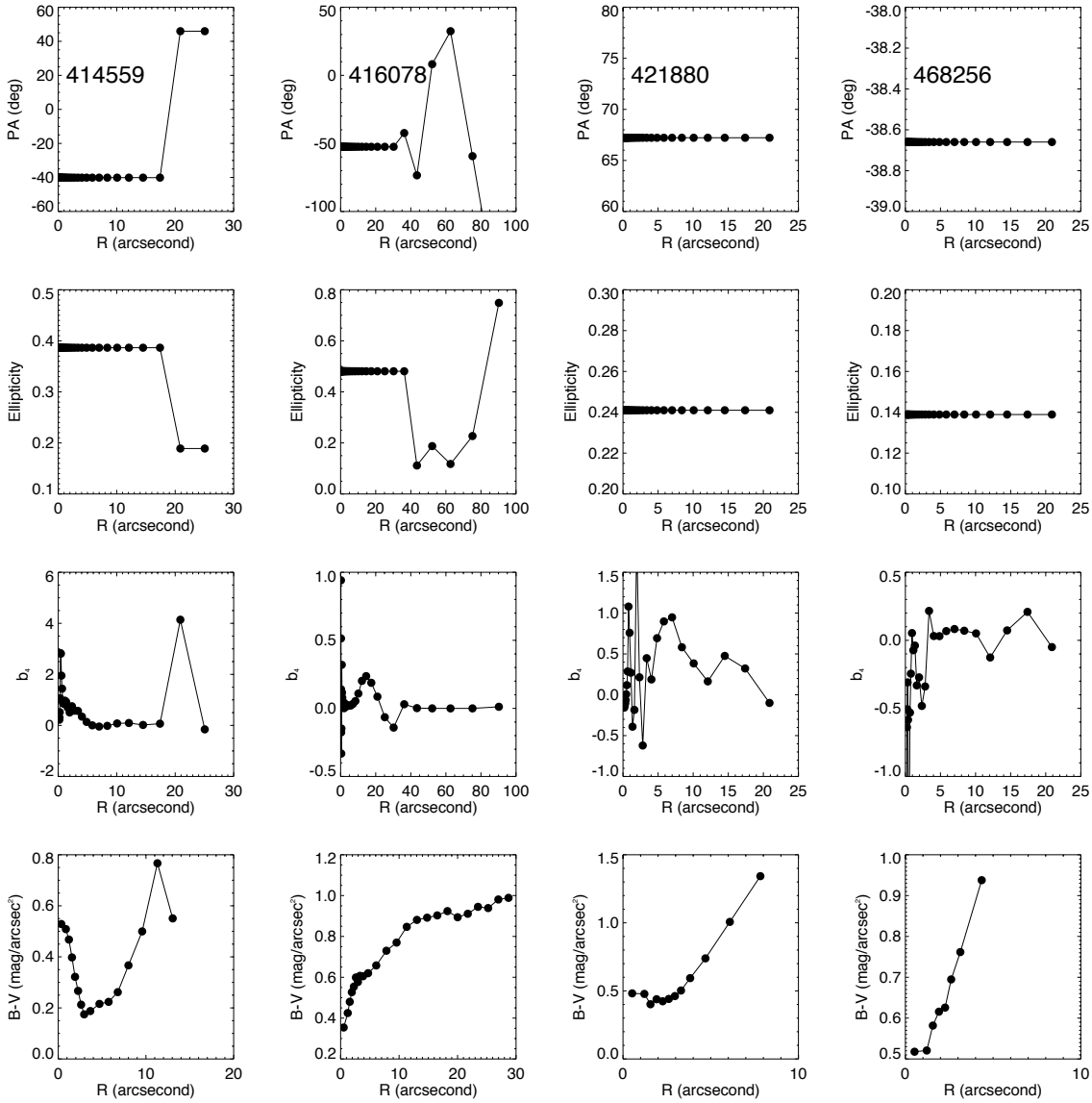

Figure 4.21 continued

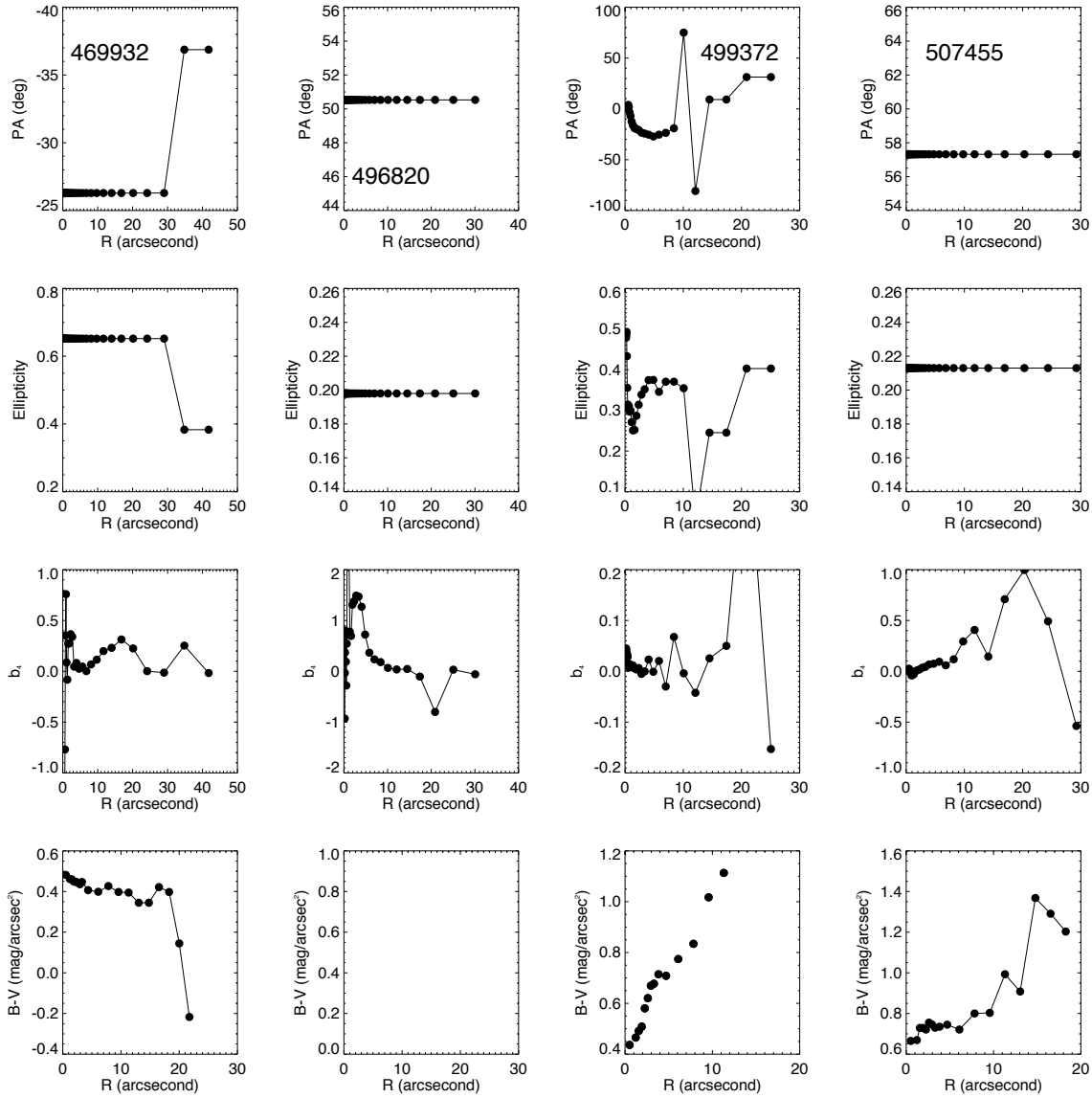

Figure 4.21 continued

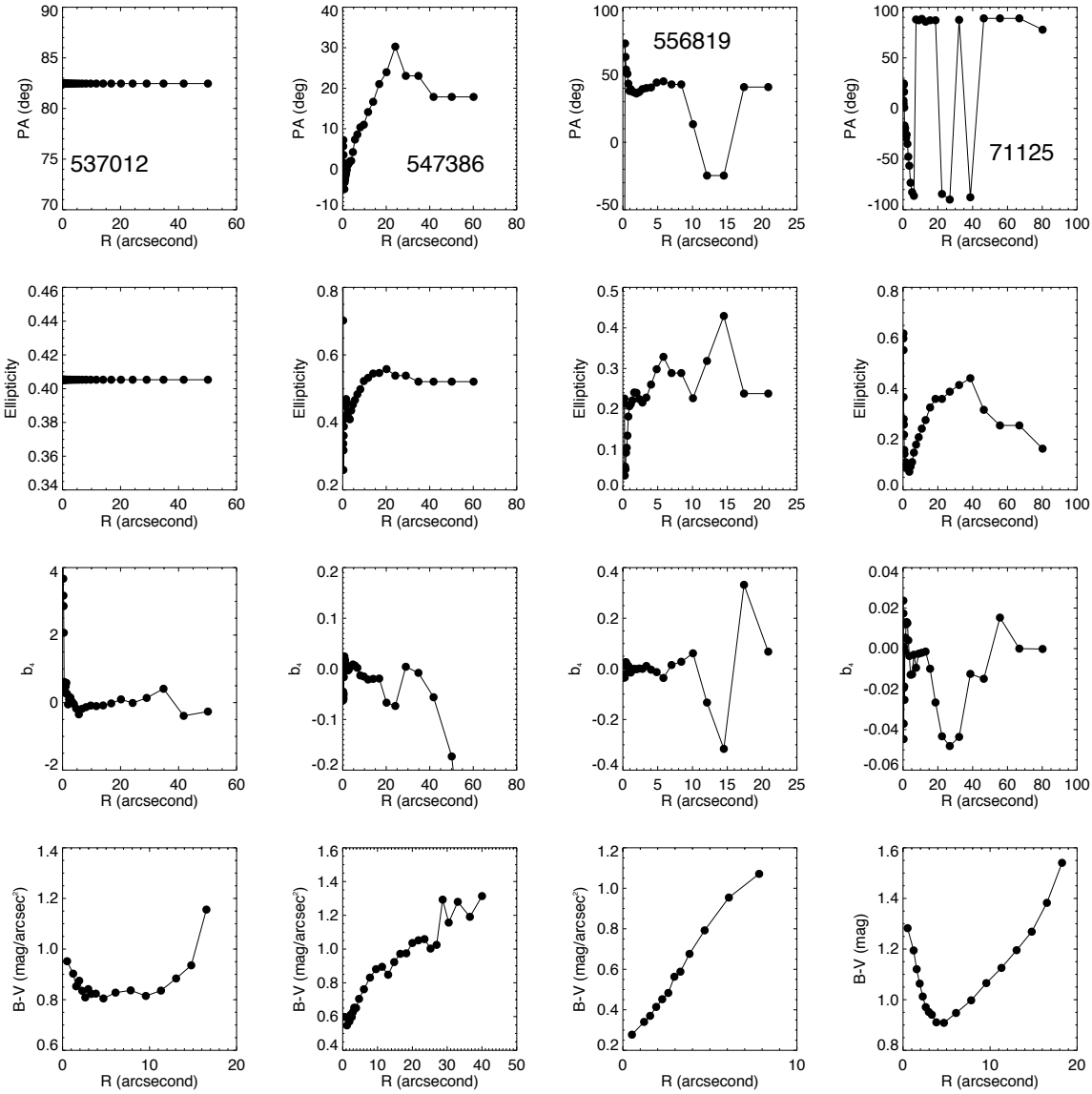

Figure 4.21 continued

Table 4.7 contains the isophotal data for the last radial point fit in the ellipse-fitting procedure. Some of the IEGs (348427, 383210, 547386 and 71125) show strong PA twists. The majority of IEG have relatively constant PA values. The measure of boxy/diskiness, b_4, varied among the isolated galaxies. Five (5/24, 21%) of the IEGs were found to have negative b_4 values over most of their radii. Diskiness was detected in slightly more IEGs, with eight (8/24, 33%) having positive values for a large portion of their radial extent. The remaining IEGs had $\sim b_4 = 0.0$ or had mixed values of boxiness and diskiness that averaged to near 0.0. The IEGs with boxy structure had overall weak boxiness, while the disky IEGs had very large positive b_4 values, indicating strong disks.

As seen in Figure 4.21, six galaxies (IEGs 121923, 182356, 248883, 369001, 375, and 469932) have B−V profiles that follow the general trend of color becoming bluer at larger radii (Michard 2000). IEG 248883, as was previously discussed has a red core surrounded by a blue region of star formation that may have been triggered by a merger event. In a review of dwarf galaxies by Hodge (1971), it was noted that the color profiles of some dwarf galaxies are blue to the center and become redder with radius. A recent discussion of a SDSS detected dwarf galaxy, IC 225 (Gu et al. 2007), also noted a blue core surrounded by a redder envelope. Twelve (12/22, 54%) of the IEGs with B & V data have reverse colors reminiscent of the IC 225 color profile. IEGs 348427 and 537012 have color profiles that remain nearly constant. Finally, IEGs 414559 and 71125 have color profiles that decrease over the first 4 arcseconds

and then increase to redder values. These two IEGs are very different, IEG 71125 is a larger red galaxy that closely resembles a normal elliptical, while IEG 414559 is a blue galaxy whose best-fit effective radii and surface brightness are the smallest of the IEG sample.

4.6.5 Notes on Individual Galaxies

IEG 375. – At a distance of 46.8 Mpc, IEG 375 has an absolute V band magnitude of -17.2 and a global color of $(B-V)_0 = 0.61$. The galaxy has some extended diffuse structure and slight extension to the SW. The residual image shows what appears to be a bright fan to the NW. The light profiles are not perfectly fit by an $R^{1/4}$ law, with the outer radii being underluminous for the de Vaucouleurs law. The profiles have disk-like shape, suggesting that IEG 375 may be an S0. The position angle undergoes a severe twist of nearly 80 degrees. The b_4 parameter remains close to zero for all but a few radial points. The galaxy color remains fairly constant over much of the galaxy and eventually becomes bluer at large radii. The blue color and fan feature in the residual image may be evidence that IEG 375 has accreted a small gaseous satellite.

IEG 71125. – One of the redder IEGs with $(B-V)_0 = 0.86$, and brightest galaxies of the sample, $M_V^0 = -18.8$, IEG 71125 has the appearance of a typical elliptical. The residual highlights a probable bar oriented perpendicular to the galaxy's elongation. The surface brightness in the V band is linear when plotted against $R^{1/4}$ and well fit by the de Vaucouleurs law. Radially the galaxy has a wildly changing PA, shifting

more than 100 degrees. Negative b_4 values at intermediate radii may indicate an embedded disk.The color profile, mentioned in the previous section, gets bluer until a radius of 4 arcseconds when it becomes significantly more red. Data from the 2MASS (Cutri et al. 2003) All-sky survey in the H, J, and K bands for the IEGs can be found in Table 4.8. IEG 71125 has an H−K value of 0.31, above the H−K = 0.26 value found to separate S0 and Sa galaxies. IEG 71125 and the other sample galaxies are more similar to dwarf galaxies than brighter Sa galaxies. It is unclear if any separation of contaminating galaxies can be made for intermediate-luminosity galaxies and dwarf galaxies using the H−K method.

IEG 114366. – Similar to IEG 71125, IEG 114366 has a bar-like feature perpendicular to the galaxy semi-major axis. Located 44 Mpc away, the galaxy has relatively blue colors, 0.69, and the sample's average brightness, $M_V^0 = -17.3$. The PA remains nearly constant, while the galaxy becomes more disky with larger radius. The B−V profile is reversed from the typical E galaxy, however the galaxy does follow the profile of some dwarf galaxies, such as IC 225 (Gu et al. 2007). For the increasingly disky nature of the galaxy, the optical light profiles in BVR are all fit by an $R^{1/4}$ law. It should be noted that many S0 galaxies are fit by an $R^{1/4}$ law, even though they possess a disk.

IEG 121923. – The residual shows some overly bright regions in the core to the SE. The bright region doesn't have the morphology of a fan and may simply be a star forming region at the galaxy center. The galaxy has $M_V^0 = -17.6$ with a

surface brightness profile that is brighter than an $R^{1/4}$ fit for the inner radii and underluminous for the outer regions. Both the position angle and the ellipticity are constant for all radii, while the color profile follows the common trend of a typical elliptical. The infrared color was determined to be H−K = 0.39.

IEG 122985. – The galaxy at a redshift of z = 0.000165 is one of the brighter IEGs, $M_V^0 = -18.4$. No global color or color profile was calculated as the galaxy was not observed in the B band. The H−K infrared color is the largest of the IEGs at H−K = 1.56. The body of IEG 122985 is well fit by the de Vaucouleurs profile, with deviations at the innermost and outermost radii. All of the radial parameters are constant across the galaxy. The residual image is one of the more unusual in the sample as there appears to be an inner disk. Another interpretation is that the bright regions in the residual are two distinct cores that have yet to fully merge.

IEG 182356. – Previously described as the next stage of evolution of a merging group of dwarf galaxies, similar to the system found by Fanelli et al. (2007). The galaxy has two obvious cores, seen in both the V band image and the residual. Other than the bright cores, the residuals show no additional features. The surface brightness profiles in V and B bands are both linear in $R^{1/4}$, suggesting that any merger occurred long ago and IEG 182356 has dynamically settled. The galaxy shows no boxy/disky structures. The color profile becomes bluer with radius but is not smooth. A significant peak is seen in the profile at a radius of 7 arcseconds, roughly the position of the second core.

IEG 229036. – The blue, $(B-V)_0 = 0.66$, galaxy at a distance of 65.4 Mpc has an integrated brightness of $M_V^0 = -16.9$. Infrared color from the 2MASS survey was found to be H−K = 1.28. The color profile shows a reversed gradient, while the b_4 profile suggests a disky morphology. The residual, as was previously mentioned, may have a fan feature that implies the galaxy may have suffered a merger with another spheroidal galaxy. The fan in IEG 229036 is not as broad or bright as in IEGs 375 and 248883, which complicates the interpreatation of the feature. The surface brightness profile supports the disky morphology found by the b_4 parameter. The galaxy light follows more of a bulge+disk profile than an $R^{1/4}$ law.

IEG 248883. – The galaxy has a prominent fan-like feature seen clearly in the residual image. As was previously posited, IEG 248883 may have merged with a gas-rich spheroidal companion that caused the fan and the galaxy's blue color. Otherwise, the galaxy is bright for the sample, −18.9, and exhibits a red global color. The radial variation of V band light is not fit by a de Vaucouleurs model, with intermediate radii being overluminous. The galaxy displays diskiness in the inner regions. The color profile remains nearly constant at $(B-V)_0 \sim 0.8$ for much of the inner radii before becoming increasingly blue. IEG 248883 has an H−K color at the S0-Sa separation value, 0.26.

IEG 261992. – Near the edge of our searched region of the SDSS at 71.8 Mpc, IEG 261992 is bright, $M_V^0 = -18.5$, and blue, $(B-V)_0 = 0.58$. A galaxy, not interacting with the IEG, can be seen to the SW. While the galaxy to the SW was masked out

before analysis was performed, some of the light may have caused contamination. The residual image shows a bar-like structure similar to that seen in other IEGs. The V and R band surface brightness profiles are well fit by a de Vaucouleurs model, while the B band data is poorly fit. The color profile displays reverse color gradients and the b_4 data indicates the galaxy has a disky nature.

IEG 348427. – The surface brightness profile of the galaxy is linear when plotted versus $R^{1/4}$ for all three bandpasses. The position angle is observed to vary at all radii, while there appears to be no disk or box-like features. The galaxy color profile is approximately constant at 0.57. IEG 348427 has an optical brightness of -17.5 in the V band and the residual has a weak bar-like structure. The infrared color of the galaxy was determined to be 0.31.

IEG 369001. – The reddest galaxy in the sample, $(B-V)_0 = 0.91$, IEG 369001 has features associated with a typical elliptical. Still an intermediate-luminosity system at $M_V^0 = -18.0$, the galaxy has odd structures in the residual image. A bright ridge on the NW side of the galaxy can be seen. The ridge does not correspond to any noticeable structures, but could be an offset bar, given that many other IEGs display probable bars. The radial parameters display a slight PA twist as well as a weak disk in the inner regions. The color profile is approximately constant before becoming bluer beyond 7 arcseconds. The galaxy's surface brightness profiles are easily fit with a de Vaucouleurs model. The galaxy displays an infrared color, H−K, slightly above the S0-Sa separator value, similar to many of the IEGs.

IEG 383210. – Another of the IEGs that resemble a typical elliptical, IEG 383210 is bright, $M_V^0 = -18.5$, and red $(B-V)_0 = 0.89$. The light profiles are all very well fit by an $R^{1/4}$ law, furthering the similarities with a normal elliptical. The galaxy displays a bar-like feature, which seems to be common for the IEG sample. While the galaxy has no disky or boxy features, the PA twists by more than 50 degrees. The (B−V) profile remains constant near 1.0 before becoming redder at larger readii.

IEG 391175. – At 56 Mpc, the galaxy is one of the fainter and bluer ($(B-V)_0 = 0.51$) of the sample. A de Vaucouleurs model fits the B band light profile, however the V band is only fit for the inner radii. The outer radii in the V band are underluminous compared to the $R^{1/4}$ law. Predominantly negative b_4 values describe a likely disk structure. The residual reveals what may be a disk. The feature could also be interpreted as a bar, but unlike the other IEGs with bar-like features, IEG 391175 has the bar oriented along the semi-major axis and not perpendicular to it.

IEG 414559. – Similar to IEG 369001, IEG 414559 has a residual image that shows an increased brightness on one side of the core and a brightness depression on the opposite side. The galaxy's surface brightness profile are all well fit by the $R^{1/4}$ law. Slight diskiness is seen near the core and both the PA and ellipticity are nearly constant. As mentioned in earlier sections, IEG 414559 has a color profile like that of IEG 71125, first becoming blue than suddenly reddening. The global H−K color is 0.27.

IEG 416078. – The brightest sample galaxy detailed here, $M_V^0 = -19.2$, the galaxy is also one of the most blue, $(B-V)_0 = 0.49$. The IR color was determined to be 0.41. The radial surface brightness variation can be fit in the BVR bands with an $R^{1/4}$ profile. Displayed in the residual image is a bright region to the North that doesn't appear as a fan or offset bar. The nature of the bright region remains unknown. Fairly constant radial parameters are detected with little features, while the color profile shows an inverse gradient.

IEG 421880. – The faintest IEG, $M_V^0 = -14.8$, has a luminosity that is similar to dwarf galaxies. The galaxy is absent of structure in the residual image. Contradicting the lack of underlying structures, the b_4 parameter indicates the galaxy is very strongly disky, with $b_4 \geq 0.1$.The color profile remains constant at 0.5 for the first 4 arcseconds before rising to redder values. The inner-most regions are fit by the de Vaucouleurs model, with the V band data having excess light at the outermost radii.

IEG 468256. – With a faint optical brightness of $M_V^0 = -16.7$, IEG 468256 has the sample average color, 0.65. Like IEG 421880, IEG 468256 displays a featureless residual. The $R^{1/4}$ law describes the light profiles of IEG 468256 very well. The inner regions have boxy structures and the outer radii display perfectly elliptical isophotes. The B−V profile is observed to sharply rise to the red.

IEG 469932. – The galaxy has features previously discussed that could be spiral arms or tidal tails. While a bright IEG with $M_V^0 = -18.3$, the galaxy has the bluest color of $(B-V)_0 = 0.40$. The extreme color, falling far below the average value of a typical

elliptical, could be due to merger induced star formation. If in fact the galaxy has spiral arms, the blue color would be expected. The residual image highlights the arm features and a bright knot near the galaxy center. The surface brightness profiles are not fit with the de Vaucouleurs law, but instead have bulge+disk morphology. Diskiness in the galaxy is reinforced by the b_4 parameter, which remains positive across much of the galaxy. The color profile becomes only slightly bluer with radius, indicating a nearly uniform color for the entire galaxy.

IEG 496820. – Residing 38.0 Mpc away, the galaxy was observed only in the B band, yielding $M_B^0 = -15.8$. No color profile was calculated. The optical brightness profile is not well fit by an elliptical profile, instead showing a weak bulge+disk morphology. The residual map is mostly devoid of structure with the exception of two bright spots along the galaxy semi-major axis. The two spots don't appear to be distinct nuclei. The galaxy has strong disky features as indicated by the b_4 radial plot. The high degree of diskiness and the bright residual spots suggest that IEG 496820 harbors an inner disk.

IEG 499372. – The IEG at redshift, z = 0.000193, is well fit in all three bandpasses with an $R^{1/4}$ law. The galaxy features an optical brightness below the sample average and color of the average IEG, $M_V^0 = -16.8$ and $(B-V)_0 = 0.64$, respectively. A 15% degree twist is observed in the position angle and the ellipticity changes for all radii. The color profile displays an inverse color gradient. Finally, the residual map features

an overly bright core region that is difficult to interpret. The global IR color is given as H−K = 0.65.

IEG 507455. – The residual image offers a unique feature not seen in other IEGs. The core of the galaxy has what appears to be a prominent disk. B band residual images (not shown) clearly display a disk. Evidence that the disk is real can be found in the b_4 data, where values remain positive for much of the radii. The color profile has an inverse gradient, but also has structure that may be due to the inner disk. The V band light profile displays a slight S0 type profile. IEG 507455 was determined to have an IR color of 0.38, close to many other candidate galaxies.

IEG 537012. – The galaxy has an intermediate-luminosity, $M_V^0 = -16.3$, and a color falling slightly bluer than the range found for typical ellipticals, $(B-V)_0 = 0.80$. The light profile are fit only moderately by an $R^{1/4}$ law. The light of IEG 537012 are overluminous at intermediate radii when compared to the de Vaucouleurs profile. The variation of color with radius is nearly constant at 0.81 and the other radial parameters show no significant variations. The residual map has a bright region in the core of the galaxy. The region doesn't appear to be a bar or a fan and clearly does not resemble a set of distinct cores. The global IR color of IEG 537012 is given as, H−K = 0.80.

IEG 547386. – The surface brightness profiles of the galaxy are all fit with an $R^{1/4}$ law. The global color is very blue, $(B-V)_0 = 0.54$, while the global IR color is H−K = 0.56. The bright, $M_V^0 = -17.9$ galaxy has a residual that displays a bar-like structure

perpendicular to the galaxy semi-major axis. The PA is observed to twist by ~ 35 degrees and the b_4 profile reveals slightly boxy isophotes. The reverse color gradients seen in many of the other IEGs is also present in IEG 547386.

IEG 556819. – The blue IEG has surface brightness profiles poorly fit by a de Vaucouleurs model. The light profiles appear to be more S0-like than elliptical-like. No significant boxy or disky values were detected in the b_4 profile. The color profile of IEG 556819 features a reversed gradient. The residual map is largely absent of any structure other than a bright region surrounding the galaxy center. It is possible that the bright "ring" in the residual is the disk being seen in the light profile. IEG 556819 displays one of the reddest IR colors with a value of H−K = 0.97.

4.7 Discussion

4.7.1 Why So Many Faint Blue Galaxies?

The number of IEGs with colors more blue than the typical elliptical (17/22, 77%) is unusual when compared to previous samples of isolated early-type galaxies. A direct comparison of the IEG sample to other samples may not be possible because no other compilations of intermediate-luminosity IEGs have been made. The detection of isolated early-type galaxies with blue colors is not unprecedented. In the study of Marcum et al. (2004), nearly 50% of the isolated ellipticals analyzed had blue colors. A re-analysis of the KIG galaxies (Sulentic et al. 2006) by the AMIGA

project found a small population of early-type KIGs to have magnitudes as faint as the IEGs described here. The KIG average M_B is -19.6, three magnitudes brighter than the IEG average of -16.8.

If the blue colors found in the IEG sample are the result of recent mergers, then other merger/interaction signatures have since faded. As mentioned in earlier sections, the merger signatures around lower mass, intermediate-luminosity galaxies may last for only a fraction of the lifetime those features would have around larger ellipticals. The steady and slow accretion of gas would partially explain the blue colors and lack of merger signatures. An extensive study of the neutral hydrogen in the vicinities of the IEGs is needed to better understand the nature of the sample of isolated early-type galaxies and detect any reservoirs of gas.

In a study of ellipticals in compact groups, Zepf, Whitmore, & Levison (1991) had expected a large number of blue ellipticals due to the increased merger rate in higher density environments. They found that only $\sim$7% of compact group ellipticals have blue colors. Of importance to the IEGs, Zepf, Whitmore & Levison noted that the fainter ellipticals had a higher likelihood of having blue colors, similar to the results of Burstein et al. (1987). The fainter luminosity of the sample was somewhat expected as work by Tovmassian et al. (2004) pointed out that the absolute magnitudes of group E+S0s were 0.75 magnitudes brighter than field early-type galaxies. The blue galaxies in the IEG sample are all significantly less luminous than those in the Zepf and Burstein samples.

One question that needs to be addressed is, what change could be made to the isolation and selection criteria that would result in more luminous and redder galaxies? One major limit imposed was the 72 Mpc redshift edge. The limit was made to ensure that companion galaxies with $M_V = -16.5$ would have been observed by the SDSS as part of the spectroscopic survey. The edge limit could be extended if we imposed a magnitude difference between the candidate IEG and any companion galaxy. For example if we had used a 2 magnitude difference, we would have been able to detect an IEG ($M_V = -20.0$) with a neighboring galaxy as bright as $M_V \geq -18.0$. The IEG in the scenario would not have made our candidate list as its companion would have failed our -16.5 dwarf magnitude limit. The use of a magnitude difference, standard for many of the isolated galaxy samples described in earlier sections, may have allowed for the detection of fossil groups and much brighter IEGs.

4.7.2 Clue to the Evolutionary History of the IEGs

The average M_B value for the IEGs is -16.8, which is three magnitudes more dim than the isolated galaxies studied by Aars et al. (2001) and at least four magnitudes fainter than the average fossil group (Mulchaey & Zabludoff 1999; Vikhlinin et al. 1999). Based on integrated luminosity, the IEGs are a different class of galaxies than fossil groups and may not be the remains of major mergers.

While the IEGs are not compact group remnants, they may be a lower mass extension of the same phenomena. Based on the merging group of dwarfs galaxies

noted by Fanelli et al. (2007) and the apparent evolutionary connection between IEG 182356 and MDG1, a number of the IEGs may be the remains of a group of dwarf galaxies. The dwarf group scenario is unique and has not yet been explored by other researchers. The detection of a group of dwarf galaxies poses a number of challenges, such as the extensive telescope time required to detect a very faint set of galaxies. The properties of MDG1, IEG 182356, and any other probable dwarf group remnants will be studied to better understand the properties expected from a merged dwarf group. Comparing the properties to those of the many compact groups and fossil group galaxies could result a deeper understanding of galaxy and group formation mechanisms.

The disky nature of 33% of the sample should have been expected as disky ellipticals were found to have fainter luminosities than boxy or normal ellipticals (Lauer et al. 2005). Observations of some IEGs at X-ray wavelengths are being proposed. It is possible that no X-ray emission will be detected for the faint and disky galaxies, as Lauer et al. also noted a lack of radio and X-ray emission for disky, faint ellipticals.

Of the remaining sample galaxies, IEGs 375, 229036, and 248883 are the galaxies most likely to have undergone a merger. All three galaxies have what appears to be a fan in their residual maps that may reveal past mergers with a spheroidal system. IEG 248883 is more luminous than the other two IEGs by 1.6 and 1.9 magnitudes. Similar luminosities and colors are observed for IEGs 375 and 229036. IEG 248883 is different, because the fan is associated with a blue star forming region surrounding

the otherwise red galaxy. The blue region only partially affects the global color, as IEG 248883 has a relatively red color at $(B-V)_0 = 0.84$.

The multitude of reversed color gradients may be one of the more important formation clues. More than half of the IEGs have reversed color profiles that, along with the intermediate-luminosities and blue colors, stand as defining trends. Further analysis of these three commonalities may be the key to unlocking the formation histories of the IEG galaxies.

The IEGs 71125, 369001, 383210, and 537012 have the red colors and lack of merger and interaction signatures that suggest they may be a set of galaxies that have remained free from perturbations for much of their lifetimes. IEGs 71125, 369001 and 383210, are the most likely pristine isolated early-type galaxies in the sample. These three galaxies might serve as the near-zero interaction baseline necessary to understand the properties intrinsic to all early-type galaxies and those properties caused by external interactions.

4.8 Conclusions

A BVR imaging study has been performed on 24 isolated early-type galaxies selected using the spectroscopic survey of the Sloan Digital Sky Survey. Structural and optical brightness profiles, integrated photometry, and residual imaging were performed and provided the following conclusions:

- Integrated photometry reveals that the sample is abnormally faint. The IEGs are 2–3 magnitudes fainter than the average brightness found in previous studies of isolated early-type galaxies.

- The sample displays an unusually large fraction of blue early-type galaxies. The blue colors indicate that the sample galaxies have undergone a recent star formation event. Lack of merger signatures, beyond the enhanced star formation, suggests that the IEGs may be accreting clouds of low-mass neutral gas.

- Three sample galaxies, IEGs 71125, 369001, and 383210 are strong primordial isolated early-type galaxy candidates. These galaxies may have passively evolved and remained free from large-scale interactions for much of their lifetimes.

- Residual and radial analysis reveals that the sample is lacking in merger and interaction signatures other than the enhanced star formation.

- The IEG sample falls below the Kormendy relation, which may suggest that low- and intermediate-luminosity early-type galaxies are not described by the Fundamental Plane.

- IEG 182356 appears to have been formed via the coalescence of a group of dwarf galaxies. Deep optical imaging reveals the galaxy to have to cores and an extended halo of diffuse light. Formation via the merger of a group of dwarf galaxies may represent the low mass and low luminosity end of the fossil group

mass function and may be the dominant formation mechanism for intermediate-luminosity early-type galaxies.

Table 4.1. IEG Sample Dynamical Properties

IEG	α	δ	size	radial velocity	Distance	M_V	B−V
(1)	(2)	(3)	(4)	(5)	(6)	(7)	(8)
375	09:44:10.9	+00:10:47.11	13.5	3503.0	46.8	−17.4	0.74
4177	10:42:55.43	−00:08:25.08	10.3	2537.3	33.9	−16.0	0.75
27750	13:24:26.63	−03:28:22.68	13.5	2810.1	37.6	−16.1	0.75
51108	03:06:52.41	−00:47:40.14	60.1	3400.2	45.5	−20.8	0.90
71125	02:42:48.69	−08: 23:56.63	19.6	4513.6	60.4	−18.6	0.88
114366	15:53:25.18	+52:04:16.50	18.3	3288.0	44.0	−17.2	0.79
121923	21:06:35.38	−05:40:58.77	8.1	5364.0	74.0	−17.3	0.76
122985	21:27:53.52	−07:01:13.92	21.9	3698.4	49.5	−18.5	0.68
166582	14:52:42.14	+61:34:02.71	12.2	3176.8	42.5	−15.9	0.70
171890	22:13:19.49	−09:35:46.32	15.0	5293.0	70.9	−16.7	0.63
182356	23:50:21.44	+14:13:42.56	12.6	5323.1	71.3	−16.9	0.97
229036	12:19:47.35	+51:39:05.67	9.9	4885.8	65.4	−17.2	0.72
248883	13:27:18.56	+59:30:10.25	24.0	5135.9	68.8	−19.0	0.95
261992	23:40:42.68	−09:23:36.59	12.4	5359.1	71.8	−18.4	0.69
348427	14:35:38.00	+43:59:37.10	10.1	5322.0	73.6	−17.3	0.79
369001	15:03:15.54	+37:45:58.07	13.8	2740.2	36.6	−17.9	0.90
383210	09:11:05.57	+09:20:58.40	15.0	3848.9	51.5	−18.4	0.94

Table 4.1 (continued)

IEG	α	δ	size	radial velocity	Distance	M_V	B−V
(1)	(2)	(3)	(4)	(5)	(6)	(7)	(8)
391175	10:48:07.05	+43:05:25.47	9.3	4184.3	56.0	−16.5	0.65
414559	10:21:45.89	+38:32:49.79	9.4	4436.6	59.4	−17.6	0.65
416078	10:38:37.24	+44:31:23.08	42.1	3879.3	51.9	−19.0	0.56
421880	11:32:37.43	+47:26:58.65	19.1	1454.0	19.4	−14.6	0.52
468256	07:43:06.83	+44:01:47.59	7.8	5292.4	70.9	−16.4	0.74
469932	09:26:57.99	+10:03:01.36	17.6	5316.0	73.5	−18.4	0.43
496820	16:16:22.68	+34:54:05.18	7.5	2877.4	38.0	−16.1	0.65
499372	16:51:15.43	+26:43:30.61	8.8	4361.0	58.0	−16.8	0.73
507455	11:10:29.61	+13:45:58.13	11.7	4510.6	60.0	−17.3	0.65
537012	09:31:27.40	+32:03:40.11	11.9	2632.2	35.0	−16.2	0.85
547386	11:35:23.86	+31:39:15.15	20.7	3584.2	48.0	−17.6	0.68

Table 4.1 (continued)

IEG	α	δ	size	radial velocity	Distance	M_V	B−V
(1)	(2)	(3)	(4)	(5)	(6)	(7)	(8)
556819	12:21:23.12	+39:36:59.47	10.0	4661.8	62.0	−16.5	0.62
557287	13:23:37.69	+29:17:17.08	11.0	4247.0	56.8	−16.2	0.61
557849	13:36:20.08	+38:06:53.60	11.1	5347.2	72.0	−17.1	0.71
558496	12:57:55.19	+33:33:53.12	10.4	5238.3	70.0	−16.7	0.72
570457	09:13:55.47	+24:45:52.36	11.6	5043.5	68.0	−17.5	0.75

Note. — Col. (1): IEG number. Col. (2) and (3): SDSS right ascension and declination. Col. (4): Galaxy size calculated at the V- or gri-band r_{25} radius, in units of arcseconds. Col. (5): Radial velocity calculated from the SDSS redshift, in km s^{-1}. Col. (6): Distance, in Mpc, calculated from Col. (5) and $H_0 = 72$ km s^{-1} Mpc^{-1}. Col. (7): Absolute V magnitude calculated from Col. (6) and apparent magnitude derived from integrated photometry. Col. (8): B − V color calculated from integrated photometry.

Table 4.2. SDSS Filter Parameters

Filter	Wavelength	Magnitude Limit
(1)	(2)	(3)
u	3351	22.0
g	4686	22.2
r	6165	22.2
i	7481	21.3
z	8931	20.5

Note. — Col. (1): SDSS filter name. Col. (2) Effective wavelength of the bandpass, in Å. (3): Limiting magnitude for photometric detection as calculated by SDSS.

Table 4.3. Observing Log For Broadband Imaging

IEG	Date	Seeing			# coadd frames?		
		B	V	R	B	V	R
(1)	(2)	(3)	(4)	(5)	(6)	(7)	(8)
375	12/2006, 3/2007	1.9	1.5	1.5	5×600	3×600	3×600
71125	10/2006	1.4	1.8	3×900	4×900	—	
114366	3/2007	1.3	1.6	1.4	3×600	3×600	3×600
121923	10/2006	2.7	1.4	—	3×900	3×900	—
122985	10/2006	—	2.0	2.0	—	3×900	3×300
182356	10/2006, 12/2006	2.8	1.8	—	3×900	3×900	—
229036	3/2007	1.1	1.5	0.70	3×600	3×600	3×600
248883	2/2007	1.8	1.4	1.5	4×600	3×600	3×600
261992	10/2006, 12/2006	1.9	2.4	2.4	4×900	4×900	3×300
348427	3/2007, 3/2008	2.8	2.7	1.4	3×600	3×600	6×600
369001	2/2007	1.7	1.5	1.9	3×600	3×600	6×600
383210	10/2006, 12/2006	1.8	1.9	2.2	8×900	7×900	3×900
391175	3/2007	1.3	1.4	1.6	3×600	3×600	3×600
414559	10/2006, 2/2007, 3/2007	2.5	2.8	1.5	4×900	5×900	5×600
416078	2/2007, 3/2007	1.4	2.8	2.0	3×600	3×900	3×600
421880	3/2008	2.6	1.9	—	3×600	3×600	—

Table 4.3 (continued)

IEG	Date	Seeing			# coadd frames?		
		B	V	R	B	V	R
(1)	(2)	(3)	(4)	(5)	(6)	(7)	(8)
468256	2/2007	1.7	1.9	2.2	3×600	3×600	3×600
469932	2/2007	2.8	2.8	2.8	3×600	3×600	3×900
496820	3/2007, 3/2008	1.6	—	—	3×400	—	—
499372	3/2007	1.2	1.4	1.5	3×600	3×600	4×600
507455	3/2007	1.3	1.1	1.5	6×600	6×600	7×600
537012	12/2006, 3/2007	1.9	1.6	1.9	4×900	4×900	3×600
547386	3/2007	1.3	1.2	1.4	3×600	3×600	3×600
556819	3/2008, 3/2008	1.4	1.5	—	3×600	3×600	—

Note. — Col. 1: IEG name. Col. 2: Date(s) of observations. Col. 3–5: Average seeing in B, V, R bands, units of arcseconds. Col. 6–8: Number of frames that went into the final coadded image.

Table 4.4. Limiting Magnitudes and Surface Brightnesses of McDonald Imagery

IEG	m_B	μ_B	m_V	μ_V	m_R	μ_R
(1)	(2)	(3)	(4)	(5)	(6)	(7)
375	19.36	27.69	19.37	27.29	19.10	26.55
71125	19.52	27.69	17.92	27.36	—	—
114366	19.46	27.73	19.08	27.61	18.72	26.47
121923	20.33	27.16	18.84	28.76	—	—
122985	—	—	19.11	26.72	18.75	25.38
182356	19.64	26.69	19.53	26.68	—	—
229036	20.22	27.83	19.32	27.46	18.92	26.51
248883	19.58	26.68	19.37	27.32	18.08	26.95
261992	19.81	27.75	19.39	26.82	18.53	24.99
348427	19.89	28.33	20.14	27.52	18.91	27.26
369001	18.48	28.15	17.36	27.53	16.78	27.51
383210	17.96	27.29	18.40	26.38	17.63	27.89
391175	19.81	28.02	19.74	27.54	19.34	26.71
414559	19.44	26.33	19.28	26.30	18.30	26.82
416078	18.63	27.50	18.38	27.66	17.45	26.84
421880	18.94	27.18	20.45	27.44	—	—
468256	19.93	26.01	20.02	26.10	19.41	25.76

Table 4.4 (continued)

IEG	m_B	μ_B	m_V	μ_V	m_R	μ_R
(1)	(2)	(3)	(4)	(5)	(6)	(7)
469332	19.65	26.93	20.08	26.60	19.49	26.69
496820	19.58	27.61	—	—	—	—
499372	19.56	27.68	19.69	26.93	19.04	26.49
507455	19.87	27.85	19.08	26.71	18.57	27.18
537012	19.66	27.11	19.44	26.83	17.87	26.21
547386	19.37	27.57	18.74	27.38	18.37	26.77
556819	19.98	26.84	19.74	27.45	—	—

Note. — Col. (1): Galaxy name. Col. (2): Limiting B magnitudes. Col. (3): Limiting B surface brightness. Col. (4): Limiting V magnitudes. Col. (5): Limiting V surface brightness. Col. (6): Limiting R magnitudes. Col. (7): Limiting R surface brightness. Limiting values were determined assuming a signal-to-noise ratio of 5 over an aperture area of 3 × PSF.

Table 4.5. Integrated Photometric Properties of McDonald Imagery

IEG	$M(B)_0$	$M(V)_0$	$M(R)_0$	$(B-V)_0$	$(V-R)_0$	Corrections			
(1)	(2)	(3)	(4)	(5)	(6)	(7)	(8)	(9)	(10)
375	−16.6	−17.2	−18.1	0.61	0.92	0.60	0.46	0.37	0.139
71125	−17.9	−18.8	—	0.86	—	0.10	0.08	0.06	0.02
114366	−16.6	−17.3	−18.2	0.69	0.87	0.05	0.04	0.03	0.01
121923	−16.9	−17.6	—	0.73	—	0.43	0.33	0.27	0.10
122985	—	−18.4	−18.8	—	0.71	0.42	0.32	0.26	0.10
182356	−16.8	−17.4	—	0.55	—	0.16	0.12	0.10	0.04
229036	−16.3	−16.9	−17.8	0.66	0.82	0.11	0.08	0.07	0.03
248883	−18.1	−18.9	−19.6	0.84	0.68	0.08	0.07	0.05	0.02
261992	−17.9	−18.5	−19.3	0.58	0.83	0.13	0.10	0.08	0.03
348427	−16.8	−17.5	−18.3	0.61	0.83	0.08	0.06	0.05	0.02
369001	−17.1	−18.0	−18.9	0.91	0.93	0.07	0.05	0.04	0.02
383210	−17.6	−18.5	−19.4	0.89	0.96	0.31	0.24	0.20	0.07
391175	−15.9	−16.4	−17.2	0.51	0.82	0.06	0.04	0.04	0.01
414559	−17.2	−17.8	−18.5	0.57	0.78	0.08	0.06	0.05	0.02
416078	−18.7	−19.2	−19.9	0.49	0.91	0.06	0.05	0.04	0.01
421880	−14.3	−14.8	—	0.54	—	0.08	0.06	0.05	0.02
468256	−16.0	−16.7	−17.5	0.65	0.86	0.15	0.12	0.09	0.04

Table 4.5 (continued)

IEG	$M(B)_0$	$M(V)_0$	$M(R)_0$	$(B-V)_0$	$(V-R)_0$	Corrections			
(1)	(2)	(3)	(4)	(5)	(6)	(7)	(8)	(9)	(10)
469932	−17.9	−18.3	−19.0	0.40	0.76	0.14	0.11	0.09	0.03
496820	−15.8	—	—	—	—	0.09	0.07	0.06	0.02
499372	−16.2	−16.8	−17.6	0.64	0.85	0.39	0.31	0.25	0.09
507455	−16.9	−17.5	−18.3	0.63	0.78	0.08	0.06	0.05	0.02
537012	−15.5	−16.3	−17.3	0.80	0.83	0.09	0.07	0.05	0.02
547386	−17.3	−17.9	−18.6	0.54	0.76	0.10	0.08	0.07	0.02
556819	−16.1	−16.7	—	0.60	—	0.10	0.08	0.06	0.02

Note. — Col. (1): IEG number. Col. (2): Absolute B band magnitude. (3): Absolute V band magnitude. Col. (4): Absolute R band magnitude. Col. (5): B−V color in magnitudes. Col. (6): V−R color in magnitudes. Col. (7)-(10): B-, V-, R-band extinction corrections and color excess, respectively. All magnitudes were calculated from integrated photometry and a bootstrap calibration from the SDSS g & r magnitudes of Smith et al. (2002). All colors and luminosities have been corrected for extinction. Extinctions and color excess were calculated from Galactic extinctions calculated from Schlegel et al. (1998).

Table 4.6. Bulge/Disk Deconvolution

		Bulge component		Disk component		
Name	Filter	R_e	μ_e	R_d	μ_0	B/T
(1)	(2)	(3)	(4)	(5)	(6)	(7)
375	B	19.4 (4.4)	26.9	2.2 (0.5)	21.3	0.584
	V	17.9 (4.1)	26.1	2.2 (0.5)	20.4	0.557
	R	19.7 (4.5)	25.3	2.6 (0.6)	19.7	0.560
71125	B	9.8 (2.9)	24.4	2.0 (0.6)	19.9	0.565
	V	5.0 (1.5)	21.7	1.3 (0.4)	19.9	0.914
114366	B	8.1 (1.7)	23.9	2.3 (0.5)	20.9	0.730
	V	12.8 (2.7)	24.1	2.3 (0.5)	20.5	0.803
	R	12.7 (2.7)	23.4	2.9 (0.6)	19.6	0.688
121923	B	15.6 (5.6)	27.0	1.9 (0.7)	21.7	0.656
	V	7.9 (2.8)	24.7	1.5 (0.5)	19.9	0.551
122985	V	11.6 (2.8)	23.5	4.3 (1.0)	20.6	0.640
	R	18.5 (4.4)	23.9	3.9 (0.9)	19.7	0.633
182356	B	12.1 (4.2)	25.4	7.0 (2.4)	25.4	0.912
	V	19.6 (6.8)	25.9	2.7 (0.9)	21.6	0.765
229036	B	10.9 (3.5)	26.7	1.5 (0.5)	20.6	0.423
	V	13.1 (4.2)	25.5	1.5 (0.5)	19.6	0.559

Table 4.6 (continued)

		Bulge component		Disk component		
Name	Filter	R_e	μ_e	R_d	μ_0	B/T
(1)	(2)	(3)	(4)	(5)	(6)	(7)
	R	18.7 (5.9)	26.5	1.8 (0.6)	19.4	0.364
248883	B	16.8 (5.6)	24.9	4.3 (1.4)	23.9	0.956
	V	19.5 (6.5)	24.6	5.4 (1.8)	21.8	0.788
	R	19.1 (6.4)	24.2	4.1 (1.4)	19.6	0.528
261992	B	2.4 (0.8)	21.5	—	—	1.00
	V	3.1 (1.1)	21.4	0.41 (0.1)	18.6	0.940
	R	1.7 (0.6)	19.8	9.1 (3.2)	22.2	0.557
348427	B	2.9 (1.0)	22.7	4.1 (1.5)	24.4	0.894
	V	2.4 (0.9)	21.8	3.8 (1.4)	22.7	0.764
	R	6.6 (2.4)	23.1	1.8 (0.6)	20.5	0.816
369001	B	2.3 (0.4)	21.4	2.4 (0.4)	20.4	0.572
	V	1.6 (0.3)	20.4	2.4 (0.4)	18.9	0.296
	R	1.4 (0.2)	18.9	2.5 (0.4)	18.1	0.346
383210	B	2.4 (0.6)	21.3	2.7 (0.7)	23.0	0.931
	V	2.5 (0.6)	20.4	8.3 (2.1)	26.6	0.990
	R	6.0 (1.5)	21.7	1.2 (0.3)	17.8	0.707

Table 4.6 (continued)

		Bulge component		Disk component		
Name	Filter	R_e	μ_e	R_d	μ_0	B/T
(1)	(2)	(3)	(4)	(5)	(6)	(7)
391175	B	12.6 (3.4)	26.7	1.4 (0.4)	20.5	0.506
	V	14.4 (3.9)	26.0	1.4 (0.4)	20.3	0.631
	R	5.0 (1.4)	23.8	1.7 (0.5)	20.7	0.653
414559	B	0.29 (0.09)	16.5	2.2 (0.6)	20.9	0.789
	V	0.12 (0.03)	12.3	2.7 (0.8)	21.0	0.953
	R	1.6 (0.5)	19.6	1.5 (0.4)	19.2	0.724
416078	B	16.0 (4.0)	23.5	2.6 (0.7)	19.2	0.728
	V	12.8 (3.2)	22.2	2.0 (0.5)	19.1	0.887
	R	16.7 (4.2)	22.1	2.5 (0.6)	18.5	0.858
421880	B	11.1 (1.0)	25.4	1.3 (0.1)	20.2	0.679
	V	18.1 (1.7)	25.6	0.84 (0.08)	24.8	0.999
468256	B	0.31 (0.1)	18.9	1.6 (0.5)	21.4	0.554
	V	3.5 (1.2)	23.1	—	—	1.00
	R	0.15 (0.06)	14.9	2.6 (0.9)	20.7	0.724
469932	B	17.8 (6.3)	26.4	3.2 (1.1)	17.6	0.507
	V	10.8 (3.8)	24.9	3.3 (1.2)	20.9	0.469

Table 4.6 (continued)

		Bulge component		Disk component		
Name	Filter	R_e	μ_e	R_d	μ_0	B/T
(1)	(2)	(3)	(4)	(5)	(6)	(7)
	R	19.7 (7.0)	25.9	3.4 (1.2)	20.1	0.350
496820	B	19.0 (3.6)	27.5	1.4 (0.3)	20.6	0.539
499372	B	4.0 (1.1)	24.2	1.2 (0.3)	20.9	0.654
	V	5.1 (1.4)	23.0	1.3 (0.4)	19.8	0.747
	R	5.4 (1.5)	23.5	1.6 (0.4)	19.6	0.525
507455	B	3.3 (1.0)	22.8	1.8 (0.5)	20.7	0.643
	V	7.6 (2.2)	23.8	1.5 (0.4)	19.6	0.629
	R	4.2 (1.2)	21.9	1.9 (0.6)	19.2	0.608
537012	B	2.1 (0.4)	22.4	2.8 (0.5)	21.4	0.429
	V	3.5 (0.6)	22.6	2.6 (0.4)	20.6	0.507
	R	3.5 (0.6)	21.7	2.7 (0.5)	19.6	0.468
547386	B	17.6 (4.1)	24.9	1.4 (0.3)	18.9	0.694
	V	19.6 (4.6)	24.4	1.5 (0.3)	18.8	0.778
	R	16.5 (3.8)	23.3	1.5 (0.3)	18.2	0.812
556819	B	19.6 (5.9)	27.5	0.91 (0.3)	19.9	0.620
	V	17.9 (5.4)	26.3	0.86 (0.3)	20.1	0.864

Table 4.6 (continued)

		Bulge component		Disk component		
Name	Filter	R_e	μ_e	R_d	μ_0	B/T
(1)	(2)	(3)	(4)	(5)	(6)	(7)
SDSS gri Data						
4177	*gri*	1.8 (0.33)	20.2	—	—	1.00
27750	*gri*	1.5 (0.3)	19.7	—	—	1.00
51108	*gri*	7.0 (1.5)	19.1	11.0 (2.4)	19.5	0.674
166582	*gri*	0.24 (0.05)	14.5	4.3 (0.9)	21.6	0.892
171890	*gri*	9.6 (3.3)	24.5	2.9 (1.0)	20.3	0.463
557287	*gri*	0.25 (0.07)	14.9	11.1 (3.1)	23.6	0.840
557849	*gri*	1.2 (0.4)	19.4	—	—	1.00
558496	*gri*	1.8 (0.6)	20.8	—	—	1.00
570457	*gri*	—	—	—	—	—

Note. — Col. (1): IEG name. Col. (2): Filter. Col. (3): Effective radius, in units of arcsec (kiloparsec in parenthesis). Col. (4): Effective surface brightness, calibrated using the SDSS magnitudes, in mag arcsec^{-2}. Col. (5): Scale length of the disk component, in units of arcsec (kiloparsec in parenthesis). Col. (6): Central surface brightness of the disk, calibrated using the SDSS magnitudes, in mag arcsec^{-2}. Col. (7): Bulge-to-Total ratio derived from best fit R$^{1/4}$ profile.

Table 4.7. Best-Fit Radial Parameters of the IEG Sample

IEG	ellipticity	position angle	b_4 shape	a_4/a shape
(1)	(2)	(3)	(4)	(5)
McDonald Observatory Data				
375	0.40	29.0	0.0	0.0
71125	0.15	77.2	0.001	0.0
114366	0.46	17.3	-0.15	0.002
121923	0.38	18.45	0.79	0.15
122985	0.53	51.2	0.0	0.0
182356	0.41	80.0	0.05	0.0
229036	0.36	3.20	0.36	0.0
248883	0.09	-87.0	0.0	0.0
261992	0.66	1.0	0.0	0.0
348427	0.28	0.0	0.22	0.0
369001	0.19	-11.1	-0.28	0.0
383210	0.06	50.0	0.01	-0.004
391175	0.386	21.0	-0.20	0.003
414559	0.19	46.0	-0.10	0.0
416078	0.75	-60.0	0.0	0.0
421880	0.24	67.0	-0.10	0.0
468256	0.14	-38.5	-0.05	0.0

Table 4.7 (continued)

IEG	ellipticity	position angle	b_4 shape	a_4/a shape
(1)	(2)	(3)	(4)	(5)
469932	0.39	-37.0	0.0	0.1
496820	0.20	50.5	0.0	0.0
499372	0.41	32.0	-0.16	0.01
507455	0.21	57.4	-0.55	0.02
537012	0.45	82.5	-0.20	0.0
547386	0.53	18.0	-0.18	0.0
556819	0.24	40.0	0.06	0.04
SDSS gri Data				
4177	0.61	81.0	0.19	-0.06
27750	0.053	-32.3	0.14	0.03
51108	0.46	54.0	0.0	0.0
166582	0.50	41.0	-0.01	-0.01
171890	0.05	-14.0	0.0	0.0
557287	0.36	31.0	0.0	0.0
557849	0.34	-24.0	0.0	0.0
558496	0.40	23.0	0.0	0.0
570457	0.26	-49.5	0.0	0.09

Note. — Col. (1): IEG number. Col. (2): Ellipiticity is defined by Eqn. 4.5. (3): Position angle in degrees. Col. (4): b_4 shape parameter, defined as the n = 4 sine term in equation 4.6. Col. (5): a_4 shape parameter, defined as the n = 4 cosine term in equation 4.6. The data for IEG 496820 is for the B-band.

Table 4.8. Near Infrared Data for the IEG sample

IEG	J	H	K	Alternative Names
(1)	(2)	(3)	(4)	(5)
375	14.96	14.28	14.08	SDSSJ094410.80+001047.3
4177	16.56	15.97	15.09	SDSS J104255.43-000825.0
27750	16.99	15.89	15.56	SDSS J132426.63-032822.7
51108	12.59	11.77	11.17	NGC 1211
71125	14.41	13.77	13.46	SDSS J024248.69-082356.6
114366	16.05	14.89	15.27	SDSS J155325.18+520416.5
121923	16.13	16.03	15.64	SDSS J210635.38-054058.7
122985	15.51	15.61	14.05	SDSS J212753.52-070113.9
166582	—	—	—	SDSS J145242.14+613402.7
171890	—	—	—	SDSS J221319.50-093546.3
182356	13.42	12.84	12.65	SDSS J235021.45+141342.6
229036	16.81	16.51	14.87	SDSS J121947.35+513905.7
248883	13.89	12.98	12.72	SDSS J132718.57+593010.3
261992	15.63	15.17	14.95	SDSS J234042.69-092336.6
348427	15.29	14.71	14.37	SDSS J143538.00+435937.1
369001	14.03	13.38	13.07	SDSS J150315.55+374558.1
383210	13.36	13.11	13.12	VIII Zw 40

Table 4.8 (continued)

IEG	J	H	K	Alternative Names
(1)	(2)	(3)	(4)	(5)
391175	11.69	11.07	10.92	SDSS J104807.06+430525.5
414559	15.59	14.96	14.69	SDSS J102145.89+383249.8
416078	14.43	13.85	13.44	Mrk 0150
421880	—	—	—	SDSS J113237.43+472658.7
468256	16.05	15.44	15.50	SDSS J074306.84+440147.6
469932	14.49	14.09	14.00	SDSS J092657.99+100301.4
496820	16.63	16.04	15.88	SDSS J161622.69+345405.2
499372	16.13	15.42	14.77	SDSS J165115.43+264330.6
507455	16.20	15.58	15.20	SDSS J111029.62+134558.1
537012	16.18	15.66	14.86	SDSS J093127.41+320340.1
547386	15.69	15.24	14.68	Mrk 0737
556819	16.79	16.12	15.15	SDSS J122123.13+393659.5
557287	16.43	15.94	15.57	SDSS J132337.69+291717.1
557849	16.37	15.83	14.96	SDSS J133620.08+380653.6
558496	—	—	—	SDSS J125755.20+333353.1
570457	15.86	15.07	14.79	SDSS J091355.48+244552.4

Note. — Col. (1): IEG number. Col. (2): 2MASS J-band magnitude. (3): 2MASS H-band magnitude. Col. (4): 2MASS K-band magnitude. Col. (5): Alternative Name.

Chapter 5

Spectroscopy of the IEG Sample

5.1 Introduction

In Chapters I–IV, we defined a sample of the most isolated early-type galaxies currently known to exist. These galaxies are separated from non-dwarf ($M_V \leq -16.5$) neighbors by at least 2.5 megaparsec. Isolation was confirmed through radial and redshift searches for neighboring galaxies in the Sloan Digital Sky Survey (SDSS) spectroscopic data. IEGs on the edge of the SDSS footprint were additionally searched using the NASA/IPAC Extragalactic Database (NED).

The motivation for the research is presented in Chapters I, III, and IV, and is not repeated here. A full synthesis of model spectra and a determination of the age of the stellar populations is beyond the scope of the work presented here. The objective of the current chapter is to use the spectroscopic properties of the IEGs to (1) determine the Hα derived star formation rates (SFR) and (2) estimate the metallicity of these galaxies relative to that of cluster ellipticals. The results of these analyses, as well as optical properties, are then used to develop a general evolutionary history, particularly with regard to past mergers and interactions.

The concept of stellar populations was first introduced by Baade (1944), who attempted to simplify galaxy spectra as being composed of two simple, yet distinct

populations. As it turns out, such a simplification is inadequate for describing the stellar systems within a galaxy. Stellar light in a galaxy cannot be broken down into a few populations. Star formation is a continual process, where the rate and duration of star formation episodes dictate the observed spectrum.

The enrichment of gas and the rate of star formation in early-type galaxies can be vitally important to constraining the history of a galaxy. While features such as tidal tails and shell structure can fade and disappear with time, traces of interactions and gas-rich mergers will persist in the spectrum. Analysis of spectra could verify merger origins and place limits on last major merger event (Caon et al. 1994; Mulchaey & Zabludoff 1999). The standard perception of early-type galaxies is that they are simple systems with old stellar populations formed during a single star forming event early in the galaxy's history. Assuming no major mergers or interactions inject new gas into the galaxy, the population of stars formed in the initial burst would have evolved passively with few new stars formed (Searle, Sargent, & Bagnuolo 1973; Larson 1975).

Understanding the how stellar populations and spectra are affected by a galaxy's environment would yield a powerful tool in formation and evolution scenarios. Denicolo et al. (2005) found no clear role in environment determining the stellar population histories of group and isolated early-type galaxies, however further analysis is needed. Analysis of IEG spectra can be used to create a more complete picture of the formation mechanisms. Work by Trager et al. (1998) found evidence for intermediate-

age stellar populations (between 1 and 10 Gyr) favor formation via the hierarchical build-up of smaller companions. Such a formation would result in star formation being extended over a greater time than the simple initial burst model. Contradicting Trager et al., Willis et al. (2002) have presented a sample of luminous field early-type systems with old stellar populations that have evolved passively since their formation epoch.

Numerous techniques have been developed that enable a determination of the star formation rate (SFR) of nearby galaxies. The Balmer lines, in particular Hα emission, arising from the recombination of electrons with a previously ionized Hydrogen atom, can give a measure of the instantaneous SFR. In practice, Hα luminosity is used to estimate the SFR for galaxies with redshifts up to z = 0.4. The significance of using Balmer lines is that photons carrying UV radiation are needed to ionize the Hydrogen atoms. While all stars are capable of producing UV photons, O & B stars are responsible for very strong Hα emission. The basic relation follows that the presence of Balmer emission is indicative of a young stellar population.

The largest difficulty to analyzing the emission lines of spectra comes from the determination of the effects of dust and extinction. The presence of dust in emission line galaxies is inevitable and dust can cause extreme modification the spectra of such dusty objects (Veilleux & Osterbrock 1987). Accurate extinction estimates are difficult, as the optical properties and dust distributions are poorly constrained. The

technique most widely used to correct for extinction relies on the relative strengths of the lower Hα and Hβ lines (Veilleux & Osterbrock 1987).

Another means of studying the spectra comes through the use of BPT diagrams, where the type of activity in the galaxy nucleus is quantified. Use of the line ratios, [OIII]/Hβ and [NII]/Hα, are ideal to separate AGN activity types (Baldwin, Phillips, & Terlevich 1981). BPT diagrams have been used to separate galaxies into samples of starbursting, Seyferts, and LINER systems. Seyferts, the most frequent type of active galactic nuclei have bright semi-stellar nuclei and spectra with broad emission lines (Khachikian & Weedman 1974). Seyferts of type 2 and AGN of low ionization nuclear emission line regions (LINERS) have narrow line-emission (Heckman 1980).

The metallicity of a galaxy is yet another powerful diagnostic which represents the aggregate history of its star formation, mergers, gas infall, and galactic winds. Strong metallicity diagnostics come in three categories: theoretical, empirical, and combined. The first uses theoretical artificial spectra to calibrate emission line flux ratios. Empirical methods rely on fitting functions to metallicities determined via direct methods versus strong line flux ratios, such as Pilyugin (2001). The metallicity estimates examined for the IEGs is discussed below.

The paper is organized as follows, Section 2 details the SDSS spectroscopic survey data and reduction pipeline. The common features of the IEG spectra are highlighted in Section 3. The Hα derived star formation rates are discussed in Section 4. Section 5

details the estimates of galaxy metallicity and active galactic nuclei. Finally, Section 6 and 7 present conclusions and discussion, respectively.

5.2 SDSS Data & Reduction

The Sloan Digital Sky Survey (York et al. 2000) is carrying out imaging in five photometric bands in the northern Galactic cap. Objects from the photometric survey that are classified as galaxies were then evaluated for further spectroscopic observations. Spectra were taken for two samples, the first a flux-limited sample to r-band Petrosian magnitudes of 17.77 and the second, a flux- and color-selected Luminous Red Galaxy sample extending to r = 19.5. The survey uses a dedicated 2.5 m modified Ritchey-Chretien telescope, where spectra are taken for 640 objects simultaneously.

The spectra are taken using a fiber-fed plug plate and cover the wavelength range of 3800–9200 Å. Due to the 3 arcsecond size of the fibers a practical limit of how close two adjacent fibers can be was set to 55". For any given spectral observation, a series of 15 minute exposures was carried out until the mean signal-to-noise ratio (S/N) per resolution element exceeds a threshold value.

Spectra are bias-subtracted and flat-fielded before normalization. The spectra are then flux-calibrated using a synthetic composite F8 subdwarf spectrum (Pickles 1998). A pipeline for spectroscopic data determines emission and absorption redshifts and measures a number of line parameters. Equivalent widths (EW) and continuum values are calculated for the most important emission lines. Additionally, Lick line

indices for 21 absorption-line strengths and the strength of the 4000 Å break are measured. The flux values in each calibrated emission line have units of 10^{-17} ergs s^{-1} cm^{-2}.

One issue has been noted by Kewley et al. (2005). They have suggested that if the fiber aperture covering fraction is less than 20% of the galaxy area, errors up to 40% in metallicity can be encountered. For the majority of the IEG sample, the fiber covers upwards of 50% of the galaxy.

5.3 Common Features of the IEG Spectra

There is no single feature that all of the IEGs possess. The IEG spectra run the gamut from elliptical galaxy-like with strong absorption features to starbursting emission-line spectra. The majority show emission-line features, and are consistent with active star forming galaxies.

The Balmer emission lines are very distinct and can be detected to Hγ and Hδ for most of the IEGs. In past studies, higher order Balmer lines in the range 3800–4000Å have been taken to be unambiguous evidence of intermediate age ($\sim 10^8$ yr) stellar populations (Gonzalez Delgado et al. 1999). All of the galaxies show emission at [OIII]λ4363 Å, a feature associated with nebular emission and often strong in the spectra of AGN such as Seyferts (e.g. Osterbrock & Pogge 1985; Stasinska & Szczerba 2001; Melbourne & Salzer 2002). Galaxies with early-type morphologies and evidence

of active star formation, very similar to the IEGs, have been detected by Fukugita et al. (2004).

Figure 5.1 displays the IEG spectra. Five of the IEGs (51108, 71125, 121923, 383210, 537012) have absorption lines. All of these IEGs have colors commonly associated with an old stellar population, $B - V \sim 0.9$. The red IEGs have spectra often associated with elliptical galaxies and stellar populations passively evolving. IEG 121923 is unique, as its spectrum has absorption features, yet the color is rather blue at $B - V = 0.76$. Without the ability to observe [OII] emissions, which are outside of the SDSS spectral window, the features of IEG 121923 appear consistent with E+A galaxies. The spheriodal galactic systems, E+A galaxies have absorption lines consistent with both old and young stellar populations, yet lack strong [O II] emission. These E+A characteristics are often interpreted as high levels of star formation 1–2 Gyr ago (Dressler & Gunn 1983, Newberry, Boroson, & Kirshner 1990, and Schweizer 1998).

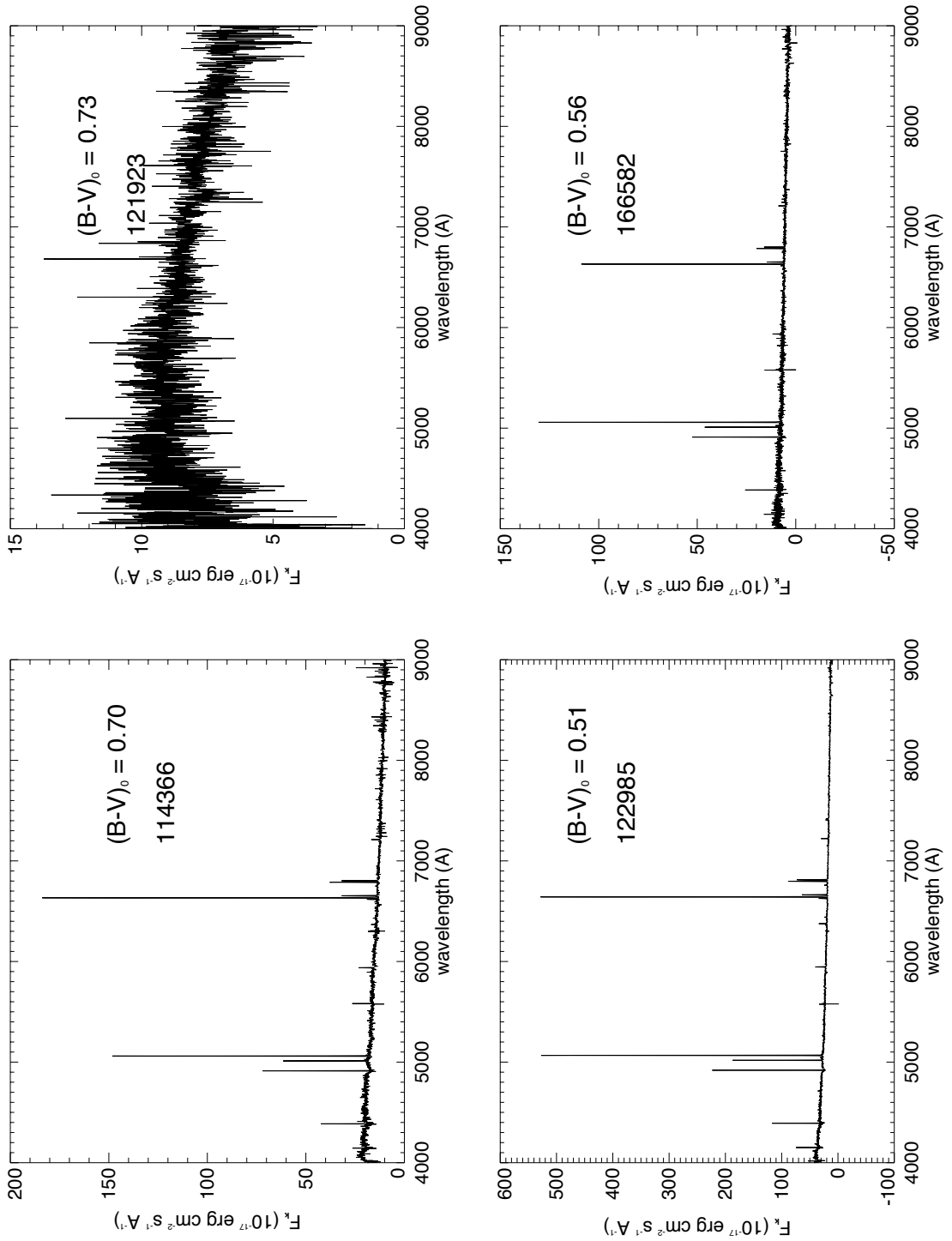

Figure 5.1: SDSS spectra for the isolated early-type galaxy sample. The $(B-V)_0$ colors of IEGs 122985 and 166582 were derived using SDSS data and Smith et al. (2002) conversions.

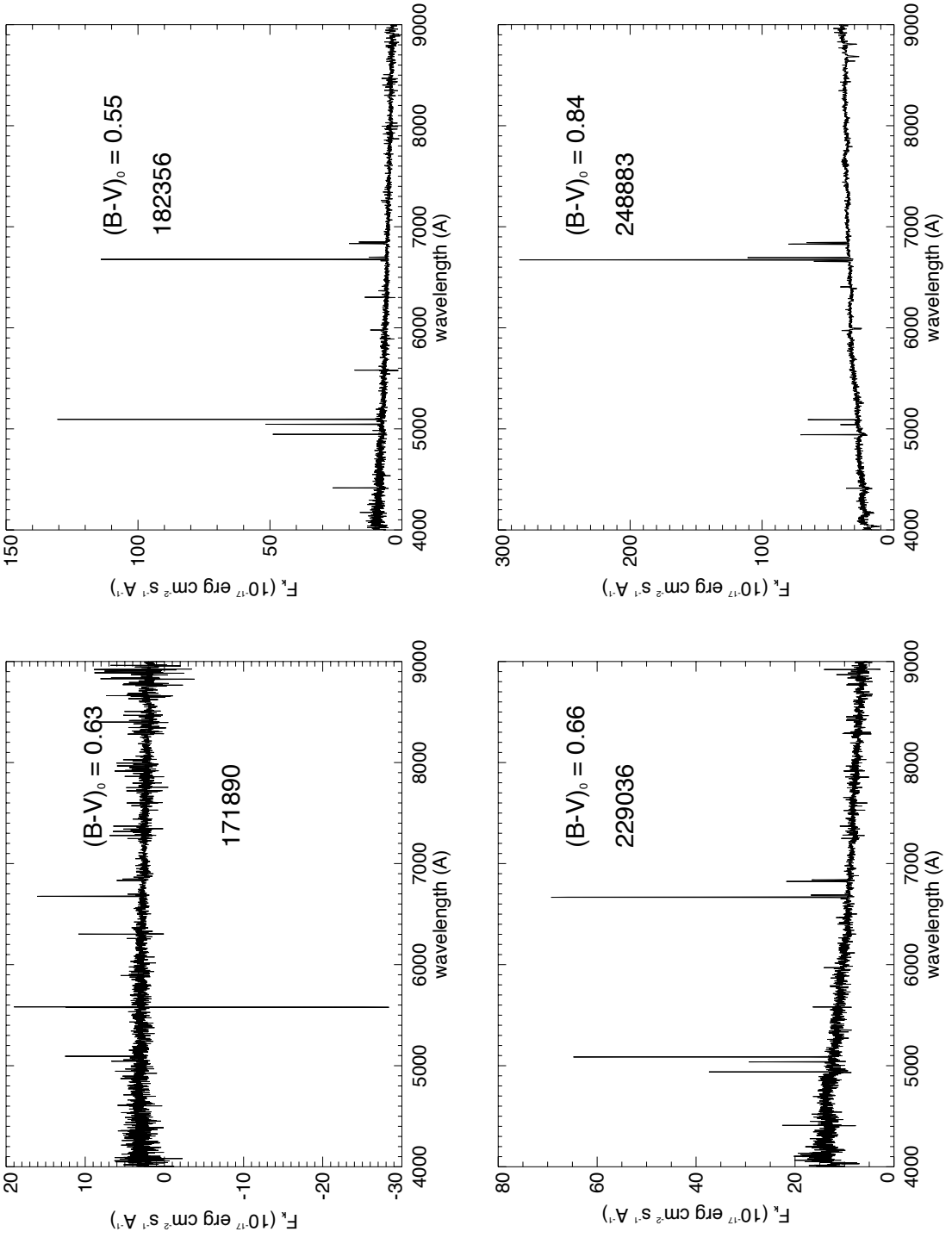

Figure 5.1 continued. The $(B-V)_0$ color of IEG 171890 was derived using SDSS data and Smith et al. (2002) conversions.

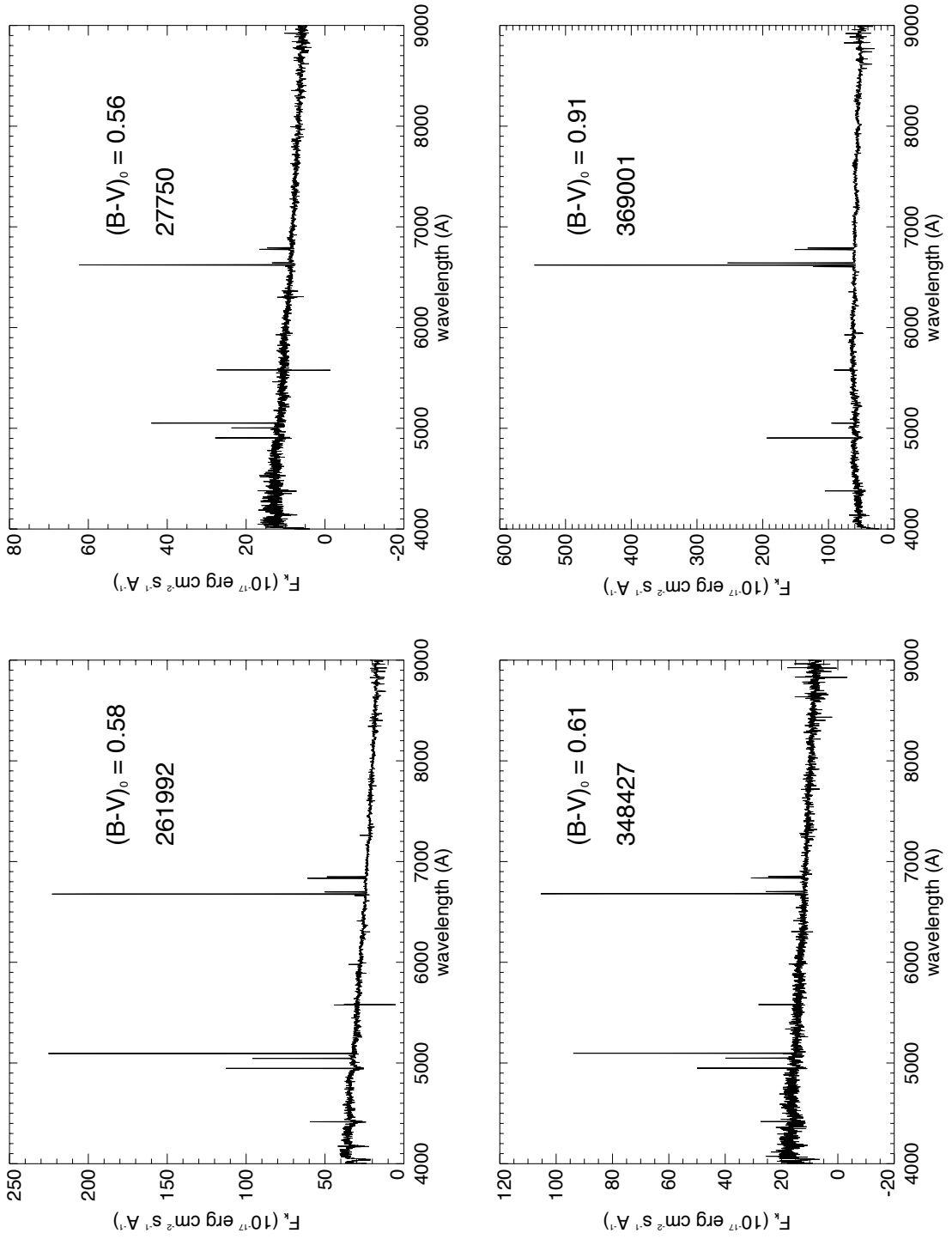

Figure 5.1 continued. The $(B-V)_0$ colors of the upper left spectrum of IEG 27750 was derived using SDSS data and Smith et al. (2002) conversions.

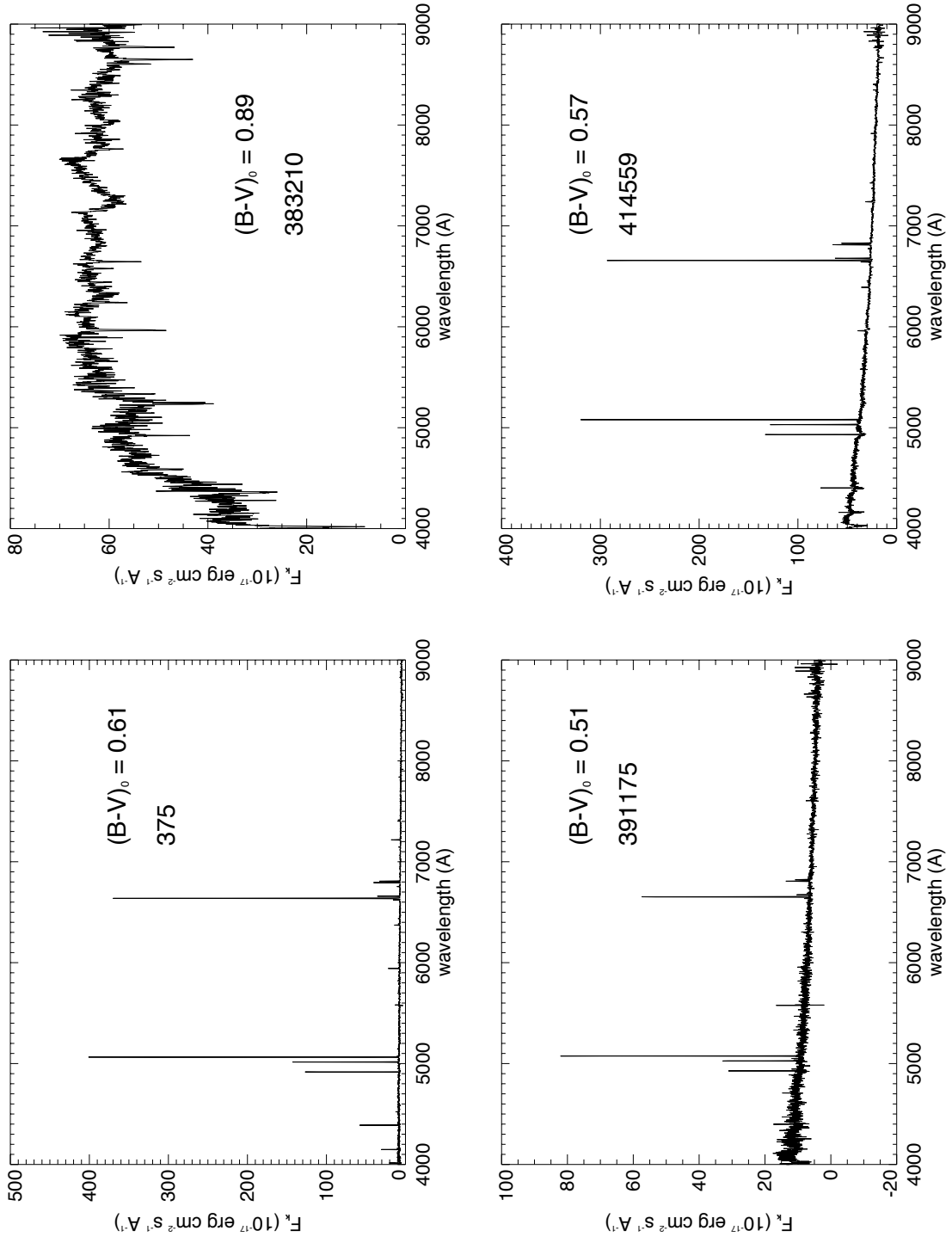

Figure 5.1 continued.

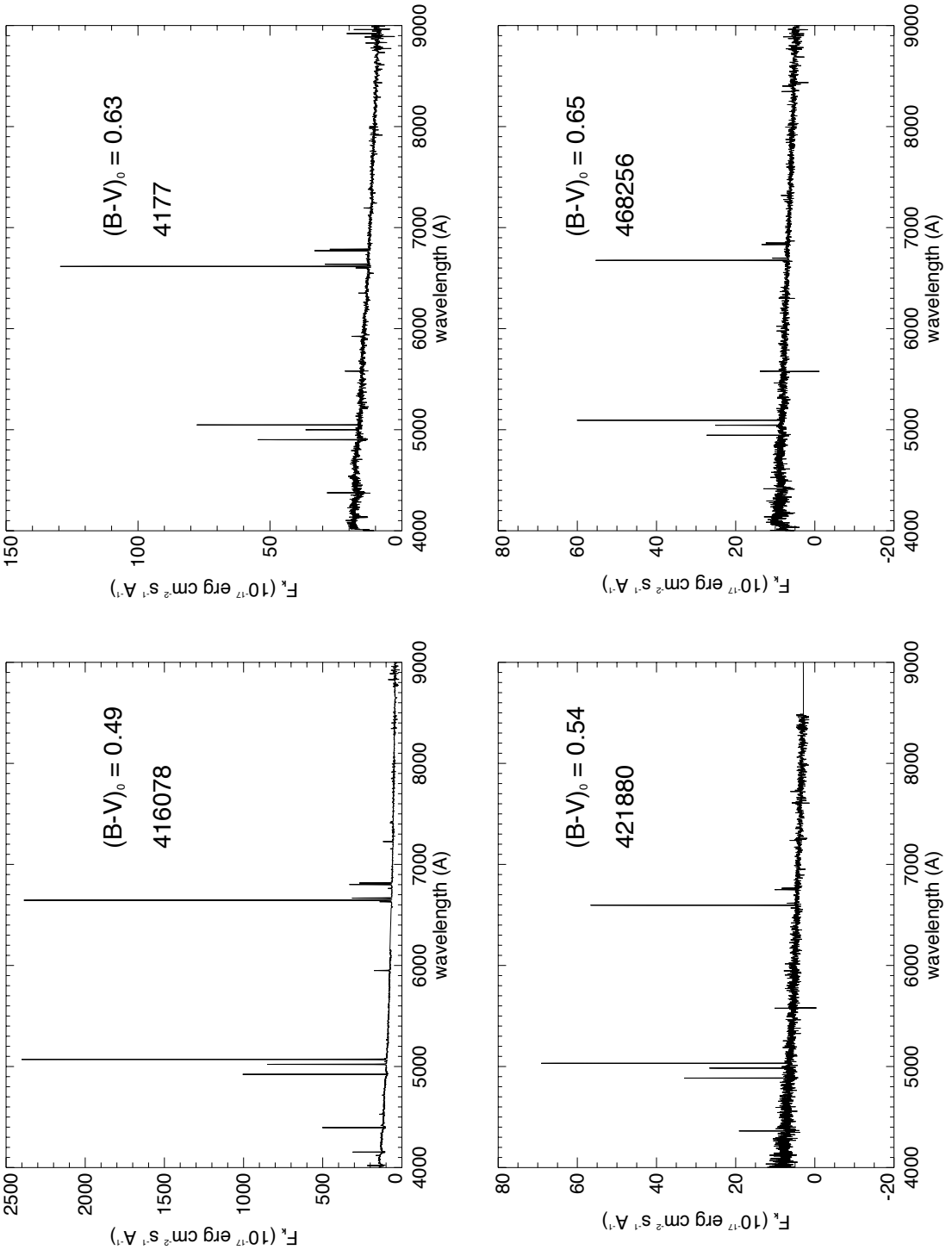

Figure 5.1 continued. The $(B-V)_0$ colors of the upper left spectrum of IEG 4177 was derived using SDSS data and Smith et al. (2002) conversions.

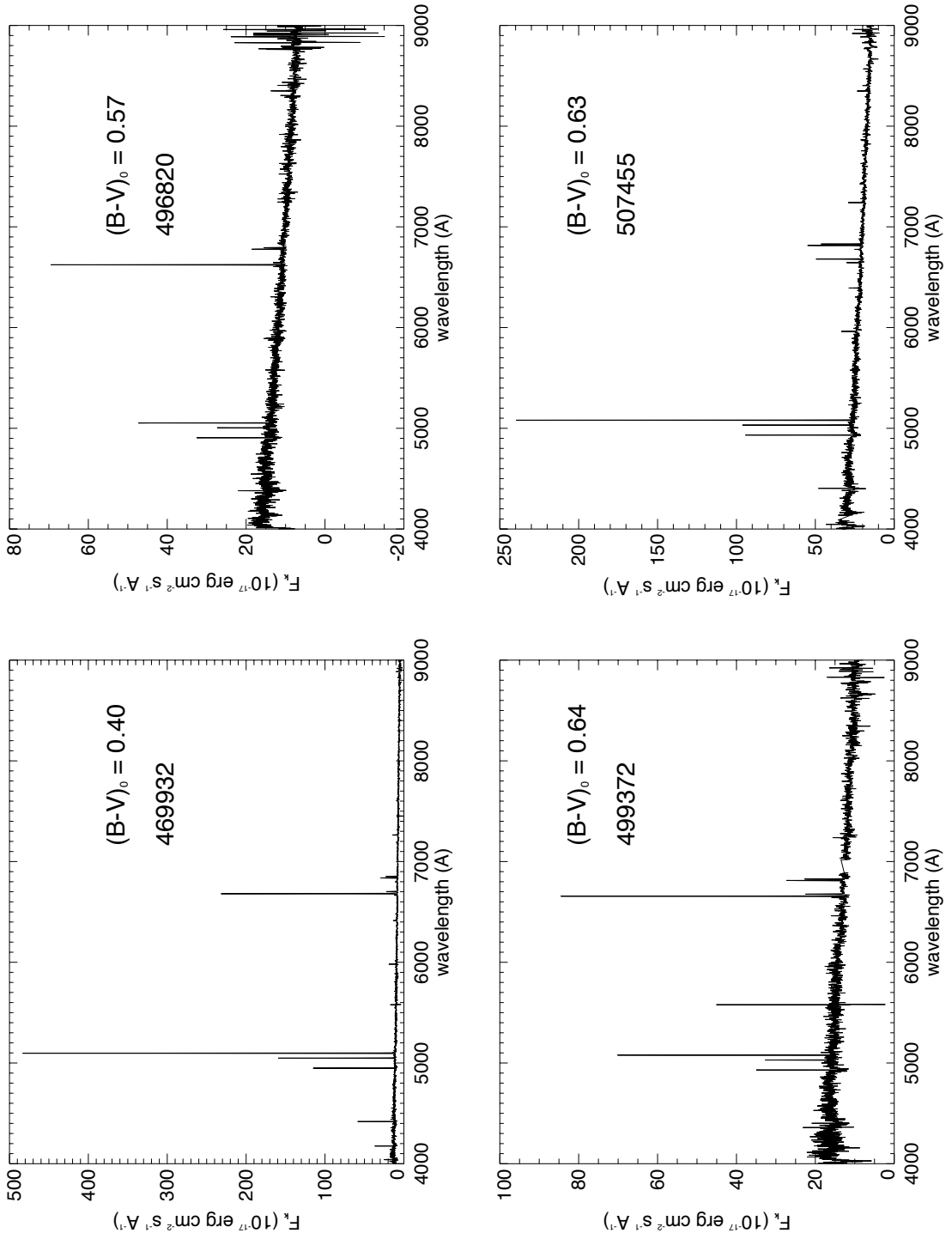

Figure 5.1 continued. The $(B-V)_0$ colors of the upper left spectrum of IEG 496820 was derived using SDSS data and Smith et al. (2002) conversions.

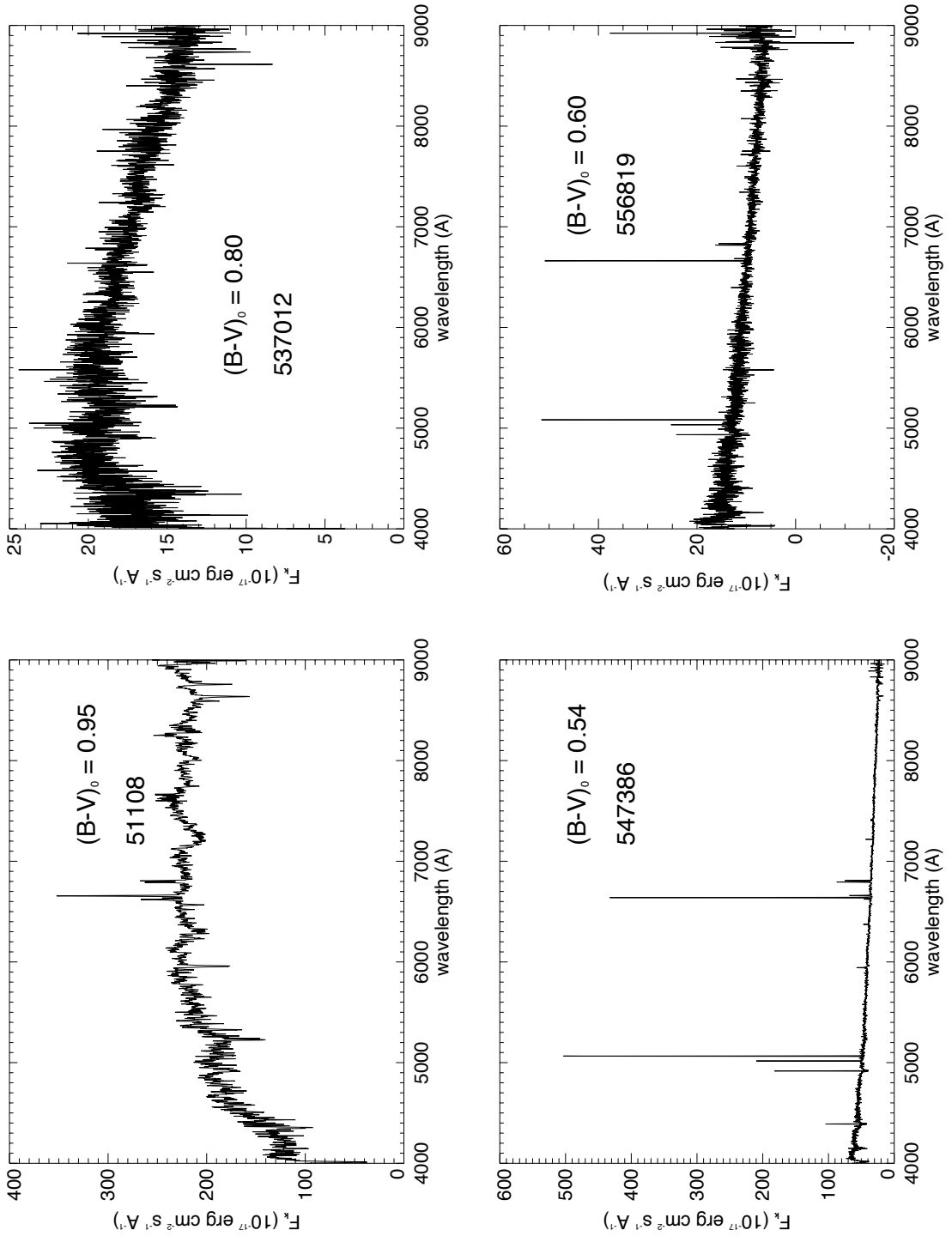

Figure 5.1 continued. The $(B-V)_0$ colors of the upper left spectrum of IEG 51108 was derived using SDSS data and Smith et al. (2002) conversions.

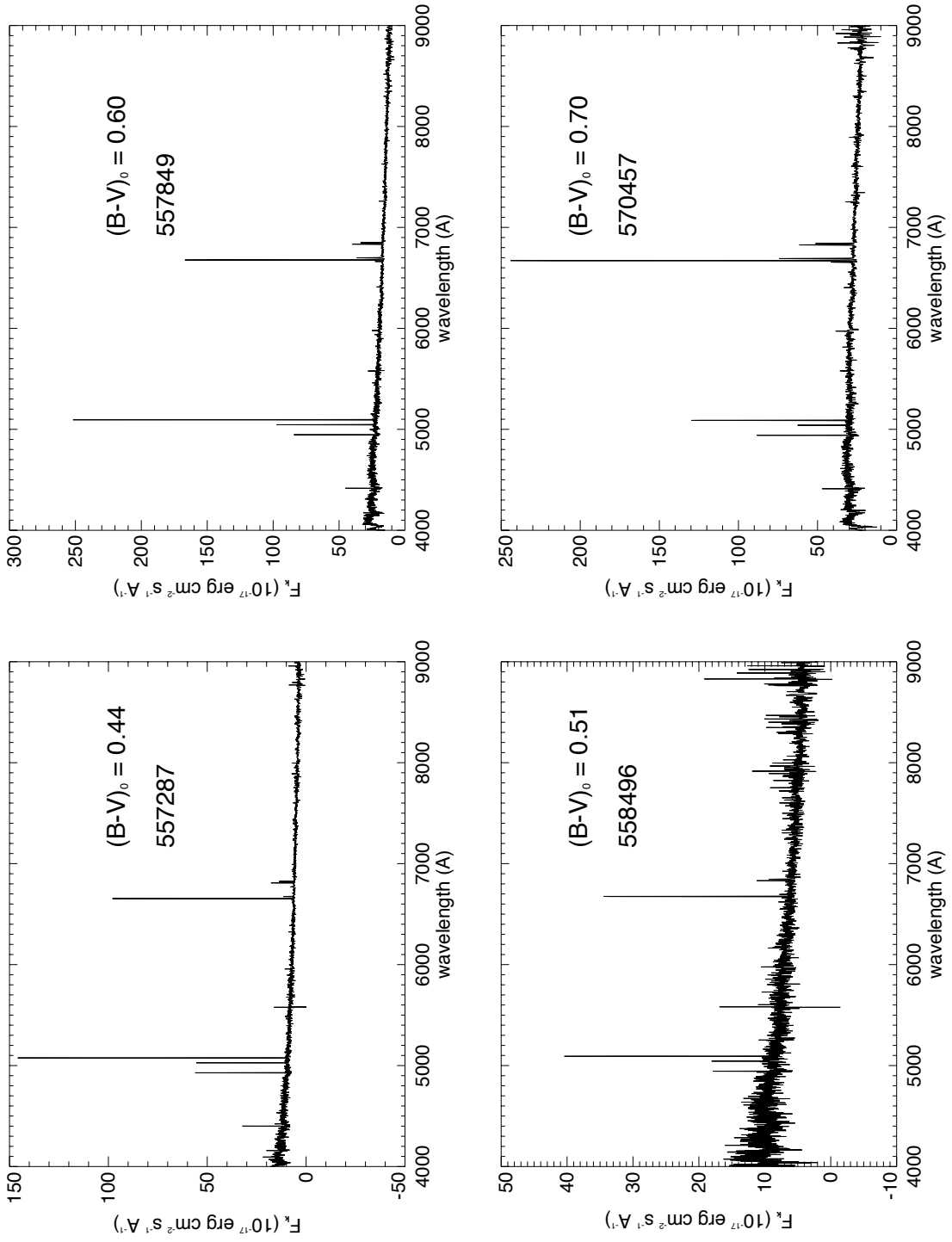

Figure 5.1 continued. The $(B-V)_0$ colors of the spectra for the above IEGs were derived using SDSS data and Smith et al. (2002) conversions.

A final IEG of note is 369001. The galaxy has a red color of 0.90 and a spectrum dominated by emission lines. The color points to an old stellar population, while the spectrum indicates more recent star formation. IEG 369001 may have undergone a recent minor merger and experienced an infusion of gas, triggering new star formation. Surprisingly, 369001 shows no optical signs of a merger.

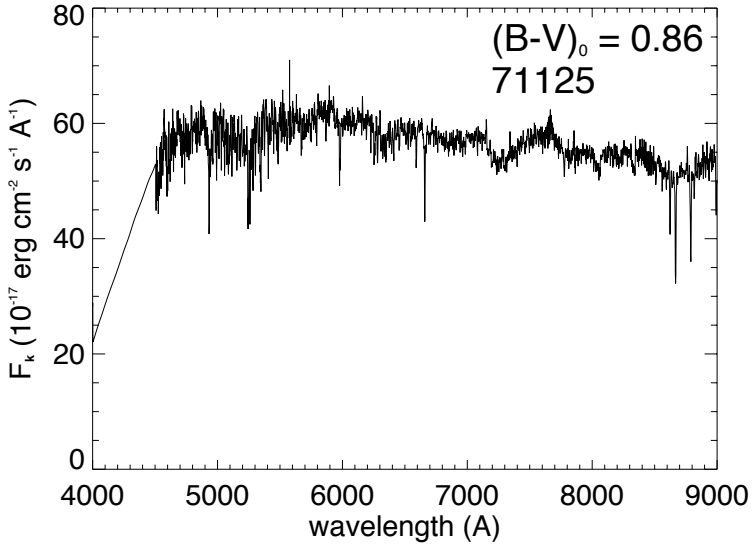

Figure 5.1 continued.

5.4 Hα Star Formation Rates

The star formation rates were calculated following commonly used procedures (Kennicutt et al. 1994; Zhao et al. 2006). A detailed discussion of the process of measuring the Hα flux, correcting for extinction, and the assumptions involved in determining the star formation rate can be found in Appendix C. The star formation

as derived by the corrected Hα flux is given by (Kennicutt 1998),

$$SFR(H\alpha) = L_{corr}^{H\alpha} \times 7.9 \times 10^{-42} \mathrm{M}_{\odot}\,\mathrm{yr}^{-1} \tag{5.1}$$

where the star formation rate is calculated in units of solar masses per year.

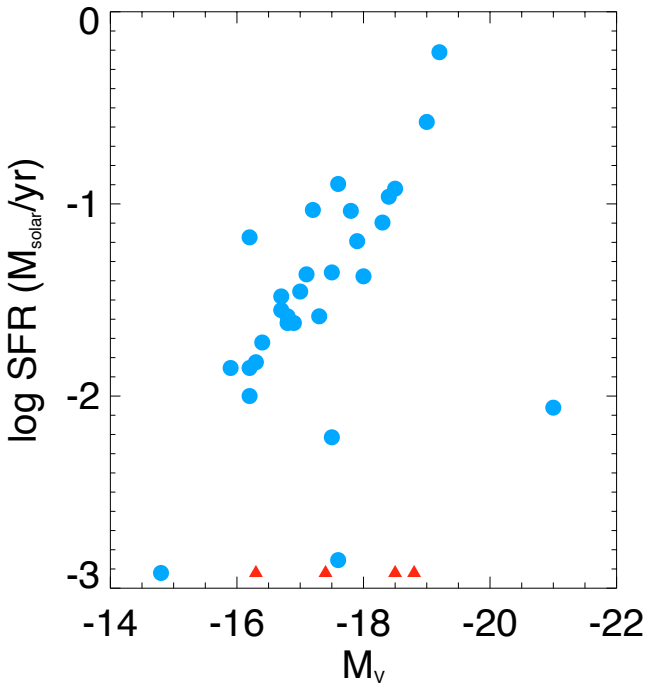

Figure 5.2: Relation between Hα derived SFRs and the optical brightness, M_V.

Table 5.1 displays the observed and corrected Hα luminosities, the extinction values and the derived star formation rates. Figure 5.2 shows the distribution of SFRs plotted against absolute V magnitude. From Figure 5.2 we can investigate whether the brightest galaxies are intrinsically luminous or are bright due to increased luminosity from the ongoing star formation.

The data in Figure 5.2 suggests that, with the exception of the IEG 51108 ($M_V = -21$), as the galaxy brightness increases, the SFR likewise increases. The observed trend may be due to the absence of sample galaxies brighter than -19. The fainter IEGs, possible dwarf galaxies, display low SFRs. Lack of new stars in these systems is expected, as dwarf ellipticals are assumed to have lost their gas and dust early in their lifetime (Mori et al. 1997). Star forming dEs are thought to be rare, however a few IEGs display SFRs near 0.1 $M_\odot$ yr^{-1}. The isolated dwarf elliptical, IC 225, may be a close relative to our sample (Gu et al. 2006). IC 225 features blue colors and a star formation rate in concordance with the many of the IEGs.

Figure 5.3 displays the log of star formation rate versus $(B - V)_0$ color. The data plotted in Fig. 5.3 can provide some insight into the duration and intensity of star formation. If the plot reveals IEGs with very low SFRs and excessively blue colors it implies global and long duration star formation. Conversely, if IEGs are detected with high levels of star formation and red colors, the implication is that those IEGs are experiencing a short term and core concentrated star formation event.

Figure 5.3, while displaying a large dispersion, reveals some features of the sample. For the complete sample, the star formation rate is low which would imply that the extreme blue colors are due to extended periods of star formation.

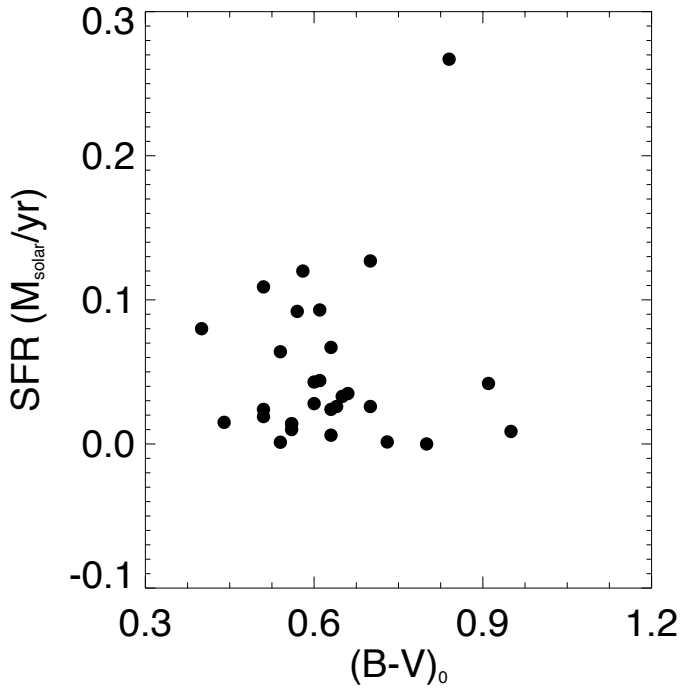

Figure 5.3: The corrected B−V color plotted against the Hα derived SFRs.

5.5 Metallicities & Active Nuclei

A number of procedures have been suggested for determining metal abundances in galaxies. The measure of metallicity in H II regions has been hailed as a powerful probe of galaxy formation and evolution (Liu et al. 2008). As metal describes all elements above hydrogen and helium, the term metallicity can taken on various meanings. A discussion of estimating abundance can be found in Appendix C. For the work presented here, metallicity is expressed as 12 + log (O/H), and the standard comparison is solar metallicity, 12 + log (O/H) = 8.66 (Allende Prieto et al. 2002; Asplund et al. 2004).

Multiple indicators using both theoretical and analytical measures of metallicity were inspected. The schemes often use ratios of emission lines located in a very small wavelength range. Two well established schemes (Zaritsky et al. 1994; Tremonti et al. 2004) were of little use due to their use of the [O II] line, which is not observed in SDSS spectra.

Metallicity was determined using analytical functions derived by Yin et al. (2007):

$$12 + \log(O/H) = 6.486 + 1.401 \log([OIII]/H\beta) \tag{5.2}$$

$$12 + \log(O/H) = 8.203 + 0.63\,(O3N2) - 0.327\,(O3N2)^2 \tag{5.3}$$

$$O3N2 = \log(([OIII]/H\beta)/([NII]/H\alpha) \tag{5.4}$$

The equations are valid for metallicities less than 9.0. The estimated metallicities for the IEG sample can be found in Table 5.2. Figure 5.4 displays the optical brightness of the IEGs versus the metallicity. Based on Figure 5.4 we can resolve whether the IEGs formed by major mergers as they would be both optically bright and likely metal-enriched. Based on the results of Chapter 4, the probability remains that the material fueling the current star formation is low-density neutral gas. The accretion of such gas is unlikely to result in bright merger signatures such as shells or tidal tails.

The metallicity of the sample shows very distinct trends, seen in Figure 5.4. The majority of the emission-line galaxies in the sample have metallicities in a very narrow range. The only possible explanations for the sharp limit to abundance are that the the sample was drawn from young galaxies that have not had time to process gas or

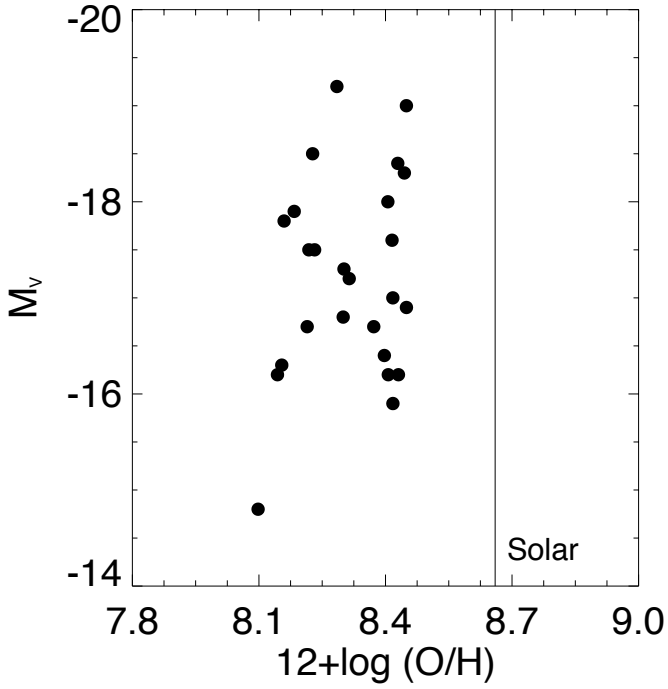

Figure 5.4: Corrected Hα star formation rates plotted against the absolute magnitudes of the isolated early-type galaxy sample.

that the IEGs have accreted nearly primordial gas, which would result in blue colors and sub-solar metallicities.

The relation between IEG $(B-V)_0$ color and galaxy metallicity is highlighted in Figure 5.5. The relation between color and metallicity will allow us to determine if the IEGs are similar to blue compact galaxies which have extremely low metallicities and blue colors. As can be seen in the figure, the IEG metallicities are sub-solar but do not reach the low abundances found in galaxies like I Zw 18 with 12 + log (O/H) = 7.2 (Searle & Sargent 1972).

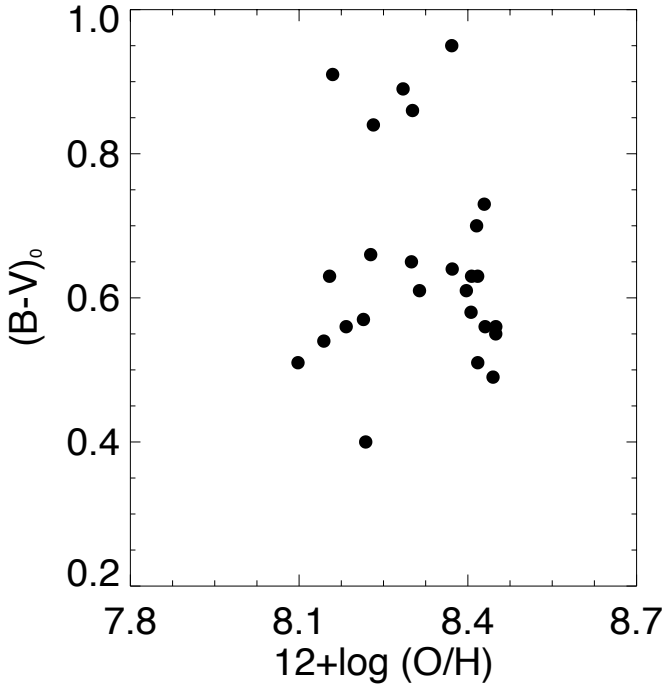

Figure 5.5: Plot of the corrected IEG colors and the extinction corrected Hα star formation rates.

In addition to calculating the IEG metallicity, an estimate of the nuclear activity can be used to create a more complete understanding of the colors and emission processes within a galaxy. The BPT diagram (Baldwin, Phillips, & Terlevich 1981) has become the mainstay of AGN study, using the [N II]/Hα and [O III]/Hβ ratios. Figure 5.6 displays the BPT diagram for the IEGs, which provides a means of determining the cause of the emission line spectra. Both star formation and an AGN can produce emission line spectra and understanding the cause of emission can help to further constrain the history of the IEGs. Lines overplotted come from Veilleux

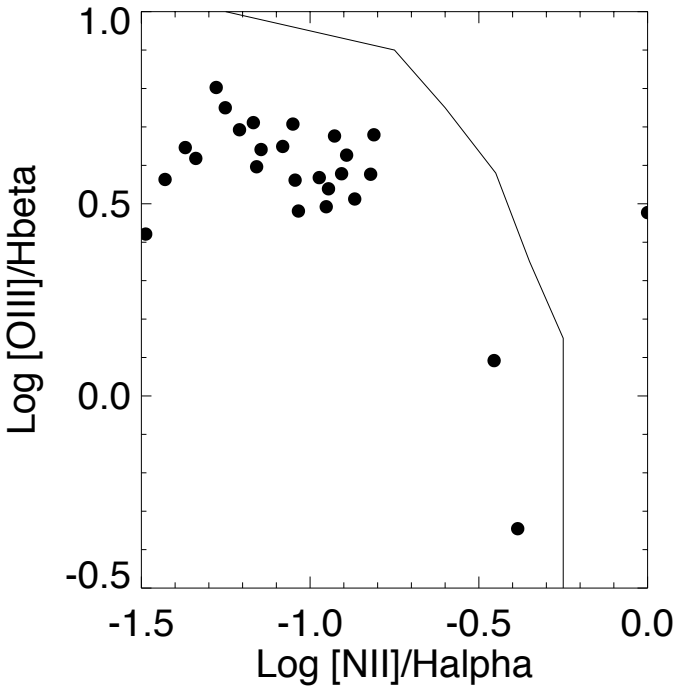

Figure 5.6: [N II]/Hα versus [O III]/Hβ plot for the IEGs. The line comes from an expression of Veilleux & Osterbrock (1987) and can be used to separate AGN from star forming galaxies.

& Osterbrock (1987). Objects falling to the left of the line are H II-like regions that are undergoing star formation. Galaxies to the right are Seyfert and LINER type objects. The line ratios used in Figure 5.6 can be found in Table 5.2.

An inspection of Figure 5.6 reveals very clearly that the IEGs with emission lines are active star forming systems. One galaxy, IEG 182356, does meet the criterion for having a LINER active nuclei. The BPT diagram provided the last piece of evidence that the sample galaxies are indeed actively forming stars.

5.6 Discussion

The IEGs show a distribution of star forming rates, from the extreme star forming system IEG 416078 to IEG 537012 where star formation has nearly ceased. The average SFR for the sample is 0.07 $M_{\odot}$ yr^{-1}. The average values are similar to estimates obtained for intermediate-luminosity ($M_B \sim -18$) ellipticals in the SDSS (Zhao et al. 2006).

All of the IEGs have sub-solar metallicities, with an average value of 12+log (O/H) = 8.28. The narrow range of abundance, $8.09 \leq 12 + \log (O/H) \leq 8.45$, is a unique feature. The fact that there is a "wall" at a metallicity of 8.45 is interesting. The only possible explanations for the sharp limit to abundance are that the the sample was drawn from young galaxies that have not had time to process gas or that the IEGs have accreted nearly primordial gas, which would result in blue colors and sub-solar metallicities.

5.7 Conclusions

We have performed a basic study of the parameters of the SDSS spectra for a sample of early-type galaxies with well established isolation. The analysis included estimates of metallicity, star formation rate, and nuclear activity. The values quoted for the above parameters were calculated within the 3 arcsecond spectral aperture of the SDSS.

- The spectral properties of the IEGs do not possess features of typical early-type galaxies. The assumption was made that a sample of early-type galaxies would have absorption features and no current star formation.

- Five IEGs (51108, 71125, 121923, 383210, 537012) have elliptical-like spectra, dominated by Balmer absorption. IEGs 71125 and 383210 are candidate primordial ellipticals.

- IEG 369001 is a unique sample galaxy with a red color and morphology associated with an elliptical, but possessing an emission line spectra. The nature of IEG 369001 may be that the galaxy has accreted a small gaseous satellite that left few morphological traces but increased star formation.

- IEG 121923 is a galaxy with blue colors and a spectra with no emission line features and weak Balmer absorption. IEG 121923 may be a young galaxy whose stellar population is aging and slowly becoming redder.

- The average star formation rates of 0.07 $M_{\odot}$ yr^{-1} suggest that the IEGs should have consistently been forming or have recently begun to form stars in order to explain the blue colors of the galaxies.

- The IEG metallicities and nuclear activity are very clear to interpret. The IEGs are young galactic systems or have been accreting near-primordial neutral gas.

- One formation scenario supported by the spectral data is that the IEGs are the remains of a group of dwarf galaxies that have now coalesced. The interactions between the dwarf galaxy members may have distributed large reservoirs of neutral gas. The neutral gas would have since accreted onto the IEGs, supplying them with fuel to continue star formation.

Table 5.1. Star Formation Rate for the IEG Sample

IEG	Hα flux	Hα/Hβ	$A_{H\alpha}$	$L_{H\alpha}^{corr}$	log SFR
(1)	(2)	(3)	(4)	(5)	(6)
375	2208	3.75	0.769	117.5	1.03
4177	696	6.57	2.38	7.88	0.07
27750	355	4.29	1.15	1.55	0.01
51108	446	1.47	—	1.11	0.01
71125	—	0.723	—	—	—
114366	1147	3.09	0.217	3.08	0.03
121923	27	—	—	18.15	0.01
122985	3100	3.36	0.449	13.41	0.11
166582	663	3.11	0.231	1.71	0.01
171890	81.2	5.75	1.99	3.06	0.02
182356	—	—	—	—	—
229036	392	3.86	0.849	4.39	0.04
248883	1696	4.63	1.37	30.96	0.27
261992	1376	3.58	0.632	14.03	0.12
348427	450	3.67	0.705	5.44	0.04
369001	3012	2.98	0.107	4.91	0.04
383210	—	1.01	—	—	—

Table 5.1 (continued)

IEG	Hα flux	Hα/Hβ	$A_{H\alpha}$	$L_{H\alpha}^{corr}$	log SFR
(1)	(2)	(3)	(4)	(5)	(6)
391175	338	3.69	0.726	2.29	0.02
414559	1787	3.38	0.472	11.65	0.09
416078	15470	3.39	0.485	77.92	0.612
421880	304	2.99	0.116	0.152	0.01
468256	299	3.94	0.908	3.76	0.03
469932	1352	3.04	0.164	9.92	0.08
496820	268	4.25	1.13	1.15	0.01
499372	315	4.10	1.02	2.85	0.03
507455	179	0.529	—	0.50	0.01
537012	1.5	0.117	—	0.002	0.00
547386	1708	3.52	0.583	7.53	0.06

Table 5.1 (continued)

IEG	Hα flux	Hα/Hβ	$A_{H\alpha}$	$L_{H\alpha}^{corr}$	log SFR
(1)	(2)	(3)	(4)	(5)	(6)
556819	166	5.11	1.65	3.52	0.03
557287	472	2.94	0.07	0.69	0.02
557849	710	3.11	0.233	5.06	0.04
558496	145	4.66	1.38	2.65	0.02
570457	1082	4.17	1.07	14.81	0.13

Note. — Col. (1): IEG name. Col. (2): Hα flux, in units of 10^{-17} ergs s^{-1} cm^{-2} . (3): Ratio between hydrogen emission lines. Col. (4): Nebular extinction derived from equation 5.1. Col. (5): Corrected Hα luminosity, from Cols. 2, 4, and $H_0 = 72$ km s^{-1} Mpc^{-1}. Col. (6): Star formation rate, units of $M_\odot$ yr^{-1}.

Table 5.2. Line Ratios and Metallicity Estimates

IEG	[N II]/Hα	[O III]/Hβ	12+log (O/H)
(1)	(2)	(3)	(4)
375	0.083	4.46	8.31
4177	0.144	—	—
27750	0.092	3.02	8.41
51108	3.23	—	—
71125	—	—	—
114366	0.112	3.11	8.43
121923	0.343	-0.50	—
122985	0.090	3.64	8.37
166582	0.069	3.95	8.30
171890	0.155	4.78	8.42
182356	1.00	3.00	—
229036	0.113	3.46	8.42
248883	0.351	1.24	8.45
261992	0.124	3.78	8.42
348427	0.136	3.26	8.45
369001	0.412	0.45	8.23
383210	—	—	—

Table 5.2 (continued)

IEG	[N II]/Hα	[O III]/Hβ	12+log (O/H)
(1)	(2)	(3)	(4)
391175	0.068	5.14	8.23
414559	0.128	4.23	8.41
416078	0.106	3.69	8.39
421880	0.037	3.66	8.16
468256	0.072	4.38	8.28
469932	0.053	6.35	8.09
496820	0.033	2.64	8.45
499372	0.151	3.78	8.44
507455	0.043	4.43	8.14
537012	—	—	—
547386	0.089	5.10	8.29
556819	0.062	4.93	8.22

Table 5.2 (continued)

IEG	[N II]/Hα	[O III]/Hβ	12+log (O/H)
(1)	(2)	(3)	(4)
557287	0.046	4.15	8.18
557849	0.118	4.75	8.37
558496	0.056	5.54	8.15
570457	0.218	2.63	8.29

Note. — Col. (1): IEG number. Col. (2): Line ratio of the 6583 Å emission line to the Hα line. (3): [O III]/Hβ line ratio, which was derived using Yin et al. (2007), where [O III] si the combination of the 4363, 4959, 5007 Å emission lines. Col. (4): Metallicity in units of 12+log (O/H), derived using equation of Yin et al. 2007.

Chapter 6

Conclusions

A Chandra Observatory archival investigation was performed for samples of compact groups, fossil groups, and isolated ellipticals. As optical signatures of past mergers and interactions have been found to be transient phenomena, it was hoped that the hot diffuse gas associated with most galaxies and galaxy groups would represent a long-lasting diagnostic that could be used to study galaxy evolution. Based on the results of the archival analysis it is clear that X-ray emission is indeed a temporally extensive and robust method that can evaluate a galaxy′s evolutionary history.

A number of surprising results were discovered in the investigation of the theorized evolutionary connection between compact groups, isolated ellipticals, and fossil groups. The current paradigm posits that a fossil group is the remains of a collapsed compact group. Our results indicate that less than 50% of all fossil groups could have formed from the coalescence of galaxies in a compact group.

The X-ray properties of the isolated ellipticals most closely resemble the properties of the compact groups. The implication of the common X-ray features is that the isolated ellipticals are likely the remains of a merged compact group. There is a correlation between optical brightness and X-ray luminosity of the fossil groups and isolated ellipticals that is interpreted as evidence the both types of galaxies have formed as a result of major mergers.

The data suggest that the fossil group galaxies are not a homogeneous sample of galaxies. The X-ray properties of the FGs suggest that there are two populations of fossil groups. The population 1 FGs have X-ray features closely related to both the compact groups and the isolated ellipticals. The population 2 FGs, which comprise more than half of all fossil groups, are extremely hot (kT $\sim$ 3.0 keV), X-ray luminous ($L_X \sim 42.5$ ergs s^{-1}) systems.

One piece of evidence reinforcing the result that compact groups might not evolve into a fossil group comes from Mendes de Oliveira (2006). In an investigation of the environments around the Hickson groups, Mendes de Oliveira found the environments of some HCGs to be too sparse to evolve into a fossil group. Based on the X-ray properties of the population 2 FGs, the birthplace of most fossil groups may be a poor cluster with an extensive network of dwarf galaxies. No optical evidence for a collapsing poor cluster has been observed and the formation mechanism remains a tenuous theory. The possibility exists that the two populations of fossil groups are the opposite ends of a naturally occurring mass distribution.

In the first investigation into the hot gas properties of a substantial number of S0 galaxies, a set of general trends were discovered. Provided that the sample is a fair representation of all lenticular galaxies, the results yield useful intrinsic and environmental properties. The discovery of isolated S0s in prior isolated galaxy studies and in the work of Marcum et al. (2004) necessitated a more complete understanding of the X-ray properties intrinsic to all S0s and those features induced by environment.

The S0 sample galaxy, NGC 3115, is particularly important representing one of the few field/isolated lenticulars ever observed at X-ray wavelengths.

The most important result from the X-ray study of S0 galaxies is that environment appears to be the single most important factor in determining the X-ray features of an S0. The morphology of the hot gas halo would show signs of stripping in cluster S0s, likely due to ram pressure stripping or galaxy-galaxy interactions. The S0 galaxies in groups would be found with a diffuse halo extending beyond the optical extent of the galaxy. The extension of the gas halo would suggest that the gas had been pulled from the galaxy, yet remained under the influence of the galaxy potential well. Field lenticulars would have hot gas very tightly bound to the galaxy center. The absence of a large diffuse halo in field S0s is interpreted as due to a lack of interactions and perturbations to pull the gas from the galaxy. Diffuse emission properties of any lenticular could also be predicted, as the S0 sample followed the trends found for early-type galaxies in the L_X:kT and L_X:M_B planes.

All sample S0 galaxies had distinct sources located at the galaxy center, with four of the eleven sample galaxies (36%) having a strong likelihood of harboring an AGN at their core. The majority of the sample's central sources had X-ray luminosities falling in the range consistent with either an AGN or a low-mass X-ray binary. We estimate that twenty to seventy-five point sources would be detected in any lenticular galaxy observation. Approximately 10% of sources will have super-soft X-ray colors and $\sim$1% of the sources would have very hard colors.

As the isolated ellipticals used in the Chandra analysis were not selected using a consistent isolation criteria, we required a sample of galaxies selected using a robust measure of galaxy isolation. Use of the excellent optical, spectral, and redshift data of the Sloan Digital Sky Survey allowed for the investigation of parameters that could be employed to morphologically select early-type galaxies. The morphological investigation revealed that the eClass parameter is insufficient for classifying galaxies and results in spiral contamination at greater than 90%. The fracpsf and the axial ratio classifiers were able to select early-type samples, however the contamination was still larger than 40%.

We expected that the most useful classification would involve some measure of a galaxy′s light profile. The morphological classifier chosen, the inverse concentration index, does use light distribution as a means to separate galaxy types. An inverse concentration index value, $P_{50}/P_{90} \leq 0.38$, would select 100% of elliptical galaxies, $\sim$ 95% of S0s and give a manageable 20% spiral contamination.

All morphological classifications suffer from the inability to select a single galaxy type, i.e. S0s. We began an assessment of optical and infrared parameters that could be used to detect spirals, specifically Sa galaxies, in our sample of isolated early-type galaxies. The method most often used to remove contaminating morphologies is visual inspection of images, which is both inefficient and non-quantitative. A separation between Sa and S0 galaxies was observed in an infrared color-color diagram at a value of H$-$K = 0.26. While not perfect, the H$-$K color separates $\sim$77% of Sa

galaxies from S0s. The infrared color presented represents one of the first parameters that is capable of separating between two distinct morphological types.

The isolation criteria chosen to select a sample of low-density early-type galaxies from the SDSS is the most extreme and innovative, as the research detailed here marks the first time that three-dimensional isolation was determined from redshift data. The two-dimensional isolation employed in the current study is a minimum 2.5 Mpc separation from any neighbor brighter than $M_V = -16.5$. The neighbor brightness criterion does not prevent the possibility that the candidate galaxy has an associated system of dwarf galaxies. Three-dimensional isolation is imposed by applying a minimum recessional velocity difference of 350 km s^{-1} between the candidate galaxy and a bright neighbor falling two-dimensionally within 2.5 Mpc. The 350 km s^{-1} recessional velocity difference is greater than twice the line-of-sight velocity dispersion of a typical loose group (Huchra & Geller 1982; Tucker et al. 2000).

In addition to the photometry of the SDSS, we undertook a *BVR* imaging study on 24 of the isolated early-type galaxies. The deeper imaging was necessary to more easily identify features associated with past merger events and interactions. Structural and optical brightness profiles, integrated photometry, and residual imaging were performed.

The most unexpected features of the IEG sample has been the extremely blue colors and intermediate-luminosities. The assumption was that the sample of isolated early-type galaxies would contain large bright galaxies showing the red colors of an

evolved stellar population with at least half of the galaxies displaying morphological signatures of past mergers. Integrated photometry reveals that the sample is 2–3 magnitudes fainter than the average brightness found in previous studies of isolated early-type galaxies. The sample displays an unusually large fraction of blue early-type galaxies, which indicates that the sample galaxies have undergone a recent star formation event.

The average M_B value for the IEGs is -16.8, which is three magnitudes fainter than the isolated galaxies studied by Aars et al. (2001) and at least four magnitudes fainter than the average fossil group (Mulchaey & Zabludoff 1999; Vikhlinin et al. 1999). Based on integrated luminosity, the IEGs are a different class of galaxies than fossil groups and may not be the remains of either a collapsed bright group or merger between disk galaxies.

Analyses of radial profiles and residual imaging reveals that the sample is lacking in merger and interaction signatures other than the enhanced star formation. Lack of merger signatures suggests that the isolated early-type galaxies may be accreting clouds of low-mass neutral gas. The number of sample galaxies with colors more blue than a typical elliptical (17/22, 77%) is unusual when compared to previous samples of isolated early-type galaxies. As mentioned in earlier sections, the merger signatures around lower mass, intermediate-luminosity galaxies may last for only a fraction of the lifetime that merger features have around larger ellipticals.

Formation via the coalescence of a group of dwarf galaxies could however explain some of the features seen in the isolated early-type galaxies sample. IEG 182356 appears to have been formed in such a scenario. Deep optical imaging reveals the galaxy to have two cores and an extended halo of diffuse light. Formation via the merger of a group of dwarf galaxies may represent the low mass and low luminosity end of the fossil group mass function and may be the dominant formation mechanism for intermediate-luminosity early-type galaxies. A group of merging dwarf galaxies (MDG1) was first found by Fanelli et al. (2007) in the Sloan Digital Sky Survey. The visual appearance and optical properties of IEG 182356, suggests an evolutionary connection between the galaxy and MDG1. The collapse of a dwarf group is unique theory and has not yet been explored by other researchers.

IEGs 375, 229036, and 248883 are the most likely sample galaxies to have undergone a relatively recent merger. All three galaxies have fan-like structures in their residual imaged that may reveal a past merger with a spheroidal system. IEGs 375 and 229036 have similar colors and luminosities. IEG 248883 is different from the other two, being the most luminous of the three galaxies at $M_V^0 = -18.9$. The fan in IEG 248883 is associated with a blue star forming region surrounding the otherwise red galaxy. The blue region only partially affects the global color, as IEG 248883 has a relatively red color at $(B-V)_0 = 0.84$.

One of the ultimate goals of extracting and examining isolated early-type galaxies was to find systems having a pristine nature, remaining free from large-scale inter-

actions for much of their lifetime. Three sample galaxies, IEGs 71125, 369001, and 383210 are strong candidates for having a primordial nature. These three galaxies might serve as the near-zero interaction baseline necessary to understand the properties intrinsic to all early-type galaxies and those properties caused by external interactions. IEG 369001 has red colors and morphology associated with an elliptical, but its spectra has emission features. IEG 369001 may have accreted a small gaseous satellite that left few morphological traces but increased star formation. One peculiarity is observed in IEG 71125, that being a blue core. IEG 383210 no unusual characteristics and remains the most likely primordial galaxy in the sample.

In a basic study of the parameters of the SDSS spectra, analyses included estimates of metallicity, star formation rate, and nuclear activity. The spectral properties of the IEGs do not possess features of typical early-type galaxies. The spectra of the isolated ealry-type galaxies were expected to have strong absorption features and no current star formation, both typical of normal bright ellipticals. Instead the sample galaxies exhibit strong emission-line spectra, which indicates current star formation.

The average star formation rates of 0.07 $M_{\odot}$ yr^{-1} suggest that the IEGs should have consistently been forming or have recently begun to form stars in order to explain the blue colors of the galaxies. The sub-solar metallicity and lack of nuclear activity are interpreted as the isolated early-type galaxies being young galactic systems or having been continually accreting near-primordial neutral gas.

The extremely blue colors and the emission line spectra, indicating a young stellar population, is consistent with the on-going accretion of dwarf companions. The implication is that in even the most isolated galaxies, minor mergers and accretion events strongly influence galaxy evolution. As has been noted in previous research (Smith et al. 2004a,b), isolated galaxies often are surrounded by a rich system of dwarf companions. Extensive populations of dwarf galaxies have been predicted and observed around many fossil groups (Mulchaey & Zabludoff 1999). Di Serego-Alighieri et al. (2006) discussed the possibility that field ellipticals were the last early-type galaxies to form. It is possible that some of the blue IEGs are now in the late stages of their initial formation.

Appendix A

Glossary

Absolute magnitude ($\mathbf{M}_\lambda$): The brightness an object would have if it were placed at a distance of 10 pc from the Sun. In terms of the apparent magnitude, distance, and extinction correction, the absolute magnitude is given by:

$$M = m + 5 - 5 \log d - A, \tag{A.1}$$

where d is in parsecs and A is a term correcting for extinction occurring between the object and Earth.

Abundance: Proportion of galaxy gas and dust made up of chemical elements other than hydrogen and helium. Often defined in terms of 12 + log (O/H). Also referred to as metallicity.

Apparent magnitude ($\mathbf{m}_\lambda$): A measure of an object's flux as viewed from Earth. Magnitude is related to flux by:

$$m - m(0) = -2.5 \log \left(\frac{f}{f(0)} \right), \tag{A.2}$$

where m(0) and f(0) represent the magnitude and flux of a zeroth magnitude star.

Bremsstrahlung: Radiation produced by the deflection of an electron by a charged particle. The emitted radiation has a continuous spectrum. Commonly referred to as braking radiation or free-free radiation.

Ellipticity: Flattening or oblateness of a spheroid. Defined as the relative difference between the equatorial radius, a, and the polar radius, b,

$$E = \frac{a - b}{a} \tag{A.3}$$

Extinction: The dimming of light via scattering and absorption as it passes through some medium.

Fossil group (FG): Elliptical galaxy that is theorized to be the remains of a coalesced group of galaxies. Fossil groups are 2 R-band magnitudes brighter than the next brightest companion galaxy and have an X-ray luminosity greater than 10^{42} ergs s^{-1}.

Galaxy cluster: Galaxies bounded together by their mutual gravitational attraction. Clusters contain from 50 to 100 galaxies within a diameter of tens of megaparsecs across.

Galaxy group: Galaxies bounded together by their mutual gravitational attraction. Groups contain up to 50 galaxies within a diameter of several megaparsecs across.

Hα: The emission arises from the electron transition in a hydrogen atom from n = 3 to n = 2. Emission occurs at 6562.8 Å.

Hard X-ray band: High-energy range covering 2.5 to 8.0 keV.

Hubble's constant: Proportionality constant that defines the linear relation between galaxy redshift, interpreted as recessional velocity, and distance. The relation

is expressed as follows,

$$v = H_0 \, D \tag{A.4}$$

where v is the recessional velocity in km s^{-1}, D is the distance in Mpc, and H_0 is Hubble′s constant. The value used in the current dissertation is H_0 = 72 km s^{-1} Mpc^{-1}.

Infrared band system: Employed by the 2MASS survey to cover three wavebands around 2 μm,

- J band is a broadband near-infrared filter centered at 12,500 Å.
- H band is a broadband near-infrared filter centered at 16,500 Å.
- K band is a broadband near-infrared filter centered at 21,700 Å.

Initial mass function: An empirical function that describes the mass distribution of a population of stars at birth. The properties of and evolution of a star are closely related to mass, making the theoretical initial mass an important diagnostic tool for studying a large quantity of stars.

Isophote: Contour joining points of equal light intensity from a given source.

Johnson broad-band system: Most commonly used magnitude system in optical astronomy. Comprised of the UBVRI bands where,

- U band is an ultraviolet filter centered at 3650 Å.
- B band is a blue filter centered at 4400 Å.

- V band is a visual filter centered at 5500 Å.
- R band is a red filter centered at 7000 Å.
- I band is a near-infrared filter centered at 8800 Å.

Low-mass X-ray binary (LMXB): Binary star where one of the components is either a black hole or a neutron star. Typically, LMXB systems emit almost all radiation in X-rays, with less than one percent radiation emitted at visible wavelengths.

Medium X-ray band: High-energy range covering 1.5 to 2.5 keV.

Optical depth (τ): A measure of how much light is absorbed when traveling through some medium from a point of origin to an observer. If the intensity of radiation at the source is given by I_0 and I is the observed intensity after a given path, the optical depth is defined as:

$$I = I_0\, e^{-\tau} \tag{A.5}$$

Parsec: A unit of distance defined in terms of the parallax angle (half the maximum change in angular position of an object as viewed from Earth).

$$d = \frac{1}{p''}\, pc \tag{A.6}$$

One parsec is equivalent to 3.262 ly.

Point-spread function: The probability density that a photon will hit the imaging device at a point offset by some vector d from where it would have hit in the absence of seeing, and is given by:

$$P(d) = \frac{1}{2\pi\sigma} e^{\left(\frac{-d}{2\sigma^2}\right)}. \tag{A.7}$$

SDSS photometric system: Filter system employed by the Sloan survey, covering five bandpasses,

- u band is an ultraviolet filter centered on 3551 Å.
- g band is a filter approximately corresponding to blue light centered at 4686 Å.
- r band is a red filter centered on 6165 Å.
- i band is a red filter centered on 7481 Å.
- z band is an infrared filter centered on 8931 Å.

Seeing: Smearing effect caused by turbulence in the Earth's atmosphere. Measured in units of arcseconds.

Seeing disk: Diameter of the best possible angular resolution which can be achieved by an optical telescope. The seeing disk is determined by fitting a gaussian (hence, fitting the PSF) of a star in an image. The FWHM of the gaussian gives the size of the seeing disk.

Sloan Digital Sky Survey (SDSS): Eight year operation to scan one quarter of the sky in five photometric wavebands and obtain spectra for galaxies and quasars. Located at Apache Point Observatory, New Mexico, the survey used a 2.5-meter telescope and catalogued 930,000 galaxies.

Soft X-ray band: High-energy range covering 0.3 to 1.5 keV.

Star formation rate (SFR): Derived frequency at which a galaxy is forming new stars. As individual stars are unresolved for all but the closest galaxies, the rate of

star formation must be derived via integrated light measurements in the ultraviolet, infrared, or from nebular emission (such as Hα). Given in units of solar mass per year, $M_\odot$ yr^{-1}.

Surface brightness: Radiative flux per unit solid angle, the concept is used to describe extended objects such as galaxies. Given in units of magnitudes per square arcsecond and defined as,

$$S = m + 2.5 \log A \tag{A.8}$$

where m is the apparent magnitude of the galaxy that extends over an area A and S is the surface brightness.

Surface brightness profile: Calculated as the average surface brightness within a series of annuli. Plots are often used to highlight the radial variation of surface brightness for a galaxy.

Appendix B

X-ray Radiation

Bremsstrahlung radiation is emitted during encounters between charged particles in a hot, ionized plasma. Bremsstrahlung is also referred to as free-free radiation because the radiating particle is not bound to an atom either before or after emission. Free-free radiation occurs over a continuous spectrum, extending into X-ray energies. To derive the emission properties of a thermal plasma, one needs to assume a Maxwellian distribution of velocities, the probability dP of finding an electron in the d^3v velocity range is,

$$dP \propto e^{(-\frac{E}{k_b T})} d^3v = e^{(\frac{mv^2}{2k_b T})} 4\pi v^2 dv \tag{B.1}$$

The minimum velocity to emit a photon with energy $h\nu$ leads to the photon discreteness effect. For a thermal distribution of electrons,

$$\frac{dW(T,\omega)}{dV dt d\omega} = \frac{\int_{v_min}^{\infty} (dW(v,\omega/d\omega dV dt) v^2 exp(-mv^2/2k_b T) dv}{\int_0^{\infty} v^2 exp(-mv^2/2k_b T) dv} \tag{B.2}$$

using, $d\omega = 2\pi dv$, the free-free emission of a thermal plasma in units of ergs s^{-1} cm^{-3} Hz^{-1},

$$\frac{dW}{dV dt dv} = \frac{2^5 \pi e^6}{3mc^3} \left(\frac{2\pi}{3k_b m}\right)^{1/2} Z^2 n_e n_{ion} T^{-1/2} e^{-(\frac{hv}{k_b T})} g_v^{ff} \tag{B.3}$$

where g_v^{ff} is the velocity averaged Gaunt factor. Integrating over all frequencies one can obtain the total power emitted by thermal Bremsstrahlung,

$$\frac{dW}{dVdt} = \frac{2^5\pi e^6}{3hmc^3}\left(\frac{2\pi k_b}{3m}\right)^{1/2} Z^2 n_e n_{ion} T^{-1/2} g_v^{ff} \tag{B.4}$$

Following the above equations, the thermal Bremsstrahlung emissivity of a gas at frequency, ν, is given by,

$$\epsilon(\nu) = A n_e^2 T_X^{-1/2} \tag{B.5}$$

where T_X is the temperature of the gas, A is a constant and n_e is the electron number density. The temperature and density of X-ray emitting gas can then be used to estimate the total gravitational mass of the system provided the gas is in thermostatic equilibrium,

$$M_{grav}(r) = \frac{-rkT}{G\mu m_p}\left(\frac{\mathrm{d}\ \ln \rho(r)}{\mathrm{d}\ \ln\ \mathrm{r}} + \frac{\mathrm{d}\ \ln\ \mathrm{T}}{\mathrm{d}\ \ln\ \mathrm{r}}\right) \tag{B.6}$$

where, m_p is the proton mass and the mean particle mass, $\mu = 0.6$ (Fabricant, Lecar, & Gorenstein 1980). The X-ray surface brightness profile can often be fit by a two-dimensional β-model (King 1962; Cavaliere & Fusco-Femiano 1976),

$$S(r) = S_0\left(1 + (\frac{r}{r_{core}})^2\right)^{-3\beta+0.5} \tag{B.7}$$

$$\beta = \frac{\mu m_p \sigma^2}{kT_{gas}} \tag{B.8}$$

where, σ is the velocity dispersion. The equation for β describes the ratio of the specific energy in galaxies to the specific energy in the gas. Equation 2.8 can be

simplified given an estimate of the slope of the radial brightness profile. Provided that the surface brightness profile is well fit by the β model, the total gravitational mass is simplified to (Jeltema et al. 2006),

$$M_{grav}(r) = \frac{3\beta T r_{core}}{G\mu m_p}\left(\frac{x^3}{1+x^2}\right) \tag{B.9}$$

where x = $\frac{r}{r_{core}}$, G is the gravitational constant and m_p is the proton mass.

Appendix C

Nebular Line Diagnostics

C.1 Star Formation Rates

Optical emission lines from H II regions are the primary means of determining the gas-phase chemical composition in galaxies (Searle 1971, Shields 1990). When hot, massive O and B stars reach the main sequence, the majority of their radiation is emitted at UV wavenegths. If the O and B stars produce photons with energies in excess of 13.6 eV ($\lambda < 912$ Å), H II regions will be produced. H II regions are generally assumed to be in equilibrium, meaning the rate of ionization will equal the rate of recombination. Only high mass, M $>$ 10 $M_{\odot}$, short-lived stars produce a significant ionizing flux. The emission lines are produced by short-lived stars which means that the emission lines are good probes of the current star formation rate (SFR), irrespective of past star formation events. The primary advantages to using nebular emission lines are a high sensitivity and a strong coupling between the emission and the rate of massive star formation (Gavazzi et al. 1991).

The presence of dust in galaxies can modify spectra and result in incorrect emission line flux. The nebular emission line method is not perfect, as it does have uncertainties, primarily unknowns in extinctions and the initial mass function (IMF) employed. Much of the error occurs with the estimates of extinction. Work by Kennicutt (1983)

and Niklas et al. (1997) have found mean extinction values A(Hα) = 0.8 – 1.1 mag. Other studies have derived extinction to range between A(Hα) = 0.5 and 1.8 mag (Kaufman et al. 1987, Caplan et al. 1996).

The technique most widely used to correct for extinction uses the relative strength of lower Balmer lines, Hα and Hβ (Veilleux & Osterbrock 1989). In order to derive star formation rates from Hα emission, the Hα flux must first be corrected for extinction using an intrinsic ratio, $\mathrm{I}_{H\alpha} / \mathrm{I}_{H\beta} = 2.87$. Assuming a case B recombination and a standard reddening law (Cardelli et al. 1989), estimates of the extinction are given by (Torres-Peimbert et al. 1989):

$$A_{H\alpha} = 6.6 \times \log \left(\frac{\frac{H\alpha}{H\beta}}{\frac{I_{H\alpha}}{I_{H\beta}}} \right) \tag{C.1}$$

where $\mathrm{I}_{H\alpha} / \mathrm{I}_{H\beta}$ is the intrinsic ratio quoted above and Hα / Hβ is the flux ratio calculated from the SDSS spectra.

The corrected Hα flux is then determined using,

$$F_{corr}^{H\alpha} = F_{H\alpha} \times 10^{\frac{A_{H\alpha}}{2.5}} \tag{C.2}$$

The initial mass function is an empirical function that describes the mass distribution of a population of stars. The properties of a star are strongly dependent on mass, which makes the IMF a very important diagnostic to studying stellar populations. The star formation rate is particularly sensitive to the choice of the IMF, as the SFR is tightly dependent on the number of high mass O stars. If using a Scalo (1986) IMF, the derived SFR would be a factor of 3 higher than the rate derived using a Salpeter

IMF (Salpeter 1955). Dispersions among other SFR methods are primarily due to differences in the selected IMF and the stellar evolution models (Kennicutt 1998).

Derivations of the current star formation rate from the Hα line emission are made with the following assumptions, firstly that the average abundance of the stellar population is solar and secondly, the IMF used is a Salpeter model (0.1 – 100 $M_{\odot}$. The assumptions and calibrations by Kennicutt et al. (1994) provide,

$$SFR(H\alpha) = L_{corr}^{H\alpha} \times 7.9 \times 10^{-42}\, \mathrm{M_{\odot}\,yr^{-1}} \tag{C.3}$$

where the star formation rate is calculated in units of solar masses per year.

C.2 Gas-Phase Abundances

Emission lines also can be used to estimate the degree to which gas has been enriched. The most commonly used proxy for determining metallicity is oxygen abundance. Oxygen is important because approximately half of the metal content in the interstellar medium is oxygen and it displays strong emission lines from multiple ionization states that are easily measured. Metallicity is expressed as 12 + log (O/H), and the standard comparison is solar metallicity, 12 + log (O/H) = 8.66 (Allende Prieto et al. 2002; Asplund et al. 2004).

Nebular oxygen abundances were estimated for those IEGs showing emission lines using a specific set of line ratios. We adopted the method of Yin etal (2007). The benefit of utilizing two lines in a small $\delta\lambda$ is that both lines will be equally effected

by absorption and no absorption corrections need be applied. Ratios most commonly employed are, [N II]/Hα, [O III]/Hβ, and ([O II] + [O III])/Hβ. [N II] emission line is a result of the CNO-cycle, while the [O II] line is due to collisional excitations. [N II] and [O III] are both forbidden lines. Forbidden lines arise from atoms undergoing energy transitions not normally allowed by the selection rules of quantum mechanics. The low-densities found in nebular clouds are ideal for the production of forbidden line photons, as the likelihood of atomic collision is very small.

Metallicity was determined using analytical functions derived by Yin et al. (2007). The sample of Yin et al. derived O/H abundances for 695 galaxies using a direct temperature method. Analytical fits were made to the direct metallicity measurements and the fits are presented below:

$$12 + \log(\mathrm{O/H}) = 6.486 + 1.401\ \log([\mathrm{O\ III}]\ /\ \mathrm{H}\beta) \tag{C.4}$$

$$12 + \log(\mathrm{O/H}) = 8.203 + 0.63\,(\mathrm{O3N2}) - 0.327\,(\mathrm{O3N2})^2 \tag{C.5}$$

$$\mathrm{O3N2} = \log(([\mathrm{O\ III}]\ /\ \mathrm{H}\beta)\ /\ ([\mathrm{N\ II}]\ /\ \mathrm{H}\alpha) \tag{C.6}$$

Equation C.4 is valid for extremely metal poor galaxies, 12 + log (O/H) $\leq$ 7.9, of which none are found in the IEG sample. Equation C.5 is valid for galaxies with $1.4 \leq \mathrm{O3N2} \leq 3.0$, which corresponds to all emission line galaxies in the IEG sample. The equations are valid for metallicities less than 9.0. The estimated metallicities for the IEG sample can be found in Table 5.2. We used the observed [O III]/Hβ and

[N II]/Hα ratios, which were derived from the SDSS spectra, to estimate the oxygen abundance based on equation C.5.

C.3 Ionization Sources

Line ratios have also proven to be excellent measures of central activity in a galaxy. As star formation and active galactic nuclei can both produce emission lines, a means of estimating the dominant cause of emission is vital to understanding a galaxy′s evolution. The BPT diagram (Baldwin, Phillips, & Terlevich 1981) has become the mainstay of AGN study, using the [N II]/Hα and [O III]/Hβ ratios.

Systems that are not undergoing star formation are likely either a LINER or a Seyfert 1 or 2 galaxy. Seyfert galaxies, powered by a strong AGN, will be able to ionize a large range of elements. Broad emission lines of the elements of helium, nitrogen, and oxygen have been observed for Seyferts, indicating the material in the galaxy cores are moving at speeds $\sim$1,000 km s^{-1}. LINER galaxies, powered by a weaker AGN, exhibit emission lines from oxygen, nitrogen, and sulfur. It has been proposed that the ionization observed in LINERs may be due to mechanical heating via shocks. Both types of AGN differ from star forming H II regions, which are dominated by Balmer emission.

A BPT diagram is denoted by three regions, gas photoionized by youngs stars, by an AGN, and by shock heating. When examining a BPT diagram, one will find LINERs located with large values of [N II]/Hα. Seyfert 2 galaxies will have large

values of both [N II]/Hα and [O III]/Hβ. Processes common in AGN are capable of producing photons with energies above 35 eV, which are necessary to create [O III]. Stellar processes are unlikely to yield such energetic photons. The star forming galaxies will be dominated by hydrogen emission and will be found to the lower left of the BPT diagram. A BPT diagram of the emission line IEGs was made in order to determine the mechanism responsible for the sample′s spectral features. Verification of recent enhanced star formation would also help explain the anomalously blue colors observed.

Bibliography

Aaronson, M. 1985 in Star Forming Dwarf Galaxies and Related Objects, ed. D. Knuth, T. X. Thuan, & J. T. T. Van (Paris: Editions Frontieres), 125

Aars, C.E., Marcum, P.M., Fanelli, M.N. 2001, AJ, 122, 2923

Abazajian, K., Adel-McCarthy, J. K., et al. 2003, AJ, 126, 2081

Abazajian, K., Adel-McCarthy, J. K., et al. 2004, AJ, 128, 502

Abazajian, K., Adel-McCarthy, J. K., et al. 2005, AJ, 129, 1755

Abraham, R. G., Tanvir, N. R., Santiago, B. X., Ellis, R. S., Glazebrook, K., & van den Bergh, S. 1996a, MNRAS, 279, L47

Abraham, R. G., van den Bergh, S., Glazebrook, K., Ellis, R. S., Santiago, B. X., Surma, P., & Griffiths, R. E. 1996b, ApJS, 107, 1

Adelman-McCarthy, J. K., Agueros, M. A., Allam, S. S., et al. 2006, ApJS, 162, 38

Adelman-McCarthy, J. K., Agueros, M. A., Allam, S. S., et al. 2007, ApJS, 172, 634

Aguilar, L.A. White, S.DM. 1986, ApJ, 307, 97

Aguilar, L.A. & Merritt, D. 1990 ApJ, 354, 33

Allam, S., Assendorp, R., Longo, G., Braun, M., & Richter, G. 1996, A&AS, 117, 39

Allam, S., Tucker, D., Lee, B., Smith, A. 2005, AJ, 129, 2062

Allen, S. W., di Matteo, T., & Fabian, A. C. 2000, MNRAS, 311, 493

Allende Prieto, C., Lambert, D. L., & Asplund, M. 2002, ApJ, 573, L137

Arp, H. 1966, Science, vol. 151, 3715, 1214

Asplund, M., Grevesse, N., Sauval, A. J., Allende Prieto, C., & Kiselman, D. 2004, A&A, 417, 751

Balcells, M. & Quinn, P.J. 1990 ApJ 361 381

Balcells, M., van Gorkom, J.H., Sancisi, R., & del Burgo, C. 2001, AJ, 122, 1758

Baldwin, J. A., Phillips, M. M., & Terlevich, R. 1981, PASP, 93, 5

Bally, J. & Thronson, H. A., Jr. 1989, AJ, 97, 69

Barnes, J. 1985, MNRAS, 215, 517

Barnes, J. 1989, Nature, 338, 123

Barnes, J.E. 1996, in Galaxies: Interactions and Induced Star Formation, ed D. Friedli

Bekki, K., Shioya, Y., & Couch, W.J. 2002, ApJ, 577, 651

Benacchio, L. & Galetta, G. 1980, MNRAS, 193, 885

Bernardi, M., Sheth, R. K., Annis, J., Burles, S. et al. 2003, AJ, 125, 1817

Binggelli, B., Sandage, A., & Tammann, G. A. 1988, ARA&A, 26, 509

Binney, J. & Merrifield, M. 1998, Galactic Astronomy, Princeton University Press

Binney, J.& Tremaine, S. 1987, Galactic Dynamics, Princeton University Press

Blanton, E. L., Sarazin, C. L., & Irwin, J. A. 2001, ApJ, 552, 119

Blanton, M. R. et al. 2003, ApJ, 594, 186

Bothun, G. D. & Sullivan, III, W. T. 1977, PASP, 89, 5

Bower, R. G., Lucey, J. R., & Ellis, R. S. 1992, MNRAS, 254, 589

Bridges, T. J. & Hanes, D. A. 1990, ApJ, 99, 1100

Brighenti, F. & Mathews, W.G. 1998, ApJ, 495, 239

Brinchmann, J., et al. 1998, ApJ, 499, 112

Brown, B. & Bregman, J. 2000, ApJ, 539, 592

Burstein, D. 1979, ApJ, 234, 435

Burstein, D., Davies, R. L., Dressler, A., Faber, S. M., Stone, R. P. S., Lynden-Bell, D., Terlevich, R. J., & Wegner, G. 1987, ApJS, 64, 601

Canizares, C. R., Fabbiano, G., & Trinichieri, G. 1987, ApJ, 312, 503

Capaccioli, M., Held, E. V., & Nieto, J. L. 1987, AJ, 94, 1519

Capaccioli, M., Vietri, M., & Held, E. V. 1988, MNRAS, 234, 335

Caplan, J., Ye, T., Deharveng, L., Turtle, A. J., Kennicutt, R. C. 1996, A & A, 307, 403

Cardelli, J. A., Clayton, G. C., & Mathis, J. S. 1989, ApJ, 345, 245

Carter, D. 1978, MNRAS, 182, 797

Cavaliere, A. & Fusco-Femiano, R. 1976, A&A, 49, 137

Chiosi, C. & Carraro, G. 2002, MNRAS, 335, 335

Christlien, D. & Zabludoff, A. I. 2004, ApJ, 616, 192

Ciotti, L. & Pellegrini, S. 2004, MNRAS, 350, 609

Colbert, J.W., Mulchaey, J.S., Zabludoff, A.I. 2001, AJ, 121, 808

Collobert, M., Marc, S., Davies, R. L., Kuntschner, H., & Colless, M. 2006, MNRAS, 370, 1213

Connolly, A. J., Szalay, A. S., Bershady, M. A., Kinney, A. L., & Calzetti, D. 1995, AJ, 110, 1071

Conselice, C. J. ApJS, 147, 1

Couch, W. J., Barger, A. J., Smail, I., Ellis, R. S., & Sharples, R. M. 1998, ApJ, 497, 188

Coziol, R., Brinks, E., Bravo-Alfaro, H. 2004, AJ, 128, 68

Cutri, R. M., Skrutskie, M. F., van Dyk, S., Beichman, C. A., Carpenter, J. M., Chester, T., Cambresy, L., Evans, T., Fowler, J., Gizis, J., Howard, E., Huchra, J., Jarrett, T., Kopan, E. L., Kirkpatrick, J. D., Light, R. M., Marsh, K. A., McCallon, H., Schneider, S., Stiening, R., Sykes, M., Weinberg, M., Wheaton, W. A., Wheelock, S., & Zacarias, N. 2003, IRSA 2MASS All-Sky Point Source Catalog (NASA/IPAC Infrared Science Archive)

Davis, D. S. & White, R. E., III 1996, ApJ, 470, L35

Davis, D.S., Mulchaey, J.S., Mushotzky, R.F. 1999, ApJ, 511, 34

de Carvalho, R.R. & da Costa, L.N. 1988, ApJS, 68, 173

Denicolo, G., Terlevich, R., Terlevich, E., Forbes, D., Terlevich, A., Carrasco, L. 2005, MNRAS, 356, 1440

de Vaucouleurs, G. 1948, AnAp, 11, 247

de Vaucouleurs, G. 1961, ApJS, 5, 233

de Vaucouleurs, G., de Vaucouleurs, G., & Corwin, H. G. 1976, Second Reference Catalog of Bright Galaxies (Austin: Univ. of Texas Press)

de Vaucouleurs, G., de Vaucouleurs, A., Corwin, H. G., Jr., Buta, R. J., Paturel, G., & Fouque, P. 1991, Third Reference Catalog of Bright Galaxies (New York: Springer) (RC3)

de Vaucouleurs, G., de Vaucouleurs, A., Corwin, H. G., Jr., Buta, R. J., Paturel, G., & Fouque, P. 1992, yCat, 7137, 0

Diehl, S. & Statler, T.S. 2006, astro.ph, 6215

di Serego Alighieri, S., Lanzoni, B., & Jorgensen, I. 2006, ApJ, 647, 99

di Tullio, G.A. 1979 A&AS, 37, 591

Djorgovski, S. & Davis, M. 1987, ApJ, 319, 59

Doi, M., Fukugita, M., & Okamura, S. 1993, MNRAS, 264, 832

D′Onghia, E., Sommer-Larsen, J., Romeo, A.D., Burkert, A., Pedersen, K., Portinari, L., & Rasmussen, J. 2005, ApJ, 630L, 109

Dressler, A. 1980, ApJ, 236, 351

Dressler, A., & Gunn, J.E. 1983, ApJ, 270, 7

Dressler, A., Lynden-Bell, D., Burstein, D., Davies, R. L., Faber, S.M., Terlevich, R. J., & Wegner, G. 1987, ApJ, 312, 42

Dressler, A., Smail, I., Poggianti, B., Butcher, H., Couch, W. J., Ellis, R. S., & Oemler, A., Jr. 1999,ApJS, 78, 1

Drinkwater, M. J., Gregg, M. D., Holman, B. A., & Brown, M. J. I. 2001, MNRAS, 326, 1076

Ebeling, H., Voges, W., & Bohringer, H. 1994, ApJ, 436, 44

Eggen, O.J., Lynden-Bell, D., & Sandage, A.R. 1962, ApJ, 136, 748

Eskridge, P. B., et al. 2002, ApJS, 143, 73

Evstigneeva, E. A., de Carvalho, R. R., Ribeiro, A. L., & Capelato, H. V. 2004, MNRAS, 349, 1052

Faber, S.M. & Gallagher, J. 1976, ApJ, 204, 356

Faber, S.M. & Jackson, R.E. 1976, ApJ, 204, 668

Faber, S. M., Dressler, A., Davies, R. L., Burstein, D., Lynden-Bell, D., Terlevich, R. J., & Wegner, G. 1987, in Nearly Normal Galaxies, From the Planck Time to the Present, ed. S. M. Faber (NY:Springer), 175

Fabbiano, G., Kim, D. - W., & Trinichieri, G. 1994, ApJ, 429, 94

Fabbiano, G. 2006, Ann. Rev. Astron. Astrophys., 44, 323

Fabricant, D., Lecar, M., & Gorenstein, P. 1980, ApJ, 241, 552

Fanelli, M. N., Marcum, P. M., Fuse, C., & Aars, C. 2007, BAAS, 211, 970

Fasano, G. Bonoli, C. 1989, A&A Suppl. Ser. 79, 291

Feretti, L., Giovannini, G., Gregorini, L., Padrielli, L., Roland, J., & Valentijn, E. A. 1985, A&A, 147, 321

Forbes, D. A. & Thomson, R. C. 1992, MNRAS, 254, 723

Forman, W., Schwarz, J., Jones, C., Liller, W., & Fabian, A. C. 1979, ApJ, 234, 27

Forman, W., Jones, C., & Tucker, W. C. 1985, ApJ, 293, 102

Frogel, J. A., Persson, S. E., MAtthews, K., & Aaronson, M. 1978, ApJ, 220, 75

Fukugita, M., Ichikawa, T., Gunn, J. E., Doi, M., Shimasaku, K., & Schneider, D. P. 1996, AJ, 111 1748

Fukugita, M., Osamu, N., Turner, E. L., Helmboldt, J., & Nichol, R. S. 2004, ApJ, 601, 127

Gallagher, J. S. 1998, in The Magellanic Clouds and other Dwarf Galaxies, ed. T. Richtler & J. M. Braun (Aachen: Shaker Verlag), 25

Galletta, G., Rodighiero, G., Bettoni, D., Moles, M., Varela, J. 2006, AA, 456, 91

Garcia, A. M. 1993, A&AS, 100, 47

Gavazzi, G., Boselli, A., & Kennicutt, R. 1991, AJ, 101, 1207

Giacconi, R., Branduardi, G., Briel, U., Epstein, A., Fabricant, D., et al. 1979, ApJ, 230, 540

Gisler, G.R. 1976, A&A, 51, 137

Gonzalez Delgado, R., Leitherer, C., & Heckman, T. 1999, ApJS, 125, 489

Gonzalez-Garcia, A.C. & Balcells, M. 2005, MNRAS, 357, 753

Goto, T., Okamura, S., Sekiguchi, M., Bernardi, M., & 12 other authors 2003, PASJ, 55, 757

Grebel, E. K. 2001, Ap&SSS, 277, 231

Grimm, H. - J., Gilfanov, M., & Sunyaev, R. 2002, A&A, 391, 923

Grogin, N. A. & Geller, M. J. 1999, AJ, 118, 256

Gu, Q., Zhao, Y., Shi, L., Peng, Z., & Luo, X. 2006, AJ, 131, 806

Gunn, J.E., Stryker, L.L. & Tinsley, B.M. 1981, ApJ, 249, 48

Gunn, J. E., Carr, M., Rockosi, C. et al. 1998, AJ, 116, 3040

Hao, C. N., Mao, S., Deng, Z. D., Xia, X. Y., & Wu, H. 2006, MNRAS, 370, 1339

Hau, G.K.T. Forbes, D. 2006, MNRAS, 371, 633

Haynes, M. P., Jore, K. P., Barrett, E. A., Broeils, A. H. & Murray, B. M. 2000, AJ, 120, 703

Heckman, T. M. 1980, A&A, 87, 142

Helsdon, S. F. & Ponman, T. J. 2000, MNRAS, 315, 356

Hickson, P. 1982, ApJ, 255, 382

Hickson, P., Kindl, E., & Auman, J.R. 1989, ApJS, 70, 687

Hickson, P., Mendes de Oliveira, C., Huchra, J. P., & Palumbo, G. G. C. 1992, ApJ, 399, 353

Hodge, P. 1971, ARA&A, 9, 35

Hogg, D.E., Roberts, M.S., & Sandage, A. 1993, AJ, 106, 907

Horellou, C., Black, J.H., van Gorkon, J.H., Combes, F., van der Hulst, J.M. & Charmandaris, V. 2001, A&A, 376, 837

Hubble, E.P. 1926, ApJ, 64, 321

Hubble, E. P. 1936, The Realm of the Nebulae (New Haven: Yale Univ. Press)

Huchra, J. P. & Geller, M. J. 1982, ApJ, 257, 423

Huchra, J. P., Vogeley, M. S., & Geller, M. J. 1999, ApJS, 121, 287

Humason, M. L., Mayall, N. U., & Sandage, A. R. 1956, AJ, 61, 97

Humphrey, P. J. & Buote, D. A. 2004, ApJ, 612, 848

Irwin, J. A. & Sarazin, C. L. 1998, ApJ, 494, L33

Irwin, J. A., Sarazin, C. L., & Bregman, J. N. 2002, ApJ, 570, 152

Jarrett, T. H., Chester, T., Cutri, R., Schneider, S. E., & Huchra, J. P. 2003, AJ, 125, 525

Jedrzejewski, R.I. 1987, MNRAS, 226, 747

Jeltema, T.E., Mulchaey, J.S., Lubin, L.M., Rosati, P., & Bohringer, H. 2006, ApJ, 649, 649

Jeltema, T. E., Binder, B., & Mulchaey, J. S. 2008, arXiv0801.2570J

Jerjen, H., Binggeli, B., & Freeman, K. C. 2000, AJ, 119, 593

Jimenez, R., Friaca, A.C.S., Dunlop, J.S., Terlevich, R.J., Peacock, J.A., & Nolan, L.A. 1999, MNRAS, 305L, 16

Jones, L. R., Ponman, T. J., & Forbes, D. A. 2000, MNRAS, 312, 139

Jones, L.R., Ponman, T.J., Horton, A., Babul, A., Ebeling, H., & Burke, D.J. 2003, MNRAS, 343, 627

Kahabka, P. & van den Heuvel, E. P. J. 1997, ARA&A 35, 69

Karachentseva, V.E. 1973, SaSAO, 8, 3

Karachentsev, I. D. & Makarov, D. A. 1996, AJ, 111, 794

Karhunen, H. 1947, Ann. Acad. Science Fenn, Ser. A.I. 37

Kauffmann, G., White, S. D. M. & Guiderdoni, B. 1993, MNRAS, 264, 201

Kaufman, M., Bash, F. N., Kennicutt, R. C., Hodge, P. W. 1987, ApJ, 319, 61

Kennicutt, R. C. 1983, ApJ, 272, 54

Kennicutt, R. C. Jr., Tamblyn, P., & Congdon, C. E. 1994, ApJ, 435, 22

Kennicutt, R. C. Jr., 1998, Ann. Rev. Astron. & Astrophys., 36, 189

Kewley, L. J., Jansen, R. & Geller, M. 2005, PASP, 117, 227

Khachikian, E. Y. & Weedman, D. W. 1974, ApJ, 192, 581

Khosroshahi, H. G., Maughan, B. J., Ponman, T. J., & Jones, L. R. MNRAS, 369, 1211

Kraft, R. P., Jones, C., Nulsen, P. E. J., & Hardcastle, M. J. 2006, ApJ, 640, 762

Khosroshahi, H. G., Ponman, T. J., & Jones, L. R. 2007, MNRAS, 377, 595

Kikuchi, K., Itoh, C., Kushino, A., Furusho, T., Matsushita, K., Yamasaki, N. Y., Ohasi, T., Fukazawa, Y., Ikebe, Y., Bohringer, H., Matsumoto, H. 2000, ApJ, 531L, 95

Kim, D. - W., Fabbiano, G., & Trinichieri, G. 1992, ApJ, 393, 134

Kim, D. - W., Fabbiano, G., Matsumoto, H., Koyama, K., & Trinichieri, G. 1996, ApJ, 468, 175

King, IR 1962, Astron. J., 67, 471

Kochaneck, Pahre, & Falco 2000, astro.ph11458

Kochefar, S. & Burkertt, A. 2003, ApJ, 597, L117

Kormendy, J. 1977, ApJ, 218, 333

Kormendy, J. 1980, Proceedings of the ESO Workshop Nov. 21, 1979, ed. Crane, P. & Kjar, K., 191

Kormendy, J. 1982, in *Morphology and Dynamics of Elliptical Galaxies*, 12th Advanced Course of the Swiss Society of Astronomy and Astrophysics, eds. L. Martinet & M. Mayor (Sauverny: Geneva Observatory) p. 115

Kormendy, J. & Djorgovski, S. 1989, ARA&A, 27, 235

Kraft, R. P., Nolan, L. A., Ponman, T. J., Jones, C., & Raychaudhury, S. 2005, ApJ, 625, 785

Kuntschner, H., Smith, R.J., Colless, M., Davies, R.L., Kaldare, R., & Vazdekis, A. 2002, MNRAS, 337, 172

Larson, J. 1975, MNRAS, 173, 671

Larson, R.B., Tinsley, B.M., & Caldwell, C.N. 1980, ApJ, 237, 692

Laurikainen, E., Salo, H., & Buta, R. 2005, MNRAS, 362, 1319

Lea, S.M. & De Young, D.S. 1976, ApJ, 210, 647

Lee, H., McCall, M.L., & Richer, M.G. 2003, AJ, 125, 2975

Lin, D. N. C. & Murray, S. D. 1994, in Dwarf Galaxies, ed. G. Meylan & P. Prugniel (Garching: ESO), 535

Lisenfeld, U., Verdes-Montenegro, L., Sulentic, J., Leon, S., Espada, D., Bergond, G., Garcia, E., Sabater, J., Santander-Vela, J. D., Verley, S. 2007, A&A, 462, 507

Liu, X., Shapley, A. E., Coil, A. L., Brinchmann, J., & Ma, C.-P. 2008, ApJ, 678, 758

Loeve, M. 1948, Processus Stochastiques et Mouvement Brownien, Hermann, Paris, France

Malin, D. F. & Carter, D. 1980, Nature, 285, 643

Madejsky, R. & Möllenhoff, C. 1990, A&A, 234, 119

Madore, B.F., Freedman, W.L., Bothun, G.D. 2004, ApJ, 607, 810

Malin, D.F. & Carter, D. 1983, ApJ 274, 534

Marcum, P.M., Aars, C.E., & Fanelli, M.N. 2004, AJ, 127, 3213

Matsumoto, H., Koyama, K., Awaki, H., Tsuru, T., Loewenstein, M., & Matsushita, K. 1997, ApJ, 482, 133

Menanteau, F., Ellis, R. S., Abraham, R. G., Barger, A. J., & Cowie, L. L. 1999, MNRAS, 309, 208

Melbourne, J., & Salzer, J.J. 2002, AJ, 132, 2302

Mendes de Oliveira, C. & Hickson, P. 1994, ApJ, 427, 684

Mendes de Oliveira, C. 2006, RMxAC, 26, 105

Menon, T. K. 1992, MNRAS, 255, 41

Merluzzi, P., Shaker, A. A., & Longo, G. 2000, ASPC, 209, 205

Merritt, D. 1985, ApJ, 289, 18

Mewe, R., Gronenschild, E. H. B. M., & van den Oord, G. H. J. 1985, A&AS, 62, 197

Michard, R. 1985, A&AS, 59, 205

Michard, R. 2000, A&A, 360, 85

Mihos, C. 1999, Ap&SS, 266, 195

Milvang-Jensen, B. & Jorgensen, I. 1999, Baltic Astronomy, 8, 535

Moran, S. M., Ellis, R. S., Treu, T., Smith, G. P., Smail, I., Dressler, A., & Coil, A. L. 2005, ApJ, 634, 977

Mori, M., Yuzuru, Y., Takuji, T., Kenichi, N. 1997, ApJ, 478, L21

Morgan, W. M. & Mayall, N. U. 1957, PASP, 69, 291

Morgan, W. W. 1958, PASP, 70, 364

Mori, M., Yoshii, Y., Tsujimoto, T., & Nomoto, K. 1997, ApJ, 478, L21

Morita, U., Yoshitaka, I., Yamasaki, N. Y., Ota, N., Kawano, N., Fukazawa, Y., & Ohashi, T. 2006, PASJ, 58, 719

Mulchaey, J. S., Davis, D. S., Mushotzky, R. F., Burstein, D. 1996, ApJ, 456, 80

Mulchaey, J. S. & Zabludoff, A. I. 1999, ApJ, 514, 133

Mulchaey, J. S., Davis, D., Mushotzky, R., Burstein, D. 2003, ApJS, 145, 39

Mushotzky, R. 1996, Proceedings of Rontgenstrahlung from the Universe, ed. Zimmermann, H.U.., Trumpler, J., & Yorke, H., 545

Mushotzky, R. 1998, in Proceedings from a National Academy of Science Colloquium, NAS, 7

Naab, T., Jesseit, R., & Burkert, A. 2006, MNRAS, 372, 839

Newberry, M.V., Boroson, T.A., & Kirshner, R.P. 1990, ApJ, 350, 585

Nigoche-Nerto, A., Moles, M., Ruelas-Mayorga, A., Franco-Balderas, A., & Kjaergaard, P. 2007, A&A, 472, 773

Niklas, S., Klein, U., Wielebinski, R. 1997, A&A, 322, 19

Nulsen, P.E.J, Stewart, G.C. & Fabian, A.C. 1984, MNRAS, 208, 185

Oosterloo, T.A., Morganit, R., Sadler, E.M., Vergani, D. & Caldwell, N. 2002, AJ, 123, 729

Osterbrock, D.E, & Pogge, R.W., 1985, ApJ, 297, 166

O′Sullivan, E., Ponman, T.J., & Collins, R.S. 2003, MNRAS, 340, 1375

O′Sullivan, E. & Ponman, T.J. 2004, MNRAS, 354, 935

Ota, N., Morita, U., Kitayama, T., & Ohashi, T. 2004, PASJ, 56, 753

Park, C. & Choi, Y.-Y. 2005, ApJ, 635, L29

Partridge, R.N. & Peebles, P.J.E. 1967, ApJ, 147, 868

Paturel, G., Petit, C., Prugniel, Ph., Theureau, G., Rosseau, J., Brouty, M., Dubois, P., & , L. 2003, A&A, 412, 45

Pellegrini, S.1994, A&A, 292, 395

Petrosian, V. 1976, ApJ, 209, L1

Pickles, A. J. 1998, PASJ, 110, 863

Pildis, R., Bregman, J., & Evrard, A. 1995, ApJ, 443, 514

Pilyugin, L. S. 2001, A&A, 369, 594

Plana, H., Mendes de Oliveira, C., Amram, P., & Boulesteix, J. 1998, AJ, 116, 2123

Poggianti, B. M., Smail, I., Dressler, A., Couch, W. J., Barger, A. J., Burtcher, H., Ellis, R. S., & Oemler, A., Jr. 1999, ApJ, 518, 576

Ponman, T. J. & Bertram, D. 1993, Nature, 363, 51

Ponman, T. J., Allan, D. J., Jones, L. R., Merrifield, M., McHardy, I. M., Lehto, H. J., & Luppino, G. A. 1994, Nature, 369, 462

Ponman, T. J., Bourner, P., Ebeling, H., & Bohringer, H. 1996, MNRAS, 283, 690

Prieur, J.-L. 1990, International Conference on Dynamics and Interactions of Galaxies, p. 72

Reda, F.M., Forbes, D.A., Beasley, M.A., OSullivan, E.J., & Goudfrooij, P. 2004, MNRAS, 354, 851

Reda, F. M., Forbes, D. A., & Hau, G. K. T. 2005, MNRAS, 360, 693

Reduzzi, L., Longhetti, M. & Rampazzo, R. 1996, MNRAS, 282, 149

Roberts, M. S. & Haynes, M. P. 1994, Ann. Rev. Astron. Astrophys., 32, 115

Romanishin, W. 1987, ApJ, 323, L113

Rubin, V. C., Hunter, D. A., & Ford, W. K., Jr. 1991, ApJS, 76, 153

Quinn, P. J. 1984, ApJ, 279, 596

Sabatini, S., Roberts, S., & Davies, J. 2003, Ap&SS, 285, 97

Salpeter, E. E. 1955, ApJ, 121, 161

Sandage, A. 1973, ApJ, 183, 711

Sandage, A. & Visvanthan, N. 1978, ApJ, 225, 742

Sanders, R.H. 1981, ApJ, 244, 820

Saracco, P. & Ciliegi, P. 1995, A&A, 301, 348

Sarazin, C.L. & O'Connell, R.W. 1983, ApJ, 268, 552

Sarazin, C. L., Irwin, J. A., & Bregman, J. N. 2000, ApJ, 544, L101

Sarazin, C.L., Irwin, J.A., & Bregman, J.N., 2001, ApJ, 556, 533

Scalo, J. M. 1986, Fundam. Cosm. Phys., 11, 1

Schlegel, D. J., Finkbeiner, D. P., & Davis, M. 1998, ApJ, 500, 525

Schombert, J. M. 1986, ApJS, 60, 603

Schweizer, F. 1982, ApJ, 252, 455

Schweizer, F. 1992, in Structure, Dynamics and Chemical Evolution of Elliptical Galaxies, eds. Danzinger, I. J., Zeiliger, W. W., Kjar, K., ESO/IPC, p. 651

Schweizer, F. 1996, in Galaxies: Interactions and Induced Star Formation, eds. Kennicutt, R. C. Jr., Scweizer, F., & Barnes, J. E., p. 105

Schweizer, F. 1998, in Galaxies: Interactions and Induced Star Formation, ed D. Friedli, L. Martinet, & D. Pfenniger (New York: Springer)

Searle, L. 1971, ApJ, 168, 327

Searle, L., & Sargent, W. L. W. 1972, ApJ, 173, 25

Searle, L., Sargent, W. L. W., & Bagnuolo, W. G. 1973, ApJ, 179, 427

Severgnini, P., Garilli, B., Saracco, P., & Chincarini, G. 1999, A&AS, 137, 495

Shields, G. A. 1990, ARA&A, 28, 525

Shimasaku, K., Fukugita, M., Doi, M., Hamabe, M. et al. 2001, AJ, 122, 1238

Shioya, Y. & Taniguchi, Y. 1993, PASJ, 45, 39

Silva, D. R., Boroson, T. A., Thompson, I. B., Jedrzejewski, R. I. 1989, AJ, 98, 131

Simien, F. & de Vaucouleurs, G. 1986, ApJ, 302, 56

Smith, R. K., Brickhouse, N. S., Liedahl, D. A., & Raymond, J. C. 2001, ApJ, 556, 91

Smith, J. A., Tucker, D. L., Kent, S. et al. 2002, AJ, 123, 2121

Smith, R.M., Martinez, V.J., & Graham, M.J. 2004a, ApJ, 617, 1017

Smith, R.M. & Martinez, V.J. 2004b, ASPC, 327, 328

Spitzer, L. Baade, W. 1951, ApJ, 113, 413

Stasinska, G., & Szczerba, R. 2001, A&A, 379, 1024

Stocke, J.T., Keeney, B.A., Lewis, A.D., Epps, H.W., & Schild, R.E. 2004, AJ, 127, 1336

Stoughton, C., Lupton, R. H., Bernardi, M. et al. 2002, AJ, 123, 485

Strateva, I. et al. 2001, AJ, 122, 186

Strauss, M. A., Weinberg, D. H., Lupton, R.H. et al. 2002, AJ, 124, 1810

Strom, K.M. & Strom, S.E. 1978, AJ, 83, 1293

Sulentic, J. W. & Rabaca, C. R. 1994, ApJ, 429, 531

Sulentic, J. W., Verdes-Montenegro, L., Bergond, G., Lisenfeld, U., Durbala, A., Espada, D., Garcia, E., Leon, S., Sabater, J., Verley, S., Casanova, V., & Sota, A. 2006, A&A, 449, 937

Sun, M., Forman, W., Vikhlinin, A., Hornstrup, A., & Murray, S.S. 2003, ApJ, 598, 250

Sun, M., Forman, W., Vikhlinin, A., Hornstrup, A., Jones, C., & Murray, S. S. 2004, ApJ, 612, 805

Takeda, H., Nulsen, P.E.J. & Fabian, A.C. 1984, MNRAS, 208, 261

Tammann, G. A. 1980, in Dwarf Galaxies, ed. M. Tarenghi & K. Kjar (Geneva: ESO), 3

Tanaka, Y., Inoue, H., & Holt, S. S. 1994, PASJ, 46, L37

Thomson, R.C. & Wright, A.E. 1990, MNRAS, 247, 122

Toomre, A. & Toomre, J. 1972, ApJ, 178, 623

Toomre, A. 1977, in The Evolution of Galaxies and Stellar Populations, ed. B.M. Tinsley, R.B. Larson, D.C. Gehret (New Haven: Yale University Observatory)

Torres-Peimbert, S., Peimbert, M., & Fierro, J. 1989, ApJ, 345, 186

Tovmassian, H. M., Plionis, M., & Andernach, H. 2004, ApJ, 617, L111

Trager, S.C, Worthey, G., Faber, S. M., Burstein, D., & Gonzalez, J. J. 1998, ApJS, 166, 1

Tremonti, C. A. et al. 2004, ApJ, 613, 898

Trinichieri, G. & Fabbiano, G. 1985, ApJ, 296, 447

Trinichieri, G., Noris, L., & di Serego Alighieri, S. 1997, A&A, 326, 565

Truemper, J. 1982, Adv. Space Res., 2, 241

Trumper, J. 1991, A&A, 246, L1

Tucker, D. L. et al. 2000, ApJS, 130, 237

Tully, R. B. 1987, ApJ, 321, 280

van Albada, T.S. 1982,MNRAS, 201, 939

van den Bergh, S. 1994, AJ, 107, 153

van den Bergh, S. 1989, PASP, 101, 1072

van den Bergh, S., Cohen, J. G., & Crabbe, C. 2001, AJ, 122, 611

Van Dokkum, P. G. 2005, AJ, 130, 2647

van Zee, L. 2000, AJ, 119, 2757

Veilleux, S. & Osterbrock, D. E. 1987, ApJS, 63, 295

Veilleux, S. & Osterbrock, D. E. 1989, in Astrophysics of Gaseous Nebulae and Active Galactic Nuclei

Verdes-Montenegro, L., Yun, M. S., Williams, B. A., Hutchmeier, W. K., Del Olmo, A., & Perea, J. 2001, A&A, 377, 812

Verdes-Montenegro, L., Sulentic, J., Lisenfeld, U., Leon, S., Espada, D., Garcia, E., Sabater, J., & Verley, S. 2005, A&A, 436, 443

Verdes-Montenegro, L., Yun, M. S., Borthakur, S., Rasmussen, J., Ponman, T. J. 2007, New Astron Revs., 51, 87

Verley, S., Odewahn, S. C., Verdes-Montenegro, L., Leon, S., Combes, F., Sulentic, J., Bergond, G., Espada, D., Garcia, E., Lisenfeld, U., & Sabater, J. 2007, A&A, 470, 505

Vincent, R. A. & Ryden, B. S. 2005, ApJ, 623, 137

Vikhlinin, A., McNamara, B. R., Hornstrup, A., Quintana, H., Forman, W., Jones, C., & Way, M. 1999, ApJ, 520, L1

Voges, W. 1992, in Proc. of Satellite Symp., 3, ed. T. D. Guyenne & J. J. Hunt, ESA ISY-3 (Noordwijk : ESA), 223

Weisskopf, M. C., Tananbaum, H. D., Van Speybroeck, L. P., & O'Dell, S. L. 1999, SPIE, 4012, 2

White, S.D.M. & Frenk, C.S. 1991, ApJ, 379, 52

White, N. & Ghosh, P. 1998, ApJ, 504, L31

White, N. E. & Marshall, F. E. 1984, ApJ, 281, 354

Willis, J. P., Hewett, P. C., Warren, S. J., & Lewis, G. F. 2002, MNRAS, 337, 953

Worthey, G. 1997, in: S.S. Holt, L. G. Mundy, eds., AIP Conf. Ser. Vol. 393, Star Formation Near and Far: Seventh Astrophysics Conference, Woodbury: AIP, p. 525

Wu, K. 2001, Publ. Astron. Soc. Australia, 18, 443

Yamaguchi, C., Ichikawa, S., Doi, M., Yasuda, N., Yagi, M., Fukugita, M., Okamura, S., Nakamura, O., Sekiguchi, M., & Goto, T. 2005, AJ, 130, 1545

Yasuda, N., Fukugita, M., et al. 2001, AJ, 122, 1104

Yin, S. Y., Liang, Y. C., Hammer, F., Brinchmann, J., Zhang, B., Deng, L. C., Flores, H. 2007, A&A, 462, 535

Yip, C. W., et al. 2004, AJ, 128, 585

York, D., et al. 2000, AJ, 120, 1579

Zabludoff, A.I., 2003, in The IGM/Galaxy Connection, ed. J.L. Rosenberg M.E. Putman (Dordrecht: Kluwer), 291

Zaritsky, D., Kennicutt, R. C., & Huchra, J. P. 1994, ApJ, 420, 87

Zaritsky, D., Zabludoff, A. I., & Willick, J. A. 1995, AJ, 110, 1602

Zepf, S.E., Whitmore, B.C. & Levison, H.F. 1991, ApJ, 383, 524

Zhao, Y., Gu, Q., et al. 2006, ChJAA, 6, 15

Zombeck, M. 2006, Handbook of Space Astronomy and Astrophysics: Third Edition, (Cambridge: Cambridge University Press)

VITA

Christopher R. Fuse was born on October 16, 1977 in St. Louis, Missouri to Robert and MaryBeth Fuse. He graduated from Saratoga Central Catholic High School in 1996 and enrolled in St. Bonaventure University. He graduated from Saint Bonaventure University with a Bachelor of Science degree in Physics. Following graduation he married Marisa Biette on June 3, 2000. He enrolled in the Physics Department at Miami University. He earned a Master of Science degree in Physics from Miami University in August 2002.

He was offered and accepted a visiting Instructor of Physics position at Miami University during 2003 – 2004. He later served as a chemistry teacher at Bishop Gorman High School in Las Vegas, Nevada during 2004 – 2005. In the fall of 2005, he enrolled in the graduate program at Texas Christian University and accepted a research assistantship. He was accepted into the doctoral program in the spring of 2007 and was also awarded a Texas Space Grant Fellowship.

Christopher earned his Doctor of Philosophy degree from TCU in December of 2008 and went on to an assistant professor position at Rollins College in Winter Park, Florida. He is a member of the American Astronomical Society, the American Physical Society, and the American Geophysical Union.

ABSTRACT

Isolated Early-Type Galaxies & the Use of X-ray Diagnostics to Determine the Evolution History of Merging and Merged Systems

by Christopher Robert Fuse, Ph.D., 2008

Department of

Texas Christian University

Director of Dissertation: Pamela M. Marcum, Associate Professor of Physics & Astronomy

The dissertation presented details the search for isolated early-type galaxies (IEG). A strict set of isolation criteria were employed, requiring the candidate galaxy to be separated from nearest neighbors of $M_V \leq -16.5$ by a distance of 2.5 Mpc and a redshift-space separation of 350 km s^{-1}. Such extreme isolation produces galaxies well suited as laboratories for the study of galaxy evolution, absent from the continual galaxy harassment observed for galaxies in group and cluster environments.

Global and surface photometry is used in verification of early-type morphology of the candidate galaxies. Two-dimensional residual maps, produced by model galaxy subtractions, are used to search for fine structure as well as isophotal deviations from a perfectly elliptical shape in the candidates. Clues provided by these analysis techniques are used to derive estimates of the past interaction history of the galaxies.

Also investigated was the viability of X-ray diagnostics to probe the evolutionary connection between compact groups, fossil groups (FG) and isolated ellipticals. Using the X-ray luminosity and gas temperatures, it was discovered that fossil groups are composed of two distinct populations. Population 1 FGs have X-ray characteristics similar to those of the compact groups and isolated ellipticals, while population 2 FGs are significantly hotter and more luminous. The results suggest that compact groups are the predecessors of isolated ellipticals and population 1 FGs. Population 2 FGs appear to be the remnants of a collapsed poor cluster.

The highlights of the research are summarized as: 84% of the IEGs have blue colors and spectra indicative of young stellar populations and recent star formation. The conclusion is that the IEGs have continued to experience accretion of dwarf-companions, which implies that even in extremely isolated galaxies, minor mergers strongly influence galaxy evolution. The faint nature of the IEGs, which are magnitudes fainter than previous isolated galaxy samples, imply that the IEGs are unlikely the remains of a collapsed group. Three sample galaxies are strong candidates for having a pristine nature and might serve as the near-zero interaction baseline necessary to separate the intrinsic galaxy properties and those properties induced by external interactions.